



# LUND UNIVERSITY

## Study of the production of $\pi$ , K and p in pp collisions at $\sqrt{s} = 13$ TeV as a function of the Transverse Spherocity and the Relative Transverse Activity

Vazquez Rueda, Omar

2022

*Document Version:*

Publisher's PDF, also known as Version of record

[Link to publication](#)

*Citation for published version (APA):*

Vazquez Rueda, O. (2022). *Study of the production of  $\pi$ , K and p in pp collisions at  $\sqrt{s} = 13$  TeV as a function of the Transverse Spherocity and the Relative Transverse Activity*. [Doctoral Thesis (monograph), Faculty of Science]. Lund.

*Total number of authors:*

1

*Creative Commons License:*

Unspecified

**General rights**

Unless other specific re-use rights are stated the following general rights apply:

Copyright and moral rights for the publications made accessible in the public portal are retained by the authors and/or other copyright owners and it is a condition of accessing publications that users recognise and abide by the legal requirements associated with these rights.

- Users may download and print one copy of any publication from the public portal for the purpose of private study or research.
- You may not further distribute the material or use it for any profit-making activity or commercial gain
- You may freely distribute the URL identifying the publication in the public portal

Read more about Creative commons licenses: <https://creativecommons.org/licenses/>

**Take down policy**

If you believe that this document breaches copyright please contact us providing details, and we will remove access to the work immediately and investigate your claim.

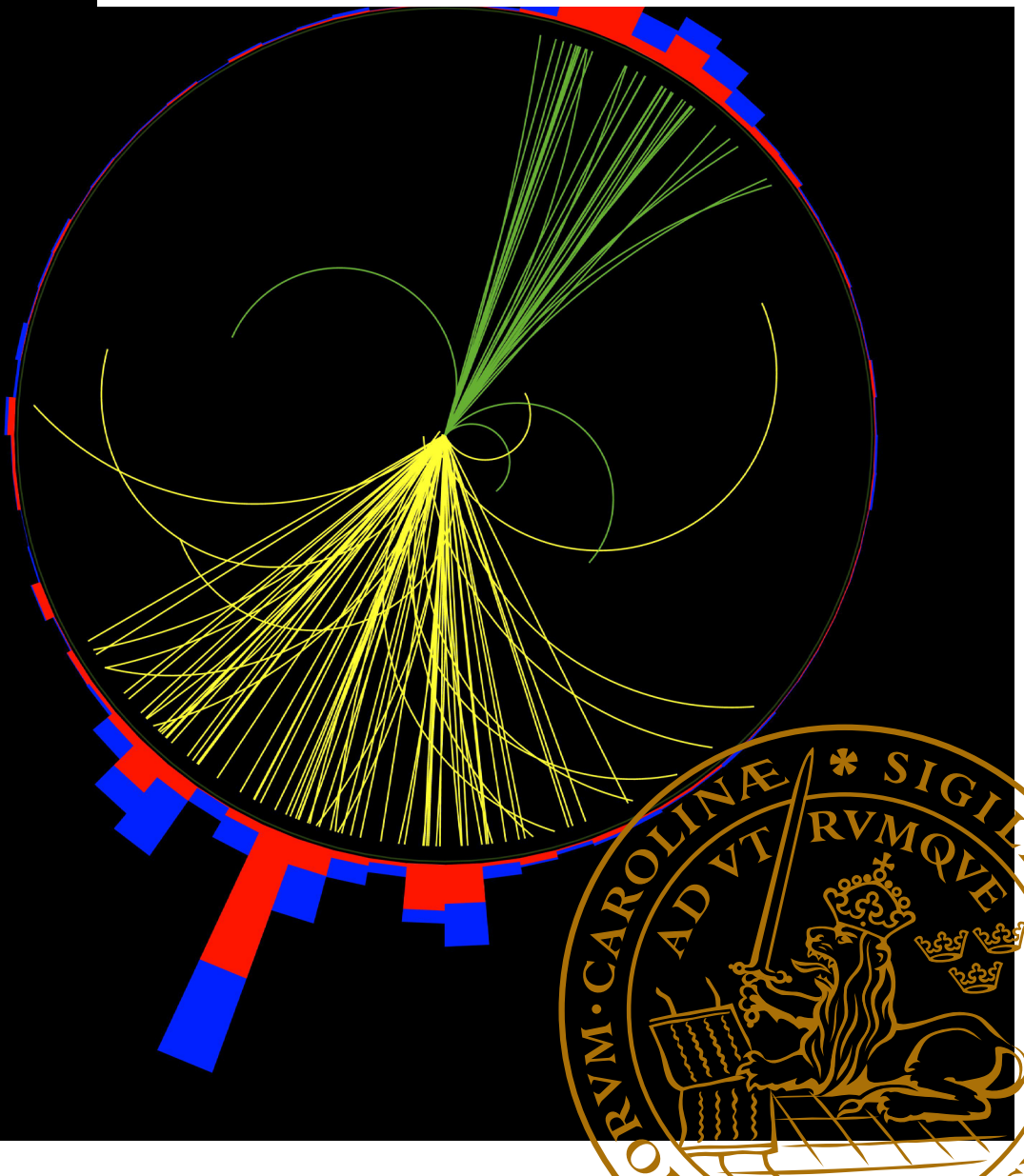
LUND UNIVERSITY

PO Box 117  
221 00 Lund  
+46 46-222 00 00

# Study of the production of $\pi$ , K and p in pp collisions at $\sqrt{s} = 13$ TeV as a function of the Transverse Spherocity and the Relative Transverse Activity

OMAR VÁZQUEZ RUEDA

DEPARTMENT OF PHYSICS | LUND UNIVERSITY | 2022





# Study of the production of $\pi$ , K and p in pp collisions at $\sqrt{s} = 13$ TeV as a function of the Transverse Spherocity and the Relative Transverse Activity

by Omar Vázquez Rueda



LUND  
UNIVERSITY

Thesis for the degree of Doctor of Philosophy  
Thesis advisors: Dr. Alice Ohlson, Prof. Peter Christiansen,  
Dr. David Silvermyr

To be presented, with the permission of the Faculty of Science of Lund University, for public criticism in  
the Rydberg lecture hall (Rydbergsalen) on Friday, the 10th of June 2022 at 13:15.

Organization <b>LUND UNIVERSITY</b>	Document name <b>DOCTORAL DISSERTATION</b>
	Date of disputation 2022-06-10
Department of Physics Box 118 S-221 00 LUND Sweden	Sponsoring organization
Author(s) Omar Vázquez Rueda	
Title Study of the production of $\pi$ , K and p in pp collisions at $\sqrt{s} = 13$ TeV as a function of the Transverse Spherocity and the Relative Transverse Activity	
<p><b>Abstract</b>          High-energy heavy-ion collisions allow the Quark–Gluon Plasma (QGP) production and study, a state of high-density QCD matter in which quarks and gluons are no longer confined inside hadrons for a very short time. Different observables reveal an enhanced production of strange hadrons, signatures of collective effects and opacity to jets due to the QGP formation. However, collective effects and strangeness enhancement are also observed in pp and p–Pb collisions (small systems) with high charged-particle multiplicity. These observations in small systems are very puzzling since the QGP is not expected to be formed since the small systems are considered too dilute and too short-lived.</p> <p>In this thesis, I present a study on the production of <math>\pi</math>, K and p in pp collisions at <math>\sqrt{s} = 13</math> TeV using data recorded by the ALICE experiment. To investigate the origins of collective effects and strangeness enhancement, I measure the particle production as a function of the Relative Transverse Activity (<math>R_T</math>) and the Transverse Spherocity (<math>S_0^{p_T=1}</math>). In the <math>R_T</math> analysis, particle production is measured in different topological regions (toward, away, and transverse) with respect to the leading charged track per event. The toward and away regions mainly contain the fragmentation products of the jet, while the Underlying Event dominates the transverse. The <math>p_T</math> spectra and <math>K/\pi</math> and <math>p/\pi</math> ratios are measured as a function of <math>R_T = N_T/\langle N_T \rangle</math>, where <math>N_T</math> is the charged-particle multiplicity in the transverse region. It is observed that the <math>K/\pi</math> and <math>p/\pi</math> ratios increase with increasing <math>R_T</math> in the toward region, while little <math>R_T</math> dependence is observed in the transverse. Models tuned to <math>e^+e^-</math> results describe the low-<math>R_T</math> particle ratios qualitatively.</p> <p>The transverse spherocity is an event shape observable that can disentangle jet-like from isotropic topologies. I studied particle production in high-multiplicity events as a function of spherocity. I contrast the results obtained using a forward and a mid-pseudorapidity multiplicity estimator. The results show that the mid-pseudorapidity estimator combined with the spherocity selection allows selecting events with more significant variations in the average transverse momentum (<math>\langle p_T \rangle</math>) than the forward estimator. I present the <math>p_T</math> spectra and particle ratios as a function of <math>S_0^{p_T=1}</math>. Finally, all the data results are contrasted with microscopic models.</p>	
<p><b>Key words</b>          LHC, ALICE, quark-gluon plasma, small systems, pp collisions, underlying event, spherocity, transverse activity.</p>	
<p><b>Classification system and/or index terms (if any)</b></p>	
<p><b>Supplementary bibliographical information</b></p>	
<p>Language English</p>	
<p><b>ISSN and key title</b></p>	
<p>ISBN 978-91-8039-281-5 (print) 978-91-8039-282-2 (pdf)</p>	
<p><b>Recipient's notes</b></p>	
<p>Number of pages 198</p>	
<p>Price</p>	
<p>Security classification</p>	

I, the undersigned, being the copyright owner of the abstract of the above-mentioned dissertation, hereby grant to all reference sources the permission to publish and disseminate the abstract of the above-mentioned dissertation.

Signature

Date 2022-06-10

# Study of the production of $\pi$ , K and p in pp collisions at $\sqrt{s} = 13$ TeV as a function of the Transverse Spherocity and the Relative Transverse Activity

by Omar Vázquez Rueda



LUND  
UNIVERSITY

**Cover illustration front:** An event display by the CMS Collaboration with two top quarks, each decaying into a jet.

© Omar Vázquez Rueda 2022

Faculty of Science, Department of Physics

isbn: 978-91-8039-281-5 (print)

isbn: 978-91-8039-282-2 (pdf)

Printed in Sweden by Media-Tryck, Lund University, Lund 2022



Media-Tryck is a Nordic Swan Ecolabel certified provider of printed material.  
Read more about our environmental work at [www.mediatryck.lu.se](http://www.mediatryck.lu.se)

MADE IN SWEDEN

## Abstract

High-energy heavy-ion collisions allow the Quark–Gluon Plasma (QGP) formation and study. It is a state of high-density QCD matter in which quarks and gluons are free to roam over distances more considerable than the size of the nucleon. Then, the QGP thermalises, cools down, and eventually, hadronisation occurs. Since quarks and gluons can not be directly detected, everything that can be known about the QGP is through the detection of final state hadrons. In some sense, these hadrons are imprinted with information about the QGP properties. For example, the low transverse momentum ( $p_T$ ) identified particles can provide information about radial and anisotropic flow, phenomena associated with collective effects, while high- $p_T$  hadrons can be used as jets proxies for studying parton energy loss in the medium. However, in recent years, signatures of collective effects and strangeness enhancement have also been observed in pp and p–Pb collisions with high charged-particle multiplicity. The systems created in such collisions are commonly called “small systems” due to their much smaller size than those of Pb–Pb collisions. However, these signatures in small systems are pretty puzzling since QGP formation is not expected, given that they are too dilute and short-lived.

The core of this thesis is the results from four physics data analyses performed with the data collected by the ALICE experiment. In chronological order, the first study uses Pb–Pb data at  $\sqrt{s_{NN}} = 5.02$  TeV to measure the  $p_T$  spectra of  $\pi$ , K and p as a function of the centrality of the event. The spectra is reported in the  $p_T$  interval,  $0.1 - 20$  GeV/ $c$  and in  $|\eta| < 0.8$ . This study revealed the presence of a strong radial flow that increases with the centrality of the event. Furthermore, comparisons with results at lower energies suggest an increase of the transverse radial velocity with the colliding energy. In addition, the high- $p_T$  spectra are used to study the effects of parton energy loss in the medium. By measuring the Nuclear Modification Factor ( $R_{AA}$ ) as a function of the centrality of the event, it is observed that all high- $p_T$  hadrons are equally suppressed. Furthermore, the  $R_{AA}$  measured in Pb–Pb collisions at  $\sqrt{s_{NN}} = 2.76$  TeV and  $\sqrt{s_{NN}} = 5.02$  TeV is the same.

The second study reports the production of  $\pi$ , K and p in pp collisions at  $\sqrt{s} = 13$  TeV as a function of the forward multiplicity. The  $p_T$  spectra is reported in the  $p_T$  interval,  $0.1 - 20$  GeV/ $c$  in  $|\eta| < 0.8$ . The  $p_T$ -differential  $p/\pi$  ratio exhibits an enhancement at  $p_T \approx 3$  GeV/ $c$ , being more relevant for events with the highest multiplicities. This effect is attributed to collective radial flow. The results in Pb–Pb and pp collisions as a function of the multiplicity will not be discussed in the results section. Instead, they are added to the introductory sections to the field of high-energy heavy-ion collisions and experimental overview of small collision systems since they are by now the standard experimental measurements in heavy-ion collisions.

The two remaining analyses are also performed in the realm of small systems. They aim to investigate the origins of collective effects in pp collisions. I analysed data from pp collisions at  $\sqrt{s} = 13$  TeV to measure the production of  $\pi$ , K, and p at mid-pseudorapidity ( $|\eta| < 0.8$ ) as a function of the Relative Transverse Activity ( $R_T$ ) and the Unweighted Transverse Spherocity ( $S_0^{p_T=1}$ ). In the first study, I measured the production of  $\pi$ , K, and p as a function of the Underlying Event (UE). However, only events with a leading charged-particle track detected at mid-pseudorapidity and in the transverse momentum interval,  $5 - 40$  GeV/c, are considered. Particle production is measured in different topological regions based on the angular difference,  $|\Delta\varphi| = |\varphi^{\text{lead}} - \varphi^{\text{track}}|$ : “toward” ( $|\Delta\varphi| < 60^\circ$ ), “transverse” ( $60^\circ < |\Delta\varphi| < 120^\circ$ ) and “away” ( $|\Delta\varphi| > 120^\circ$ ). While the toward and away regions contain the fragmentation products of the near-side and the away-side jet, respectively, the UE dominates the transverse. The transverse activity classifier,  $R_T = N_T/\langle N_T \rangle$ , where  $N_T$  is the charged-particle multiplicity measured in the transverse region, is used to control the amount of UE. In this study, I present a method based on the Bayesian unfolding to correct the  $R_T$  distribution for detector effects. Furthermore, I describe an extension of the method to obtain the fully corrected  $p_T$  spectra of identified particles as a function of  $R_T$ . It is observed that the relative production of high transverse momentum particles decreases with increasing  $R_T$  in both the toward and away regions, indicating a dilution of the jet with increasing UE. Conversely, the spectral shapes in the transverse region harden with increasing  $R_T$ , i.e., the production of high- $p_T$  particles grows with increasing  $R_T$  with respect to the  $R_T$ -integrated spectrum. These observations suggest a complex interplay in the UE between radiative processes and radial-flow like effects. Finally, it was observed that the  $p_T$ -differential particle ratios (K/ $\pi$  and p/ $\pi$ ) in the low UE limit ( $R_T \rightarrow 0$ ) approach expectations from fragmentation models tuned to  $e^+e^-$  results.

The unweighted transverse spherocity is an event shape observable that can disentangle jet-like from isotropic topologies. The topology of an event is characterised by the geometrical distribution of the azimuthal angles of the particles. In this analysis, I study the particle production in pp collisions at  $\sqrt{s} = 13$  TeV in high-multiplicity events as a function of spherocity. I contrast the results obtained using a forward and a mid-pseudorapidity multiplicity estimator. The results show that the mid-pseudorapidity estimator combined with the spherocity selection allows one to select events based on their hardness. The average transverse momentum ( $\langle p_T \rangle$ ) measured in events selected with the mid-pseudorapidity estimator showed a clear evolution towards higher values going from isotropic to jet-like topologies. Conversely, the forward estimator showed that the behaviour of the  $\langle p_T \rangle$  was a rather tenuous one when plotted as a function of spherocity.

# Populärvetenskaplig sammanfattning

Högenergikollisioner med tunga joner gör det möjligt att skapa och studera det s.k. Quark-Gluon Plasma (QGP). Det är ett tillstånd av QCD-materia med hög densitet där kvarkar och gluoner är fria att röra sig över avstånd som är större än storleken av en nukleon. Sedan termaliseras QGP, kyls ner och så småningom binds kvarkarna i hadroner. Eftersom kvarkar och gluoner inte kan detekteras direkt, studeras via QGP indirekt genom detektering av hadroner från kollisions sluttillstånd. I någon mening bär dessa hadroner med sig information om QGP-egenskaperna. Till exempel kan identifierade partiklar med låga transversella rörelsemängder ( $p_T$ ) ge information om radiellt och anisotrop flöde, fenomen som är förknippade med kollektiva effekter, medan high- $p_T$  hadroner kan användas som alternativ till jets för att studera partoners energiförlust i mediet. Dock har under de senaste åren signaturer av kollektiva effekter och förstärkning av antalet sär-kvarkar också observerats i pp- och p–Pb-kollisioner med ett hög antal laddade partiklar. Systemen som skapas i sådana kollisioner kallas vanligtvis ”små system” på grund av deras mycket mindre storlek än motsvarande system i Pb–Pb-kollisioner. Dessa signaturer i små system är dock ganska förbryllande eftersom QGP-bildning inte förväntats där, med tanke på att de har mindre täthet och är mer kortlivade.

Kärnan i denna avhandling är resultaten från fyra fysikanalyser utförda med data som samlats in av ALICE-experimentet. I kronologisk ordning använder den första studien Pb–Pb-data vid  $\sqrt{s_{NN}} = 5.02$  TeV för att mäta  $p_T$ -spektra för  $\pi$ , K och p som en funktion av kollisionshändelsens centralitet. Spektrat rapporteras i  $p_T$ -intervallet,  $0,1 - 20$  GeV/c och i  $|\eta| < 0,8$ . Denna studie avslöjade närvaron av ett starkt radiellt flöde som ökar med händelsens centralitet. Jämförelser med resultat vid lägre energier antyder också en ökning av den transversella radiella hastigheten med kollisionsenergin. Dessutom används hög- $p_T$ -spektra för att studera effekterna av energiförlust för partonerna i mediet. Genom att mäta modifieringsfaktorn ( $R_{AA}$ ) som en funktion av händelsens centralitet, observeras att alla hög- $p_T$  hadroner är lika undertryckta. Dessutom är  $R_{AA}$  uppmätt i Pb–Pb-kollisioner vid  $\sqrt{s_{NN}} = 2.76$  TeV och  $\sqrt{s_{NN}} = 5.02$  TeV densamma.

Den andra studien rapporterar produktionen av  $\pi$ , K och p i pp kollisioner vid  $\sqrt{s} = 13$  TeV som en funktion av antalet partiklar i en framåtgående riktning.  $p_T$  spektra rapporteras i  $p_T$  intervallet,  $0,1 - 20$  GeV/c i  $|\eta| < 0,8$ .  $p/\pi$  förhållandet uppvisar en ökning vid  $p_T \approx 3$  GeV/c, vilket är mer relevant för händelser med den högsta multipliciteten. Denna effekt tillskrivs kollektivt radiellt flöde. Resultaten i Pb–Pb och pp-kollisioner som funktion av multipliciteten diskuteras inte i resultatavsnittet. Istället beskrivs de i de inledande avsnitten, om högenergikollisioner med tunga joner och den experimentella översikten över små kollisionssystem, eftersom de vid det här laget

är standardmätningar för tungjonskollisioner.

De två återstående analyserna utförs också inom ”små system” området. De avser att undersöka ursprunget till kollektiva effekter i pp-kollisioner. Jag analyserade data från pp-kollisioner vid  $\sqrt{s} = 13$  TeV för att mäta produktionen av  $\pi$ , K och p vid mid-pseudorapiditet ( $|\eta| < 0.8$ ) som en funktion av den relativas transversella aktiviteten ( $R_T$ ) och den oviktade transversella sfärociten ( $S_0^{p_T=1}$ ). I den första studien mätte jag produktionen av  $\pi$ , K och p som en funktion av den underliggande händelsen (UE). Endast händelser med ett ledande laddad-partikel-spår som detekterats i ett visst pseudorapiditets- och transversellt rörelsemängs-intervall,  $5 - 40$  GeV/c, beaktas dock. Partikelproduktion mäts i olika topologiska regioner baserat på skillnaden i azimutvinkel,  $|\Delta\varphi| = |\varphi^{\text{lead}} - \varphi^{\text{track}}|$ : ”mot” ( $|\Delta\varphi| < 60^\circ$ ), ”transversell” ( $60^\circ < |\Delta\varphi| < 120^\circ$ ) och ”bort” ( $|\Delta\varphi| > 120^\circ$ ). Medan mot- och bortområdena innehåller fragmenteringsprodukterna från jet-skuren på nära- och bortsidan, domineras UE av transversella området. Den transversella aktivitetsklassificeraren,  $R_T = N_T/\langle N_T \rangle$ , där  $N_T$  är antalet laddade partiklar uppmätt i det transversella området, används för att styra mängden UE. I denna studie presenterar jag en metod baserad på betingad sannolikhet för att korrigera  $R_T$ -fördelningen för detektoreffekter. Vidare beskriver jag en utökning av metoden för att erhålla fullt korrigrade  $p_T$ -spektra av identifierade partiklar som en funktion av  $R_T$ . Det observeras att den relativas produktionen av partiklar med hög transversell rörelsemängd minskar med ökande  $R_T$  i både mot- och bortområdena, vilket indikerar en utspädning av jet-skuren med ökande UE. Omvänt hårdnar de spektrala formerna i det transversella området med ökande  $R_T$ , dvs produktionen av hög- $p_T$  partiklar växer med ökande  $R_T$  med avseende på  $R_T$ -integrerade spektrum. Dessa observationer antyder ett komplext samspel i UE mellan strålningsprocesser och radiella flödesliknande effekter. Slutligen observerades det att  $p_T$ -differentialpartikelförhållandena (K/ $\pi$  och p/ $\pi$ ) i den låga UE-gränsen ( $R_T \rightarrow 0$ ) närmrar sig förväntningarna från fragmenteringsmodeller som anpassats till  $e^+e^-$  resultat.

Den oviktade transversella sfärociten är en observabel baserad på händelsens struktur och kan urskilja mellan jetliknande och isotropiska topologier. Topologin för en händelse kännetecknas av den geometriska fördelningen av partiklarnas azimutvinklar. I denna analys studerar jag partikelproduktionen i pp-kollisioner vid  $\sqrt{s} = 13$  TeV i händelser med högt antal laddade partiklar som en funktion av sfärocitet. Jag jämför resultaten som erhållits med en framåt- alternativt en mid-pseudorapiditet-uppskattare. Resultaten visar att mid-pseudorapiditet-uppskattaren i kombination med valet av sfärocitet tillåter en att välja händelser baserat på deras hårdhet. Det genomsnittliga transversella momentumet ( $\langle p_T \rangle$ ) uppmätt i händelser valda med mid-pseudorapiditet-uppskattaren visade en tydlig utveckling mot högre värden från isotropa till jetliknande topologier. Omvänt, med den framåtriktade uppskattaren, upptäcktes  $\langle p_T \rangle$  en otydlig utveckling när

det studerades som en funktion av sfärocitet.

## Acknowledgements

First of all, I am very thankful for Lund University's opportunity to become a doctoral student at a very prestigious university and great place. Because of this opportunity, I could meet fascinating and intelligent people and visit many exciting places during conferences, workshops, and schools. But, more importantly, during the last four years, I have grown as a scientist. Many of these accomplishments were possible thanks to the help of my advisors, Peter Christiansen, David Silvermyr and Alice Ohlson.

Peter, you inspired me in the field of particle physics. Thank you for the time you spent discussing physics with us, and for the many times I asked you for feedback regarding conference proceedings, presentations, abstracts, and the careful review of my thesis. I enjoyed the freedom you gave me to develop things and test ideas. Many of the results presented in my thesis would not have been possible without your guidance. David, thank you for reading my thesis, providing feedback and your help with the administrative things throughout the years. Finally, Alice, thank you for the discussions and suggestions regarding my analysis.

To the ALICE PhDs, you have all been excellent friends. Jonatan and Adrian, thank you for helping me when I arrived in Lund. Adrian also for booking my flights during my first months. We had great times during the schools and conferences that we attended at the beginning of our PhDs: Tel Aviv, Helsinki, Copenhagen, and CERN. Oliver, we also had great times at Lund and when going to conferences. Thanks for planning the trip to China. Thank you, Vytautas and Sumit, for generating the Herwig and Epos predictions.

I also want to thank Florido for the IT support. You were always very effective. Furthermore, Bozena, for the administrative work regarding my employment and Vincent, for reviewing my thesis. Finally, I want to thank the ATLAS students and professors for the excellent working environment and the "Fikas".

To my wife, Ana Cristina, thank you for the patience and support during the last stage of my PhD. You have also been a critical element in my PhD's successful conclusion. Finally, to my brother Eduardo and my parents, Benjamin and Olimpia, thank you for all the support and love.

# Contents

<b>I Analysis Motivation</b>	<b>1</b>
<b>1 Introduction</b>	<b>3</b>
<b>2 Fundamental Theory</b>	<b>6</b>
2.1 Kinematic Variables . . . . .	6
2.2 The Standard Model of Particle Physics . . . . .	9
2.3 Interactions . . . . .	10
2.3.1 The Boson Propagator . . . . .	11
2.3.2 Electromagnetic Interactions . . . . .	12
2.3.3 Strong Interactions . . . . .	14
2.3.4 Running Couplings in QED and QCD . . . . .	16
2.3.5 Lattice QCD . . . . .	18
<b>3 High-Energy Nuclear Collisions</b>	<b>20</b>
3.1 The QCD Phase Diagram . . . . .	20
3.2 History of a Heavy-Ion Collision . . . . .	21
3.2.1 The Early Time Dynamics . . . . .	22
3.2.2 The Quark-Gluon Plasma . . . . .	25
3.2.3 The Temperature of the QGP . . . . .	25
3.2.4 The Chemical Freeze-Out . . . . .	26
3.2.5 The Kinetic Freeze-Out . . . . .	29
3.3 Anisotropic Flow . . . . .	32
3.4 Parton Energy Loss . . . . .	35
3.5 Heavy-Quarkonia Suppression . . . . .	37
3.6 Experimental Overview on Small Collision Systems . . . . .	39
3.7 The CLASH Project . . . . .	44
<b>4 Phenomenological Models</b>	<b>45</b>
4.1 The Lund String Model . . . . .	45
4.1.1 Multiple Parton Interactions and Colour Reconnection . . . . .	49
4.2 The EPOS Model . . . . .	51

<b>II Experimental Setup</b>	<b>53</b>
<b>5 Charged-Particle Detection</b>	<b>55</b>
5.1 Momentum Measurement . . . . .	55
5.2 Energy Loss of Charged Particles by Ionisation . . . . .	58
5.2.1 The Bethe-Bloch Formula . . . . .	59
5.2.2 Statistical Fluctuations of Energy Loss . . . . .	61
5.2.3 The Landau-Vavilov Distribution . . . . .	62
5.2.4 Suppression of Fluctuations . . . . .	64
5.3 Time-Of-Flight Measurements . . . . .	65
<b>6 The ALICE Detector</b>	<b>68</b>
6.1 Detector Overview . . . . .	68
6.2 The V0 Detector . . . . .	70
6.2.1 Centrality Determination in ALICE . . . . .	71
6.2.2 Particle Production Dependence on $N_{\text{part}}$ and $N_{\text{coll}}$ . . . . .	72
6.3 The ITS Detector . . . . .	74
6.4 The TPC Detector . . . . .	76
6.5 The TOF Detector . . . . .	79
6.6 Track Reconstruction . . . . .	81
6.7 Interaction Vertex Reconstruction . . . . .	83
<b>III Proton-Proton Data Analysis</b>	<b>85</b>
<b>7 Event, Vertex and Track Selection</b>	<b>87</b>
7.1 Event Selection . . . . .	87
7.2 Vertex Selection . . . . .	88
7.3 Track Selection . . . . .	88
<b>8 Particle Identification and Event Shape Observables</b>	<b>92</b>
8.1 Particle Identification . . . . .	93
8.1.1 Signal Extraction . . . . .	93
8.1.2 Particle Fractions . . . . .	99
8.1.3 Corrections . . . . .	101
8.1.4 Constructing the $p_T$ Spectra . . . . .	105
8.2 Relative Transverse Activity Classifier . . . . .	106
8.2.1 One-Dimensional Unfolding . . . . .	109
8.2.2 Statistical Uncertainties in the Bayesian Unfolding Method . . . . .	112
8.2.3 Unfolding the Particle Spectra . . . . .	113
8.2.4 Monte Carlo Closure Test . . . . .	115
8.3 Unweighted Transverse Spherocity . . . . .	117
8.3.1 High-Multiplicity Studies . . . . .	119
8.3.2 Spherocity Cuts . . . . .	120

8.3.3	Evaluation of the Experimental Bias . . . . .	120
<b>9</b>	<b>Systematic Uncertainties</b>	<b>123</b>
9.1	PID Systematic Uncertainties . . . . .	123
9.2	Tracking Uncertainties . . . . .	126
9.3	$R_T$ and $S_0^{p_T=1}$ Dependent Systematic Uncertainty . . . . .	127
<b>10</b>	<b>Results and Discussion</b>	<b>129</b>
10.1	Production of $\pi$ , K and p as a Function of the UE Activity . . . . .	129
10.1.1	$\langle p_T \rangle$ and $p_T$ -Integrated Particle Ratios . . . . .	131
10.1.2	Transverse Momentum Spectra of $\pi$ , K and p . . . . .	135
10.1.3	$p_T$ -Differential Particle Ratios . . . . .	140
10.2	Production of $\pi$ , K and p as a Function of the Transverse Spherocity . . . . .	143
10.2.1	Studying the Extremes of Multiplicity and Spherocity . . . . .	147
<b>11</b>	<b>Conclusions</b>	<b>159</b>
<b>IV</b>	<b>Appendices</b>	<b>161</b>
<b>A</b>	<b>Geometrical Cut In The rTPC Analysis</b>	<b>163</b>
<b>B</b>	<b>Complementary Figures</b>	<b>164</b>
	<b>References</b>	<b>173</b>



## **Part I**

# **Analysis Motivation**



# Chapter 1

## Introduction

The potential between a quark-antiquark pair separated by a large distance  $r$  is proportional to the distance between the two. This potential is associated with the confinement of quarks and gluons inside hadrons. Because of the linear proportionality, attempts to free a quark from a hadron result in the production of fresh  $q\bar{q}$  pairs, i.e. mesons. Quarks and gluons are the building blocks of “nucleons” (collective term for protons and neutrons). Nucleons build up the nuclei. Under normal conditions the nuclear ground state energy density ( $\varepsilon_0$ ) is about  $0.15 \text{ GeV}/\text{fm}^3$ . However, at high densities and/or temperatures, quarks and gluons are expected to deconfine and can roam freely over distances larger than the size of the nucleon (about  $1 \text{ fm} = 10^{-15} \text{ m}$ ) [1, 2]. Such a medium in which quarks and gluons are deconfined is named the Quark-Gluon Plasma (QGP), and it is believed that this was the state of the universe for a few microseconds after the Big Bang [3]. Nowadays, high-energy nuclear collisions aim to produce and study the QGP properties.

With the advent of the heavy-ion programme of the Relativistic Heavy-Ion Collider (RHIC) at Brookhaven in the United States, many experimental results have been gathered. One of the most surprising results was the creation of a strongly interacting medium of deconfined QCD matter [4–6]. In the year 2010, the LHC at CERN in Geneva, Switzerland started to collide lead nuclei at the unprecedented collision energy of  $\sqrt{s_{\text{NN}}} = 2.76 \text{ TeV}$ , this represents more than a factor of 10 larger than previously available. Measurements of direct photons in central Pb–Pb collisions at the LHC revealed a temperature of an equilibrated QGP of about  $297 \pm 12^{\text{stat}} \pm 41^{\text{syst}} \text{ MeV}$  [7]. This temperature is well above the critical temperature ( $T_c$ ) calculated in lattice QCD to be in the range  $155 – 160 \text{ MeV}$  [8] in which nuclear matter undergoes a phase transition to a deconfined state of quarks and gluons. Currently, it is well known that the quark-gluon plasma evolves through a collective expansion and that the medium is opaque to

jets.

Interestingly, the study of pp and p–Pb collisions has revealed effects reminiscent of heavy-ion collisions. Such effects include the observations of flow-like phenomena [9] and enhanced production of strange hadrons in high multiplicity events [10]. Consequently, a new community devoted to studying small collision systems was born.

My thesis is divided into three parts. Part I includes chapters 2, 3 and 4. In Ch. 2, I introduce the theory of elementary particle physics and their interactions. Then, Ch. 3 presents the history of a high-energy nucleus-nucleus collision, describing the different stages of the collision and some QCD inspired models commonly used to describe the data at the LHC. My results in Pb–Pb collisions complement this chapter. The reason is that these measurements are now part of the new standard set of heavy-ion results. At the end of this chapter, I discuss selected results in small systems related to effects reminiscent of nuclear collisions — namely, collective effects and strangeness enhancement. Here, I also show my results about the inclusive measurement of  $\pi$ , K and p as a function of the multiplicity in pp collisions at  $\sqrt{s} = 13$  TeV. The discussion about small systems is helpful since the primary motivation of this thesis lies in understanding the origins of collective effects and the underlying physics mechanisms for particle production in pp collisions. Finally, Ch. 4 gives an overview of Monte Carlo event generators.

Part II includes chapters 5 and 6. Chapter 5 starts with a discussion about charged-particle detection and identification. Since this thesis is about measurements of identified particles, I would like the reader to appreciate the physics behind particle detection before describing the ALICE apparatus. Next, Ch. 6 introduces the ALICE experiment. Here, the focus is on the detectors used in my analyses.

Part III includes chapters 7, 8, 9 and 10. Chapters 7 to 9 presents the physics analyses using data collected by ALICE in pp collisions. I will not present details on the analysis methods used in the Pb–Pb analysis since the particle identification performed there is the same as the one done in pp collisions. Furthermore, the pp analyses comprise more elaborated methods, such as unfolding. Finally, in Ch. 10, I present the results and discuss their physics interpretation.

## My Contributions

My doctoral studies were mainly dedicated to analysing data recorded by ALICE during the Run 2 of the LHC. The Run 2 data taking started in 2015 and ended with the start of the Long Shutdown 2 (LS2) in 2018.

The first part of my PhD is marked by the publication of my first ALICE paper, which is about the measurement of the  $p_T$  spectra of charged  $\pi$ , K and p in Pb–Pb collisions at  $\sqrt{s_{NN}} = 5.02$  TeV. The  $p_T$  spectra is reported in the  $p_T$  interval,  $0.1 - 20$  GeV/ $c$ . I contributed to the measurements of identified particles using the Time Projection Chamber (TPC) at low  $p_T$  ( $0.3 < p_T \lesssim 1$  GeV/ $c$ ) and in the relativistic rise of the TPC ( $2 \leq p_T < 20$  GeV/ $c$ ). After the Pb–Pb publication, I studied the small systems where I contributed to the measurement of the  $p_T$  spectra of  $\pi$ , K and p at high  $p_T$  in pp collisions at  $\sqrt{s} = 13$  TeV as a function of multiplicity of the event.

After this first approach to the small systems, I realised that including additional dimensions in the multiplicity-dependent studies was necessary. That is, go more differential better to understand the different underlying mechanisms of particle production. The first attempt used spherocity to isolate jetty-like events from isotropic ones. In a combined effort, it was possible to measure the  $p_T$  spectra of  $\pi$ , K, p,  $K_S^0$ ,  $\Lambda$ ,  $\Xi$ ,  $\phi$  and  $K^{*0}$  as a function of spherocity.

My last physics analysis is about measuring the production of  $\pi$ , K and p as a function of the UE. In this analysis, I developed a correction procedure based on the Bayesian unfolding to fully correct the  $p_T$  spectra of identified particles as a function of  $R_T$ . This approach has been applied to the  $p_T$  spectra of  $\pi$ , K and p, but it will be used for strange and multi-strange hadrons.

I show below the list of publications obtained within my PhD. The last two are paper proposals approved by ALICE.

1. Production of charged pions, kaons, and (anti-)protons in Pb–Pb and inelastic pp collisions at  $\sqrt{s_{NN}} = 5.02$  TeV. *Phys. Rev. C* **101**, 044907.
2. Multiplicity dependence of  $\pi/K/p$  production in pp collisions at  $\sqrt{s} = 13$  TeV. *Eur. Phys. J. C* **80** (2020) 693.
3. Identified light-flavour particle production in “jetty” and “isotropic” events in pp collisions at  $\sqrt{s} = 13$  TeV with ALICE at the LHC.
4. Production of pions, kaons and (anti-)protons as a function of  $R_T$  in pp collisions at  $\sqrt{s} = 13$  TeV.

# Chapter 2

## Fundamental Theory

The first section of this chapter introduces the kinematic variables used in high-energy physics experiments. Then I present a brief description of the Standard Model of Particle Physics (SM). The SM describes ordinary matter, such as protons, atoms and nuclei, in terms of elementary particles and their interactions. Since all the material included in this chapter corresponds to university courses, the discussion presented here is based on the books of Cheuk-Yin Wong [11], Donald H. Perkins [12] and Brian R. Martin and Graham Shaw [13].

### 2.1 Kinematic Variables

In high-energy physics and relativistic heavy-ion collision experiments, it is convenient to use kinematic variables with simple properties under a change of reference frame. For example, quantities such as the rapidity ( $y$ ), the pseudorapidity ( $\eta$ ) and the  $p_T$  have simple properties under Lorentz transformations. This section will discuss the definition of such variables to set the language of particle collisions at relativistic energies.

The space-time coordinates of a point  $x$  are defined by a four-vector with components  $x^\mu$  defined as:

$$x^\mu = (x^0, x^1, x^2, x^3) = (t, \mathbf{x}) = (t, x, y, z), \quad (2.1)$$

where the  $x, y$  and  $z$  components represent the coordinates in the Euclidean space. The

four-momentum vector  $p$  is defined in a similar way with components  $p^\mu$  as:

$$p^\mu = (p^0, p^1, p^2, p^3) = (E, \mathbf{p}) = (E, p_x, p_y, p_z), \quad (2.2)$$

where  $E$  is the total energy of the particle and  $p_x, p_y$  and  $p_z$  are the  $x, y$  and  $z$  components of the three-momentum vector. The transverse momentum of a particle is defined as:

$$p_T^2 = p_x^2 + p_y^2. \quad (2.3)$$

The transverse momentum is a helpful quantity because it is Lorentz invariant under Lorentz transformations along the beamline ( $z$ -axis). Furthermore, the  $p_T = 0$  for the beams before the collision, thus all the  $p_T$  in the final state particles must be dynamically created in the collision.

The rapidity of a particle is defined as:

$$y = \frac{1}{2} \ln \left( \frac{E + p_z c}{E - p_z c} \right), \quad (2.4)$$

where  $c$  is the speed of light. Equation 2.4 defines the rapidity of a particle measured in the laboratory frame  $F$ . The rapidity  $y'$  of the particle in a boosted Lorentz frame  $F'$  which moves with a velocity  $v$  in the  $z$ -direction with respect to the laboratory frame  $F$  is given by:

$$y' = \frac{1}{2} \ln \left( \frac{E' + p'_z c}{E' - p'_z c} \right). \quad (2.5)$$

Under a Lorentz transformation the total energy  $E$  and momentum component  $p_z$  transform according to:

$$\begin{aligned} E' &= \gamma(E - vp_z) = \gamma(E - c\beta p_z). \\ p'_z &= \gamma(p_z - vE/c^2) = \gamma(p_z - \beta E/c), \end{aligned} \quad (2.6)$$

where  $\beta = v/c$  and  $\gamma = 1/\sqrt{1 - \beta^2}$ . Substituting Eq. 2.6 into Eq. 2.5 yields:

$$y' = y - y_\beta, \quad (2.7)$$

where  $y_\beta = \frac{1}{2} \ln \left( \frac{1+\beta}{1-\beta} \right)$ . Therefore, under a Lorentz transformation from the laboratory frame  $F$  to a new coordinate frame  $F'$  moving with a velocity  $v$  in the  $z$ -direction the rapidity  $y'$  of the particle in the new frame  $F'$  is related to  $y$  up to an additive constant  $y_\beta$ . This simple property of the rapidity variable under a Lorentz transformation makes it a suitable choice to describe the dynamics of relativistic particles.

To compute the rapidity of a particle, it is necessary to measure its energy and its longitudinal momentum. However, in many experiments, it is only possible to measure the angle of the particle with respect to the beam axis. One can use this information to define the pseudorapidity  $\eta$  of a particle as:

$$\eta = -\ln(\tan(\theta/2)) , \quad (2.8)$$

where  $\theta$  is the angle between the particle momentum  $\mathbf{p}$  and the beams axis. One can express the rapidity variable  $y$  in terms of the pseudorapidity  $\eta$  as:

$$y = \frac{1}{2} \ln \left( \frac{\sqrt{p_T^2 \cosh^2 \eta + (mc)^2} + p_T \sinh \eta}{\sqrt{p_T^2 \cosh^2 \eta + (mc)^2} - p_T \sinh \eta} \right) . \quad (2.9)$$

Conversely the pseudorapidity variable  $\eta$  can be expressed in terms of the rapidity variable  $y$  as:

$$\eta = \frac{1}{2} \ln \left( \frac{\sqrt{m_T^2 \cosh^2 y - (mc)^2} + m_T \sinh y}{\sqrt{m_T^2 \cosh^2 y - (mc)^2} - m_T \sinh y} \right) , \quad (2.10)$$

where  $m$  is the rest mass of the particle and  $m_T^2 = p_T^2 + (mc)^2$  is the transverse mass.

In the high energy limit ( $p \gg m$ ), one has the following approximation:

$$y = \frac{1}{2} \ln \left( \frac{\sqrt{(pc)^2 + (mc^2)^2} + p_z c}{\sqrt{(pc)^2 + (mc^2)^2} - p_z c} \right) \approx \frac{1}{2} \ln \left( \frac{pc + p_z c \cos \theta}{pc - p_z c \cos \theta} \right) = -\ln(\tan \theta/2) = \eta .$$

## 2.2 The Standard Model of Particle Physics

The SM of particle physics is the theory that describes elementary particles and their interactions. They are elemental because they have no known structure, i.e., they are pointlike. According to the SM, matter is comprised of a small number of elementary particles called *fermions*: six *quarks* and six *leptons*. Fig. 2.1 shows the symbol, mass, spin and the ratio of its electric charge  $Q$  to the elementary charge  $e$  for each fundamental particle.

The leptons carry an integral charge. The most familiar lepton is the electron  $e$ , carrying a unit of negative charge. The other two charged leptons are the muon ( $\mu$ ) and the tauon ( $\tau$ ). These two are heavier versions of the electron with masses:  $m_\mu \approx 200 m_e$  and  $m_\tau \approx 3477 m_e$ . The neutral leptons are called neutrinos, denoted by the symbol  $\nu$ . The masses of the neutrinos are only constrained, as shown in Fig. 2.1. A different “flavour” of neutrino pairs with each “flavour” of charged lepton.

The quarks carry fractional charges of  $\frac{2}{3} e$  or  $-\frac{1}{3} e$ . In Fig. 2.1, the masses of the quarks increase from left to right. The quark flavour is denoted by the symbol:  $u$  for “up”,  $d$  for “down”,  $s$  for “strange”,  $c$  for “charm”,  $b$  for “bottom” and  $t$  for “top”. Ordinary matter is made of stable particles, i.e. electrons  $e$  and the  $u$  and  $d$  quarks. For example, the  $u$  and  $d$  quarks make up protons and neutrons: a proton (neutron) consists of  $uud$  ( $ddu$ ) combination. Quarks can only be found in combinations, not singly. This phenomenon is called quark confinement. Conversely, leptons exist as free particles. The heavier quarks,  $s, c, b, t$ , also combine to form particles, although much heavier than the proton and neutron. These heavier particles are unstable and decay rapidly, just as the heavy leptons decay to electrons. The heavy quarks and leptons are produced naturally in cosmic rays or very high-energy particle colliders.

The SM also comprises the interactions among elementary particles. The different interactions are described in terms of the exchange of characteristic *bosons*. These are particles of integral spin. The boson mediators and their symbols are shown in the last column of Fig. 2.1. In addition, there are four types of fundamental interactions.

- *Strong* interactions are responsible for binding quarks to form protons and neutrons and the neutrons and protons within nuclei. The boson mediator is a massless particle called the *gluon*.
- *Electromagnetic* interactions are responsible for bounding electrons in atoms and intermolecular forces in liquids and solids. These interactions are mediated by *photon* exchange.
- *Weak* interactions are responsible for the nuclear  $\beta$ -decay. The mediators of the

weak interactions are the  $W^\pm$  and  $Z^0$  bosons.

- *Gravitational* interactions involve all types of particles. In particle physics, gravity is the weakest of all the fundamental interactions, although it is dominant in the scale of the universe. These interactions are supposedly mediated by the exchange of a spin 2 boson, the *graviton*. Note that gravitational interactions are not part of the SM.

	mass → ≈2.3 MeV/c <sup>2</sup> charge → 2/3 spin → 1/2 up	≈1.275 GeV/c <sup>2</sup> 2/3 1/2 charm	≈173.07 GeV/c <sup>2</sup> 2/3 1/2 top	0 0 1 g gluon	≈126 GeV/c <sup>2</sup> 0 0 0 Higgs boson
QUARKS	≈4.8 MeV/c <sup>2</sup> -1/3 1/2 d down	≈95 MeV/c <sup>2</sup> -1/3 1/2 s strange	≈4.18 GeV/c <sup>2</sup> -1/3 1/2 b bottom	0 0 1 γ photon	
LEPTONS	0.511 MeV/c <sup>2</sup> -1 1/2 e electron	105.7 MeV/c <sup>2</sup> -1 1/2 μ muon	1.777 GeV/c <sup>2</sup> -1 1/2 τ tau	91.2 GeV/c <sup>2</sup> 0 1 Z Z boson	GAUGE BOSONS
	<2.2 eV/c <sup>2</sup> 0 1/2 ν <sub>e</sub> electron neutrino	<0.17 MeV/c <sup>2</sup> 0 1/2 ν <sub>μ</sub> muon neutrino	<15.5 MeV/c <sup>2</sup> 0 1/2 ν <sub>τ</sub> tau neutrino	80.4 GeV/c <sup>2</sup> ±1 1 W W boson	

**Figure 2.1:** Summary table of the elementary particles and bosons included in the Standard Model of Particle Physics.

## 2.3 Interactions

In quantum theory, interactions at a distance between one charged-particle acting on another are viewed as an *exchange* interaction, where the exchanged object carries momentum from one charge to the other. The exchange corresponds to a specific quantum (boson) associated with a particular type of interaction. To satisfy conservation laws, the exchange processes should occur within a timescale  $\Delta t$  limited by the Uncertainty Principle, i.e.  $\Delta E \Delta t \lesssim \hbar$ . Such transient quanta are said to be *virtual*. For example, the quantum concept of an electromagnetic interaction (EM) is the charges' continual exchange (emission and absorption) of virtual photons by the charges. Contrary to the classical idea of an all-pervading field surrounding the source charge. Since electromagnetic fields are quantised in the form of free photons, the quantum description of

virtual photon exchange in the static case is appropriate for interaction on a microscopic scale.

### 2.3.1 The Boson Propagator

Consider a particle being scattered by a central potential  $U(\mathbf{r})$ . The effect on the scattered particle is observed through the angular deflection of the particle, or, equivalently, the momentum transfer  $\mathbf{q}$ . The potential  $U(\mathbf{r})$  in coordinate space will have an associated amplitude,  $f(\mathbf{q})$  for scattering of the particle. Such amplitude is given by the Fourier transform of the potential as:

$$f(\mathbf{q}) = g \int U(\mathbf{r}) e^{i\mathbf{q} \cdot \mathbf{r}} dV, \quad (2.11)$$

where  $g$  is the intrinsic coupling strength of the particle to the potential. For a central potential, such that  $U(\mathbf{r}) = U(r)$  the integral in Eq. 2.11 is evaluated easily using spherical coordinates. Substituting the Yukawa potential:

$$U(r) = \frac{g_0}{4\pi r} e^{-r/R},$$

in Eq. 2.11, where  $R = \hbar/mc$  and after integrating over the angular coordinates one finds:

$$\begin{aligned} f(\mathbf{q}) &= 4\pi g \int_0^\infty U(r) \frac{\sin qr}{qr} r^2 dr \\ &= g_0 g \int_0^\infty e^{-mr} \left( \frac{e^{iqr} - e^{-iqr}}{2i1} \right) dr, \end{aligned} \quad (2.12)$$

which gives

$$f(\mathbf{q}) = \frac{g_0 g}{|\mathbf{q}|^2 + m^2}. \quad (2.13)$$

Equation 2.13 describes the potential  $U(r)$  in coordinate space in momentum space: the two descriptions are equivalent. The amplitude  $f(\mathbf{q})$  from Eq. 2.13 corresponds to the one of elastic scattering of a particle of coupling  $g$  by the static potential  $U(r)$  provided by a source of strength  $g_0$ . However, in an actual collision between two particles, energy

$\Delta E$  as well as three-momentum  $\Delta \mathbf{p} = \mathbf{q}$  will be transferred. The square of the four-momentum transfer is defined as:

$$q^2 = \Delta \mathbf{p}^2 - \Delta E^2 , \quad (2.14)$$

which for a massive source gives  $q^2 \equiv |\mathbf{q}|^2$ . The result in Eq. 2.13 holds even if the integral in Eq. 2.11 is replaced by one over both space and time and  $\mathbf{q}^2$  is replaced by the relativistically invariant quantity  $q^2$ . In summary, the scattering amplitude for a single boson-exchange process is the product of two *vertex factors*  $g_0, g$  describing the coupling of the boson to the scattered and scattering particles and a *propagator term*  $(q^2 + m^2)^{-1}$ :

$$f(q^2) = \frac{g_0 g}{q^2 + m^2} . \quad (2.15)$$

Here,  $m$  represents the mass of the exchange boson, hence for the strong and EM interactions,  $m = 0$ .

### 2.3.2 Electromagnetic Interactions

Photons mediate the electromagnetic interactions between charged-particles. The coupling constant specifying the strength of such interactions is given by the dimensionless quantity:

$$\alpha = \frac{e^2}{4\pi\hbar c} , \quad (2.16)$$

where  $\alpha$  is known as the fine structure constant and has the approximate numerical value of  $1/137$ .

Interactions between elementary particles and fields are easily visualised using *Feynman* diagrams. Figure 2.2 (a) shows the Feynman diagram representing the absorption (or emission) of a photon by an electron, where the photon couples to the electron at the vertex with amplitude  $\sqrt{\alpha}$ . However, this process is forbidden for free particles since electrons cannot absorb or emit a massless photon while conserving energy and momentum. On the other hand, the photoelectric effect of photon absorption by an electron involves momentum conservation by the whole atom. Figure 2.2 (b) shows the Feynman diagram corresponding to the Coulomb scattering between two electrons via the exchange of a single virtual photon of momentum  $q$ . The coupling amplitude at

the two vertices is  $\sqrt{\alpha}\sqrt{\alpha} = \alpha$ , while the virtual photon introduces a propagator factor  $1/q^2$  as in Eq. 2.13.



**Figure 2.2:** Figures of Feynman diagrams representing basic electromagnetic processes. (a) electron-photon vertex. (b) electron-electron scattering via photon exchange. The figure is taken from [12].

Quantum Electrodynamics (QED) is the quantum field theory that describes electromagnetic processes. It is characterised by two crucial properties: *renormalisability* and *gauge invariance*. Since these topics are beyond this thesis's scope, I will only briefly explain them. Consider a single electron that emits and reabsorbs a virtual photon or a virtual positron-electron pair. This scenario is represented with the Feynman diagram of Fig. 2.3. The electron line in the Feynman diagram represents a “bare” electron. In contrast, the real observable particles are the bare particles “dressed” by these virtual processes, the so-called “self-energy” terms that contribute to the mass and charge of the measured electron. As there is no restriction on the momentum  $k$  of particles in such virtual states, such terms are of the form  $\int dk/k$  and consequently divergent. It is possible to redefine the mass or charge to overcome divergent terms. The “bare” mass or charge  $m_0$  or  $e_0$  is always found to be multiplied by a dimensionless term containing the divergent integral. Since this combination occurs in all calculations, it is therefore replaced by the physical values  $m_e$ ,  $e$  as determined from the experiment. This process is called renormalisation. A consequence of the renormalisation procedure is that the coupling “constants” such as  $\alpha$  are not constants but depend (logarithmically) on the energy scale at which measurements are being made.

For the theory to be renormalisable, it should be formulated to have the property of *gauge invariance*. For instance, in electrostatics, the energy of a system depends only on changes in the static potential and not on its absolute magnitude so that it is invariant under arbitrary redefinitions of the global potential scale or gauge. As a consequence of demanding local gauge invariance, the electric charge is conserved.

Feynman diagrams such as those shown in Fig. 2.2 represent leading order processes. In addition to these, there will be further diagrams for contributions of higher-order in  $\alpha$ . For example, diagrams of processes contributing to the electron’s magnetic moment are shown in Fig. 2.4. Figure 2.4 (a) represents the leading interaction of an external magnetic field  $B$  with a “bare” electron, yielding a magnetic moment equal to

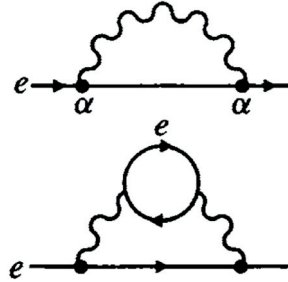


**Figure 2.3:** Feynman diagram representing an electron and self-energy terms. The figure is taken from [12].

$\mu_B = e\hbar/(2mc)$ , as given by the Dirac theory of a pointlike electron. Figure 2.4 (b) represents the next-to-leading-order correction, where the electron is shown temporally dissociated into a “bare” electron, with which the field interacts, and a virtual photon. This correction to the moment is of magnitude proportional to  $\alpha$ . Finally, possible processes contributing with corrections of the order of  $\alpha^2$  are represented by the diagrams of Fig. 2.4 (c).

The diagrams of higher order are a graphical representation of the perturbation series in powers of  $\alpha$  that predicts the correction to, or anomaly in, the magnetic moment of the “Dirac” electron. The quantity  $(g - 2)/2$  represents the anomaly, with a calculated value of:

$$\begin{aligned} \left(\frac{g-2}{2}\right)^{\text{theory}} &= 0.5\left(\frac{\alpha}{\pi}\right) - 0.32848\left(\frac{\alpha}{\pi}\right)^2 + 1.19\left(\frac{\alpha}{\pi}\right)^3 + \dots \\ &= (115965230 \pm 10) \times 10^{-11} \end{aligned} \quad (2.17)$$

This may be compared with the experimental value:

$$\left(\frac{g-2}{2}\right)^{\text{expt}} = (115965219 \pm 1) \times 10^{-11}$$

The level of agreement between theory and experiment is quite convincing evidence of the predictive power of quantum field theory.

### 2.3.3 Strong Interactions

The interactions between quarks are mediated by bosons called *gluons*. Gluons are neutral, massless and carriers of the strong force, similar to photons in QED.

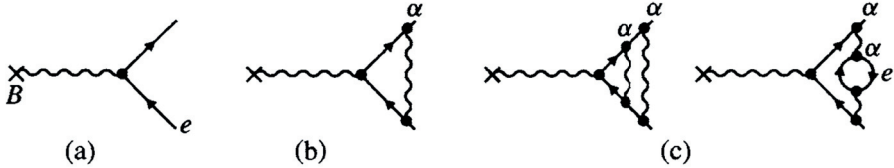


**Figure 2.4:** See text for explanation. The figure was taken from [12].

Quantum Chromodynamics (QCD) is the theory of strong interactions, it includes six types of strong charges, which are referred to as “colour” charges. A quark can carry one of the three primary colours: red (r), blue (b) or green (g), and its direct anti-quark carries the corresponding anti-colour. On the left of Fig. 2.5, one example of colour exchange is shown: a red quark interacts with a blue quark via the exchange of red-antiblue gluon. Consequently gluons are endowed with a colour charge ( $r\bar{b}$  in this example). Since gluons carry one colour and one anti-colour, there should be  $3^2 = 9$  possible colour combinations. However, one of these combinations turns out to be a colourless singlet, resulting in eight different gluons states. Since gluons are colour-charged particles, gluons can self-interact with triple (and quadruple) gluon vertices, as shown on the right figure in Fig. 2.5. The left diagram of Fig. 2.5 is drawn for single-gluon exchange. The single-gluon exchange is a good approximation in the case of high energy collisions at very high  $q^2$ , where the strong coupling  $\alpha_s \ll 1$ . However, at low  $q^2$  or large distances, the strong coupling becomes very large, and multiple exchanges are involved.

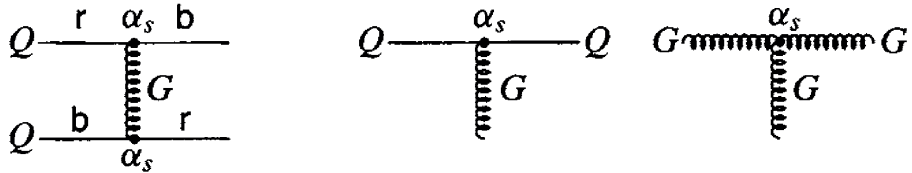


**Figure 2.5:** (Left) Diagram representing the interaction between two quarks via the exchange of one gluon. (Right) Quark-gluon and gluon-gluon vertices in QCD. The figure is taken from [12].

The classical potential between a heavy quark and a heavy anti-quark is of the form:

$$V_s(r) = -\frac{4}{3} \frac{\alpha_s}{r} + \kappa r . \quad (2.18)$$

The first term, dominating at small  $r$ , arises from the single-gluon exchange. The second term in the potential is associated with the confinement at large  $r$ . The constant  $\kappa$  is

known as the *string tension*, and its value is equal to 0.85 GeV/fm.

At large distances, one can imagine the lines of force of the colour field between two quarks to form a string. As the string continues to grow, the stored energy  $\kappa r$  eventually reaches the point where it is energetically more favourable to create a new  $q\bar{q}$  pair, i.e. a meson. At high energies the process  $e^+e^- \rightarrow$  hadrons is viewed as the elementary process:

$$e^+e^- \rightarrow q\bar{q},$$

plus final-state gluon radiation. This is followed by “fragmentation” of the quarks to hadrons via the string breaking process. In Sec. 4.1, I will describe how the fragmentation process is the underlying mechanism in Monte Carlo event generators such as PYTHIA.

### 2.3.4 Running Couplings in QED and QCD

In Sec. 2.3.2, it was mentioned that corrections to the magnetic moment of the electron are expressed in terms of the departure of the gyromagnetic ratio  $g$  from 2 and appears in the form of a perturbation expansion in series of  $\alpha$ , see Eq. 2.17. This perturbation expansion can also be described as a single, first-order correction, with  $\alpha$  depending on the masses or momentum transfers in the virtual processes involved. Thus the anomaly can be expressed as:

$$\left( \frac{g-2}{2} \right) = \frac{0.5}{\pi} \alpha_{\text{eff}} . \quad (2.19)$$

This approach treats  $\alpha$  as a “running coupling constant” dependent on the masses or momentum transfers in any particular case. The general dependence of the coupling on momentum transfer is expressed by the so-called renormalisation group equation, in which the coupling is expanded in powers of  $\ln(q^2/\mu^2)$ :

$$\frac{1}{\alpha(\mu^2)} = \frac{1}{\alpha(q^2)} + \beta_0 \ln \left( \frac{q^2}{\mu^2} \right) + \dots . \quad (2.20)$$

The purpose of representing the value of  $\alpha$  at one value of  $q^2$  in terms of that at another value, say  $q^2 = \mu^2$  is to avoid the problem of the coupling becoming infinite for  $q^2 \rightarrow 0$ .

The quantity  $\beta_0$  depends on the number of degrees of freedom,  $n_b$  for bosons and  $n_f$  for fermions, in the loops of the vacuum polarisation terms:

$$\beta_0 = \frac{1}{12\pi} (4n_f - 11n_b) . \quad (2.21)$$

For the electromagnetic interaction, where there can be no loops containing photons,  $n_b = 0$  and at high energies the  $n_f = 3$ , so that  $\beta_0 = 1/\pi$ . Inserting this in Eq. 2.20 and considering only the first two terms, the following expression is obtained for the QED coupling parameter:

$$\alpha_{\text{em}}(q^2) = \frac{\alpha(\mu^2)}{\left[1 - \frac{1}{\pi}\alpha(\mu^2)\ln\left(\frac{q^2}{\mu^2}\right)\right]} . \quad (2.22)$$

For QCD,  $n_b = 3$  so that  $n_f = 3$  one obtains from Eq. 2.21,  $\beta_0 = -7/4\pi$ , thus Eq. 2.20 yields:

$$\alpha_s(q^2) = \frac{\alpha_s(\mu^2)}{1 + \frac{7}{4\pi}\alpha_s(\mu^2)\ln\left(\frac{q^2}{\mu^2}\right)} . \quad (2.23)$$

The above expression can be put in the simpler form:

$$\alpha_s(q^2) = \frac{1}{B \ln(q^2/\Lambda^2)} , \quad (2.24)$$

where  $B = -\beta_0$  and  $\Lambda^2 = \mu^2 \exp(-1/B\alpha_s(\mu^2))$ . From Eq. 2.24 one can see that  $\alpha_s$  decreases with increasing  $q^2$ . This behaviour is typical of a non-Abelian field, in which the field particles, in this case, gluons, carry a colour charge and thus have self-coupling. At large  $q^2$ , the coupling  $\alpha_s(q^2) \rightarrow 0$ , and quarks are expected to behave as free particles. This phenomenon is known as *asymptotic freedom*. At low  $q^2$ , such that,  $q \sim \Lambda$ ,  $\alpha_s(q^2)$  becomes very large and the perturbation expansion of Eq. 2.20 becomes meaningless. It is worth mentioning that perturbation theory only can be applied for QCD when  $q^2 \gg \Lambda^2$ . Finally, Fig. 2.6 shows experimental data on the measurement of the QCD coupling parameter  $\alpha_s$  as a function of the energy scale,  $Q$ .

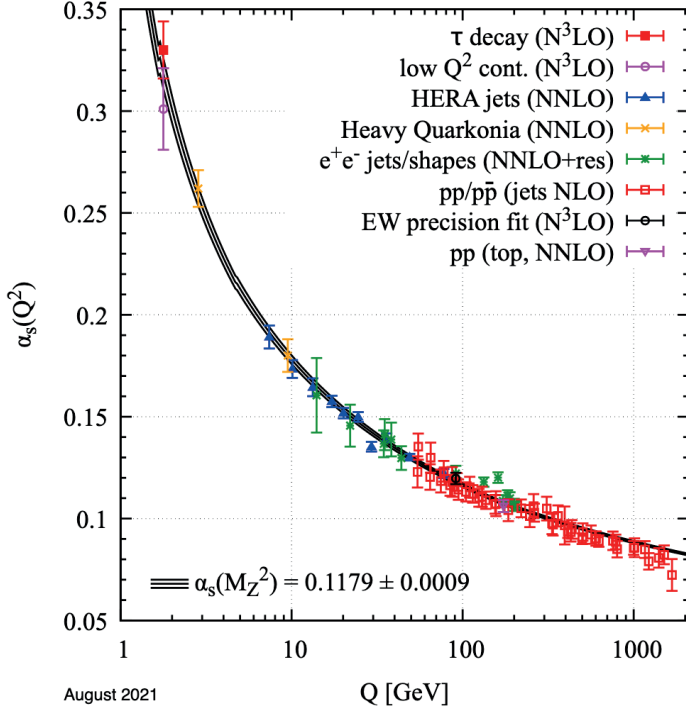


**Figure 2.6:** Summary of measurements of the QCD coupling parameter  $\alpha_s$  as a function of the energy scale  $Q$ . The figure is taken from [14].

### 2.3.5 Lattice QCD

In the previous section, it was mentioned that perturbative Quantum Chromodynamics (pQCD) is applicable only at high energies i.e., when  $\alpha_s(q^2) \rightarrow 0$ . The growth of the coupling constant at low energies requires non-perturbative methods. Lattice Quantum Chromodynamics [15] (LQCD) is the first principle-tool to extract predictions for the theory of strong interactions in the non-perturbative regime. In LQCD, the Euclidean space-time is discretised with a lattice spacing  $a$ . The lattice spacing is determined by the temporal extent  $N_\tau$ . Typical  $N_\tau$  values are 6, 8 and 12. The continuum-extrapolated theory is recovered by taking the limit  $1/N_\tau \rightarrow 0$ .

One success of LQCD is to provide a non-perturbative determination of the equation of state (EoS) of QCD. The EoS is one of the fundamental properties of QCD, and it characterises the transition from the hadronic phase into the QGP phase. The 2 + 1 flavour QCD equation of state in the continuum limit is reported in [16]. Bulk thermodynamic quantities such as the pressure ( $p$ ) and the energy density ( $\varepsilon$ ) are calculated in the temperature  $T$  range 130 – 400 MeV [17], relevant for heavy-ion phenomenology

at RHIC and LHC energies. Figure 2.7 shows the pressure, energy and entropy density as a function of the temperature [17]. One sees a steep rise of  $\varepsilon/T^4$  in the range  $150 \lesssim T \lesssim 200$  MeV. This is associated with an increased number of degrees of freedom, which changes from a hadronic to a partonic medium, resulting in a phase transition(deconfinement).

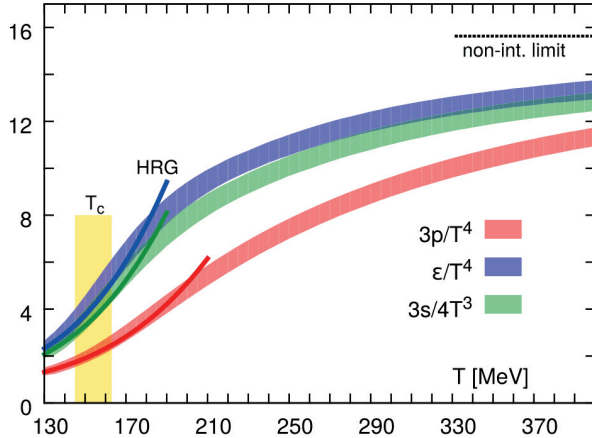


**Figure 2.7:** Pressure, energy and entropy density as a function of the temperature. The vertical band represent marks the phase transition region at a  $T_c \sim 155$  MeV. The figure is taken from [17].

# Chapter 3

## High-Energy Nuclear Collisions

This chapter presents a brief introduction to the field of high-energy nuclear collisions. This is an extensive and active field of investigation from both sides, the experimental and theoretical one. Thus, I will give a general overview of the history of a relativistic nucleus-nucleus collision and restrict the discussion to the relevant concepts for the understanding and interpretation of the measurements that I have performed in Pb–Pb collisions. For a more in-depth review on the topic of heavy-ion collisions, see for example [6, 18, 19].

In recent years, the study of pp and p–Pb collisions has attracted the heavy-ion community’s attention due to the similarities observed in high multiplicity pp and p–Pb measurements with their analogue ones from Pb–Pb collisions. These observations include the “ridge” structure in two-particle angular correlations, “collective” effects in small systems and the enhanced production of strangeness with multiplicity. Section 3.6 gives a brief experimental overview on results obtained from pp and p–Pb collisions at the LHC. This review serves as an introduction to the measurements that I have performed in pp collisions at  $\sqrt{s} = 13$  TeV aim at understanding the origins of collective effects and strangeness enhancement in high multiplicity pp collisions.

### 3.1 The QCD Phase Diagram

One of the big expectations from ultra-relativistic heavy-ion collisions is to learn about the two phase transitions predicted by QCD, *deconfinement* and *chiral phase transitions*. As mentioned in the introduction, quarks and gluons are confined in hadrons. However, with increasing temperature and/or increasing baryon number density (related

to the excess of quarks over antiquarks), a phase transition to a state of matter where quarks and gluons move freely is expected. The standard parameter used to characterise the baryon number density is the baryon chemical potential  $\mu_B$ . Figure 3.1 shows the QCD phase diagram as a function of temperature ( $T$ ) and the baryon chemical potential. Calculations based on lattice QCD predict a critical temperature for the phase transition from confined to deconfined QCD matter to be in the range 155 – 160 MeV [20] at vanishing baryon number density ( $\mu_B \approx 0$ ) but what are the experimental evidence that can prove the creation of such a state of QCD matter? Furthermore, what imprints does the presence of such a state leave on the final state hadrons that reach the detectors to produce a signal? These questions will be addressed in the following subsections.

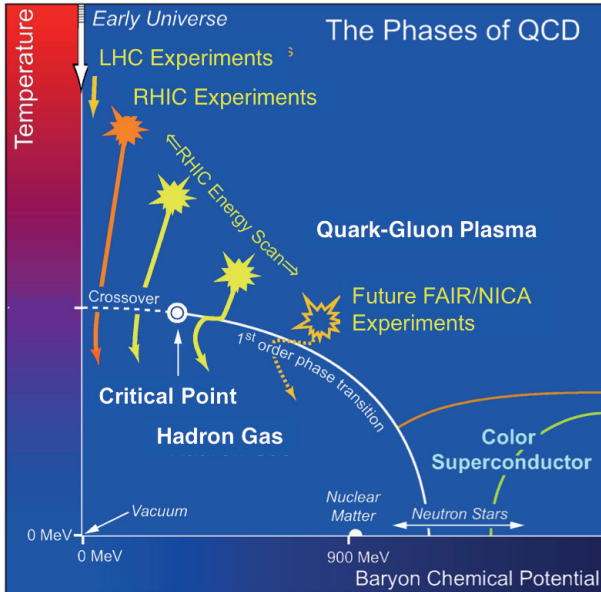


**Figure 3.1:** QCD phase diagram in the temperature  $T$  and baryonic chemical potential plane  $\mu_B$ . The phase diagram also shows different regions probed by current and future facilities. The figure is taken from [21].

## 3.2 History of a Heavy-Ion Collision

The theory of special relativity dictates that objects travelling near the speed of light will be contracted longitudinally. Thus, one can imagine two incoming heavy-ion nuclei that are about to collide as two “pancakes” approaching each other, as shown on the left of Fig. 3.2. In reality, not all the nucleons participate in the collision. The fraction of nucleons that collide and create the fireball are called *participants*. At the same time,

the *spectators* will remain unaffected and will continue their trajectories in the direction of the beam axis, as shown on the right of Fig. 3.2.

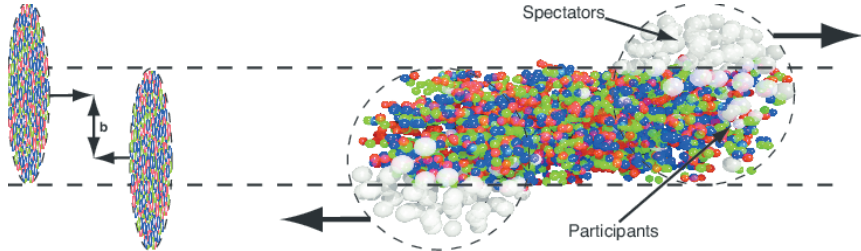


**Figure 3.2:** (Left) Two incoming heavy-ion nuclei before the collision with impact parameter  $b$ . (Right) The participant nucleons will create the fireball while the spectators continue more or less unaffected along their initial trajectories. The figure is taken from [22].

The “centrality” is used to categorise the degree of overlap in a collision. From a geometrical perspective, centrality is associated with the impact parameter,  $b$ . The impact parameter is the geometrical distance between the two nuclei centres in the plane transverse to the beam axis, see Fig. 3.2. Consequently, a vanishing impact parameter  $b \approx 0$  will result in the most “central” collisions. Therefore, the centrality of the collision will decrease with increasing impact parameter. On the other hand, collisions with  $b \approx 2 R$ , where  $R$  is the radius of the nucleus, are associated with the most peripheral collisions where few nucleons collide. In Sec. 6.2.1, I will describe how the centrality of a collision is determined in ALICE.

The history of the collision can be divided into different stages: I) early time dynamics: occurring during the passage time of the nuclei. II) thermalisation: equilibrium is established. III) expansion and cooling (in the deconfined state). IV) chemical freeze-out: inelastic collisions cease and, the hadron yields are fixed. V) kinetic freeze-out: elastic collisions cease: particles decouple during this stage (their  $p_T$  spectra freeze).

### 3.2.1 The Early Time Dynamics

I will now introduce the *colour glass condensate* and the *glasma*, and discuss how it can evolve into the QGP. The colour glass condensate is a form of matter proposed to describe the high-energy limit of strong interactions and is the part of the hadron wavefunction important at high energies that will dominantly interact (for a pedagogical introduction to the colour glass condensate, see [24]). It is universal and independent of the hadron that created it. But, how does the colour glass condensate come into play? A convenient variable to represent the fraction of energy carried by the constituent partons

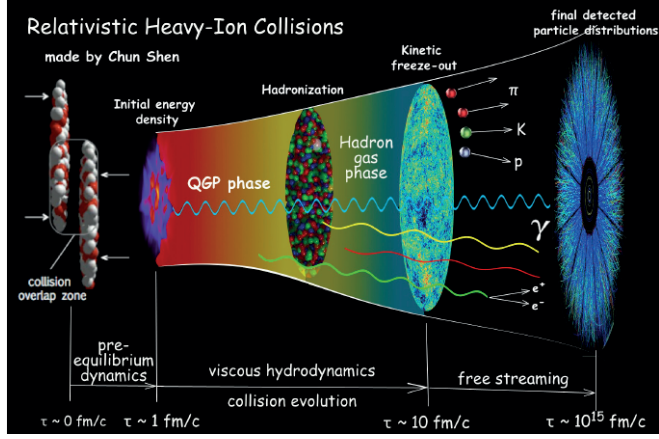


**Figure 3.3:** Sketch of the history of a high-energy nucleus-nucleus collision. The system's evolution goes from a hot-fireball in a pre-equilibrium phase through the formation of a QGP, followed by a cross-over phase transition to a hadron gas. The different particles created are represented with arrows and lines. Photons created during the evolution can be used to probe the early stages because they only interact very weakly with the medium. The figure is taken from [23].

is:

$$x = E_{\text{constituent}} / E_{\text{hadron}} . \quad (3.1)$$

As we go to higher and higher energies, partons with lower and lower  $x$  can actively participate in the collision. The following equation gives the rapidity distribution of gluons inside the hadron wavefunction [25]:

$$\frac{dN}{dy} = xG(x, Q^2) . \quad (3.2)$$

The scale  $Q^2$  appears in the rapidity distribution of gluons because the number of constituent partons that one measure depends upon the probe's resolution scale [24, 25]. The rapidity distribution of gluons inside the proton has been measured by the ZEUS collaboration [26] at different resolution scales  $Q^2$  as shown in Fig. 3.4. As can be observed, the gluon density is large at low- $x$  and decreases with increasing  $x$ . Moreover, the gluon density at a fixed  $x$  increases with increasing  $Q^2$ . Schematically, this means that if we see the proton head-on, the density of low- $x$  gluons increases with the increasing energy of the proton, see Fig. 3.4. Such a system with a high density of gluons is called the Color Glass Condensate (CGC) for the following reasons [25]. “Color”

since the gluons are coloured. “Glass” because the fields created by high-momentum constituents have their time scales Lorentz dilated relative to those which would be measured in their rest frame, i.e., low-momentum constituents are glassy in the sense that their time evolution scale is much longer compared to their natural time scale. This behaviour is reminiscent of the actual glasses: it behaves like a solid on short time scales and similar to a liquid on much longer time scales. “Condensate” because it contains a very high density of gluons. Increasing the energy forces the gluons to occupy higher momentum states (due to repulsive interactions), causing the coupling to become weaker. As a result, the gluon density saturates at a value of order  $1/\alpha_s \gg 1$ , corresponding to a multiparticle Bose condensate state. Therefore high-energy proton-proton collisions are essentially gluon colliders.

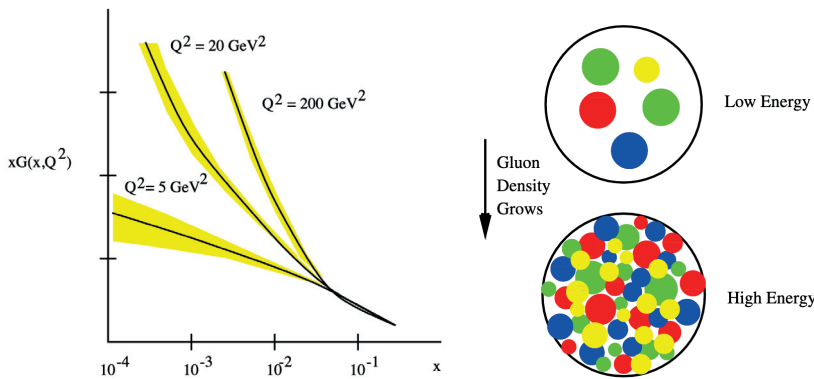


**Figure 3.4:** (Left) Gluon density as a function of  $x$  at various  $Q^2$  resolutions. (Right) Increase of the gluon density from low to high energies of the proton. The figures are taken from [25].

Due to the high occupancy (condensate), the fields associated with the colour glass condensate are treated as classical fields. They are planes polarised with mutually orthogonal colour electric and magnetic fields perpendicular to the direction of motion of the hadron [27–30], see Fig. 3.5. The state of matter created right after the collisions of two nuclei is called the glasma. It interpolates the colour glass condensate from the initial nuclei, which are about to collide and the QGP. Immediately after the collision, the sheets of the colour glass change their nature of transverse colour electric and magnetic fields, with zero longitudinal fields into longitudinal electric and magnetic fields with zero transverse fields. These longitudinal fields are how the energy density is deposited in the centre of the colliding system. Later, the glasma decays and thermalises to form the QGP [31].

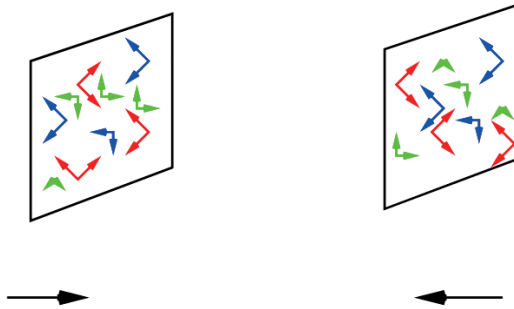


**Figure 3.5:** Two sheets of colour glass are about to collide. The figure is taken from [24].

### 3.2.2 The Quark-Gluon Plasma

Today, we are convinced that heavy-ion collisions will create a form of dense, strongly interacting system and when it thermalises, the QGP is created. Studies at RHIC [4–6, 32, 33] confirmed its existence. However, its study and characterisation represent a challenging task due to the nature of the hot fireball. Recall that the QGP is a state of deconfined QCD matter, i.e., a system in which quarks and gluons are free to roam. However, the signals produced in the detectors come from the final state hadrons, i.e., bound states of quarks and gluons. Consequently, direct access to the information of the early hot fireball is inaccessible to us with hadrons. When the fireball is created, and thermalisation is reached, the thermal pressure acting against the surrounding vacuum will lead to a collective (hydrodynamic) expansion. Consequently, the fireball will cool down, decreasing its energy density. When the energy density is about  $\epsilon_{\text{cr}} \approx 1 \text{ GeV/fm}^3$  hadronization takes place. In this sense, the hadrons we measure do not probe deconfinement but rather the confinement phase transition [34].

### 3.2.3 The Temperature of the QGP

The measurement of photons is a valuable tool to study the medium’s evolution created in a heavy-ion collision. Unlike hadrons, photons are produced at all stages of the collision. They only interact electromagnetically and hence can escape the medium essentially unaffected. Here, I focus on direct photons, defined as photons not originating from hadron decays. Direct photons are divided into *prompt* direct photons and direct *thermal* photons. Prompt direct photons are produced in hard scatterings between the incoming partons in the nuclei and can provide information on parton distributions in nuclei. The thermalised quark-gluon plasma emits direct thermal photons and can

provide information about the medium’s properties.

By measuring the  $p_T$  spectrum of direct photons, one can know about the properties of the medium, such as temperature, collective flow and space-time evolution. For example, at low transverse momenta ( $p_T \lesssim 4 \text{ GeV}/c$ ), one expects mainly the contribution from thermal production. The  $p_T$  spectrum of thermal photons is approximately exponential and is characterised by the inverse slope parameter, called “effective temperature”  $T_{\text{eff}}$ . Their usefulness as thermometers of the quark-gluon plasma is already an old idea proposed in Ref. [35, 36]. Figure 3.6 shows the  $p_T$  spectra of direct photons measured as a function of the centrality in Pb–Pb collisions at  $\sqrt{s_{\text{NN}}} = 2.76 \text{ TeV}$  measured by the ALICE collaboration [7]. To extract the  $T_{\text{eff}}$ , a  $p_T$  region is selected where the contribution of prompt photons is expected to be small. Then, the pQCD contribution is subtracted. The remaining excess yield is related to the production of thermal photons is fitted with an exponential function in the range  $0.9 < p_T < 2.1 \text{ GeV}/c$ . The extracted inverse slope is  $T_{\text{eff}} = (297 \pm 12^{\text{stat}} \pm 41^{\text{syst}}) \text{ MeV}$  for the 0 – 20% centrality class (central collisions) and  $T_{\text{eff}} = (410 \pm 84^{\text{stat}} \pm 140^{\text{syst}}) \text{ MeV}$  for the 20 – 40% centrality class (mid-central collisions). The parameter  $T_{\text{eff}}$  represents an effective temperature averaged during the different temperatures during the space-time evolution of the medium. It is worth mentioning that the extracted  $T_{\text{eff}}$  in the two centrality classes is well above the transition temperature predicted by lattice QCD.

Prompt photons dominate at high transverse momenta ( $p_T \gtrsim 5 \text{ GeV}/c$ ) and follow a power law spectrum. The centrality dependent spectra at high- $p_T$  reported in Ref. [7] agree with pQCD calculations of the direct photon yield in pp collisions at the same energy when scaled by the number of binary nucleon collisions. This agreement reflects the absence of medium influence on direct photon production at high- $p_T$ .

### 3.2.4 The Chemical Freeze-Out

After the hadronisation of the fireball, the created hadrons will continue to interact with each other until the system becomes so diluted that the average distances among hadrons are beyond the range of the strong interactions. At this stage, the inelastic scatterings cease, and the relative particle composition freezes out. This stage in the history of a heavy-ion collision is known as the *chemical freeze-out*.

The statistical thermal model [37] is used to study nucleus-nucleus collisions at the chemical freeze-out. It successfully describes the hadron yields over a wide range of energies for the AGS and SPS up to RHIC energies (see Ref. [38] for a compilation of results at different colliding energies). This approach assumes that the hadronic system is in thermal and chemical equilibrium. The partition function  $Z(T, V)$  is the fundamental quantity to calculate the thermal particle composition in heavy-ion collisions.

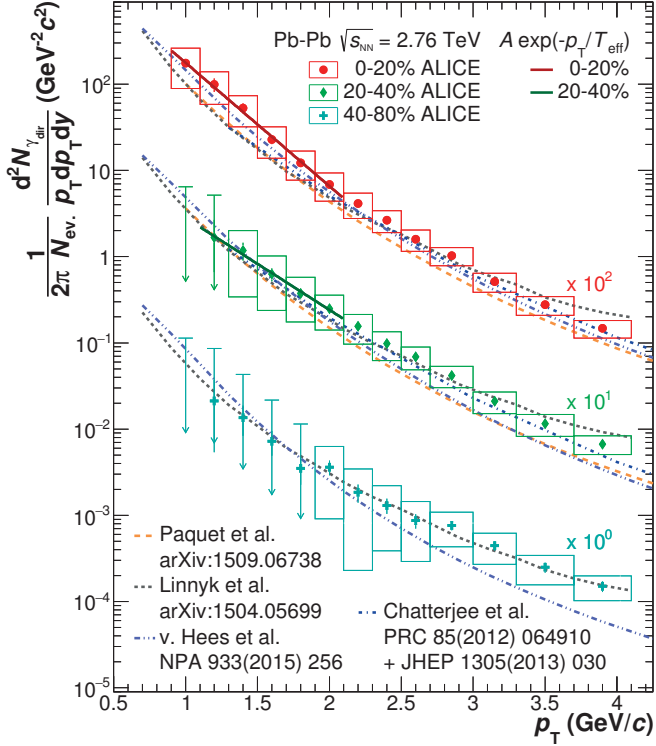


**Figure 3.6:** Centrality dependent  $p_T$  spectra of direct photons in Pb–Pb collisions at  $\sqrt{s_{NN}} = 2.76$  TeV. The fit with an exponential function is shown for the 0 – 20% and 20 – 40% centrality classes. The data measurements are compared with models (dashed lines) that assume the formation of a QGP. The figure is taken from [7].

In the Grand Canonical ensemble (GC), it is given by,

$$Z^{GC}(T, V, \mu_Q) = Tr[e^{-\beta(H - \sum_i \mu_{Q_i} Q_i)}], \quad (3.3)$$

$H$  is the Hamiltonian of the system,  $Q_i$  are the conserved charges and  $\mu_{Q_i}$  are the chemical potentials that guarantee that the charges  $Q_i$  are conserved on the average in the whole system and  $\beta = 1/T$  is the inverse temperature. The Hamiltonian describes the system of a hadron resonance gas. Choosing such a Hamiltonian contains all relevant degrees of freedom of the strongly interacting medium and implicitly includes interactions that result in resonance production [37]. In the GC ensemble, the partition

function for species  $i$  is:

$$\ln Z_i = \frac{V g_i}{2\pi^2} \int_0^\infty \pm p^2 dp \ln[1 \pm \exp(-(E_i - \mu_i)/T)] \quad (3.4)$$

where  $g_i = (2J_i + 1)$  is the spin degeneracy factor,  $E_i = \sqrt{p^2 + m_i^2}$  is the total energy and  $T$  is the temperature. The (+) for fermions and (-) for bosons. For hadron  $i$  of baryon number  $B_i$ , third component of the isospin  $I_{3i}$ , strangeness  $S_i$ , and charmness  $C_i$ , the chemical potential is  $\mu_i = \mu_b B_i + \mu_{I_3} I_{3i} + \mu_S S_i + \mu_C C_i$ . The chemical potentials related to baryon number ( $\mu_b$ ), isospin ( $\mu_{I_3}$ ), strangeness ( $\mu_S$ ) and charm ( $\mu_C$ ) ensure the conservation (on average) of the respective quantum numbers: i) baryon number:  $V \sum_i n_i B_i = N_B$ ; ii) isospin:  $V \sum_i n_i I_{3i} = I_3^{\text{tot}}$ ; iii) strangeness:  $V \sum_i n_i S_i = 0$ ; iv) charm:  $V \sum_i n_i C_i = 0$ . The (net) baryon number  $N_B$  and the total isospin  $I_3^{\text{tot}}$  of the system are input values which need to be specified according to the colliding nuclei studied. The particle density for species  $i$ , is given as an average over the GC ensemble as [38]:

$$n_i = N_i/V = -\frac{T}{V} \frac{\partial \ln Z_i}{\partial \mu} = \frac{g_i}{2\pi^2} \int_0^\infty \frac{p^2 dp}{\exp[(E_i - \mu_i)/T] \pm 1} \quad (3.5)$$

By taking into account, the conservation laws i)-iv),  $T$  and the baryon-chemical potential ( $\mu_b$ ) are the only parameters of the model that are obtained from experimental data. The volume  $V$  appears as an additional parameter when fitting hadron yields. In Ref. [39], the results about hadron yields measured by ALICE in Pb–Pb collisions at  $\sqrt{s_{\text{NN}}} = 2.76$  TeV are studied using the statistical hadronisation model. Fig. 3.7 shows a fit of the model to the data. This study concluded that in central Pb–Pb collisions at the LHC energies where  $\mu_B \approx 0$ , the temperature at the chemical freeze-out is 156 MeV.

Furthermore, the statistical thermal model provides a phenomenological link between data and the QCD phase diagram [40, 41]. Figure 3.8 shows the phenomenological phase diagram in which each point corresponds to a fit to hadron yields in Au–Au and Pb–Pb collisions as a function of  $\mu_B$ . It was found that  $T$  increases with increasing energy (decreasing  $\mu_B$ ) from about 50 MeV to about 160 MeV, where it exhibits a saturation for  $\mu_B \lesssim 300$  MeV. The saturation of  $T$  is connected with the QCD phase transition via the conjecture that the chemical freeze-out temperature can be the hadronisation temperature [40].

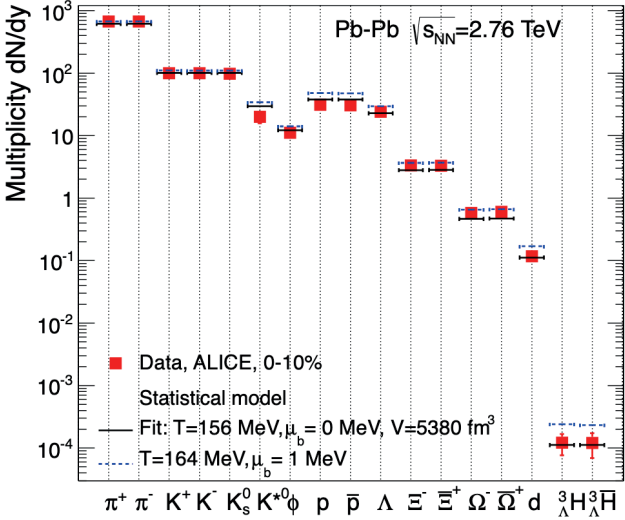


**Figure 3.7:** Hadron yields in central Pb–Pb collisions at  $\sqrt{s_{NN}} = 2.76 \text{ TeV}$  from ALICE at the LHC represented with solid red markers. The solid black and dashed blue lines represent fits to data using the statistical thermal model. The figure is taken from [39].

### 3.2.5 The Kinetic Freeze-Out

Eventually, even the elastic scatterings among hadrons will cease, and their momenta are fixed. This decoupling stage is known as the “kinetic freeze-out”. The “blast-wave” model [42] quantifies thermodynamic quantities at the kinetic freeze-out. This model assumes that particle  $p_T$  spectra are thermal with a common temperature  $T$  when viewed in the local rest frame. The final spectra are then obtained by boosting each local frame back to the global lab frame. To obtain the relevant parameters at the freeze-out, such as the temperature at the freeze-out ( $T_{\text{kin}}$ ) and the average transverse velocity of expansion ( $\langle \beta_T \rangle$ ) one performs a combined fit to the  $p_T$  distributions of  $\pi$ ,  $K$  and  $p$  with the function:

$$\frac{1}{p_T} \frac{dN}{dp_T} \propto \int_0^R r dr m_T I_0\left(\frac{p_T \sinh \rho}{T_{\text{kin}}}\right) K_1\left(\frac{p_T \cosh \rho}{T_{\text{kin}}}\right), \quad (3.6)$$

where the velocity profile  $\rho$  of the local frames is described by,

$$\rho = \tanh^{-1} \beta_T = \tanh\left(\left(\frac{r}{R}\right)^n \beta_s\right), \quad (3.7)$$

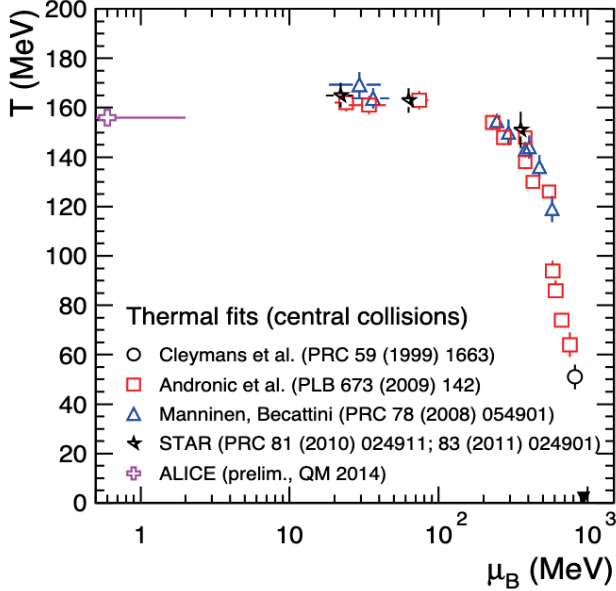


**Figure 3.8:** The phenomenological QCD phase diagram. The points represent the thermal fits of hadron yields at various collision energies. The figure is taken from [18].

where  $m_T = \sqrt{p_T^2 + m^2}$  is the transverse mass,  $I_0$  and  $K_1$  the modified Bessel functions,  $r$  is the radial distance in the transverse plane,  $R$  is the radius of the fireball,  $\beta_T$  is the transverse expansion velocity and  $\beta_s$  is the transverse expansion velocity at the surface. The free parameters in the fit are  $T_{\text{kin}}$ ,  $\langle \beta_T \rangle$  and the exponent of the velocity profile  $n$ . Since a large contribution of low- $p_T$  pions come from resonance decays the combined fit is restricted to the fitting intervals:  $0.5 - 1 \text{ GeV}/c$ ,  $0.2 - 1.5 \text{ GeV}/c$  and  $0.3 - 3 \text{ GeV}/c$  for  $\pi$ , K and p, respectively. It is worth mentioning that the values of the parameters, specially  $T_{\text{kin}}$  are sensitive to the fit range used for pions. Furthermore, it is important to mention that this model forces all the species to decouple with the same parameters, however this is arguable since different particles can in principle decouple at a different time from the hadronic system, and hence with a different  $T_{\text{kin}}$  and  $\langle \beta_T \rangle$ . The usefulness of the model lies in the ability to compare with a few simple parameters the measurements at different  $\sqrt{s_{\text{NN}}}$ .

Figure 3.9 shows the  $p_T$  spectra of  $\pi$ , K and p measured by the ALICE collaboration in Pb–Pb collisions at  $\sqrt{s_{\text{NN}}} = 5.02 \text{ TeV}$ . By performing a global fit to the spectra in the  $p_T$  intervals mentioned above, one can obtain the correlation between  $T_{\text{kin}}$  and  $\langle \beta_T \rangle$ .

Figure 3.10 shows the correlation between  $T_{\text{kin}}$  and  $\langle \beta_T \rangle$  measured in Pb–Pb collisions at  $\sqrt{s_{\text{NN}}} = 2.76, 5.02 \text{ TeV}$ . The results from the two colliding energies show the same

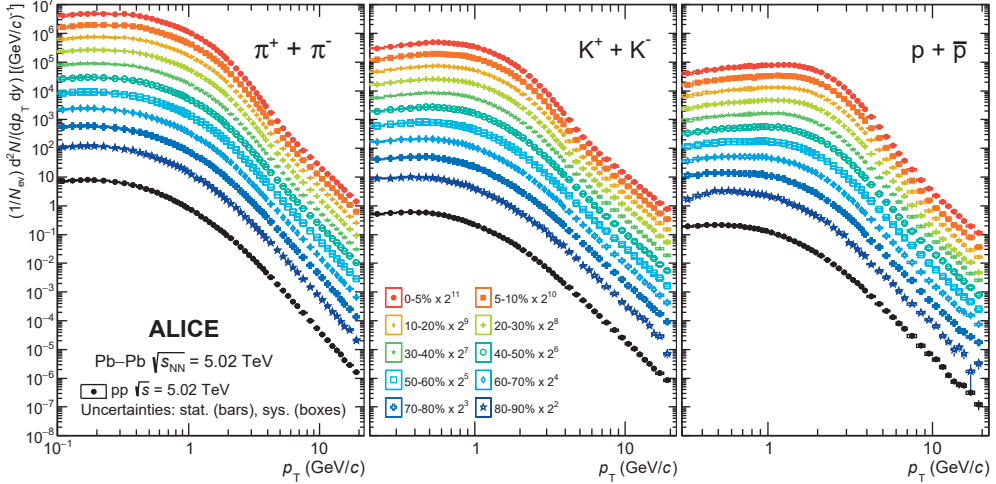


**Figure 3.9:** Transverse momentum distributions of  $\pi$ ,  $K$  and  $p$  in  $Pb-Pb$  collisions at  $\sqrt{s_{NN}} = 5.02$  TeV as a function of the collision centrality. The centrality increases from the blue to the red colour markers. Scale factors are applied for better visibility. The results are compared with the spectra measured in inelastic  $pp$  collisions at  $\sqrt{s} = 5.02$  TeV. The figure is taken from [43].

qualitative behaviour: the value of  $\langle \beta_T \rangle$  ( $T_{\text{kin}}$ ) increases (decreases) with increasing centrality. These results indicate the build up of a large collective flow with increasing centrality, indicative of a strongly interacting system.

The effects of the collective radial flow can also be observed from the  $p_T$  spectra. In Fig. 3.9 one sees a flattening of the spectral shapes going from peripheral to central collisions. In hydrodynamics, the flattening of the  $p_T$  spectra is expected due to the blue shift induced by the collective expansion. As the fireball expands, it will boost low- $p_T$  particles towards higher values. This boosting effect is imprinted in all the particles; however, its effects are more evident for heavier particles such as protons. Figure 3.11 shows the  $p_T$ -differential  $p/\pi$  in central and peripheral  $Pb-Pb$  collisions. One sees an increased baryon-to-meson ratio around  $p_T \approx 3$  GeV/ $c$ , which is attributed to collective radial flow. Furthermore, the peak measured at 5.02 TeV is shifted towards the right with respect to the one measured at 2.76 TeV. This is interpreted as the presence of a strong radial with increasing colliding energy.

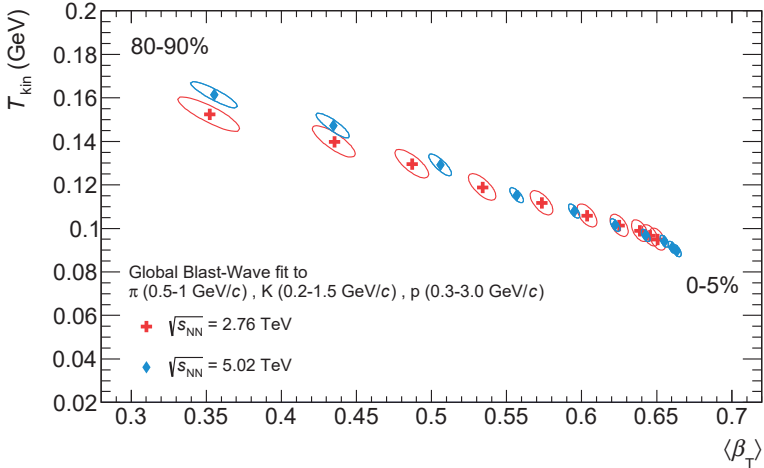


**Figure 3.10:** Correlation between  $T_{\text{kin}}$  and  $\langle \beta_T \rangle$  measured in Pb–Pb collisions at  $\sqrt{s_{\text{NN}}} = 2.76, 5.02$  TeV. The figure is taken from [43].

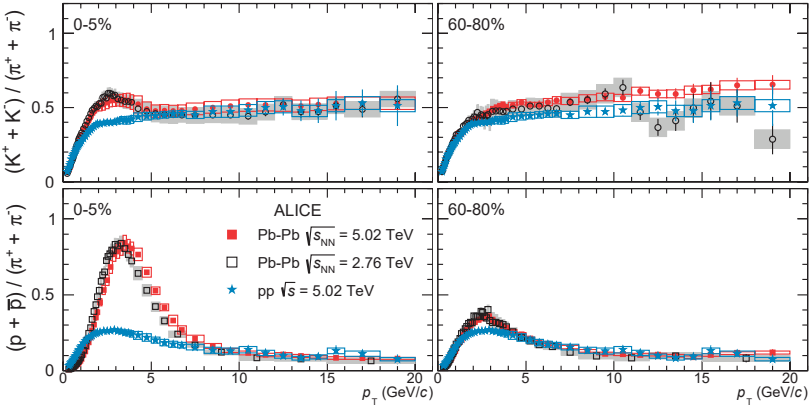


**Figure 3.11:**  $p_T$ -differential  $K/\pi$  and  $p/\pi$  ratio in central (0-5%) and peripheral (60-80%) collisions. The figure is taken from [43].

### 3.3 Anisotropic Flow

One of the most significant discoveries of the experimental heavy-ion programme is the collective flow. Collectivity is understood as the number of ejectiles that exhibit a common property. For example, the emission of many ejectiles with a common velocity field or into a common direction [44]. Because this collective flow is so strong, it can be used to map out the initial geometry of the collision. The initial geometry will cause

the fireball to develop different pressure gradients. Figure 3.12 shows a sketch of a non-central collision. The initial interaction region viewed in the transverse plane is almond-shaped. Hence, the pressure gradients are more significant close to the event plane ( $xz$ ) direction than perpendicular to it. This means that nuclear matter will flow with a larger velocity near the event plane than perpendicular to it and hence, the hydrodynamical evolution of the medium will translate into an anisotropic azimuthal distribution of the emitted particles.

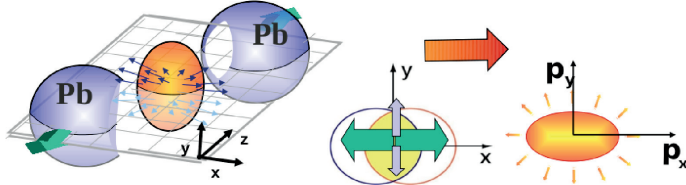


**Figure 3.12:** Initial interaction region of a non-central Pb–Pb collision.

The azimuthal distribution of the emitted particles resulting from the anisotropic expansion of the medium is commonly expressed as

$$\frac{dN}{d\varphi} = 1 + \sum_{n=1}^{\infty} 2v_n(p_T) \cos(n(\varphi - \Psi_n)) , \quad (3.8)$$

where  $v_n$  is the magnitude of the  $n$ th order harmonic term relative to the angle of the plane of symmetry  $\Psi_n$ . The  $v_n$  terms are commonly referred to as *flow coefficients*, where,  $v_2$  and  $v_3$  are known as *elliptic* and *triangular* flow coefficients, respectively.

A common technique to characterise the properties of the medium is with two-particle correlations between particle pairs consisting of a “trigger” at transverse momenta  $p_T^t$  and an “associated” partner with  $p_T^a$  [45, 46]. Trigger-associated particle correlations can be expressed as

$$\frac{dN_{\text{pairs}}}{d\Delta\varphi} \propto C(\Delta\varphi) = 1 + \sum_{n=1}^{\infty} 2v_n(p_T^t)v_n(p_T^a)\cos(n\Delta\varphi) , \quad (3.9)$$

By performing a global fit of the two-particle correlation function  $C(\Delta\varphi)$  using Eq. 3.9 one can measure the amplitudes of the harmonics  $v_n$  as shown in Fig. 3.13. The solid red line represents the global fit, which corresponds to the sum of anisotropic flow coefficients  $v_2, v_3, v_4$  and  $v_5$ . It is worth noting the doubly peaked correlation structure centred opposite to the trigger particle. This two-peak structure is interpreted as a manifestation of triangular flow [47].

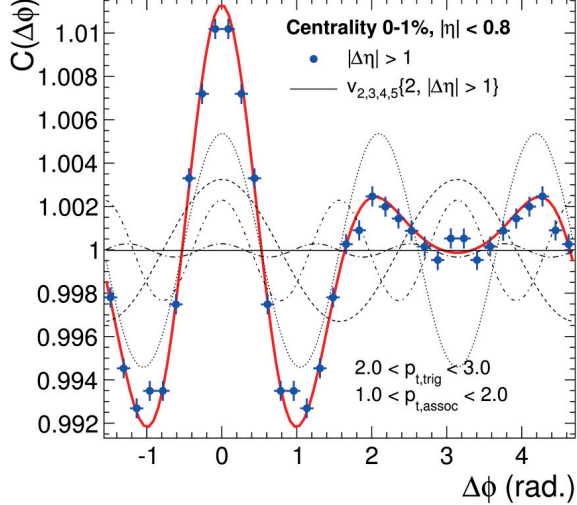


**Figure 3.13:** Fourier decomposition of two-particle angular correlations in central Pb–Pb collisions at  $\sqrt{s_{\text{NN}}} = 2.76$  TeV. The figure is taken from [46].

Figure 3.14 shows the  $v_2$  of identified particles in Pb–Pb collisions at  $\sqrt{s_{\text{NN}}} = 2.76$  TeV as a function of the  $p_T$  in different centrality classes. It can be observed that the  $v_2$  at a specific  $p_T$  value increases from central to peripheral collisions. In fact, the  $v_2$  at a fixed  $p_T$  value is maximum for the centrality class 40 – 50%. This is in line with the picture of the final state anisotropy driven by the geometry of the collision. In addition, a mass ordering is seen for all centralities in the low  $p_T$  region ( $p_T \lesssim 3$  GeV/c). This is explained as an interplay between the elliptic and radial flow. Recall that radial flow tends to decrease the particle spectrum at low  $p_T$  and its effects are more relevant for heavier particles. When radial flow is introduced in a system that exhibits azimuthal anisotropy, this depletion becomes larger in-plane (close to the reaction plane) than out-of-plane, thereby reducing  $v_2$  [48]. As a consequence, at a fixed value of  $p_T$ , heavier particles have a smaller  $v_2$  value compared to lighter ones. For example the  $v_2$  of  $\pi$  is larger than the ones of  $p$  at  $p_T \approx 0.5$  GeV/c for the centrality class 40 – 50%.

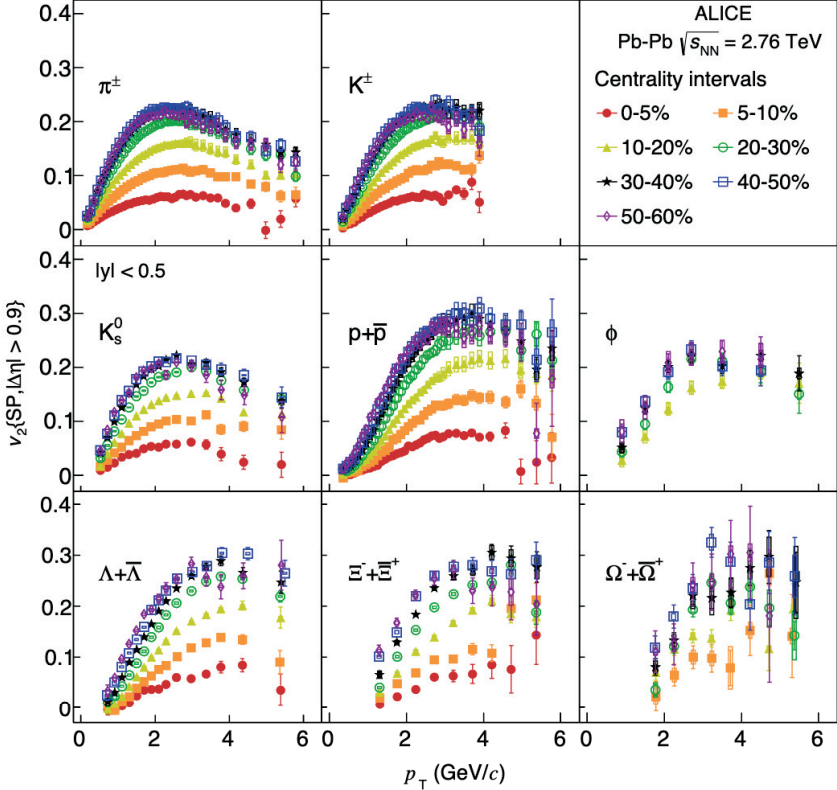


**Figure 3.14:** The  $p_T$ -differential  $v_2$  for different centralities of Pb–Pb collisions at  $\sqrt{s_{NN}} = 2.76$  TeV group by particle species. The figure is taken from [48].

### 3.4 Parton Energy Loss

In this section, I will describe one essential feature of the QGP, namely the one related to parton energy loss or jet quenching. Jet quenching was proposed by Bjorken [49] as the extinction of jets due to the energy loss of partons in the QGP. High- $p_T$  parent partons in heavy-ion collisions result from the initial hard scattering of the constituent nucleons. Then, such partons fragment to create a high-energy cluster (jet) of particles. The measurement of jets in heavy-ion collisions are important because they are created during the early stages of the collision. They experience the evolution of the medium and interact with it. Figure 3.15 shows a cartoon of a back-to-back jet traversing the QGP. Both the leading and subleading partons experience the effects of the QGP. However, the latter loses its energy mainly through induced gluon radiation and eventually gets absorbed by the medium.

Figure 3.15 shows the results of two-particle azimuthal angle correlations in both minimum bias pp and d–Au and central Au–Au collisions [50, 51]. The distributions are measured in events with trigger particles with  $4 < p_T^{\text{trigger}} < 6 \text{ GeV}/c$ . Fig. 3.15 (a) shows the typical dijet configuration observed in pp and peripheral Au–Au collisions i.e., a near-side ( $\Delta\phi \sim 0$ ) and an away-side peak ( $\Delta\phi \sim \pi$ ). Fig. 3.15 (b) shows the angular distributions for pp and central Au–Au collisions. While in pp collisions, both the near- and away-side peaks are observed, in central Au–Au collisions, only the near-side peak is measured. This is understood as a jet quenching effect, where the subleading parton lost most of its energy interacting with the medium and eventually absorbed it. However, it is important to mention that there is also triangular flow  $v_3$  and this will mix with jet quenching for low  $p_T$ . So the reduction at  $\Delta\phi \sim \pi$  is most likely an effect of jet quenching plus dip ( $v_3$  dips at  $\Delta\phi \sim \pi$ , see Fig. 3.13).

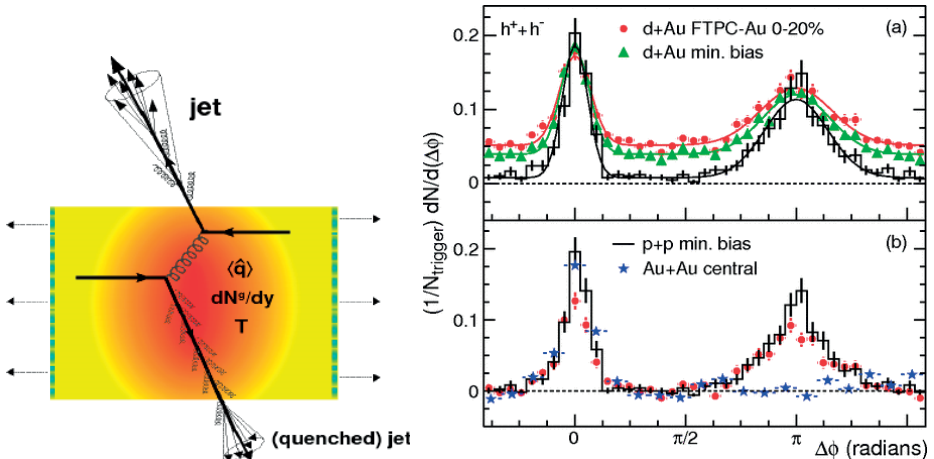


**Figure 3.15:** (Left) Cartoon of a back-to-back jet traversing the QGP. The leading jet escapes the QGP while the subleading one loses energy in the medium and gets absorbed. (Right) Two-particle azimuthal angle correlations in minimum bias pp and d–Au and central Au–Au collisions measured by the STAR collaboration. In central Au–Au collisions, the away-side peak disappeared because the subleading jet lost its energy in the medium. The figure is taken from [50].

An alternative approach to measuring the effects of jet quenching is to use the  $p_T$  distributions of (un-)identified particles via the nuclear modification factor defined as:

$$R_{\text{AA}} = \frac{d^2 N_{\text{AA}}/dp_T dy}{N_{\text{coll}} d^2 N_{\text{pp}}/dp_T dy}, \quad (3.10)$$

where  $d^2 N/dp_T dy$  represents the  $p_T$  distributions in nucleus-nucleus (AA) or proton-proton collisions (pp) and  $N_{\text{coll}}$  is the average number of binary nucleon-nucleon colli-

sions in a given centrality interval of AA. It is worth mentioning that the applicability of the scaling by the number of binary collisions in the construction of the  $R_{AA}$  is valid only to hard processes (particle production at high  $p_T$ ).

Figure 3.16 shows the  $R_{AA}$  of  $\pi$ , K and p in Pb–Pb collisions at  $\sqrt{s_{NN}} = 5.02$  TeV as a function of the centrality of the event [52]. It is observed that the production of high- $p_T$  particles ( $p_T \gtrsim 4$  GeV/c) is suppressed in central collisions. The  $R_{AA}$  of protons is larger in the interval ( $4 \lesssim p_T \lesssim 6$  GeV/c), however in this region other effects such as radial flow become relevant. However, all the different species are equally suppressed for  $p_T \gtrsim 8$  GeV/c. This means that particle production at high transverse momentum cannot be explained in terms of particle production in pp collisions scaled by  $N_{coll}$  and that a change of physics in nucleus-nucleus collisions is observed as a consequence of the medium effects. For peripheral collisions, a reduction in the suppression of high- $p_T$  particles is also observed.

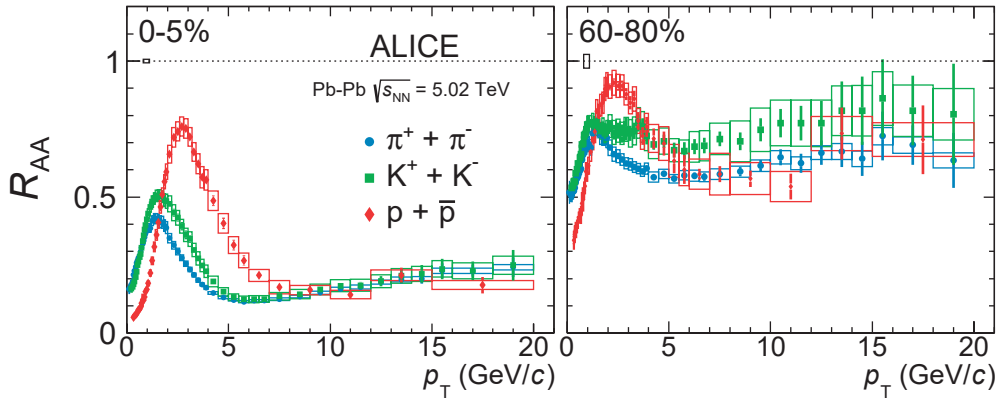


**Figure 3.16:** The nuclear modification factor of  $\pi$ , K and p in central (0-5%) and peripheral (60-80%) Pb–Pb collisions at  $\sqrt{s_{NN}} = 5.02$  TeV. The figure is taken from [43].

### 3.5 Heavy-Quarkonia Suppression

In a theoretical field approach, the interactions between a particular matter can be understood as the exchange of one or more excitations of the fields mediating these interactions. The contribution to the potential from the exchange of  $n$  field excitations with mass  $m$  is  $V \sim (e^{-mr}/r)^n$ . For example, if the leading contribution is due to the exchange of a single massless, classical field excitation, then the dominant contribution takes the form of the classical Coulomb potential, i.e.  $V_C \sim 1/r$  and the force  $F_C \sim 1/r^2$ . When the leading contribution is due to the exchange of a single

massive, classical field excitation, then the dominant contribution takes the form of the Yukawa potential [53], i.e.  $V_Y \sim e^{-mr}/r$ . The Yukawa potential is an example of a screened interaction with the Debye-Hückel or screening length  $\lambda = 1/m$  [54]. In general, *screening* refers to the presence of mobile charges that cause the falloff of the leading contribution to a potential being larger than the power law  $V \sim 1/r^n$  that would be expected for the exchange of  $n$  massless, classical field excitations [55]. When the screening radius  $r_D$  becomes less than the binding radius  $r_H$  of the quark system, i.e., less than the hadron radius, the confining force can no longer hold the quarks together and hence deconfinement sets in.

A quarkonium state is a flavorless meson whose constituents are a heavy quark and its antiquark ( $q\bar{q}$ ), making it both a neutral particle and its own antiparticle. One direct evidence of the formation of a deconfined medium of quarks and gluons in heavy-ion collisions is the suppression of quarkonium states both of the charmonium ( $J\psi, \psi(2S), \chi_c$ , etc.) and the bottomonium ( $\Upsilon(1S, 2S, 3S), \chi_b$ , etc.) families. This phenomenon was proposed, because, in the deconfined medium, the biding potential between the constituents of a quarkonium state should be screened by the colour charges of the surrounding light quarks and gluons [56, 57]. The suppression of quarkonium states is predicted to happen above the critical temperature of the medium ( $T_c$ ) and to depend of the  $q\bar{q}$  energy. This means that  $\Upsilon(1S)$ , the most tightly bound state among all quarkonia, is expected to have the highest dissociation temperature. For example, dissociation temperatures are reported in [58] for the bottomonium stater:  $T_{\text{dissoc}} \approx 2T_c, 1.2T_c$ , and  $1T_c$  for the  $\Upsilon(1S), \Upsilon(2S)$  and  $\Upsilon(3S)$  states, respectively.

Figure 3.17 (left) shows the dimoun invariant mass distribution in centrality-integrated Pb–Pb collisions measured by the CMS collaboration [59] for the kinematic range  $p_T^{\mu^+\mu^-} < 30 \text{ GeV}/c$ ,  $|y^{\mu^+\mu^-}| < 2.4$  and fits to the data (continuous blue line). The dashed red lines are derived from fits to the data. To observe the suppression of all  $\Upsilon$  states in Pb–Pb collisions, the amplitudes of the corresponding peaks are increased above those found in the fit by the inverse of the measured  $R_{AA}$  for the corresponding  $\Upsilon$  meson. Figure 3.17 (right) shows the dependence of the  $R_{AA}$  on the collision centrality, as quantified using the  $\langle N_{\text{part}} \rangle$ . One sees a strong suppression of the  $\Upsilon(3S)$  in both centrality bins studied, 0-30 % and 30-100 %. Moreover, the  $\Upsilon(2S)$  and  $\Upsilon(1S)$  show a decreasing  $R_{AA}$  with increasing collision centrality, being stronger for the  $\Upsilon(2S)$  meson. This result confirms the previously observed suppression in Pb–Pb collisions at  $\sqrt{s_{\text{NN}}} = 2.76 \text{ TeV}$  by CMS.

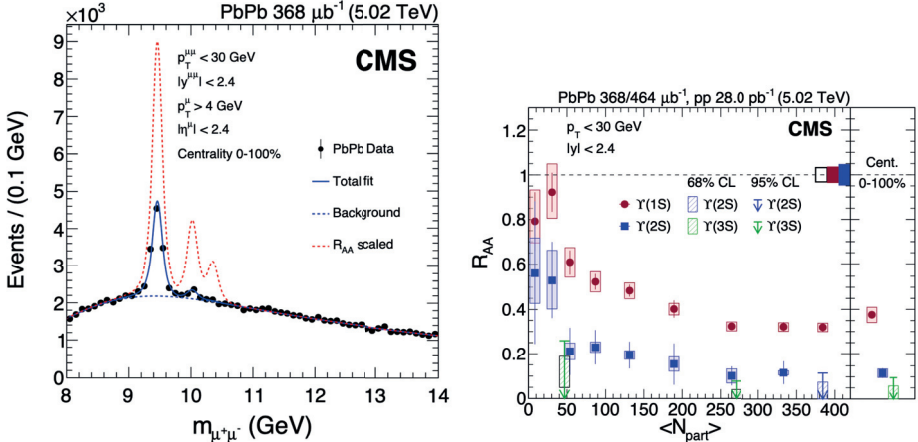


**Figure 3.17:** (Left) Invariant mass distribution of muon pairs in Pb–Pb collisions, for the kinematic range  $p_T^{\mu^+\mu^-} < 30 \text{ GeV}/c$ ,  $|y^{\mu^+\mu^-}| < 2.4$ . (Right) Nuclear modification factors for the  $\Upsilon(1S)$ ,  $\Upsilon(2S)$  and  $\Upsilon(3S)$  mesons as a function of  $\langle N_{\text{part}} \rangle$ . The figures are taken from [59].

### 3.6 Experimental Overview on Small Collision Systems

As discussed above, collective effects in nucleus-nucleus collisions are a consequence of the formation of the QGP. When acting against the surrounding vacuum, the thermal pressure will lead to a collective expansion of the fireball; hence, effects such as radial and anisotropic flow can be observed. Although in pp and p–Pb collisions, the formation of a QGP has not been confirmed, evidence of collective effects has been observed.

The first set of results that I would like to describe is the two-particle angular correlations measured in pp collisions at  $\sqrt{s} = 13 \text{ TeV}$  by the CMS collaboration [9]. Figure 3.18 shows the 2D  $\Delta\eta - \Delta\varphi$  correlation functions, for pairs of a charged (top), a  $K_S^0$  (middle), or a  $\Lambda/\bar{\Lambda}$  (bottom) trigger particle with a charged associated particle, in low-multiplicity ( $10 \leq N_{\text{trk}}^{\text{offline}} < 20$ ) (left) and high-multiplicity ( $105 \leq N_{\text{trk}}^{\text{offline}} < 150$ ) events. The first feature that one can observe from the high-multiplicity events and all three particles is the characteristic near-side peak around  $(\Delta\eta, \Delta\varphi) = (0, 0)$ , associated with the jet. For the same type of events, one can observe a long-range “ridge” structure at  $\Delta\varphi \approx 0$  over a wide range in relative pseudorapidity ( $|\Delta\eta| \approx 4$ ). In contrast, such a structure is not observed in low multiplicity events. On the away-side, ( $\Delta\varphi \approx \pi$ ) of the correlation functions one, sees a long-range structure, which was found to be larger in magnitude than that on the near-side and contains contributions from the away-side jet. Such long-range near-side correlation structure was first observed in nucleus-nucleus collisions at RHIC energies in Cu–Cu and Au–Au collisions [60–62] and it has been

suggested that the collective hydrodynamic flow of a strongly interacting and expanding medium [63–65] was responsible for these long-range correlations in large collision systems. Does this suggest the formation of a quark-gluon plasma droplet in small collision systems? One of the key pieces of evidence for the formation of the quark-gluon plasma in nucleus-nucleus collisions is the presence of jet quenching, which has not been observed in small collisions yet. Therefore, whether there is QGP in small systems is currently an active topic of investigation.

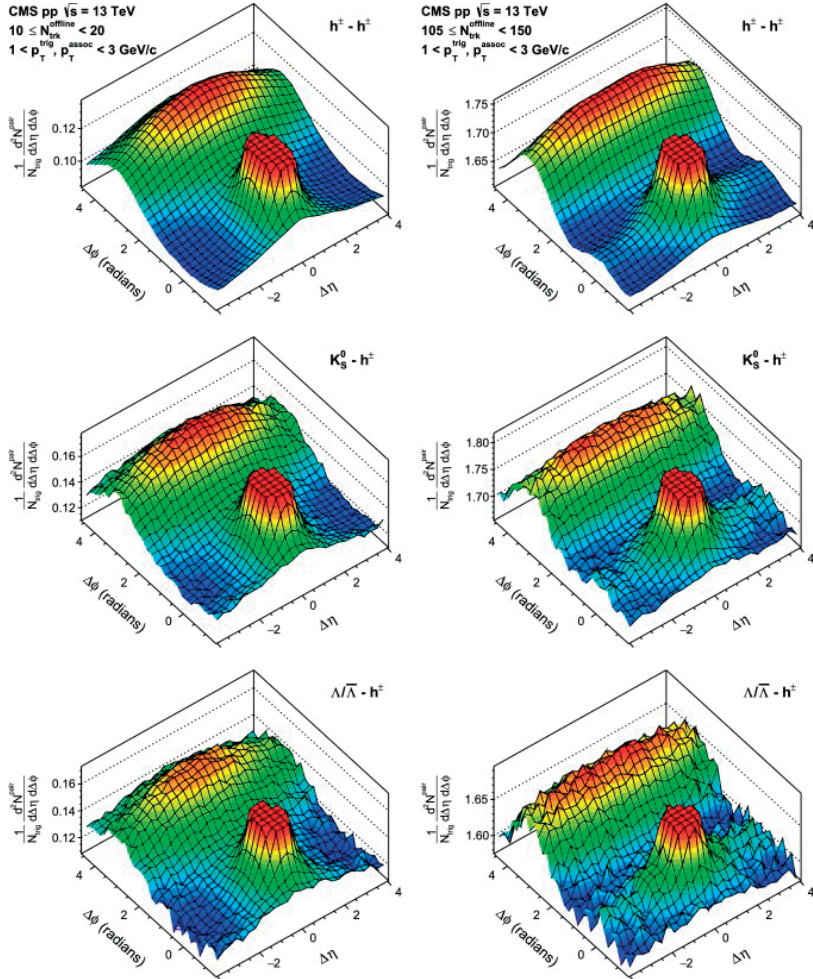


**Figure 3.18:** Two-particle  $\Delta\eta - \Delta\varphi$  correlation functions for inclusive charged particles (top),  $K_S^0$  particles (middle), and  $\Lambda/\bar{\Lambda}$  particles (bottom), with  $1 < p_T^{\text{trig}} < 3 \text{ GeV}/c$  and associated charged particles with  $1 < p_T^{\text{trig}} < 3 \text{ GeV}/c$ , in low-multiplicity ( $10 \leq N_{\text{trk}}^{\text{offline}} < 20$ ) (left) and high-multiplicity ( $105 \leq N_{\text{trk}}^{\text{offline}} < 150$ ) events in pp collisions at  $\sqrt{s} = 13 \text{ TeV}$ . The figure is taken from [9].

The second set of results that I would like to describe has to do with observing an enhancement in the  $p_T$ -differential baryon-to-meson ratio in high-multiplicity events across system size in pp, p–Pb and Pb–Pb collisions by the ALICE collaboration [66]. Figure 3.19 shows the  $p_T$ -differential  $p/\pi$  and  $\Lambda/K_S^0$  ratio for low- and high-multiplicity classes in pp, p–Pb and Pb–Pb collisions. In Pb–Pb collisions the enhancement of the  $p/\pi$  and  $\Lambda/K_S^0$  ratios at intermediate  $p_T$  ( $1 \lesssim p_T \lesssim 4 \text{ GeV}/c$ ) is typically attributed to the presence of radial flow, which increases progressively for more central collisions. However, the corresponding measurements in pp and p–Pb collisions revealed a similar structure to that observed in Pb–Pb collisions, i.e., in small collision systems, one also sees a depletion (enhance) of low- (high)- $p_T$  protons. Hence, can we say that the observations made in small collision systems are attributed to radial flow effects? Well, the origin of such observations remains unknown. On the other hand, PYTHIA has shown that its colour reconnection mechanism develops flow-like effects where the boost is introduced at the partonic state just before hadronisation in events with several multiple parton interactions [67]. In addition, the microscopic effect of PYTHIA does not require the formation of a medium. Therefore, is the enhancement observed in the  $p/\pi$  and  $\Lambda/K_S^0$  ratios a medium effect or a string effect?

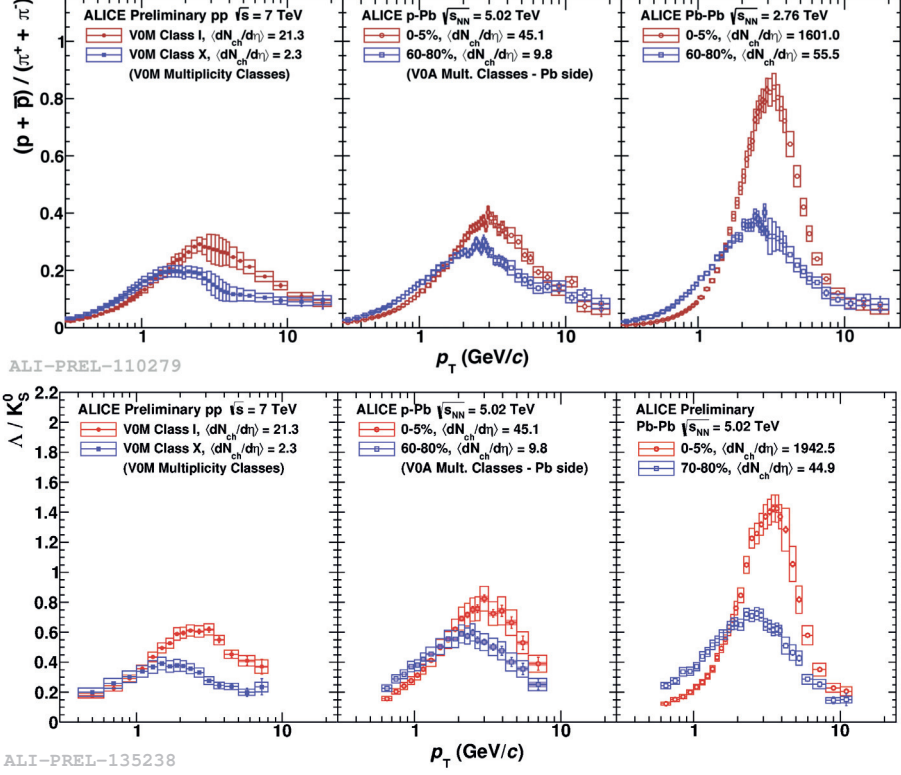


**Figure 3.19:** The  $p_T$ -differential  $p/\pi$  and  $K_S^0$  ratioz in pp, p–Pb and Pb–Pb collisions at the energies of  $\sqrt{s} = 7$  TeV,  $\sqrt{s} = 5.02$  TeV and  $\sqrt{s_{NN}} = 2.76$  TeV measured by the ALICE collaboration. The figures are taken from [66].

The last topic I would like to touch on is the enhanced production of strange hadrons in small collision systems. The ALICE collaboration has performed many measurements on the production of strange hadrons in pp and p–Pb collisions at several colliding energies [68–70]. Figure 3.20 shows the double ratios:  $(h/\pi)/(h/\pi)_{\text{INEL}>0}^{\text{PP}}$  as a function of the charged-particle density at midrapidity ( $\langle dN_{\text{ch}}/d\eta \rangle_{|\eta|<0.5}$ ) for strange hadrons. The term  $(h/\pi)_{\text{INEL}>0}^{\text{PP}}$  corresponds to the measurement made in minimum bias pp collisions. One sees a significant enhancement of the double ratio with increasing particle multiplicity. The ratios follow a hierarchy that suggests being determined by the strangeness content rather than by the mass, baryon number of the hadron or centre-of-mass energy. In summary, a steadily increase of the strangeness production was observed as a function of  $\langle dN_{\text{ch}}/d\eta \rangle$  from low-multiplicity pp to high-multiplicity p–Pb collisions. The origins of these observations remain unknown.

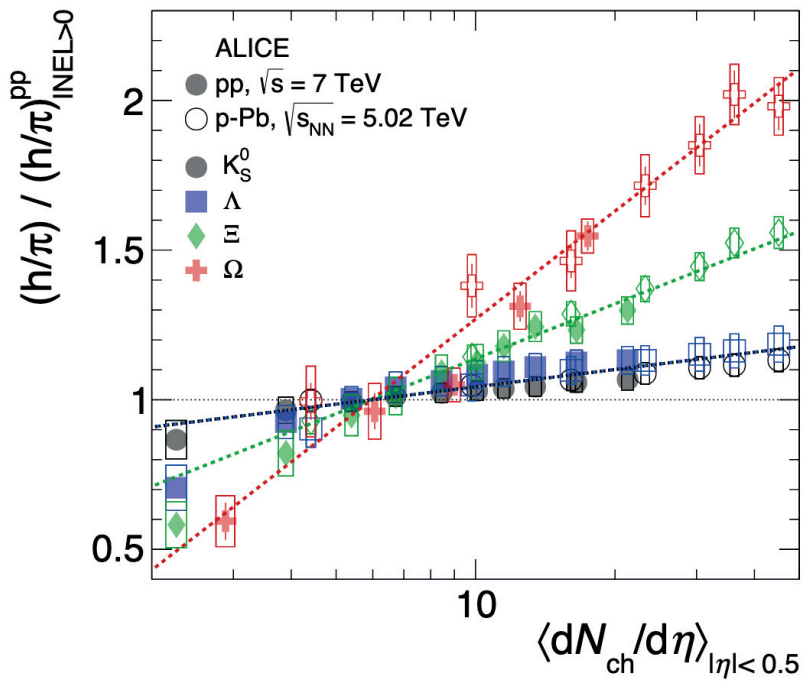


**Figure 3.20:** Particle yield ratios to pions normalised to the values measured in the inclusive pp sample. The results are shown for pp and p–Pb collisions, normalised to the inclusive pp sample. The figure is taken from [10].

### 3.7 The CLASH Project

The CLASH project is a collaboration between experimental and theoretical particle physicists at Lund University, which focuses on improving the understanding of some of the most debated experimental results from the Large Hadron Collider (LHC) at CERN. As described in Sec. 3.6, measurements in pp and p–Pb collisions have revealed QGP-like signatures in small systems; however, this does not mean the formation of a QGP since jet quenching has not been observed. Furthermore, in these systems, one did not expect a QGP to be able to form since the systems are considered too dilute and too short-lived. Thus, the goal of the CLASH project is to pin down the origin of collective effects in small collisional systems. It is funded by the Knut and Alice Wallenberg Foundation from summer 2018 to summer 2023.

The CLASH project utilises the long-standing tradition of Lund university in the studies of both large and small collisional systems. On the experimental side, Peter Christiansen (PI) leads a team that aims at proposing new observables to investigate the origins of collective effects in small systems. From the theoretical side, Leif Lönnblad (co-PI) is the author of several microscopic models. CLASH is centred around proposed new experimental measurements and the development of a new theoretical model. CLASH has three main branches:

- Angantyr. A theoretical goal is to develop new physics for the world-famous PYTHIA generator. PYTHIA can describe most of the well-known small system physics, and the theoretical team wants to extend it to describe the new QGP-like effects in small systems. But also, secondly, to extend PYTHIA to be able to model larger collision systems such as p–Pb and Pb–Pb collisions. This extension is called Angantyr.
- Jet quenching in small systems? On the experimental side, a goal is to search for other QGP-like effects in small collisional systems that have not been observed so far. The most prominent unobserved QGP-like effect is jet quenching. The experimental team wants to develop new more sensitive measurements to search for jet quenching in small systems.
- The CLASH. The project’s primary goal is to directly confront the traditional paradigm for small collision systems (microscopic models based on quarks and gluons) with the QGP-paradigm originating in large collisional systems (macroscopic models based on relativistic viscous hydrodynamics). Furthermore, the goal is to identify the most sensitive observables for differentiating between the model descriptions using Angantyr and other models and to carry out the most promising measurements then.

# Chapter 4

## Phenomenological Models

This chapter briefly describes the phenomenological models used to predict particle distributions in hadronic collisions. I will mainly describe the physics behind the PYTHIA and EPOS LHC models, which contain very different physics. The basic units in PYTHIA are the Lund strings that create colour fields when connected. Furthermore, PYTHIA does not assume the formation of a QGP. On the other hand, EPOS LHC assumes the formation of a QGP. EPOS LHC is a core-corona model, which distinguishes between particles created in the core from the corona. Comparisons between data and model predictions are helpful to understand the underlying mechanisms in particle production.

### 4.1 The Lund String Model

Consider the process of  $e^+e^-$  annihilation into a virtual photon or  $Z^0$  boson, which will subsequently decay to a  $q\bar{q}$  pair. Furthermore, assume that the  $q$  and  $\bar{q}$  are going out back-to-back in one dimension along the  $q\bar{q}$ -axis in the overall centre-of-mass frame. Due to the three-gluon coupling [71] the colour flux lines will not spread out over all space, as the electromagnetic field lines do, but rather be constrained to a thin tube-like region, see left panel of Fig 4.1. From the available energy within this tube, new  $q\bar{q}$ -pairs can be created; thus, the original system breaks into smaller and smaller pieces. Then the entire colour field can then be approximated by a one-dimensional string stretched straight between the  $q$  and  $\bar{q}$ , see the right panel of Fig. 4.1.

Furthermore, confinement implies that the tube-like field contains constant field energy stored per unit length. For large distances, the potential between  $q$  and  $\bar{q}$  can be

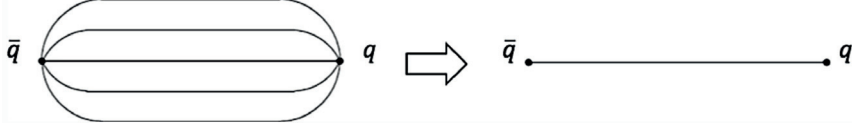


**Figure 4.1:** A simplified colour-field topology in a  $q\bar{q}$  system and its simplified string representation. The figure is taken from [72].

approximated as:

$$V(r) \approx \kappa r . \quad (4.1)$$

As one is only interested in the long range behaviour, the Coulombic term ( $\sim 1/r$ ) from Eq. 2.18 is neglected. Phenomenologically the value of the constant  $\kappa$ , known as *string tension* (energy per unit length), is usually quoted to be equal to  $0.85\text{GeV}/\text{fm}$  [73].

Neglecting the transverse degrees of freedom, the Hamiltonian of the  $q\bar{q}$  system can be written as [74]:

$$\begin{aligned} H &= E_q + E_{\bar{q}} + V(r) , \\ &= E_q + E_{\bar{q}} + \kappa|z_q - z_{\bar{q}}| , \end{aligned} \quad (4.2)$$

where  $|z_q - z_{\bar{q}}|$  is the distance between  $q$  and  $\bar{q}$ , and  $E_q$  and  $E_{\bar{q}}$  are the energies of the  $q$  and  $\bar{q}$ .

From the Hamiltonian, the equations of motion follow a linear relationship between the space-time and the energy-momentum pictures [72, 74]

$$\left| \frac{dp_{z,q/\bar{q}}}{dt} \right| = \left| \frac{dp_{z,q/\bar{q}}}{dz} \right| = \left| \frac{dE_{q/\bar{q}}}{dt} \right| = \left| \frac{dE_{q/\bar{q}}}{dz} \right| = \kappa \quad (4.3)$$

The signs of the derivatives depend both on the direction of motion of the parton and the direction the string pulls it in. For example, when the parton moves out along the  $+z$  axis, the string pulls the parton in the  $-z$  direction; hence all signs are negative.

In the absence of string breaking, the motion of the  $q\bar{q}$  and the string is viewed as a “yo-yo” motion from its rest frame, where the string is alternately “reeled out” and “reeled in” (see Fig. 4.2). During the first quarter of a period, at the time  $t = 0$ , the  $q$  and  $\bar{q}$  start to move apart from each other with the speed of light until the string reaches its maximum length and the position of the  $q$  and  $\bar{q}$  are equal to  $z = \pm t$ . Hence the

string length is equal to  $l_{\text{string}} = 2t$ . At the time  $t = E_{\text{CM}}/2\kappa$  the string carries all the energy, where  $E_{\text{cm}}$  is the centre-of-mass energy of the system, then the string tension forces the  $q$  and  $\bar{q}$  to turn around. During the second quarter, the energy and momentum are transferred back to the  $q$  and  $\bar{q}$ . At  $t = E_{\text{CM}}/\kappa$ , the string length is equal to zero, and the  $q$  and  $\bar{q}$  are back at the origin, but now moving in the  $\mp z$  direction. The motion previously described happens during the first half of the period. Therefore the second half of the period is similar to the first half, only with the role of  $q$  and  $\bar{q}$  interchanged.

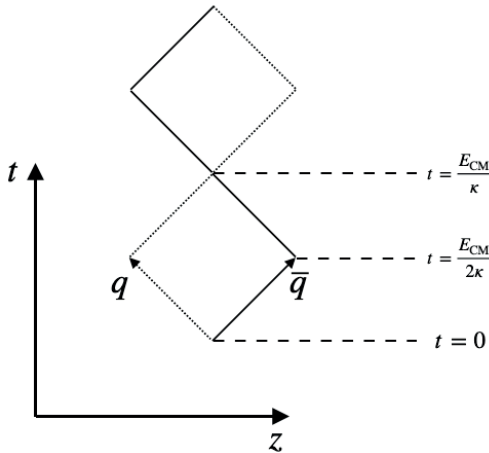


**Figure 4.2:** The yo-yo motion of a  $q\bar{q}$  system.

Equation 4.1 shows that the potential energy carried by the string increases as a function of the distance between the original  $q$  and  $\bar{q}$ . If the potential energy gets large enough, the potential energy can be used to create another  $q_i\bar{q}_i$  pair so that the long string breaks up into two shorter strings. For the energy and momentum to be conserved, both  $q_i$  and  $\bar{q}_i$  have to be massless particles and have to be created at the same space-time point with zero momentum and afterwards move with increasing momenta and in opposite directions. When a system breaks into two parts producing a pair  $q_1\bar{q}_1$  at the space-time point  $(z_1, t_1)$  and at a later time another pair  $q_2\bar{q}_2$  is created at  $(z_2, t_2)$ , a hadron can be formed by the pair  $\bar{q}_1q_2$ , see Fig. 4.3. The energy and momentum of the  $\bar{q}_1q_2$  hadron will be equal to  $\kappa(z_2 - z_1)$  and  $\kappa(t_2 - t_1)$ , respectively [74]. To obtain the correct mass of the hadron, the point  $(z_2, t_2)$  must lie on a hyperbola given by

$$(z_2 - z_1)^2 - (t_2 - t_1)^2 = m^2/\kappa^2 , \quad (4.4)$$

which can be parameterised according to

$$(z_2 - z_1, t_2 - t_1) = \frac{m}{\kappa}(\cosh y, \sinh y), \quad (4.5)$$

where  $m/\kappa$  is the maximum distance between  $\bar{q}_1$  and  $q_2$  in the rest frame of the  $\bar{q}_1 q_2$  system and  $y$  represents the rapidity of the hadron [74].

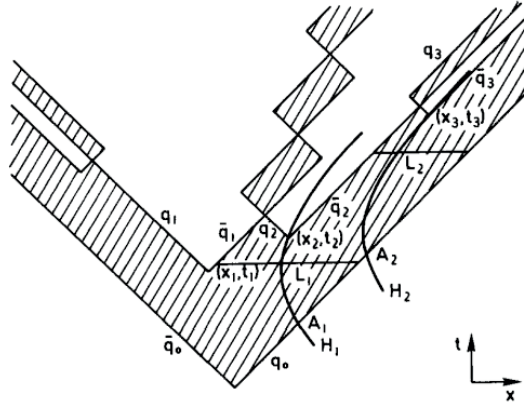


**Figure 4.3:** The original  $q_0$  and  $\bar{q}_0$  move in opposite directions. Due to the large potential energy in the string, new  $q_i\bar{q}_i$  pairs are created at the space-time points  $(z_i, t_i)$ . The figure is taken from [74].

In the discussion above, it was assumed that the pair  $q_i\bar{q}_i$  was generated from string breaking are massless and have no transverse momentum. If the pair is massive, both  $q_i$  and  $\bar{q}_i$  still have to be created in the same space-time location but as virtual particles. Each virtual particle has to tunnel out a distance  $l = m_\perp/\kappa$  to acquire enough energy from the string to correspond to its transverse mass,  $m_\perp$  [72]. This tunnelling results in a Gaussian suppression factor

$$\exp\left(-\frac{\pi m_\perp^2}{\kappa}\right) = \left(-\frac{\pi m^2}{\kappa}\right)\left(-\frac{\pi p_\perp^2}{\kappa}\right). \quad (4.6)$$

One consequence of this mechanism is the suppression of heavy quark production in string breaks, approximately like  $u\bar{u} : s\bar{s} : c\bar{c} \approx 1 : 1 : 0.3 : 10^{-11}$  [74]. Therefore it is assumed the c and b production only occurs by perturbative processes.

### 4.1.1 Multiple Parton Interactions and Colour Reconnection

The above discussion was centred around strings created between  $q\bar{q}$  pairs in a typical  $e^+e^-$  annihilation process. However, several additional complications arise moving to pp collisions, including initial-(final-)state radiation, beam remnants and multiple parton interactions (MPIs), see Fig. 4.4.

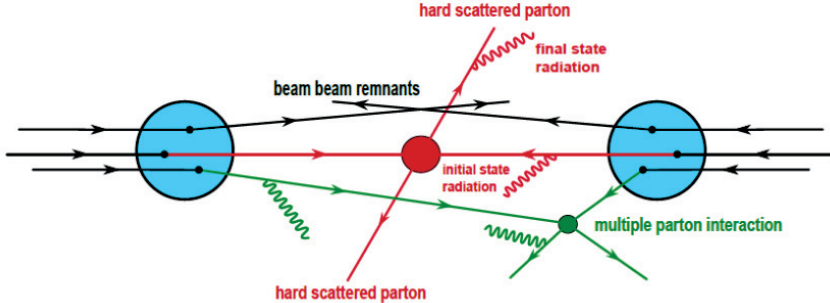


**Figure 4.4:** Sketch of a proton-proton collision. The two outgoing hard partons are shown in red. Beam remnants interactions, MPIs and initial-(final-)state radiation are shown.

Multiple parton interactions lead to the production of many low  $p_T$  particles. As reported by the LHC experiments, the average transverse momentum ( $\langle p_T \rangle$ ) of charged particles shows a rapid increase with the multiplicity of the event in pp collisions, see Refs. [75–77]. For PYTHIA to describe the behaviour of the  $\langle p_T \rangle$  as a function of the multiplicity, the *colour reconnection* (CR) mechanism was introduced [78, 79]. Essentially the outgoing gluons from a hard gluon-gluon sub collision will be colour-connected to the projectile and target remnants so that the total string length becomes as short as possible, see Fig. 4.5. This mechanism implies that a minimum number of hadrons share the transverse momentum of the partons, and hence a more significant number of high- $p_T$  hadrons will be produced.

At the particle level, the colour reconnection mechanism of PYTHIA boosts particles with low transverse momentum to higher values producing an effect that mimics the one originated by the hydrodynamic flow. In data, this effect is observed to enhance the proton-to-pion ratio for  $p_T \lesssim 4$ . PYTHIA can describe this behaviour as shown in Fig. 4.6 thanks to its colour reconnection mechanism.

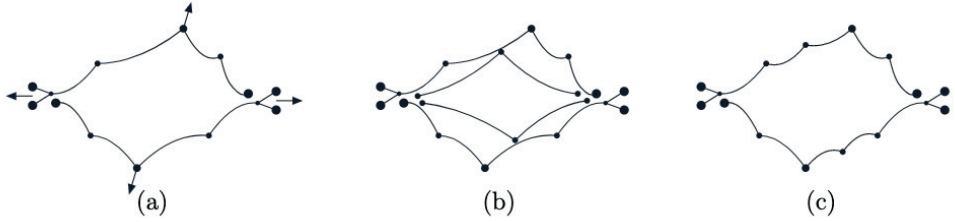


**Figure 4.5:** a) In a hard gluon-gluon sub collision, the outgoing gluons will be colour-connected to the projectile and target remnants. (b) A second hard scattering would naively be expected to give two new strings connected to the remnants. (c) In the fits to data, the gluons are colour reconnected so that the total string length becomes as short as possible. The figure is taken from [79].

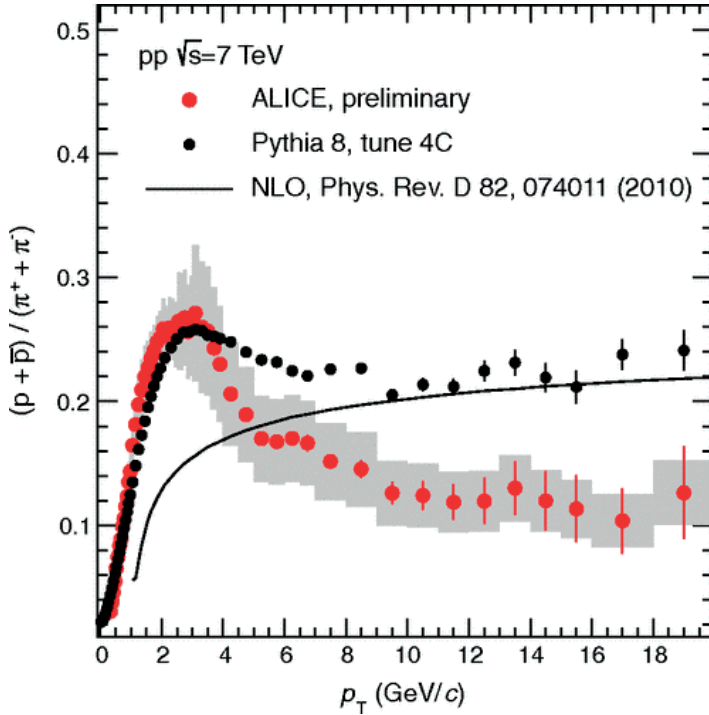


**Figure 4.6:**  $p_T$ -differential proton-to-pion ratio in minimum-bias  $pp$  collisions at  $\sqrt{s} = 7 \text{ TeV}$ . Measurements in data are represented with solid red markers, and the prediction from PYTHIA is shown with solid black markers. The figure is taken from [67].

## 4.2 The EPOS Model

In the EPOS Monte Carlo event generator, nucleus-nucleus and proton-proton collisions are viewed as many elementary scatterings happening in parallel. Each elementary scattering is called a *parton ladder* and may be considered as a longitudinal colour field [80], conveniently treated as a relativistic string as shown in Fig. 4.7. The flux tube decays via the production of  $q\bar{q}$  pairs, creating in this way string fragments. At a proper early time  $\tau_0$ , long before hadrons are formed, the collision area is divided into two regions. The former is called the *core*, characterised by a high string segments density (more than  $\rho_0$  segments per unit area in given transverse slices). The latter is called the *corona* and is characterised by a low density of string segments (see Fig. 4.7) [81]. Such division of the collision zone is motivated by simple geometrical considerations. If the local density of string segments is high enough, the core will appear. This limit is easily reached in central heavy-ion collisions at RHIC or the LHC. For central collisions, particle production from the corona is less dominant. For peripheral collisions, this contribution will even dominate. Hadronisation in the core part is motivated by statistical hadronisation models and blast-wave fits while particle production from the corona happens via string fragmentation [81].

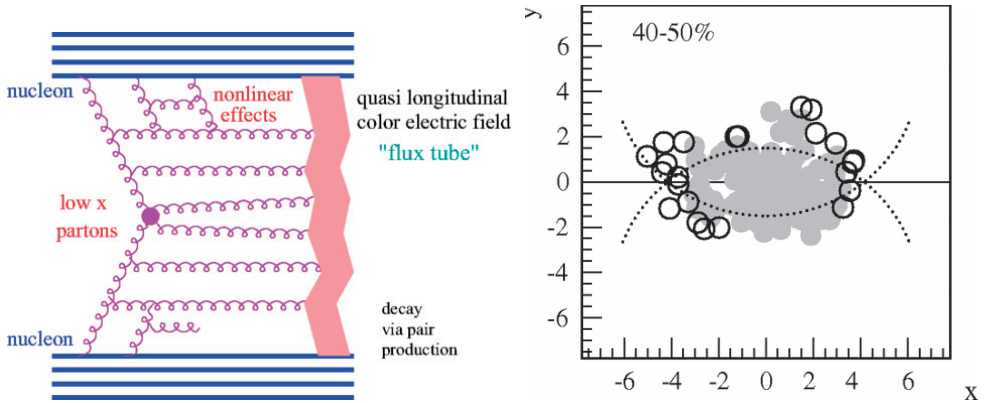


**Figure 4.7:** (Left) Elementary interaction in the EPOS model. The figure is taken from [82]. (Right) Semiperipheral (40-50 %) AuAu collision at 200 GeV. String segments in the core are represented with grey closed circles, and the corona region is shown with open circles. The figure is taken from [81].

*Clusters* are formed from string segments, which show a Bjorken-fluid-like behaviour. Therefore, clusters are considered to be collectively expanding in longitudinal and transverse directions [81]. At the freeze-out, which happens at some given energy density  $\varepsilon_{FO}$  particles have acquired at that moment a collective radial flow. In the EPOS model, radial flow is responsible for boosting particles towards higher  $p_T$  values, increasing the

$\langle p_T \rangle$  of the event.

In EPOS, a large number of string segments (cluster) implies a large event multiplicity. Figure 4.8 shows the relative contribution of particles from the core (relative to the complete spectrum, core + corona) as a function of the multiplicity of charged particles,  $N_{\text{ch}}$ . It can be observed that for the average multiplicity at 7 TeV, which is about 30, about 30% of the particles come from the core. Consequently, particle production is dominated by the core at larger multiplicities. The relative contribution of the core as a function of  $m_t - m$  for identified particles is shown in Fig. 4.8. For central collisions, the core contribution dominates, whereas for semi-central collisions (40% – 50%) and even for peripheral collisions, the contribution from the core decreases, and the corona contribution becomes significant. Furthermore, the relative contribution from the core and corona depends on the particle species.

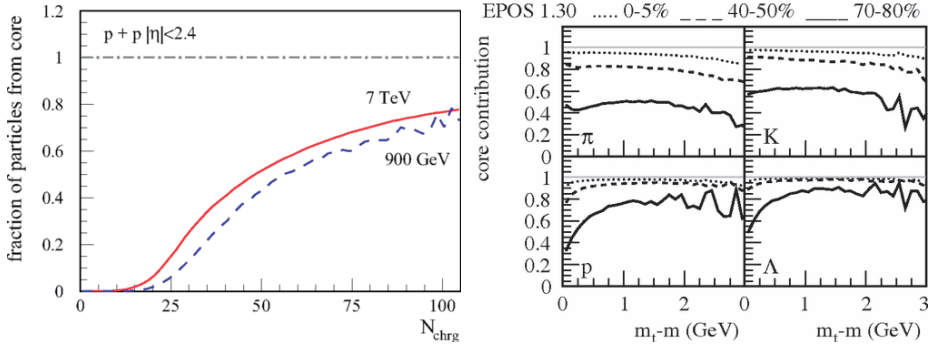


**Figure 4.8:** (Left) The relative contribution of particles from the core [core/(core + corona)] as a function of the charged-particle multiplicity  $N_{\text{ch}}$ . The figure is taken from [82]. (Right) Relative contribution of the core as a function of the transverse mass for different hadrons ( $\pi$ ,  $K$ ,  $p$ ,  $\Lambda$ ). The figure is taken from [81].

## **Part II**

# **Experimental Setup**



# Chapter 5

## Charged-Particle Detection

Experimental sciences, such as physics, can detect the existence of particles, either charged or neutral, through their interactions with matter. Indeed, different technologies and techniques are employed depending on the particle type one wants to observe. I start this chapter by describing how the  $p_T$  of a charged particle in a solenoidal magnetic field is measured. Then, I present a discussion about the underlying physical processes in particle detection. Finally, I will focus on detecting relativistic and long-live charged particles such as  $\pi$ , K and p through measurements of the energy loss and the time-of-flight. These sections present the basis for the particle identification analyses presented in this thesis.

### 5.1 Momentum Measurement

The equation of motion of a charged-particle with mass  $m$ , charge  $q$ , velocity  $\vec{v}$  and Lorentz factor  $\gamma$  in a homogeneous magnetic field  $\vec{B}$  is determined by the Lorentz force:

$$\vec{F} = \dot{\vec{p}} = q(\vec{E} + \vec{v} \times \vec{B}) \implies \dot{\vec{v}} = \frac{q}{\gamma m}(\vec{v} \times \vec{B}), \quad (5.1)$$

where,  $\vec{p}$  represents the relativistic momentum vector ( $\vec{p} = \gamma m \vec{v}$ ) and  $\vec{E} = 0$ . It is worth mentioning that although Eq. 5.1 is not written in a covariant form, it is also valid for relativistic particles (a discussion on this topic can be found in the chapter of relativistic-particle kinematics and dynamics in [83]). Here, I will assume that  $\vec{B}$  is a homogeneous magnetic field with only one component in the  $z$  direction:  $B_x = B_y = 0$ ,  $B_z = B > 0$ . This magnetic field configuration is in agreement with the one of the

L3 magnet of ALICE, where  $\vec{B} \approx 0.5 \hat{z}$  T. The solution of the differential equation, Eq. 5.1 yields:

$$\begin{aligned} v_x &= v_T \cos(\eta\omega_B t + \psi_0), \\ v_y &= -v_T \sin(\eta\omega_B t + \psi_0), \\ v_z &= v_3. \end{aligned} \quad (5.2)$$

Here,  $\omega_B$  is the cyclotron frequency,  $\eta$  the sign of the charge and  $v_T$  the absolute value of the velocity component perpendicular to the magnetic field:

$$\omega_B = \frac{|q|B}{\gamma m}, \quad \eta = \frac{q}{|q|} = \pm 1, \quad v_T = \sqrt{v_x^2 + v_y^2}. \quad (5.3)$$

The integration of Eqs. 5.2 yield the particle trajectories in position space:

$$\begin{aligned} x(t) &= \frac{v_T}{\eta\omega_B} \sin(\eta\omega_B t + \psi_0) + x_0, \\ y(t) &= \frac{v_T}{\eta\omega_B} \cos(\eta\omega_B t + \psi_0) + y_0, \\ z(t) &= v_3 t + z_0. \end{aligned} \quad (5.4)$$

The set of Eqs. 5.4 describes a particle's trajectory as a helix, which lies on a cylinder surface coaxially with the magnetic field. The projection of such helix onto the plane perpendicular to the magnetic field describes a circle with a radius:

$$R = \sqrt{(x(t) - x_0)^2 + (y(t) - y_0)^2} = \frac{v_T}{\omega_B} = \frac{\gamma m v_T}{|q|B} = \frac{p_T}{|q|B}. \quad (5.5)$$

Equation 5.5 gives a straightforward relation between  $p_T$  and  $R$ :

$$p_T = |q|BR = \frac{|q|B}{|\kappa|}, \quad (5.6)$$

where  $\kappa = -\eta/R$  is known as the “curvature” of the particle. Furthermore, Eq. 5.6 gives an easy relation between the  $p_T$  and  $R$  or  $\kappa$ . However, let's consider a proton

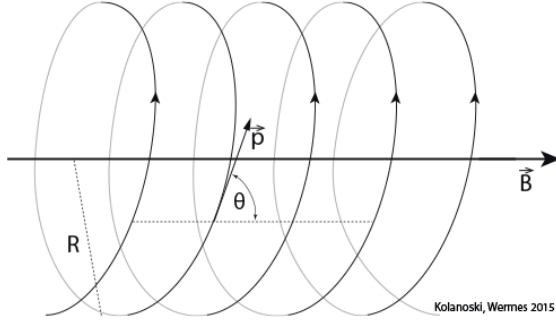


**Figure 5.1:** The trajectory of a charged particle under the influence of a homogeneous magnetic field  $\vec{B}$ . The trajectory represents that of a helix. For positively charged particles, the rotational direction is anticlockwise when looking into the direction of the  $\vec{B}$  field. The radius  $R$  represents the helix when projected in the plane perpendicular to the magnetic field. The angle  $\theta$  is taken between the momentum vector  $\vec{p}$  and a line parallel to the magnetic field. The figure is taken from [84].

with  $p_T = 1 \text{ GeV}/c$  in the TPC of ALICE. This yields a radius equal to:

$$R = \frac{1 \text{ GeV}/c}{|e| 0.5 \text{ T}} = \frac{1 \cdot 10^9 \text{ eV}/(0.3 \cdot 10^{-9} \text{ m/s})}{0.5 \text{ eV} \cdot \text{s/m}^2}, \\ = \frac{1}{0.3 \cdot 0.5} \text{ m} \approx 6.66 \text{ m}. \quad (5.7)$$

In the example above, the units of  $B$  are given in  $\text{eV} \cdot \text{s/m}^2$ . Thus, the helix's radius for a proton with  $p_T = 1 \text{ GeV}/c$  within a magnetic field  $B \approx 0.5 \text{ T}$  is larger than 6 m. However, this is larger than the TPC's outer radius, which is about 2.5 m. Therefore, the measurement of the  $p_T$  using the helix radius is not a convenient approach.

In practice, the measurement of the  $p_T$  is accomplished using the “sagitta”  $s$  (see Fig. 5.2), which is defined as the largest perpendicular distance of the trajectory from the connecting line between the particle’s entrance into and exit from the magnetic field volume [84]. The geometrical definition of the sagitta is shown in Fig. 5.2, from which the following relations are obtained:

$$\frac{R - s}{Q} = \cos \frac{\alpha}{2} \approx 1 - \frac{\alpha^2}{8} \quad \text{and} \quad \frac{L_p}{2R} = \sin \frac{\alpha}{2} \approx \frac{\alpha}{2}. \quad (5.8)$$

Naturally, the approximations are valid for small angles, i.e., high momentum particles.

Therefore, Eq. 5.8 yields a relation between the sagitta and the curvature:

$$s \approx \frac{R\alpha^2}{8} = \frac{1}{8} \frac{L_p^2}{R} = \frac{1}{8} L_p^2 |\kappa| . \quad (5.9)$$

Hence, the  $p_T$  can be written in terms of the sagitta as:

$$p_T = \frac{|q|BL_p^2}{8s} \quad (5.10)$$

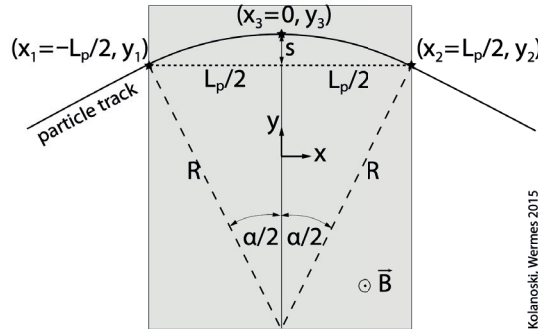


**Figure 5.2:** Sketch of a deflected charged particle due to the influence of a homogeneous magnetic field. The drawing delineates the sagitta  $s$  of the circular arc in the magnetic field and the particle's deflection angle  $\alpha$ . The figure is taken from [84].

## 5.2 Energy Loss of Charged Particles by Ionisation

When a relativistic charged particle crosses a medium, such as a gas chamber or a chunk of silicon, it loses energy primarily by ionisation of the medium's atoms, i.e., it gives up kinetic energy in exchange for liberating electrons from the atoms. Bethe and Bloch studied the quantum mechanical treatment of the energy loss in the 1930s. The outcome of their investigations is widely used nowadays, for instance, in identifying charged particles in a Pb–Pb collision at the ALICE experiment.

The following discussion assumes that the particle passing through the medium is a “heavy” particle (hereafter called the “particle”) with charge  $ze$ , where  $e$  is the elementary charge. This category includes all charged particles except electrons and positrons, for which exchange and annihilation processes must be considered. Furthermore, bremsstrahlung is another relevant mechanism for energy loss by electrons and positrons.

### 5.2.1 The Bethe-Bloch Formula

The calculation of the average energy loss ( $\langle dE/dx \rangle$ ) of a charged-particle using a quantum mechanical treatment was provided by Bethe [85] and Bloch [86, 87] in the 1930s. The relation between the average energy loss and the energy of the incoming or projectile charged-particle is known as the Bethe-Bloch formula and is given in Eq. 5.11 (I am using the formulation and the notation from Ref. [84]):

$$-\left\langle \frac{dE}{dx} \right\rangle = K \frac{Z}{A} \rho \frac{z^2}{\beta^2} \left[ \frac{1}{2} \ln \frac{2m_e c^2 \beta^2 \gamma^2 T_{\max}}{I^2} - \beta^2 - \frac{\delta(\beta\gamma)}{2} - \frac{C(\beta\gamma, I)}{Z} \right]. \quad (5.11)$$

The different quantities in the equation are defined as follows:

- $K = 4\pi N_A r_e^2 m_e c^2 = 0.307 \text{ MeV cm}^2/\text{mol}$ , using the classical electron radius:

$$r_e = \frac{e^2}{4\pi\epsilon_0 m_e c^2} = \alpha \frac{\hbar}{m_e c} \approx 2.8 \text{ fm}.$$

- $z, \beta$  are the charge and velocity of the incoming particle.
- $Z, A$  are the medium's atomic number and atomic mass, respectively.
- $\rho$  is the target mass density.
- $I$  is the mean excitation energy.
- $T_{\max}$  is the maximum possible energy transfer in a single collision.
- $\delta$  is the so-called density correction.
- $C/Z$  is a shell correction, relevant for small  $\beta$  values.

Figure 5.3 shows the average energy loss  $\langle dE/dx \rangle$  as a function of  $\beta\gamma$  ( $= p/mc$ ) of an incoming particle. The graph represents the case of  $\pi^\pm$  in silicon. Firstly, one notices the rapid decrease of energy loss with increasing  $\beta\gamma$ . The  $\sim 1/\beta^2$  dependence shown in the graph can be explained because the momentum transfer  $\Delta p$  increases with the effective interaction time  $\Delta t \simeq b/\gamma v$ , where  $b$  is an impact parameter and  $v = c/\beta$ . Thus, slower particles lead to longer interaction times, hence larger momentum transfer. Since the momentum transfer is proportional to  $\Delta t$ , it follows that the energy transfer  $\Delta E = (\Delta p)^2/2m$  is proportional to  $1/v^2 \propto 1/\beta^2$  (in this low energy regime  $\gamma \approx 1$ ). It is worth mentioning that the  $\sim 1/\beta^2$  dependence holds for  $\beta \gtrsim 0.3$ . Below that value,

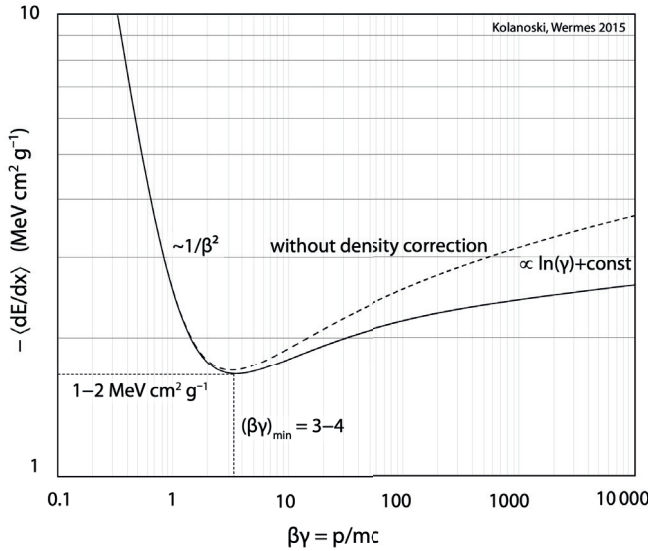


**Figure 5.3:** Mean energy loss of  $\pi^\pm$  in silicon as a function of  $\beta\gamma$ . The range indicated for the minimum energy loss is valid for most media. The figure is taken from [84].

shell corrections  $C/Z$  in Eq. 5.11 become relevant. Such corrections are not discussed in this thesis. Furthermore, the particle identification via the analysis of the  $\langle dE/dx \rangle$  in this thesis involves particles with a minimum momentum of  $300 \text{ MeV}/c$ , i.e., a  $\beta\gamma \gtrsim 2$  (in the case of  $\pi^\pm$ ).

The next feature in the Bethe-Bloch curve is the broad minimum around  $\beta\gamma \approx 3$ . The particles in this kinematic region are thus called “minimum-ionising particles” (MIPS).

At larger values of  $\beta\gamma$ , the  $\ln \gamma^2$  starts to dominate, and the  $\langle dE/dx \rangle$  starts to increase, which is referred to as the region of “relativistic rise”. In an impact-parameter picture one can understand it in this way that the relativistic deformation of the electric field of the incident particle increases the upper limit for impact parameters ( $b_{\max} \approx \gamma v/\omega$ , where  $\omega$  is a characteristic orbital frequency) involved in the collision [88], leading to an increase of the energy loss.

The effect of the relativistic rise does not continue indefinitely. In dense materials, where the interatomic spacing is small, the upper limit on allowed impact parameters ( $b_{\max}$ ) may encompass many atoms. The passage of the projectile particle leads to the polarisation of the medium and, hence, a screening of the projectile’s electric field. This phenomenon is known as the “density effect” since the density of the medium causes it. The density effect leads to flattening the  $\langle dE/dx \rangle$  curve for highly relativistic particles (see Fig. 5.3 for  $\beta\gamma \gtrsim 100$ ). The density effect is taken into account in the Bethe-

Bloch equation (see Eq. 5.11) by the  $\delta(\beta\gamma)$  term. For very large values of  $\gamma$ , the density correction  $\delta(\gamma\beta)$  takes the form:

$$\delta \rightarrow 2 \ln \frac{\hbar\omega_P}{I} + 2 \ln \beta\gamma - 1$$

where  $\omega_P$  is the so-called “plasma frequency” [84]. Therefore, in this extreme case the Bethe-Bloch formula can be written as:

$$-\left\langle \frac{dE}{dx} \right\rangle = K \frac{Z}{A} \rho z^2 \left[ \frac{1}{2} \ln \frac{2m_e c^2 T_{\max}}{(\hbar\omega_P)^2} - \frac{1}{2} \right] (\gamma \rightarrow \infty, \beta \rightarrow 1). \quad (5.12)$$

Therefore, the  $\gamma$  dependence of  $\langle dE/dx \rangle$  only enters via an increase of  $T_{\max} \propto \gamma$ . In summary, the density effect causes the energy loss to increase like  $\ln \gamma$  instead of  $\ln \gamma^2$  and hence, the Bethe-Bloch curves becomes constant at very large  $\gamma$ .

Figure 5.4 shows the measured truncated  $dE/dx$  (see Sec. 5.2.4 for the discussion on the truncated mean) of  $\pi$ ,  $K$ ,  $p$ ,  $e$  and  $d$  in the TPC of ALICE over a wide range of momentum. The solid black lines represent parameterisations of the Bethe-Bloch formula. The  $dE/dx$  of electrons does not follow the Bethe-Bloch formula. The dominant process is bremsstrahlung. The  $dE/dx$  of  $K$  and  $p$  clearly shows the  $\sim 1/\beta^2$  dependence at low momentum. Furthermore, one can see the onset of the relativistic rise at  $p \approx 1 \text{ GeV}/c$  for  $\pi$  and  $p \approx 3 \text{ GeV}/c$  for  $K$  and  $p$ .

## 5.2.2 Statistical Fluctuations of Energy Loss

The passage of a charged-particle through a medium will cause ionisation and excitation processes and will due to its statistical nature exhibit fluctuations. The energy loss  $\Delta E$  along a distance  $\Delta x$  is composed of many small contributions  $\delta E_n$  associated with individual ionisation and excitation processes. The  $\Delta E$  can be written as:

$$\Delta E = \sum_{n=1}^N \delta E_n. \quad (5.13)$$

Statistical fluctuations can occur for the number  $N$  of ionisation or excitation processes and the emitted  $\delta E$ . Thus, both together will yield fluctuations in the energy lost by the particle.

The relevant contribution to the energy loss fluctuations come from the individual  $\delta E_n$  fluctuations. The  $\delta E$  distribution between a minimal  $\delta E_{\min}$  and a maximal value  $\delta E_{\max}$

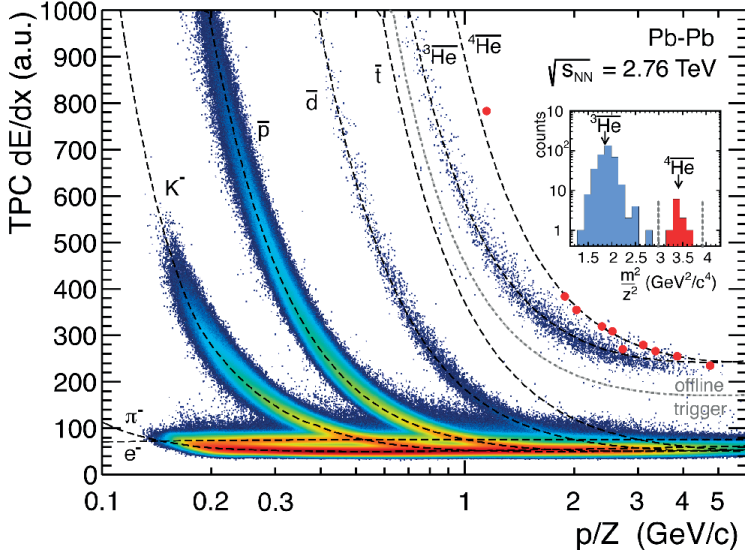


**Figure 5.4:** Correlation between  $dE/dx$  and momentum for  $\pi$ ,  $K$ ,  $p$ ,  $d$  and  $e$  in Pb–Pb collisions at  $\sqrt{s_{NN}} = 2.76$  TeV measured with the TPC of ALICE detector. The dashed black lines represent parameterisations of the Bethe-Bloch formula except for the  $dE/dx$  of electrons. The figure is taken from [89].

has a  $1/(\delta E)^2$  shape. The most probable energy transfer, the  $\delta E$  value where the maximum of the distribution is located, is in fact near to  $\delta E_{\min}$ . However, from time to time, central collisions between the incoming particle and the atom electrons will experience an energy transfer that can be as large as the maximal energy transfer,  $\delta E_{\max} \approx E$ . This will lead to a long tail in the  $\delta E$  distribution towards high energies.

### 5.2.3 The Landau-Vavilov Distribution

As described in the previous section, the energy loss  $\Delta E$  over a fixed distance  $\Delta x$  has a statistical nature. Therefore, one can talk about the existence of an energy loss probability density  $f(\Delta E, \Delta x)$ . According to the central limit theorem of statistics, the energy loss  $\Delta E$  as given by Eq. 5.13 should be Normally distributed if the individual  $\delta E_n$  are independent and in the limit of  $N \rightarrow \infty$ . However, this limit is never reached for relativistic particles.

The energy transfer fluctuations in individual collisions along the path of the incoming particle lead to an asymmetric  $f(\Delta E, \Delta x)$  distribution. Figure 5.5 shows the measured energy loss distribution of minimum-ionising pions, i.e., pions in the momentum inter-

val  $400 - 800$  MeV/ $c$ . The left side of the distribution has a Gaussian shape, associated with the many ionisation processes with small energy loss. On the other hand, the large energy transfers cause the long tail on the right side of the distribution.

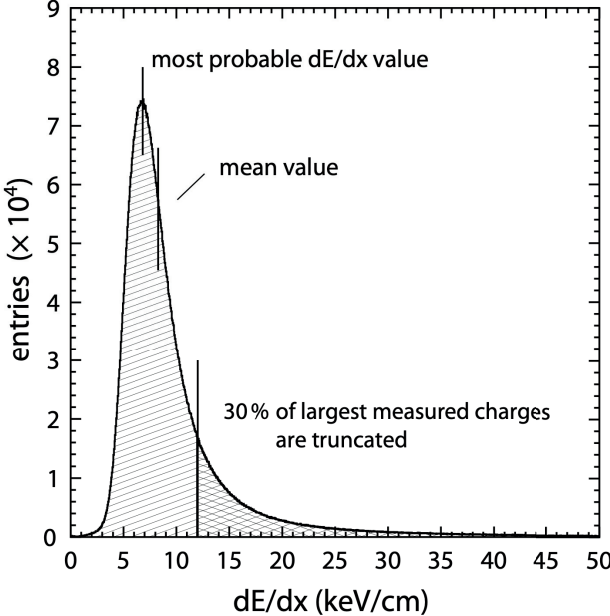


**Figure 5.5:** Distribution of measured  $dE/dx$  values for minimum-ionising pions,  $p \in (400, 800)$  MeV/ $c$ . The most probable  $dE/dx$  value, where the maximum is located, is shown left to the mean  $dE/dx$ . The onset of the shaded area represents the value above which 30% of the largest energy loss entries are located. The figure is taken from [84].

To extract the exact form of the distribution, Vavilov introduced the  $\kappa$  parameter [90] to study the Gaussian-like and the tail-like forms. The  $\kappa$  parameter is defined as:

$$\kappa = \frac{\xi}{T_{\max}} , \quad (5.14)$$

where  $\xi$  is the factor in front of the logarithm of the Beth-Bloch formula (see Eq.5.11) multiplied by the path length  $\Delta x$

$$\xi = \frac{1}{2} K \frac{Z}{A} \rho \frac{z^2}{\beta^2} \Delta x .$$

The two limiting cases are:

- $\kappa$  large  $\rightarrow f(\Delta E, \Delta x)$  a Gaussian-like distribution ( $\kappa \gtrsim 1$ ).
- $\kappa$  small  $\rightarrow f(\Delta E, \Delta x)$  a very asymmetric distribution.

Landau derived the first analytic form of the energy loss distribution in 1944 [91] for small  $\kappa$  values making the following assumptions:

- $T_{\max}$  can become infinitely large corresponding to  $\kappa \rightarrow 0$ .
- The electrons are treated as quasi-free; that is, shell effects at small energy transfers are neglected.
- The decrease of the particle's energy while penetrating the medium can be neglected.

The so derived “Landau” distribution is defined as the definite integral:

$$f_L(\lambda) = \frac{1}{\pi} \int_0^\infty e^{-t \ln t - \lambda t} \sin \pi t dt . \quad (5.15)$$

This distribution is very asymmetric with a tail towards  $\lambda = \infty$  and it has a maximum at  $\lambda = -0.22278$ . The correspondence between the energy loss  $\Delta E$  and the variable  $\lambda$  is given by:

$$\lambda = \lambda(\Delta E_w, \xi) = \frac{\Delta E - \Delta E_w}{\xi} - 0.22278 , \quad (5.16)$$

where  $\Delta E_w$  is the most probable energy loss. The Landau distribution is a good approximation for small  $\kappa$  values, roughly  $\kappa \lesssim 0.01$ . The generalisation, allowing for a maximum energy transfer  $T_{\max}$ , which is valid for larger values of  $\kappa$ , was given by Vavilov [90]. See page 48 of Ref. [84].

#### 5.2.4 Suppression of Fluctuations

Statistical fluctuations represent a disadvantage for detectors measuring ionisation because they can limit the spatial resolution in sensors that measure space points by ionisation along the particle trajectories. More importantly for this thesis, the resolution for particle identification via  $dE/dx$  measurements. The fluctuations can be reduced if the most probable energy loss value is used as the energy loss estimator rather than

the average value because the former is more stable with respect to individual fluctuations. Figure 5.6 shows the evolution of the most probable energy loss as a function of the kinetic energy of the incident particle. The most probable energy loss is relatively constant with the increasing energy of the projectile particle. Conversely, the average energy loss rises towards high energies.

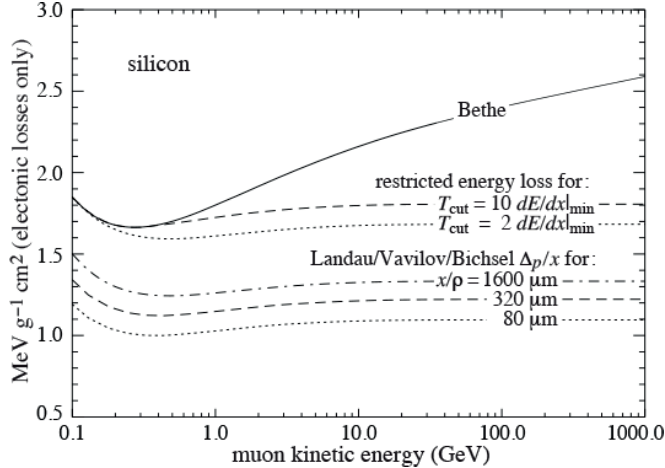


**Figure 5.6:** Energy loss of muons in silicon (excluding radiation losses). The average energy loss given by the Bethe-Bloch equation is represented with the solid line. The two curves below show the mean energy loss with a constraint on  $T_{\text{cut}}$  (see page 45 on Ref. [84]). The cut-off value  $T_{\text{cut}}$  restricts the maximally allowed energy loss in a collision to a value  $T < T_{\text{cut}}$ . The three bottom curves represent the most probable energy loss per path length in silicon layers of various thicknesses. The figure is taken from [84].

An alternative approach to suppress fluctuations and obtain an average energy loss value more consistent with the most probable value is based on the “truncated mean” method. This is the method employed by the ITS (see Sec. 6.3) and TPC (see Eq. 6.6) detectors of ALICE. The truncated mean method consists of discarding the largest (possibly also the smallest) values of a series of measurements from the calculation of the mean (truncated mean). Figure 5.5 shows the  $dE/dx$  value at which 30% of the largest measured  $dE/dx$  values are truncated.

### 5.3 Time-Of-Flight Measurements

The measurement of the flight time it takes for a particle to go from one detector to another is known as the “time-of-flight”. The time-of-flight can directly yield an esti-

mation of the velocity of the particle. Figure 5.7 shows the principle of the measurement of the time-of-flight. We assume that the particle has a momentum  $p$  and mass  $m$ . The particle traverses two detectors positioned at a distance  $L$  from each other. One of the detectors fires the start and the other the stop signal.

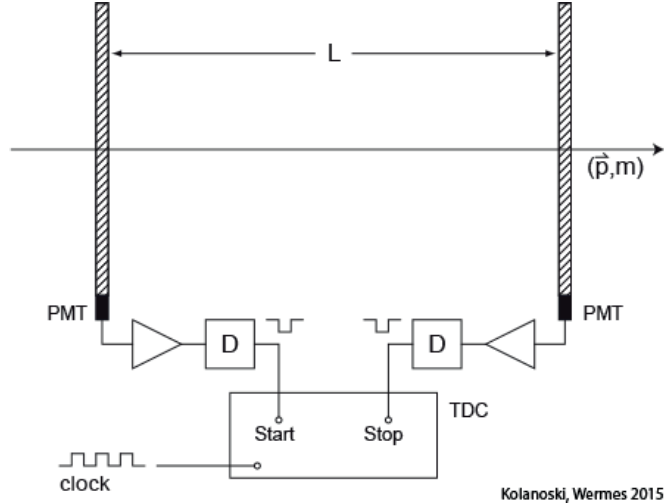


**Figure 5.7:** Principle of the time-of-flight measurement. This method uses two plastic scintillators and two photomultipliers to fire the start and the stop signals. A TDC (time-to-digital converter) digitises the time difference between the signals. The figure is taken from [84].

The flight duration can be written as:

$$\Delta t = \frac{L}{\beta c} = \frac{L}{c} \sqrt{\frac{p^2 + m^2}{p^2}} \quad (5.17)$$

Therefore the velocity is given by:

$$\beta = \frac{L}{\Delta t c} \quad (5.18)$$

Equation 5.18 gives the velocity of the particle. When performing particle identification,  $L$  represents the integrated length of the particle's trajectory. In ALICE, the tracking detectors provide both quantities  $L$  and  $p$ . In this case, the TPC detector. Therefore, the identity of the particle (it's mass) can be known from combining Eq. 5.17 and

Eq. 5.18:

$$m_{\text{TOF}}^2 = p^2 \left[ \left( \frac{\Delta tc}{L} \right)^2 - 1 \right] \quad (5.19)$$

Figure 5.8 shows the correlation between  $\beta$  and momentum for  $e$ ,  $\pi$ ,  $K$ ,  $p$  and  $d$  measured with the TOF detector of ALICE.  $\beta$  measurements serve as a potential discriminator for particle identification at intermediate momentum  $1 - 4 \text{ GeV}/c$ . In Sec. 8.1.1, I will describe an analysis technique to measure the production of  $\pi$ ,  $K$  and  $p$  in the momentum interval  $1 - 4 \text{ GeV}/c$ .

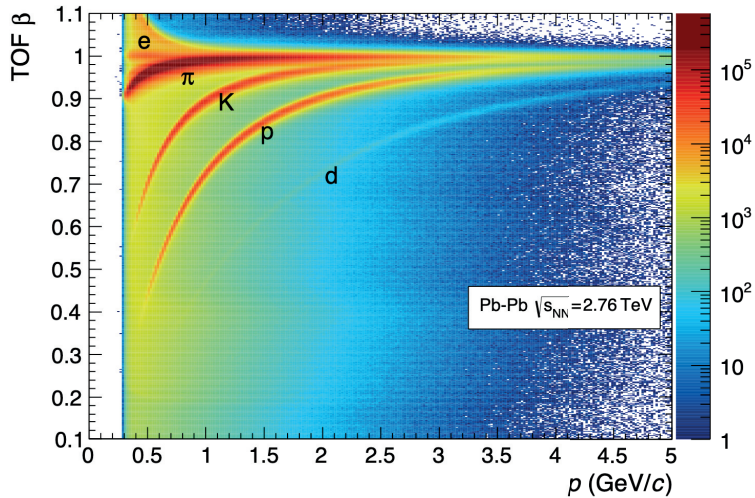


**Figure 5.8:** Correlation between  $\beta$  and momentum for  $e$ ,  $\pi$ ,  $K$ ,  $p$  and  $d$  in Pb–Pb collisions at  $\sqrt{s_{\text{NN}}} = 2.76 \text{ TeV}$  measured with the ALICE TOF detector. The figure is taken from [92].

# Chapter 6

## The ALICE Detector

This chapter provides a brief description of the ALICE apparatus. ALICE is optimized for the study of Pb–Pb collisions in which the charged particle density,  $dN_{\text{ch}}/d\eta$ , was expected to be in the range of 2000 – 8000 for the most central collisions. However, the measured  $dN_{\text{ch}}/d\eta$  in central collisions at  $\sqrt{s_{\text{NN}}} = 2.76 \text{ TeV}$  is about 2000. This puts intense demands on the tracking and particle identification detectors. Throughout the different sections of this chapter, I will restrict the description to the relevant detectors used in the analyses presented in this thesis. Namely, the V0, ITS, TPC and TOF detectors. I refer the readers to Refs. [92, 93] for a more in-depth description of the ALICE apparatus and its different detectors.

### 6.1 Detector Overview

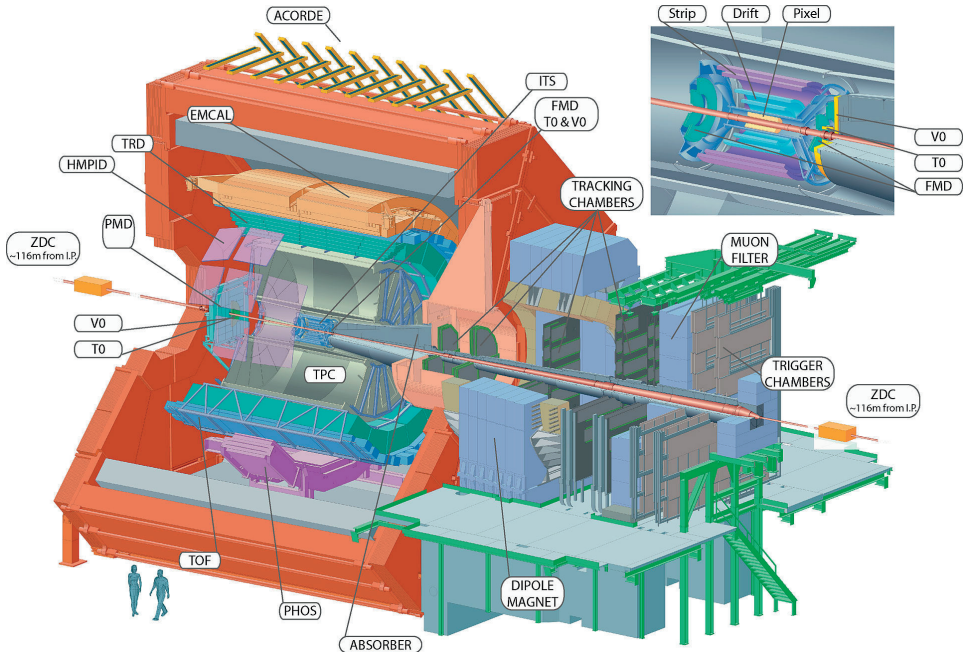
ALICE (A Large Ion Collider Experiment) is one of the four main experiments at the Large Hadron Collider (LHC) located in Geneva, Switzerland. It is optimised to studying heavy-ion collisions, Pb–Pb and Xe–Xe. However, it also has a dedicated program to study pp and p–Pb collisions. The latter collision systems are needed to separate the genuine QCD-matter signals from the cold-matter initial- and final-state effects. Moreover, as discussed in Sec. 3.6, pp and p–Pb collisions are an active field of study for the possible existence of QGP in small systems. Table 6.1 summarises the different colliding systems and energies. In the case of heavy-ion collisions and p–Pb, the energy is per colliding nucleon pair.

Figure 6.1 shows a sketch of the ALICE apparatus. It has overall dimensions  $16 \times 16 \times 26 \text{ m}^3$  and weights about 10000 t. The purpose of ALICE is to reconstruct the full

**Table 6.1:** Table of the colliding systems and energies.

System	$\sqrt{s_{\text{NN}}}$ (TeV)
Pb–Pb	2.76, 5.02
Xe–Xe	5.44
p–Pb	5.05, 8.16
pp	0.9, 2.76, 7 and 13

picture of a heavy-ion collision. Thus, it is designed to cope with high particle densities. For example, as reported in [94], the pseudorapidity density of charged particles,  $dN_{\text{ch}}/d\eta$ , at mid-rapidity in very central Pb–Pb collisions is of the order of 2000. This implies that ideally, tracking detectors should have a low transverse momentum threshold since most particles come from bulk production, i.e., low-momentum particles.



**Figure 6.1:** Sketch of the ALICE apparatus. The figure is taken from [92].

ALICE has seventeen detector systems, see Fig. 6.1. They fall into three categories: central barrel detectors, forward detectors, and the muon spectrometer. Furthermore, the central barrel detectors are embedded in the L3 solenoid magnet, which provides a magnetic field of  $B = 0.5$  T. Since not all the detector systems are used in the analyses presented in this thesis, I will restrict the discussion to the detectors used: V0, ITS, TPC and TOF. Table 6.2 summarises the acceptance values and usage of the detectors used

in the studies of this thesis.

**Table 6.2:** Table listing the relevant detectors used in this thesis.

Detector	Acceptance		Main purpose
	Polar	Azimuthal	
V0A	$2.8 < \eta < 5.1$	full	triggering, centrality
V0C	$-3.7 < \eta < -1.7$	full	triggering, centrality
ITS	$ \eta  < 1$	full	tracking, vertex
TPC	$ \eta  < 0.9$	full	tracking, PID
TOF	$ \eta  < 0.9$	full	PID

## 6.2 The V0 Detector

The V0 detector consists of two arrays of scintillator counters, called V0A and V0C [95]. The V0A detector is located 340 cm from the interaction point ( $z = 0$ ) on the side opposite the muon spectrometer. In contrast, the V0C is fixed to the front face of the hadronic absorber, 90 cm from the interaction point. Both detectors record the passage of charged particles in the pseudorapidity intervals  $-3.7 < \eta < -1.7$  (V0C) and  $2.8 < \eta < 5.1$  (V0A) and have full azimuth-angle coverage. The V0 detector is primarily used for triggering and determining the collision's centrality. In the following discussion, the V0 amplitude refers to the sum of the signals from the V0A and V0C detectors.

The interaction triggers use the V0 and SPD<sup>1</sup> detector signals coinciding with a bunch crossing corresponding to a beam-beam collision. The interaction triggers are defined as [96]:

- *V0AND*: signals in V0A and V0C.
- *3-out-of-3*: signals in V0A and V0C and at least two chips hit in the outer layer of the SPD.
- *2-out-of-3*: two of the three conditions above.

In ALICE, the final event selection is based on an offline event selection. Using an offline event selection aims to reject machine-induced background. Furthermore, the

---

<sup>1</sup>The Silicon Pixel Detector are the two innermost layers of the ITS detector and is the closest apparatus to the interaction point.

offline event selection allows rejecting events triggered by noise in the SPD. One source of machine-induced background comes from the interaction between the ions in the beams and the residual gas in the beam pipe. In addition, interactions of ions in the beam halo with the mechanical structures account for another source of background. These interactions typically occur outside of the interaction region and produce a signal that is “too early” in the same-side V0. Hence, background events are discarded using the time information of the V0. A detailed description of this procedure can be found in [95].

### 6.2.1 Centrality Determination in ALICE

The centrality of the collision can be either defined based on information provided by the forward detectors (V0) or at mid-rapidity using the ITS detector (the description of the ITS detector is given in Sec. 6.3). However, biases, such as auto-correlations, arise from measuring observables and performing the centrality classification in the same region. Figure 6.2 shows the yield,  $dN/dy$  ( $|y| < 0.5$ ), of  $K_S^0$  and  $K^\pm$  correlated with the average charged-particle density,  $\langle dN_{ch}/d\eta \rangle$ , measured at mid-rapidity ( $|\eta| < 0.5$ ) and in the forward region. A significant bias towards charged kaons is observed in the former case, while the latter selection preserves the expected neutral-to-charged kaon ratio of approximate unity. This effect arises from requiring the multiplicity to function the measured number of charged particles.

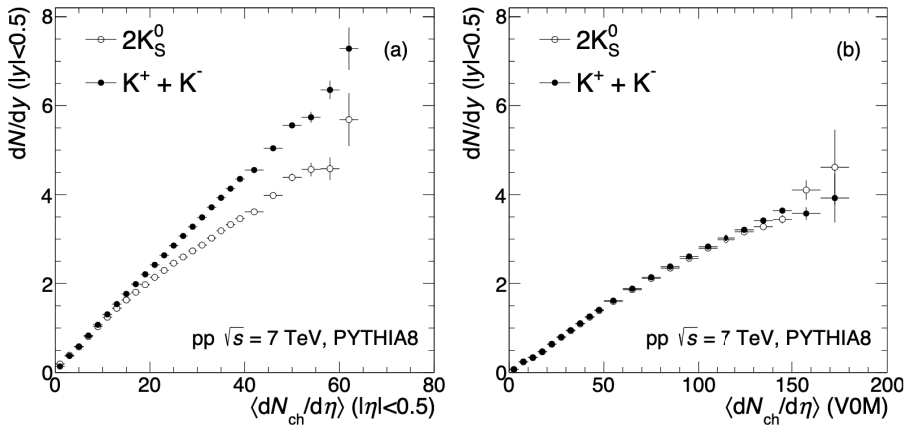


**Figure 6.2:** Correlation between the yield,  $dN/dy$  ( $|y| < 0.5$ ) of  $K_S^0$  and  $K^\pm$  with the average charged-particle density  $\langle dN_{ch}/d\eta \rangle$  measured in  $|\eta| < 0.5$  (left panel) and in the forward region (right panel). See text for details. The figure is taken from [97].

In nuclear collisions, the centrality of the event is usually expressed as a percentage of the total nuclear interaction cross section  $\sigma_{AA}$ . The centrality percentage  $c$  of a nuclear

collision with an impact parameter  $b$  is defined by integrating the impact parameter distribution  $d\sigma/db'$ :

$$c = \frac{1}{\sigma_{AA}} \int_0^b \frac{d\sigma}{db'} db' \quad (6.1)$$

In ALICE, the percentage of the hadronic cross-section is determined for any value of the V0 amplitude (see Fig. 6.3) by integrating the measured V0 amplitude distribution normalised at the anchor point  $V0_{AP}$ . The anchor point (AP) is defined as the amplitude of the V0 detector equivalent to 90% of the hadronic cross section [96]. Hence, if we define  $V$  as the V0 amplitude, the top 10% central class is defined by the value  $V0_{10}$  that satisfies:

$$\frac{\int_{V0_{10}}^{\infty} (dN_{evt}/dV)dV}{\int_{V0_{AP}}^{\infty} (dN_{evt}/dV)dV} = \frac{1}{9}. \quad (6.2)$$

The reason to define the AP as the V0 amplitude equivalent to 90% of the hadronic cross-section is that events with a measured multiplicity lower than the anchor point are contaminated by electromagnetic background and in addition to that the distribution there is affected by missing events due to trigger inefficiency. Figure 6.3 shows the V0 amplitude divided into centrality classes. The top 5% high multiplicity events lay on the far right side of the distribution, while the low multiplicity event sits on the opposite region. The determination of the centrality at mid-rapidity using the number of clusters in the SPD and the number of reconstructed tracks in the TPC follows the same procedure.

In summary, in ALICE, a nuclear collision's centrality is associated with a percentage class of the V0 amplitude. Thus, high multiplicity collisions are correlated with a large activity in the V0 detectors, whereas low multiplicity events show little activity.

### 6.2.2 Particle Production Dependence on $N_{part}$ and $N_{coll}$

The discussion above tells us little about the geometrical quantities that could describe the nuclear collision. Furthermore, neither the impact parameter nor geometrical quantities such as the number of participants ( $N_{part}$ ), the number of binary nucleon-nucleon ( $N_{coll}$ ) are directly measurable. However, such quantities can be measured indirectly by applying a phenomenological approach based on the Glauber model [98]. In prac-

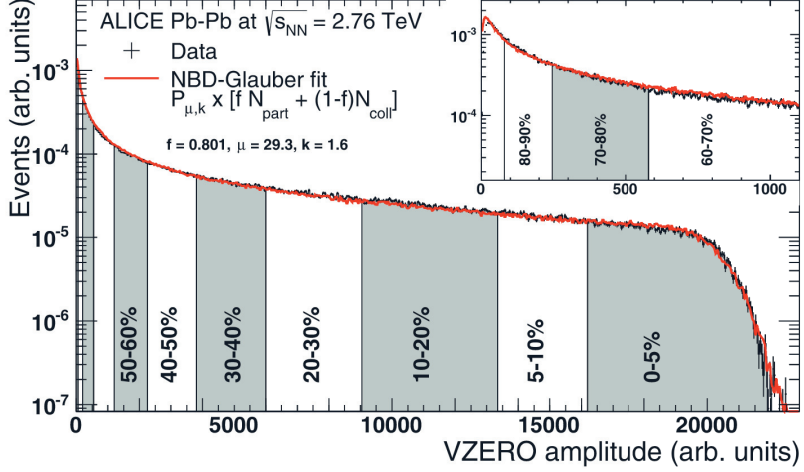


**Figure 6.3:** Measured V0 amplitude distribution in Pb–Pb collisions at  $\sqrt{s_{\text{NN}}} = 2.76$  TeV with the ALICE V0 detector. Centrality classes are represented as percentiles of the V0 amplitude distribution. The V0 amplitude distribution generated with the NBD-Glauber model (solid red line) is fitted to the measured distribution. The figure is taken from [96].

tice, the Glauber model is convoluted with a model for particle production based on a negative binomial distribution (NBD). The negative binomial distribution:

$$P_{\mu,k}(n) = \frac{\Gamma(n+k)}{\Gamma(n+1)\Gamma(k)} \frac{(\mu/k)^n}{(\mu/k + 1)^{n+k}}. \quad (6.3)$$

gives the probability of measuring  $n$  particles per nucleon-nucleon collision, where  $\mu$  is the average multiplicity in a nucleon-nucleon collision and  $k$  represents the width of the distribution. The choice of the NBD is motivated by the fact that the charged-particle multiplicity in minimum bias pp and p $\bar{p}$  has been measured over a wide range of rapidity and is well approximated by an NBD [99, 100].

The Glauber model allows one to calculate the corresponding  $N_{\text{part}}$  and  $N_{\text{coll}}$  for an event with impact parameter  $b$ . However, in nuclear collisions, we have to introduce the concept of “ancestors”. It defines the number of independently emitting sources of particles. The number of ancestors  $N_{\text{ancestors}}$  can be parameterised as follows:

$$N_{\text{ancestors}} = fN_{\text{part}} + (1 - f)N_{\text{coll}}. \quad (6.4)$$

Equation 6.4 is motivated by two-component models [101, 102], which decompose

the nucleus-nucleus collision into soft and hard interactions. To simulate the particle production in a nucleus-nucleus collision, the NBD is sampled  $N_{\text{ancestors}}$  times to obtain a simulated multiplicity distribution, for example, the V0 amplitude. Figure 6.3 shows the measured V0 amplitude fitted to the simulated V0 amplitude.

Finally, in scenarios dominated by soft processes, the charged-particle multiplicity in a nucleus-nucleus collision is expected to scale with  $N_{\text{part}}$ . In this scenario, all the participating nucleons are assumed to contribute independently with the same energy to particle production. In contrast, a scaling with  $N_{\text{coll}}$  is expected in scenarios where hard processes dominate over soft particle production. In this case, the nuclear collision can be regarded as a superposition of binary nucleon-nucleon collisions. Therefore, it is customary to employ two-component models to quantify the relative contribution of soft and hard processes in the particle production mechanisms [96]. Figure 6.4 shows the charged-particle density per participant pair as a function of  $\langle N_{\text{part}} \rangle$  measured in Pb–Pb collisions at  $\sqrt{s} = 2.76$  TeV by ALICE. The data are fitted with the tow-component model:

$$\frac{dN}{d\eta} = N[f N_{\text{part}} + (1 - f) N_{\text{coll}}], \quad (6.5)$$

where  $N$  is a normalisation constant and  $f$  is the relative contribution. The measured value of  $f$  was 0.788 [96]. This suggest that 80% the produced particles are associated with the bulk particle production.

## 6.3 The ITS Detector

The Inner Tracking System (ITS) detector surrounds the beam pipe. It is the closest detector to the interaction point. It is composed of six cylindrical layers of silicon detectors: two Silicon Pixel Detectors (SPD), two Silicon Drift Detectors (SDD), and two Silicon Strip Detectors (SSD). Fig. 6.5 shows the geometrical layout of the ITS detector, and Tab. 6.3 lists its dimensions. The first layer has the most extensive pseudorapidity coverage ( $|\eta| < 2$ ) to provide, together with the Forward Multiplicity Detectors (FMD), continuous coverage for the measurement of charged particles multiplicity. Furthermore, the ITS covers the pseudorapidity range  $|\eta| < 0.9$  for all vertices within the length of the interaction diamond ( $\pm 5.3$  cm along the beam direction).

The main tasks of the ITS detector are to reconstruct the primary vertex within a resolution better than  $100 \mu\text{m}$ , reconstruct secondary vertices from decays of hyperons, tracking and particle identification at low momentum ( $\approx 0.15 \text{ GeV}/c$ ). Moreover, it improves the momentum and angle resolution of tracks reconstructed with the TPC.

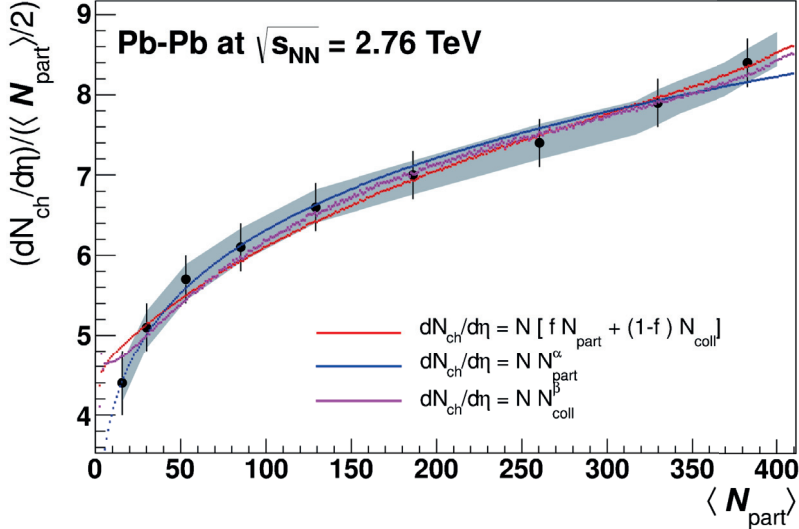


**Figure 6.4:** Correlation between the charged-particle density per participant pair and  $\langle N_{\text{part}} \rangle$  in Pb–Pb collisions at  $\sqrt{s_{\text{NN}}} = 2.76$  TeV. The data are fitted to various parameterisations of  $N_{\text{part}}$  and  $N_{\text{coll}}$ . The figure is taken from [96].

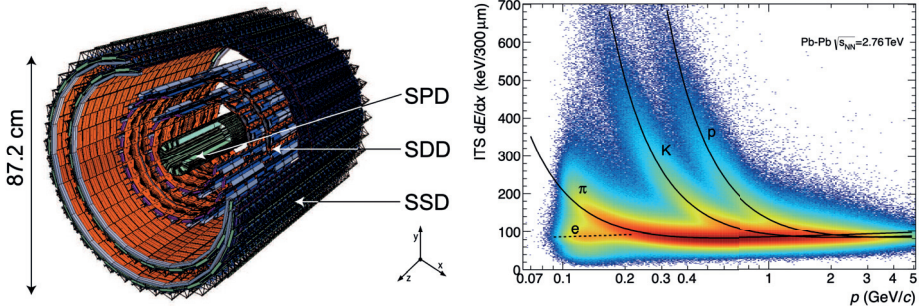


**Figure 6.5:** (Left) The layout of the SPD, SDD and SSD layers that compose the ALICE ITS detector. (Right) Correlation between  $dE/dx$  and momentum for  $\pi$ ,  $K$ ,  $p$  and  $e$  in Pb–Pb collisions at  $\sqrt{s_{\text{NN}}} = 2.76$  TeV measured with the ALICE ITS detector. The figures are taken from [92, 103].

The four outer layers of the ITS provide measurements of the ionisation energy loss of charged particles traversing sensitive elements of the detector. A charged particle will create a cluster of charges. The measured cluster charge is normalised to the path length, calculated from the reconstructed track parameters to obtain a  $dE/dx$  value for each layer. The  $dE/dx$  used in physics analyses is calculated using a truncated mean: the average of the lowest two points if four points are measured, or a weighted sum of

**Table 6.3:** Dimensions of the ITS detector.

Layer	Type	Acceptance		Radius (cm)	Length (cm)	Area m <sup>2</sup>
		Polar	Azimuthal			
1	pixel	$ \eta  < 2$	full	3.9	14.1	0.07
2	pixel	$ \eta  < 1.4$	full	7.6	14.1	0.14
3	drift	$ \eta  < 0.9$	full	15	22.2	0.42
4	drift	$ \eta  < 0.9$	full	23.9	29.7	0.89
5	strip	$ \eta  < 1$	full	38	43.1	2.2
6	strip	$ \eta  < 1$	full	43	48.9	2.8

the lowest (weight 1) and the second-lowest points (weight 1/2) if only three points are measured. Figure 6.5 shows the  $dE/dx$  as a function of momentum of  $\pi$ , K, p and e.

## 6.4 The TPC Detector

The Time Projection Chamber (TPC) is a hollow cylindrical detector with its axis aligned with the beam pipe. The TPC surrounds the ITS detector. Figure 6.6 shows a sketch of the TPC. The inner radius is about 85 cm, the outer radius is about 250 cm, and its length is 500 cm. The TPC is divided into two parts by a conducting electrode, charged at 100 kV and provides, together with a voltage dividing network at the surface of the outer and inner cylinder, a precise axial electric field of 400 V/cm [104]. When a charged particle traverses the active volume, it produces ionisation electrons. The electric field makes the ionisation electrons drift towards the end-plates of the cylinder where the readout chambers are localised. The readout chambers are Multi-Wire Proportional Chambers (MWPCs) with a segmented cathode plane (“pad plane”), which can measure the arrival position of the drifted electrons in the cylinder plane. Furthermore, together with a measurement of the arrival time (relative to some external reference such as the collision time), the complete trajectory of the charged particles traversing the TPC can be determined with good precision. The acceptance of the TPC in the polar angle is limited to  $|\eta| < 0.9$  and has full azimuthal angle coverage.

### Readout Chambers

The readout plane is situated at the end-plates and is divided into individual modular readout chambers. The segmentation of the readout plane is done in the azimuthal angle and radial directions, see Fig. 6.6. The azimuthal segmentation consists of 18 trapezoidal sectors, each covering 20°. Since the track density follows a radial depen-

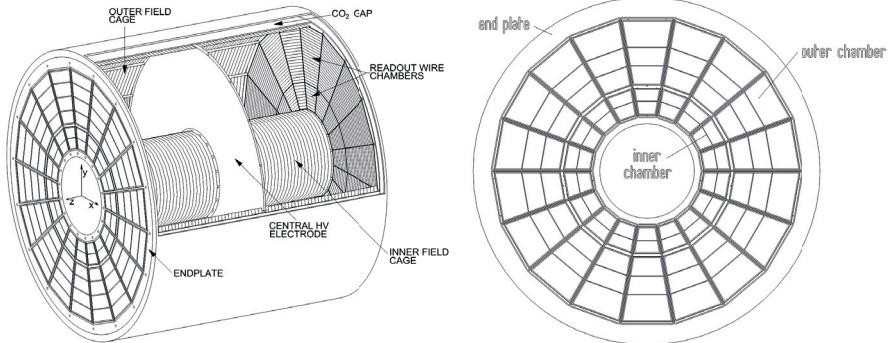


**Figure 6.6:** (Left) Sketch of the ALICE TPC detector. (Right) Illustration of the segmentation of the end-plate into 18 trapezoidal readout chambers. Each readout chamber is divided into the inner and outer readout chambers. The figures are taken from [104, 105].

dence, being largest at small radii, there are two different readout chambers, the Inner and Outer ReadOut Chamber (IROC and OROC, respectively). The effective active radial length varies from 84.1 cm to 132.1 cm (134.6 cm to 246.6 cm) for the inner (outer) readout chambers.

When a charged particle crosses the active volume of the TPC, it ionises the gas along its path, liberating electrons. The electrons drift towards the end-plates due to the influence of the electric field. However, these primary electrons do not induce a sufficiently large signal in the cathode segments or readout pads. Therefore, the signal has to be amplified.

Figure 6.7 shows the scheme of the wire planes located in the readout chamber. It consists of a grid of anode wires above the pad plane, a cathode wire grid, and a gating grid [105]. The anode wires are kept to a positive potential of 1.5 kV. Consequently, the electric field induced by the anode wire is inversely proportional to the distance to the wire ( $E \propto 1/r$ ). Therefore, the primary electrons will be accelerated in the vicinity of the anode wire, leading to an avalanche amplification process. The cathode wire grid separates the drift volume from the anode wires (amplification region). Since many ions are produced during the avalanche creation, the function of the cathode wire grid is to collect such ions. The gating wire grid is located above the cathode wire grid. Therefore, the gating grid works in an alternate mode. The gating wires are held to the same positive potential in the open gate mode, letting electrons from the drift volume enter the amplification region. Conversely, in the closed gate mode, the polarity of the potential is inverted. Hence, the electric field lines will end on the gating grid, preventing electrons from the drift volume from entering the amplification region. In

addition, the closed gate stops ions created in the avalanche processes of previous events from drifting back into the drift volume. Preventing ions from entering the drift volume is very important because escaping ions can lead to severe distortions of the drift field. The gating grid is kept in the closed mode in the absence of a valid trigger.

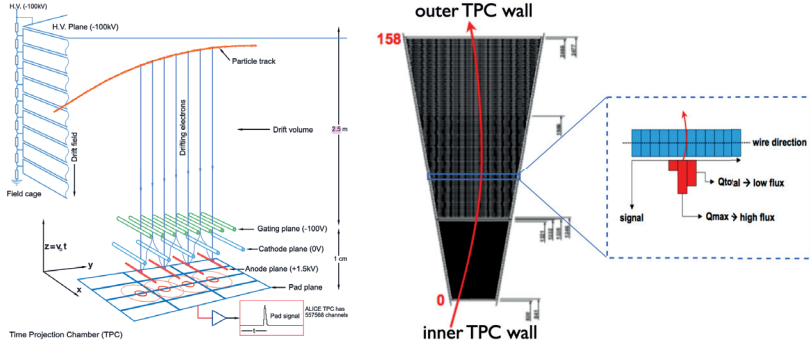


**Figure 6.7:** (Left) Illustration of the wire grids in a TPC readout chamber and the physics working principles. (Right) Sketch of a TPC pad showing the number of pad rows, the maximum charge  $Q_{\text{max}}$  and the total charge  $Q_{\text{tot}}$  in a pad row. The figures are taken from [106].

A precise measurement of the location of the avalanche process can be made if the induced signal is distributed over several adjacent readout pads. The determination of such a location involves a centre-of-mass algorithm. The position of a track particle in the drift direction can be determined by sampling the time distribution of each pad signal. The resulting two-dimensional pulse height distribution in pad-time space is called a *cluster*. For example, suppose the charge in a search window of 5 pads in wire direction (azimuthal direction) and 5 bins in time direction exceed a certain threshold and fulfil specific quality criteria. In that case, it is called a “TPC cluster” [106]. The right panel of Fig. 6.7 shows the layout of the inner and outer readout chambers. The total number of pad rows in the inner chamber is 63, while in the outer chamber, there are 96 pad rows. Therefore, the maximum number of TPC clusters,  $n_{\text{cl}}$ , a particle can have is 159.

## Energy Loss in the TPC

When a track with a certain length is reconstructed within the TPC volume, a certain  $n_{\text{cl}}$  is assigned to that track. For each cluster, the total charge  $Q_{\text{tot}}$  can be measured. It is associated with the total charge deposited in a cluster. Because of the long tail towards high energy losses values (see Fig. 5.5), the average energy loss is not a good estimator for the mean energy loss. Therefore, the TPC signal or  $dE/dx$  used in physics analyses

is given by the truncated mean instead of the raw signal. This is the same approach for measuring the  $dE/dx$  with the ITS detector. The truncated mean is defined in Eq. 6.6 and is characterised by the  $\alpha$  parameter, defined between 0 and 1.

$$S^\alpha = \frac{1}{m} \sum_{i=1}^m Q_i , \quad (6.6)$$

the average is taken over the  $m$  lowest values, corresponding to the  $m$ -fraction of the whole sample, i.e.,  $m = \alpha n$ , where  $n$  is the total number of values in the sample. In ALICE, the value of  $m$  is set to 0.7 as a result of an optimization process [104]. Figure 6.8 shows the  $dE/dx$  as a function of momentum for  $\pi$ , K, p, d and e.

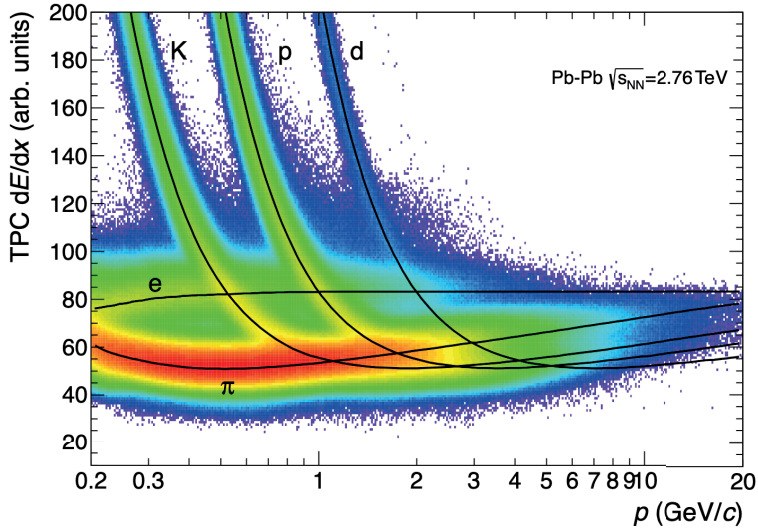


**Figure 6.8:** Correlation between  $dE/dx$  and  $p$  for  $\pi$ , K, p, d and e in Pb–Pb collisions at  $\sqrt{s_{NN}} = 2.76$  TeV measured with the ALICE TPC detector. The figure is taken from [92].

## 6.5 The TOF Detector

The Time-Of-Flight (TOF) [107] apparatus is a cylindrical detector located in the central barrel about 3.7 m from the interaction point, see Fig. 6.1. It covers the pseudorapidity region  $|\eta| < 0.9$  and has full azimuthal angle coverage. The total active area is  $141\text{ m}^2$ . The Multigap Resistive Plate Chamber (MRPC) strip detector is the basic unit of the TOF detector. The MRPC is built from two stacks of five single gas gaps (see left

panel of Fig. 6.9), 122 cm long and 13 cm wide, with an active area of  $120 \times 7.4 \text{ cm}^2$ . Each MRPC is segmented into 96 readout pads of area  $2.5 \times 3.5 \text{ cm}^2$ . The MRPCs are packed in five modules for each of the 18 azimuthal sectors of the ALICE spaceframe in a “TOF supermodule”, see left panel of Fig. 6.10. The right panel of Fig. 6.9 shows the working principle of an MRPC. When a charged particle traverses the detector’s active volume, it will start an avalanche process with the high and uniform electric field covering the sensitive gaseous volume. Hence, the signal collected in the pick-up electrodes is the analogue sum of signals from many gaps. In contrast to other gaseous detectors, in the MRPC, there is no drift time and, therefore, there is no late tail and the charge spectrum is not of an exponential shape. Furthermore, the chambers operate at atmospheric pressure.

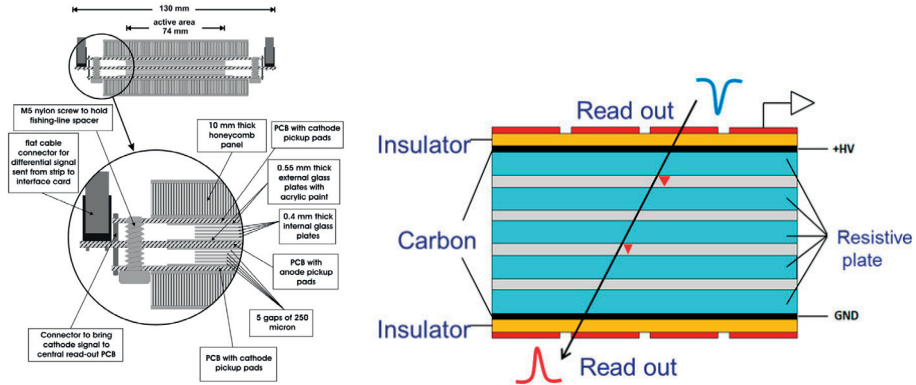


**Figure 6.9:** (Left) Schematic cross-section of a ten-gap double-stack MRPC strip. (Right) Illustration of the passage of a charged particle through an MRPC strip (see text for details). The figures are taken from [93].

## Time-Of-Flight

The fast signal produced in an MRPC module can precisely determine the position and time of the passage of a particle through the detector. The TOF detector provides precise measurements of the time-of-flight of long-lived particles. The time-of-flight is defined as follows:

$$t_{\text{TOF}} = t_{\text{STOP}} - t_{\text{START}}, \quad (6.7)$$

where  $t_{\text{START}}$  is the event collision time and  $t_{\text{STOP}}$  is the measured time. A detailed description of the measurement of  $t_{\text{START}}$  can be found in [108]. Once  $t_{\text{TOF}}$  is measured, the particle velocity is given by;  $\beta = L/(c \cdot t_{\text{TOF}})$ , where  $L$  is the length of the

track and  $c$  is the speed of light. Figure 6.10 shows the correlation between  $\beta$  and the momentum for  $\pi$ , K, p, d and e. The TOF detector provides valuable information for particle identification at intermediate momentum,  $1 - 4 \text{ GeV}/c$ .

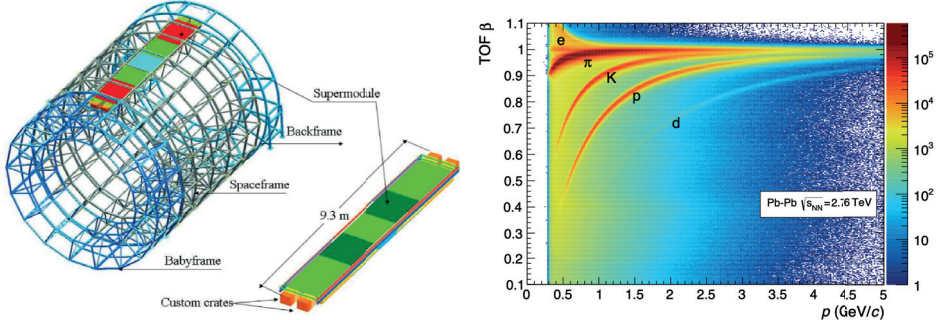


**Figure 6.10:** (Left) Schematic layout of one of the 18 TOF sectors inside the ALICE spaceframe. (Right) Correlation between  $\beta$  and momentum for  $\pi$ , K, p, d and e in Pb–Pb collisions at  $\sqrt{s_{\text{NN}}} = 2.76 \text{ TeV}$  measured with the ALICE TOF detector. The figures are taken from [92, 108].

## 6.6 Track Reconstruction

ALICE’s track reconstruction involves the central barrel detectors: ITS and TPC. The whole procedure starts with clusterisation or cluster-finding. First, the raw signals, interpreted as the crossing points of the tracks with the detectors’ sensitive elements, are converted into “clusters”. The clusters are associated with positions, signal amplitudes, signal times. The clusterisation procedure is done separately for each detector.

After the clusterisation, the track finding and fitting process start. This process follows an inward–outward–inward scheme [109, 110]. The inward stage consists of track finding and track fitting in the TPC. This process is based on the Kalman-filtering approach [111] and it starts from the outer radius of the TPC (see the direction of the blue arrows in Fig. 6.11). Track seeds<sup>2</sup> are built using information from both TPC clusters and the primary interaction vertex position. The seeds are propagated inward and, at each step, updated with the nearest cluster provided that it fulfils a proximity cut [92]. As I described in Sec. 6.4, the maximum number of TPC clusters associated with a track is 159. Such value corresponds to the number of pad rows in a readout chamber. Therefore, only tracks that have at least 20 clusters are accepted. As I will describe in Sec. 7.3, the analyses reported in this thesis use 70 clusters as the minimum number of

---

<sup>2</sup>A “track seed” is an initial direction for the track reconstruction algorithm.

crossed rows in the TPC to increase the quality of a track. If two tracks share a fraction of common clusters, one is rejected according to a quality parameter based on the cluster density, number of clusters, and momentum [109].

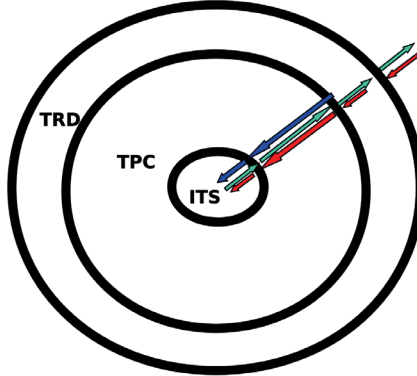


**Figure 6.11:** (Left) Sketch of the inward-outward-inward track reconstruction scheme. See text for details. The figure is taken from the presentation of Marian Ivanov at the Third International Workshop for Future Challenges for Tracking and Triggering Concepts that can be found in: <https://indico.gsi.de/event/1469/>.

The accepted tracks are then propagated to the outermost layer of the ITS detector. Therefore, these tracks become the seeds for track finding and fitting in the ITS. The seeds are updated using the clusters from each of the ITS layers together with a proximity cut that considers positions and errors. Each updated seed yields a new seed that is saved. The seeds that are not updated are further used for track finding. Furthermore, the  $\chi^2$  associated with the track fitting is increased by a penalty factor for missing a cluster. However, this does not apply when the seed is extrapolated to a dead zone.

Consequently, each TPC track yields a tree of track hypothesis in the ITS. Once all the tracks within the tree are prolonged to the innermost layer of the ITS, they are sorted according to the reduced  $\chi^2$ . Then, the track with the highest quality is checked for cluster sharing. If shared clusters are found, the following high-quality track is taken instead. Finally, the highest quality track from each hypothesis tree is added to the reconstructed event [109].

Once the reconstruction in the ITS is complete, the outward propagation starts. The tracks are refitted in the outward direction (see the direction of the green arrows in Fig. 6.11) using the clusters found at the previous stage. The integrated track length and the expected flight time for different particle species are updated for subsequent particle identification with the TOF detector. Once the track reaches the TRD detector, matching a TRD tracklet (track segment within a TRD layer) starts. Similarly, those tracks that reach the TOF detector are matched with TOF clusters. The final stage of the

track reconstruction process consists of refitting tracks towards the interaction vertex (see the direction of the red arrows in Fig. 6.11).

It is worth mentioning that the ITS and TPC detectors provide the kinematic information of a particle. Those detectors farther than the radius of the TPC only contribute with information relevant for particle identification. Furthermore, the procedure described above applies to the reconstruction of primary particles, i.e., those constrained to the primary interaction vertex. Secondary tracks from weak decays or interactions with the detector material are suppressed using a tight cut on the longitudinal and transverse distance of the closest approach to the primary interaction vertex. Since the analyses in this thesis concern measurements with primary particles, I will omit the description of the reconstruction of secondary tracks.

## 6.7 Interaction Vertex Reconstruction

In ALICE, there is a preliminary reconstruction of the primary interaction vertex. Such vertex is found using the SPD detector, i.e., the two innermost layers of the ITS detector. A “tracklet” is defined as the line connecting a pair of clusters, one from each SPD layer. Therefore, the interaction vertex is defined as the space point where the maximum number of tracklets converge. Suppose a single convergence point is not found, particularly in low-multiplicity events. In that case, the reconstruction algorithm performs a one-dimensional search of the maximum in the  $z$ -distribution of the points of closest approach (PCA) tracklets to the nominal beam axis [92].

The use of “global tracks” reconstructed using the TPC and ITS detectors yield a better precision on determining the primary interaction vertex than the one obtained using only SPD tracklets. Furthermore, by extrapolating the tracks to the point of closest approach to the nominal beamline and removing far outliers, the approximate point of closest approach of validated tracks is determined [92].



## **Part III**

# **Proton-Proton Data Analysis**



# Chapter 7

## Event, Vertex and Track Selection

The physics analyses use the data collected by the ALICE experiment during the 2016 and 2018 LHC pp run at  $\sqrt{s} = 13$  TeV. In 2016 and 2018, the gas used in the TPC was Argon. In 2017, the gas was changed to Neon. This led to a  $dE/dx$  resolution about 10% worse in the 2017 data than 2016 and 2018. As this analysis is not statistical limited and the different performance made it impossible to directly combine the results, it was decided to exclude the entire 2017 data for this analysis.

### 7.1 Event Selection

The event selection criteria that I use follow ALICE’s standard selection for spectra analyses. Events are selected using the minimum-bias trigger. This trigger requires hits in both V0A and V0C detectors in coincidence with the arrival of proton bunches from both directions. Events from machine induced background related to the passage of the LHC beams are rejected. Background events produce an “early” signal compared with the time corresponding to a collision in the nominal interaction point. Thus, background events are excluded by using the timing information of the V0 detector and taking into account the correlation between tracklets and clusters in the SPD detector [92]. Events with two or more reconstructed primary vertices are classified as “pileup” events and are discarded. Furthermore, events with incomplete DAQ readout are also rejected. Finally, the measurements use only inelastic collisions with at least one charged particle produced in  $|\eta| < 1$  and  $p_T > 0.15$  GeV/ $c$ . This class of events are called INEL  $> 0$  and correspond to about 75% of the total inelastic cross-section.

## 7.2 Vertex Selection

As described in Sec. 6.7, the primary interaction vertex is reconstructed using either tracks (using combined information from the SPD and TPC detectors) or tracklets (reconstructed only in the SPD detector). The preferred option is to use the vertex reconstructed with tracks; however, if the track vertex is unavailable, the SPD vertex is used. Moreover, a few extra criteria are required for the SPD vertex to ensure that it is a valid primary vertex:

- The SPD vertex is rejected if only its  $z$  coordinate along the beam direction is measured.
- The resolution on the  $z$ -component of the vertex reconstructed with SPD has to be better than 0.25 cm.
- If both the SPD and track vertices are reconstructed then the following condition must be satisfied:  $|z_{\text{vertex}}^{\text{track}} - z_{\text{vertex}}^{\text{SPD}}| < 0.5 \text{ cm}$ .
- The reconstructed vertex along the beam direction must satisfy the condition:  $|z_{\text{vertex}}| < 10 \text{ cm}$ , where the distance is measured from the nominal interaction point.

## 7.3 Track Selection

Chapter 8 presents this thesis’s two foremost data analyses, namely the “Relative Transverse Activity” and the “Spherocity” one. Both studies share the same definition of event and vertex selection; however, the track selection settings differ. Therefore, in the first part of this section, I describe the different sets of track cuts employed. The reason to use different track cuts definitions depends on the detector response to spherocity and transverse activity measurements.

### TPC Tracks

The first set of track cuts is called “TPC tracks”. A track that passes this track selection must satisfy the following:

- The number of rows crossed by the track in the TPC ( $N_{\text{CR}}$ ) has to be larger than 50 (out of maximum 159).

- The ratio between the  $\chi^2$  of the Kalman fit to the number of TPC clusters ( $N_{\text{TPC},\text{cl}}$ ) has to fulfill the condition:  $\chi^2/N_{\text{TPC},\text{cl}} < 4$ .
- The distance of closest approach to the reconstructed primary vertex has to be less than 3.2 (2.4) cm in the longitudinal (transverse) direction.
- The particle daughters from weak-decays and associated with a kink topology are rejected<sup>1</sup>.
- $|\eta| < 0.8$ .
- $p_T > 0.15 \text{ GeV}/c$ .

## Global Tracks

The second set of track cuts is called “Global tracks” and it is defined as follows:

- $N_{\text{CR}} > 70$  (out of maximum 159).
- The ratio  $N_{\text{CR}}/N_{\text{find}} > 0.8$ , where  $N_{\text{find}}$  is the number of geometrically possible clusters which can be assigned to a track.
- Particles associated with kink topologies are rejected.
- Tracks reconstructed in the TPC have to be present in the final refit procedure (see Sec. 6.6). This is known as the TPCRefit requirement.
- $\chi^2/N_{\text{TPC},\text{cl}} < 4$ .
- Two clusters in the ITS from which one has to be in the SPD detector.
- The ratio between the  $\chi^2$  of the Kalman fit to the number of available ITS clusters ( $N_{\text{ITS},\text{cl}}$ ) has to fulfill the condition:  $\chi^2/N_{\text{ITS},\text{cl}} < 36$ .
- Tracks reconstructed in the ITS must be present in the refit procedure. This is known as the ITSRefit.
- To limit the contamination of secondary particles, the following  $p_T$  dependent cut on the Distance of Closest Approach in the transverse plane ( $\text{DCA}_{xy}$ ) was applied:  $|\text{DCA}_{xy}| < 0.0105 + \frac{0.0350}{p_T^{1.1}}$ .
- The Distance of Closest Approach to the vertex in the  $z$ -direction has to fulfil the condition:  $|\text{DCA}_z| < 2 \text{ cm}$ .

---

<sup>1</sup>A kink topology represents the decay of charged-particle into a charged-particle plus a neutral one.

- $|\eta| < 0.8$ .
- $p_T > 0.15 \text{ GeV}/c$ .

## Hybrid Tracks

Global tracks are typically used in spectra analyses. However the inactive modules in the SPD detector together with the requirement of a hit in the SPD yield a non-uniform azimuthal angle distribution, see Fig. 7.1. This is not optimal for the analyses presented here since any  $\varphi$ -dependent detector inefficiencies introduce biases on  $\varphi$ -dependent observables such as the spherocity and the relative transverse activity. This leads to introduce “Hybrid Tracks”. Hybrid Tracks correspond to the union of two sets: Global Tracks and Complementary Tracks. Complementary Tracks are defined by the same quality cuts as the Global Tracks except that the requirement of the SPD hit is ignored. Furthermore, complementary tracks must be constrained to the primary vertex to improve the momentum resolution. Thus, if a track does not pass the Global Tracks cuts, it is tested against the Complementary Tracks cuts. Figure 7.1 shows the performance of hybrid tracks.

The relative transverse activity study analyses events with high- $p_T$  leading charged-particles. The selection of high- $p_T$  tracks uses the “Geometric Length” cut. This cut is beneficial to choose high-quality tracks with  $p_T \geq 2 \text{ GeV}/c$  since a significant fraction of the curvature of these tracks can be in between the sector boundaries. Thus, the geometric length cut considers the track’s length in the TPC’s active read-out area [112].

Table 7.1 summarises the different observables in the relative transverse activity analysis. Namely, the charged-particle multiplicity in the transverse region ( $N_T$ ), the leading charged-particle and the  $p_T$  spectra. It is worth mentioning that I use Hybrid track cuts to measure both the  $N_T$  and the  $p_T$  spectra since this selection works best when unfolding the  $p_T$  spectra as a function of the transverse activity.

**Table 7.1:** Table listing the track selection to measure  $N_T$ , the leading particle and the  $p_T$  spectra in the transverse activity analysis.

Track selection	$N_T$	Leading particle	$p_T$ spectra
Hybrid	Hybrid	Hybrid + Geometric Length	Hybrid

Table 7.2 summarises the track cuts used to measure the spherocity of an event and the  $p_T$  spectra. Notice that for the spherocity analysis, I did not use Hybrid Tracks since the measurement of the spherocity uses TPC Tracks and that set does not have the hit on the SPD requirement.

**Table 7.2:** Table listing the track selection to measure the spherocity of the event and the  $p_T$  spectra.

Track selection	Spherocity	$p_T$ spectra
	TPC Tracks + ITSRefit + TPCRefit	Global tracks

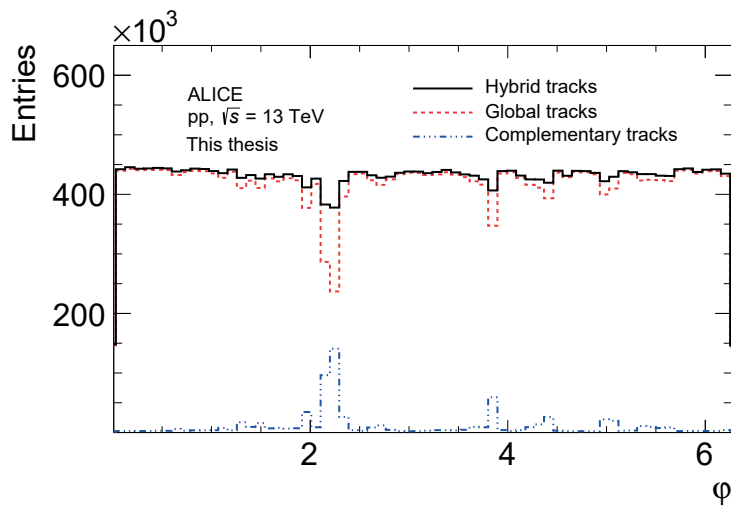


**Figure 7.1:** Azimuthal angle distribution of the measured particles using hybrid tracks. The distribution from global tracks is represented with the solid red line, while the one from complementary tracks is blue. Hybrid tracks with the solid black line (see text for details).

# Chapter 8

## Particle Identification and Event Shape Observables

This chapter describes the two pillar analyses of this thesis. These are the NOVEL analyses that has never been done before whereas Pb–Pb and pp as a function of multiplicity has been done before. This is also the reason we discuss them in more detail since they have never been described in detail before. Both analyses aim at the study of the underlying mechanisms for collective effects in pp collisions. The first analysis is about the measurement of the production of  $\pi$ , K and p as a function of the underlying event (UE) in events with a leading charged-particle. The measurements are performed in different topological regions: toward, away and the transverse. While the toward and away regions are dominated by the jet and away-side-jet, the transverse region is dominated by multiple parton interactions (MPI) and, initial and final state radiation (ISR/FSR). The second analysis is about the measurement of the production of  $\pi$ , K and p as a function of the Unweighted Transverse Spherocity. The transverse spherocity classifies events based on their topology. In this thesis, I focused mainly on jet-like and isotropic events. In essence, both analyses can be seen as complementary to each other. It is expected that in jet-like events or events with a leading track and very low event activity one primarily measures particles from the fragmentation of the jet. In isotropic topologies or events with a large amount of UE it is expected to see signatures of collective effect build up such as radial flow.

This chapter is divided into three main sections:

- Particle Identification. Here, I will describe the methods used to measure the  $p_T$  spectra of  $\pi$ , K and p using the TPC and TOF detectors. In addition, the relevant corrections such as: reconstruction efficiency and secondary particle contamina-

tion are described.

- Relative Transverse Activity Classifier.
- Unweighted Transverse Spherocity.

## 8.1 Particle Identification

The identification of  $\pi$ , K and p is divided into three different and independent analyses using the signal provided by the TPC and TOF detectors. The name of the analyses, particle identification (PID) techniques and the  $p_T$  intervals to which each study contributes to measuring the  $p_T$  spectra is summarised in Tab. 8.1. In the case of the TPC and TOF analyses, the signal extraction is done separately for positive and negative charged particles. This is mainly because the correction for the contamination of secondary particles depends on the particle's charge. However, due to statistical limitations at high  $p_T$  and because the yield of particles and antiparticles are the same, the signal extraction is done for the sum of positive and negative particles.

**Table 8.1:** Table with the name of the analysis and the corresponding PID technique used. The last columns list the  $p_T$  intervals in which the different species are identified in each study.

Analysis	PID technique	$p_T$ ranges (GeV/c)		
		$\pi$	K	p
TPC	$n\sigma$ fits	0.3 – 0.7	0.3 – 0.6	0.45 – 1
TOF	$\beta$ fits	0.7 – 3	0.60 – 3	1 – 3
rTPC	$dE/dx$ fits	2 – 20	3 – 20	3 – 20

### 8.1.1 Signal Extraction

#### TPC Analysis

The signal extraction in the TPC analysis is based on fits to  $n\sigma_i$  distributions ( $i = \pi^+, \pi^-, K^+, K^-, p$  and  $\bar{p}$ ) in  $p_T$  bins. The definition of  $n\sigma_i$  is given in Eq. 8.1.

$$n\sigma_i = \frac{dE/dx_{\text{measured},i} - \langle dE/dx_{\text{expected},i} \rangle}{\sigma}, \quad (8.1)$$

where  $dE/dx_{\text{measured},i}$  is the measured  $dE/dx$  and  $\langle dE/dx_{i,\text{expected}} \rangle$  is the expected average  $dE/dx$  from the Bethe-Bloch formula. The signal extraction is made in four narrow pseudorapidity intervals:  $|\eta| < 0.2$ ,  $0.2 < |\eta| < 0.4$ ,  $0.4 < |\eta| < 0.6$  and  $0.6 < |\eta| < 0.8$ . Tracks with large  $\eta$  have shorter drift length in TPC, hence less diffusion but also longer track length leads to more ionisation, i.e., more signal and hence a better precision. It is also important to keep in mind that the PID quantity is  $p$  but the physics quantity is  $p_T$ : for  $\eta \sim 0$ ,  $p \sim p_T$  and for  $|\eta| \gg 0$ ,  $p_T \ll p$ . Hence, to limit the dependence of the TPC and TOF signals on  $\eta$ , the signal extraction is performed in narrow pseudorapidity intervals.

Figure 8.1 shows examples of fits to  $n\sigma$  distributions for  $\pi^+$ ,  $K^+$  and  $p$  in different  $p_T$  bins. The signal is fitted to a Gaussian parameterisation. Thus, the yield is given by integral under the Gaussian parameterisation.

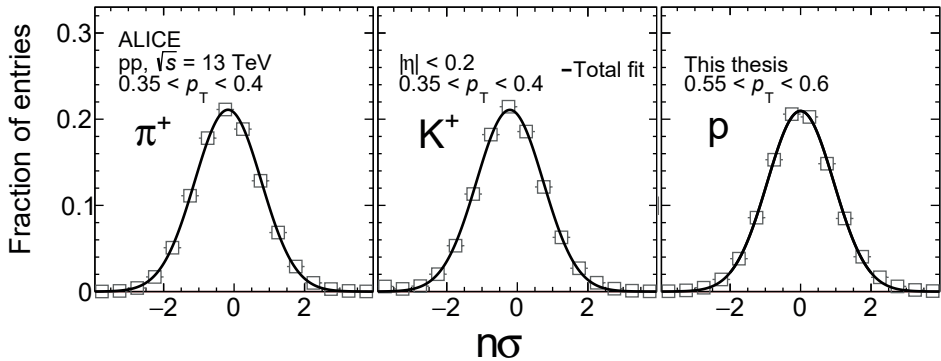


**Figure 8.1:** Fits to  $n\sigma$  distributions in different  $p_T$  intervals. The signal is fitted to a Gaussian parameterisation. The fit is represented with the solid black line. Results for  $\pi^+$ ,  $K^+$  and  $p$  in  $|\eta| < 0.2$  are shown on the left, middle and right panel, respectively.

## TOF Analysis

The PID in the TOF analysis is based on fits to  $\beta$  distributions in  $p$  intervals. The signal extraction is done using the four narrow  $|\eta|$ -intervals defined above. Figure 8.3 shows  $\beta$  distributions for two different momentum bins for tracks in  $|\eta| < 0.2$ . The signals of the different species are skewed. They all have a tail to the left of the peak's position. Equation 8.2 defines the exact and generic parameterisation to describe each species' signal. A Gaussian parameterisation describes the signal to the right of the peak's position, and a Gaussian convoluted with an Exponential function describes the

left side.

$$f(A, \beta, \mu, \sigma, \tau) = \begin{cases} G(A, \beta, \mu, \sigma), & \text{if } \beta \geq \mu + \tau . \\ G(A, \mu + \tau, \mu, \sigma) \exp \xi, & \beta < \mu + \tau , \end{cases} \quad (8.2)$$

where  $\xi = -\tau(\langle \beta \rangle - \sigma - \beta)/\sigma_\beta^2$ . The parameters  $A$  (amplitude),  $\mu$  and  $\sigma$  define the Gaussian-like distribution and  $\tau$  represents the  $\beta$  value at which the Exponential function kicks in. Note that each specie uses its own set of parameters.

The signal extraction procedure starts by parameterising  $\mu$  as a function of  $p$ , and  $\sigma$  and  $\tau$  as function of  $\beta$  for  $\pi$ , K and p. This is done in the region where there is no overlapping among the species. To extrapolate  $\mu$ , the following parameterisation was used:

$$\mu = B + C \cdot \sqrt{\frac{p_T^2}{p_T^2 + m^2}}, \quad (8.3)$$

where  $B$  and  $C$  are free parameters. The dependence of Eq. 8.3 on  $p_T^2$  is in agreement with what was obtained for the time-of-flight of a particle in Eq. 5.17. Equation 5.18 gives  $\beta \sim 1/\Delta t$ , where  $\Delta t$  is the time-of-flight, hence  $\sigma$  is expected to be inversely proportional to  $\Delta t^2$ . Figure 8.2 shows the extrapolations of  $\mu$  and  $\sigma$  for the two  $|\eta|$ -intervals:  $|\eta| < 0.2$  and  $0.6 < |\eta| < 0.8$ . In the case of the  $\mu$ , there is no dependence on the pseudorapidity. However, the  $\sigma$  is slightly lower for long tracks than for short tracks. The  $\tau$  parameter of  $\pi$  is described using a flat function over the entire range of  $\beta$ . In the case of K and p, a two-degree polynomial (flat) function is used for  $\beta \leq 0.9$  ( $\beta > 0.9$ ).

To extract the yield of  $\pi$ , K and p, the total fit function uses the sum of three parameterisations given by Eq. 8.2. The  $\mu$ ,  $\sigma$  and  $\tau$  parameters are fixed using the previously described extrapolation curves where the amplitude  $A$  is the only free parameter. Examples of fits in three different  $p$  bins are shown in Fig. 8.3. Thus, the yield is given by the integral under each of the parameterisations.

## rTPC Analysis

The TPC analysis on the relativistic rise (rTPC) or high- $p_T$  PID analysis identifies  $\pi$ , K and p with  $p_T = 2 \text{ GeV}/c$ . High- $p_T$  particles under the influence of a magnetic field will bent only a little. Thus, some of these particles will follow almost straight trajectories. This represents a problem when a significant fraction of the trajectory is near the edges of a TPC sector since, in general, it will have worse performance than

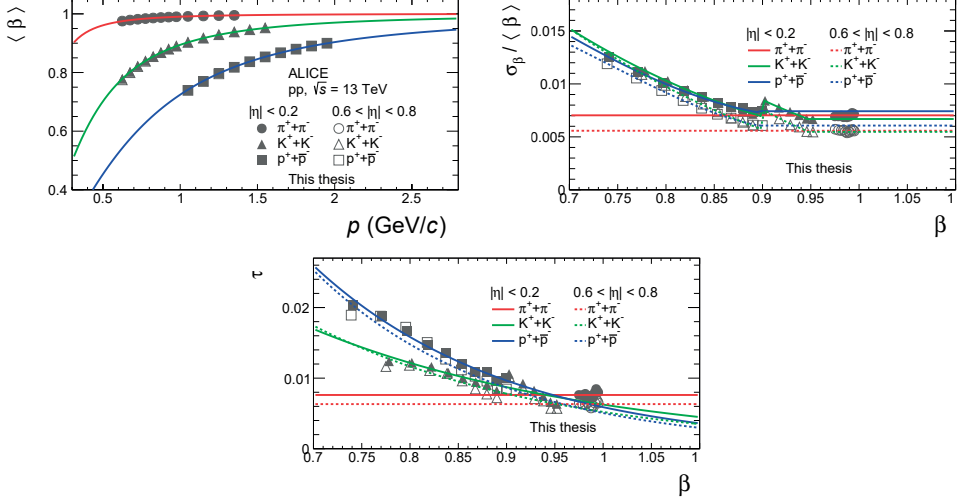


**Figure 8.2:** Extrapolation of the  $\mu$  as a function of  $p$  (top left),  $\sigma$  as a function of  $\beta$  (top right) and  $\tau$  as a function of  $\beta$  (bottom). Results in  $|\eta| < 0.2$  and  $0.6 < |\eta| < 0.8$  are represented with open and full markers, respectively.

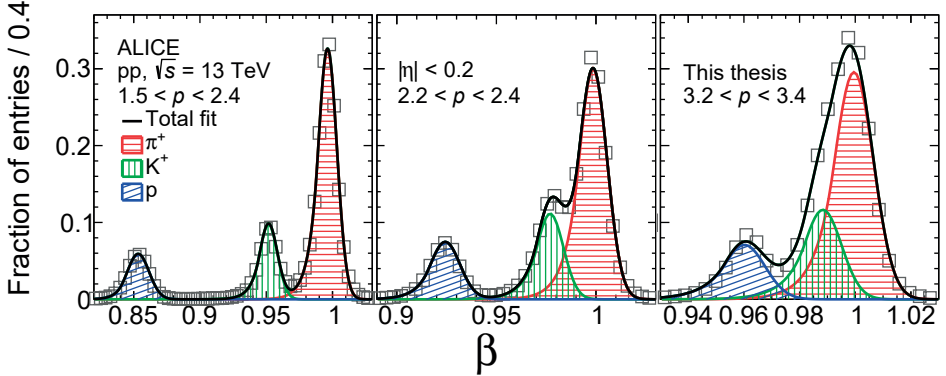


**Figure 8.3:** Examples of fits to  $\beta$  distributions in  $p$  bins. The total fit is represented with the solid black curve. The red, green and blue curves describe the signal of  $\pi^+$ ,  $K^+$  and  $p$ , respectively and the yield is represented with the shaded areas. The  $\beta$  distributions are measured in  $|\eta| < 0.2$ .

tracks far from the edges because of cluster losses. Hence, the rTPC analysis includes an additional cut to select good quality high- $p_T$  tracks for PID. The detailed description of this cut is given in Appx. A.

The signal extraction in the rTPC analysis adopted the technique employed in Refs. [43, 52, 113]. Particle identification in the relativistic rise of the TPC requires precise knowledge of the detector response. The measured  $dE/dx$  depends not only on  $\beta\gamma$  but on its pseudorapidity and the angle of inclination of the track. Hence, the first step in this analysis is to parameterise the Bethe-Bloch and resolution curves using external samples of secondary  $\pi^\pm$  from  $K_S^0$  decays,  $p(\bar{p})$  from  $\Lambda(\bar{\Lambda})$  decay, and  $e^\pm$  from  $\gamma$  conversions. In addition, primary  $\pi^\pm$  matched to the TOF detector are used to cover  $\beta\gamma$  values in the interval  $60 - 100$ . Figure 8.4 shows the  $dE/dx$  probability distributions of secondary particles and fits with a Gaussian parameterisation to describe each signal. The signal of all the secondary particles are clean and can be described with a Gaussian parameterisation. However, the signal from  $\pi^\pm$  ( $\langle dE/dx \rangle \approx 65$ ) matched to the TOF detector show a structure around  $\langle dE/dx \rangle \approx 55$ , which comes from protons.

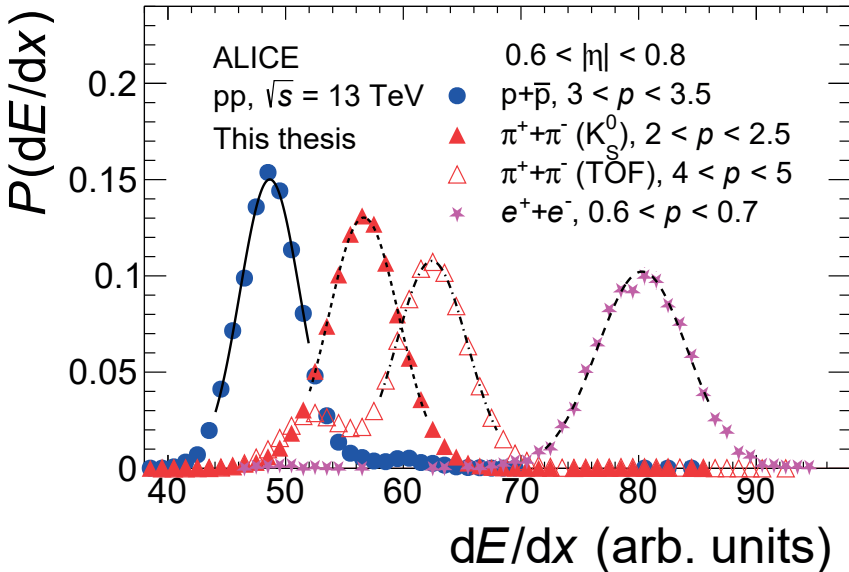


**Figure 8.4:**  $dE/dx$  probability distributions of secondary  $\pi^\pm$  from  $K_S^0$  decays, primary  $\pi^\pm$  matched to the TOF detector,  $p(\bar{p})$  from  $\Lambda(\bar{\Lambda})$  decay and  $e^\pm$  from  $\gamma$  conversions. The distributions are shown in  $0.6 < |\eta| < 0.8$  and for different momentum intervals.

The second step in the analysis is to parameterise the Bethe-Bloch ( $\langle dE/dx \rangle$ ) and relative resolution ( $\sigma_{dE/dx}/\langle dE/dx \rangle$ ) using the information from secondary particles. Both parameterisations are constructed for the same  $|\eta|$ -intervales used in the TPC and TOF analyses. This is done to limit the effects of charge diffusion.

Equation 8.4 gives the parametric form of the Bethe-Bloch:

$$\left\langle \frac{dE}{dx} \right\rangle = a \left[ \frac{1 + (\beta\gamma)^2}{(\beta\gamma)^2} \right]^e + \frac{b}{c} \log \left[ \frac{(1 + \beta\gamma)^c}{1 + d'(1 + \beta\gamma)^c} \right], \quad (8.4)$$

where  $d' = \exp[c(a - d)/b]$ ,  $a, b, c$  and  $d$  are free parameters. I want to highlight that the  $b$  parameter is related to the transition to the Fermi plateau region ( $\beta\gamma \gtrsim 1000$ ).

For  $d' \ll 1$ , as is the case here, Eq. 8.4 approaches different functional forms of the  $\langle dE/dx \rangle$  depending on the  $\beta\gamma$  region. For small  $\beta\gamma$  ( $\lesssim 4$ ),  $\langle dE/dx \rangle \approx 1/(\beta\gamma)^{2e}$ , while the relativistic rise behaves like,  $\langle dE/dx \rangle \approx a + b \log(1 + \beta\gamma)$ . Here  $1 + \beta\gamma$  is used to ensure that the logarithm term is always positive.

The relative resolution as a function of  $\langle dE/dx \rangle$  was parameterised using a second-degree polynomial:

$$\sigma_{dE/dx}/\langle dE/dx \rangle = a_0 + a_1 \langle dE/dx \rangle^1 + a_2 \langle dE/dx \rangle^2, \quad (8.5)$$

where  $a_0, a_1$  and  $a_2$  are free parameters.

The left (right) panel of Fig. 8.5 shows the Bethe-Bloch (relative resolution) parameterisation. At low  $\beta\gamma$ , the Bethe-Bloch curves are consistent among the different  $|\eta|$ -intervals. However, for  $\beta\gamma \gtrsim 20$ , the Bethe-Bloch parameterisation is higher for long tracks than short ones. In contrast, the relative resolution for short tracks is higher than for long tracks. This is expected due to the diffusion of electrons when drifting towards the endplates of the TPC. Particles in  $|\eta| < 0.2$  drift larger distances than the ones in  $0.6 < |\eta| < 0.8$ , therefore a better resolution is expected for long tracks.

To improve the Bethe-Bloch parameterisation in the transition to the Fermi plateau region, a two-dimensional fit of the correlation between  $dE/dx$  and  $p$  is done, fixing all the parameters of the Bethe-Bloch except the one that describes the approach to the Fermi plateau. This parameter corresponds to  $b$  in Eq. 8.4. Thus, the fit output corresponds to the final parameterisation used to fit individual  $dE/dx$  distribution in momentum bins.

For a given momentum bin and  $|\eta|$ -interval, the  $dE/dx$  distribution is fitted with the sum of four Gaussian parameterisations. Each Gaussian describes the signal of  $\pi$ ,  $K$ ,  $p$  and  $e$ . The  $\langle dE/dx \rangle$  and  $\sigma_{dE/dx}$  values are fixed from the Bethe-Bloch and resolution curves, respectively, while the amplitude is the only free parameter. Figure 8.6 shows examples of fits to  $dE/dx$  distributions.

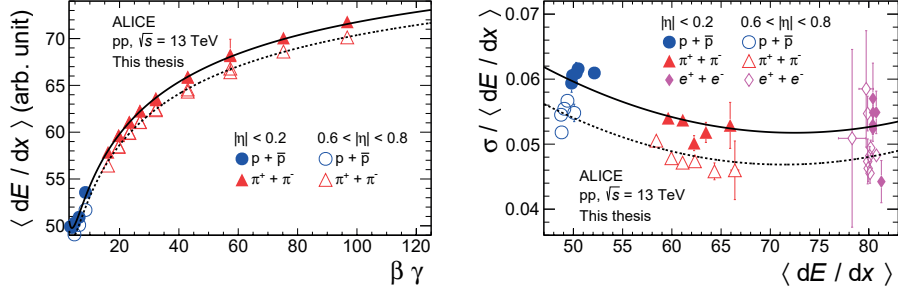


**Figure 8.5:** Bethe-Bloch (left) and relative resolution (right) parameterisations. The parameterisations are measured in  $|\eta| < 0.2$  and  $0.6 < |\eta| < 0.8$  using secondary particles. Electrons in the Bethe-Bloch parameterisations are not visible due to their large  $\beta\gamma$  ( $\gtrsim 1000$ ).

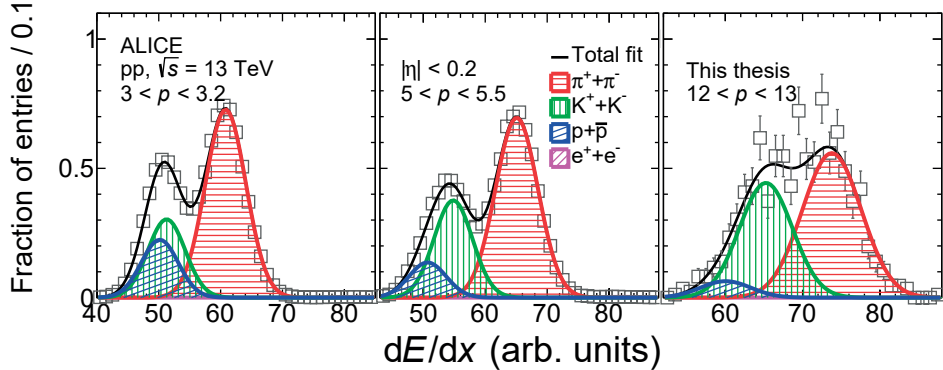


**Figure 8.6:** Examples of  $dE/dx$  fits in different  $p$  bins. The  $dE/dx$  distribution is fitted to the sum of four Gaussian parameterisations. The total fit is represented with the solid black line while the signal of  $\pi$ ,  $K$ ,  $p$  and  $e$  is represented with the solid red, green, blue and magenta, respectively. The signal of  $e$  is very small but it is located around  $dE/dx \approx 80$ . The yield of the different species is represented with the shaded areas. Results are shown in  $|\eta| < 0.2$  for minimum-bias collisions.

### 8.1.2 Particle Fractions

In Sec. 8.1.1, I explained how to measure the yield of identified particles by analysing the signal from the TPC and TOF detectors. Since more than 95% of the particle composition in a pp collision is made of  $\pi$ ,  $K$  and  $p$ , it is convenient to define the “relative particle fractions” as the ratio between the yield of  $\pi$ ,  $K$  and  $p$  to that of the total production of charged-particles. Since the yield is measured in four  $|\eta|$ -intervals, there will

be four sets of particle fractions.

In the TPC analysis, the signal extraction is done in  $p_T$  bins. However, in the TOF and rTPC studies, the signal extraction was performed in  $p$  bins. Therefore, we have to go from  $p$  dependent to  $p_T$  dependent particle fractions. The conversion in each  $|\eta|$ -interval is achieved by means of the following equation (example for  $\pi$ ):

$$f_\pi(p_T^j) = \sum_i f_\pi(p^i) R_{p_T^j p^i}, \quad (8.6)$$

where  $p_T^j(p^i)$  is the transverse momentum (momentum) in the  $j(i)$ -th bin,  $R_{p_T^j p^i}$  gives the probability that a track with measured  $p_T^j$  has measured  $p^i$  and  $f_\pi(p^i)$  is the fraction of pions in a given  $p^i$  bin. Figure 8.7 shows two examples of the conversion matrices used in  $|\eta| < 0.2$  and  $0.6 < |\eta| < 0.8$ . In total, four matrices are used and they are constructed using all the charged particles within the respective  $\eta$  interval.

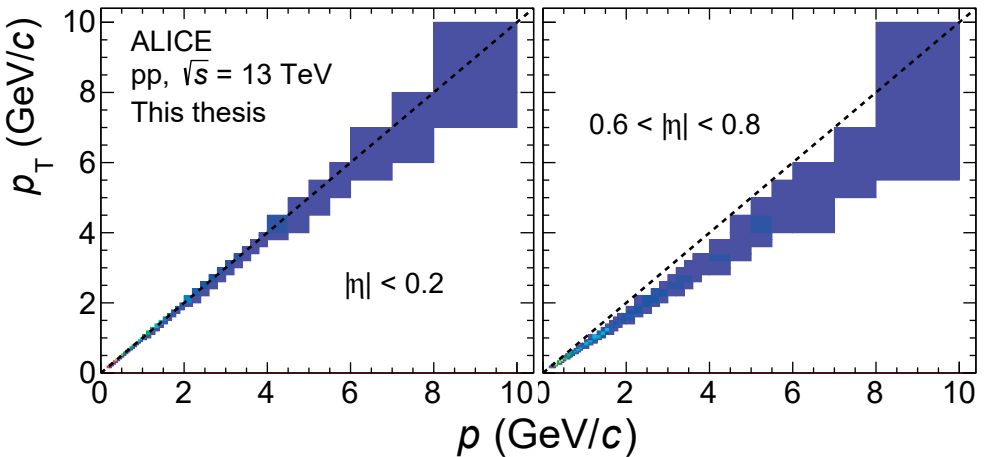


**Figure 8.7:** Examples of the conversion matrices. They are used to go from  $p$  to  $p_T$  dependent particle fractions. Two cases are shown:  $|\eta| < 0.2$  (left) and  $0.6 < |\eta| < 0.8$  (right).

Figure 8.8 shows the particle fractions of  $\pi^+$ ,  $K^+$  and  $p$  as a function of  $p_T$  in the for  $|\eta|$ -intervals. The particle fractions in  $|\eta| < 0.8$  are given as the weighted average from the four  $|\eta|$ -intervals. The statistical uncertainty gives the weight. Due to statistical limitations, the particle fractions in the rTPC analysis are presented as the sum of particles and anti-particles. The particle fractions measured in  $|\eta| < 0.8$  agree with the ones obtained from the  $|\eta|$ -intervals. There is a slight disagreement around  $p_T = 3 \text{ GeV}/c$ .

This region is challenging since the signals of kaons and protons overlap almost completely.

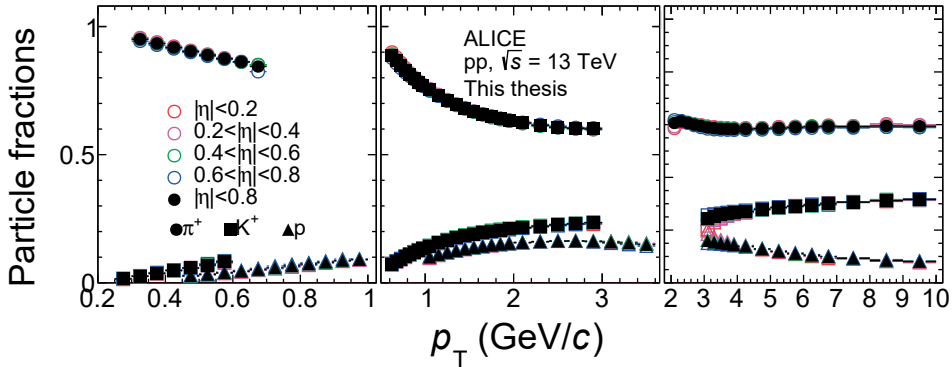


**Figure 8.8:** Particle fractions as a function of  $p_T$ . The results from each  $|\eta|$ -interval are represented with hollow markers, while the weighted average result is shown with solid black markers. The results correspond to positive-charged particles.

### 8.1.3 Corrections

In this section I go through the corrections applied to the  $p_T$  spectra.

#### Tracking and TPC-TOF matching efficiencies.

We use simulated pp collisions at  $\sqrt{s} = 13$  TeV to determine the reconstruction efficiency using the Monte Carlo event generator PYTHIA 8 Monash 2013 tune. The generated particles are then propagated through the ALICE apparatus and simulated with the GEANT 3 [114] particle transport generator. The propagated particles are selected using the same selection criteria as for data. Since this process involves simulated data, we know the properties of the particles, such as their identity, charge, mass, and if the particles are primary or secondary particles from weak decays or material interactions. In ALICE, primary particles are defined as particles with a mean proper lifetime  $\tau$  larger than  $1 \text{ cm}/c$ , which are either produced directly in the interaction or from decays of particles with  $\tau$  smaller than  $1 \text{ cm}/c$ , excluding particles produced in interactions with material [115].

The reconstruction efficiency of primary particles is defined as the ratio:

$$\varepsilon_{\text{TPC}} = \frac{N_{\text{rec}}}{N_{\text{gen}}} , \quad (8.7)$$

where  $N_{\text{rec}}$  is the number of tracks that passed the selection criteria and  $N_{\text{gen}}$  is the number of generated tracks.

In the TOF analysis, one has to consider that all the tracks reconstructed in the TOF detector have to be matched to a track reconstructed in the TPC. Hence, this leads to the definition of the “TPC-TOF matching” efficiency ( $\varepsilon_{\text{TOF}}$ ). The TPC-TOF matching efficiency is defined as a convolution between the reconstruction efficiency and the matching efficiency:

$$\varepsilon_{\text{TOF}} = \varepsilon_{\text{TPC}} \cdot \varepsilon_{\text{TOF}} = \frac{N_{\text{rec}}}{N_{\text{gen}}} \cdot \frac{N_{\text{ma}}}{N_{\text{rec}}} = \frac{N_{\text{ma}}}{N_{\text{gen}}} , \quad (8.8)$$

where  $N_{\text{ma}}$  is the number of tracks matched to the TOF detector.

The top panel of Figure 8.9 shows the charge and  $p_{\text{T}}$  dependent reconstruction and TPC-TOF matching efficiencies of primary  $\pi$ , K and p. Furthermore, the bottom panel of Figure 8.9 shows the reconstruction efficiencies applied to the  $p_{\text{T}}$  spectra measured in the rTPC analysis. The discontinuity at 2 GeV/c is due to the additional geometrical cut applied for tracks with  $p_{\text{T}} > 2$  GeV/c in the rTPC analysis.

## GEANT 3, GEANT 4 and Fluka corrections

GEANT 3, the particle transport generator used to simulate the passage of particles through the ALICE apparatus, does not accurately parameterise the energy loss of  $\bar{p}$  in the material and overestimates the absorption cross-section of  $K^-$  [116]. Consequently, the reconstruction and TPC-TOF matching efficiencies are not correctly estimated. To circumvent this problem, the standard approach in ALICE is to apply a correction factor to the reconstruction and TPC-TOF matching efficiencies of  $K^-$  and  $\bar{p}$ . Figure 8.10 shows the correction factors used in the tracking and TPC-TOF matching efficiencies. As can be seen, these corrections are only relevant for particles with  $p_{\text{T}} \leq 2$  GeV/c.

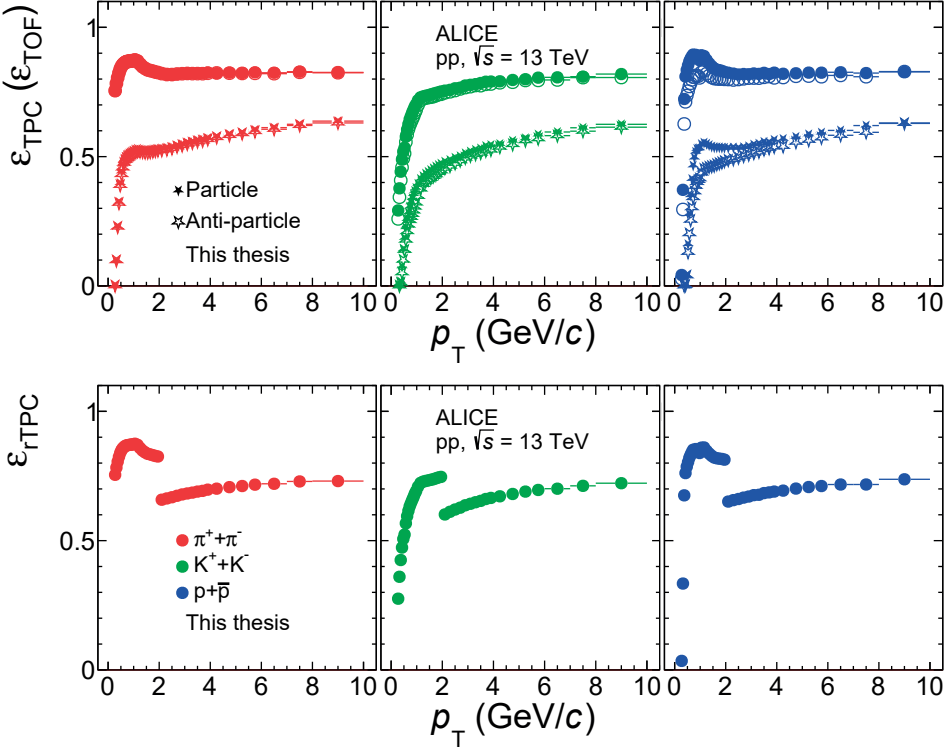


**Figure 8.9:** (Top panel) Reconstruction and TPC-TOF matching efficiencies as a function of  $p_T$ . Full (open) markers represent the results for particles (anti-particles). The efficiencies are presented for  $\pi$ ,  $K$  and  $p$  from left to right. (Bottom panel) Reconstruction efficiency for the sum of particles and anti-particles. The discontinuity at  $p_T = 2 \text{ GeV}/c$  is due to the geometrical cut applied in the rTPC analysis. All the efficiencies shown are measured in minimum-bias pp collisions at  $\sqrt{s} = 13 \text{ TeV}$ .

## Secondary Particle Contamination Correction

The measured yield of  $\pi^+$ ,  $\pi^-$ ,  $p$  and  $\bar{p}$  receive a large contribution of secondary particles from weak decays. Mainly the decays of strange and multi-strange hadrons such as:  $K_S^0 \rightarrow \pi^- + \pi^+$ ,  $\Lambda \rightarrow p + \pi^-$ ,  $\Sigma^+ \rightarrow p + \pi^0$  (and their charge conjugates). Moreover, the  $p_T$  spectra of protons receive a non-negligible contamination from protons from material interactions. To estimate the secondary particle contamination, I have adopted a data-driven method. The first step is to measure the Distributions of Closest Approach in the  $xy$  plane ( $\text{DCA}_{xy}$ ). The  $\text{DCA}_{xy}$  distributions for identified particles

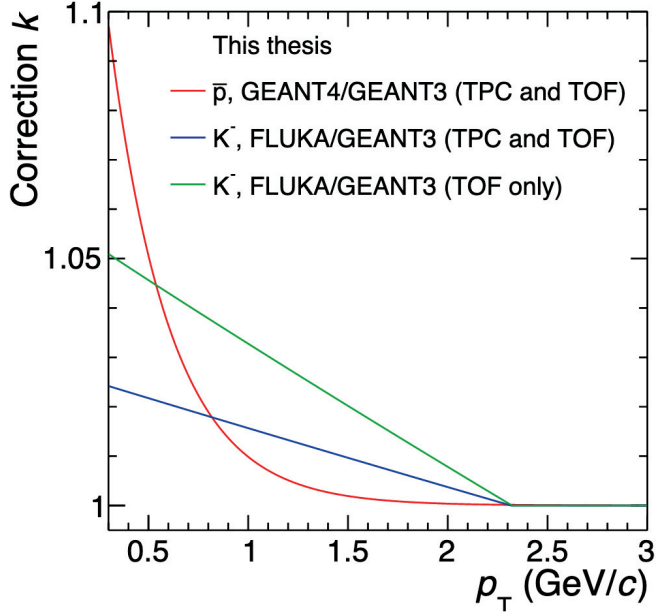


**Figure 8.10:** Correction factors applied to the reconstruction and TPC-TOF matching efficiencies of  $K^-$  and  $\bar{p}$ . The figure was taken from Ref. [117].

are constructed using the following criteria:

$$DCA_{xy} = \begin{cases} |n\sigma| < 3 & \text{TPC analysis .} \\ \sqrt{n\sigma_{\text{TPC}}^2 + n\sigma_{\text{TOF}}^2} < 2 & \text{TOF analysis .} \end{cases} \quad (8.9)$$

Figure 8.11 shows the  $DCA_{xy}$  distributions (solid gray markers) for protons in two  $p_T$  bins. It is important to notice that the distributions shown in Fig. 8.11 are measured without the  $DCA_{xy}$  cut mentioned in Sec. 7.3. The fraction of primary particles is estimated from a multi-template fit to the  $DCA_{xy}$  distributions. Three templates are considered: primary particles, secondary particles from weak decays and secondary particles from material interactions. Here, the templates are obtained from Monte Carlo simulations using PYTHIA 8 Monash 2013 tune. By fitting the data  $DCA_{xy}$  distributions to the sum of the three templates (see Fig. 8.11), one can estimate the fraction of primary particles. The range considered in the fit is fixed to the interval  $\pm 3$  cm.

Once the  $DCA_{xy}$  distributions are fitted, and the fraction of primary and secondary particles is determined, the  $DCA_{xy}$  is closed following the  $p_T$  dependent  $DCA_{xy}$  cut (notice that the equation below is one of the quality cuts described in Sec. 7.3):

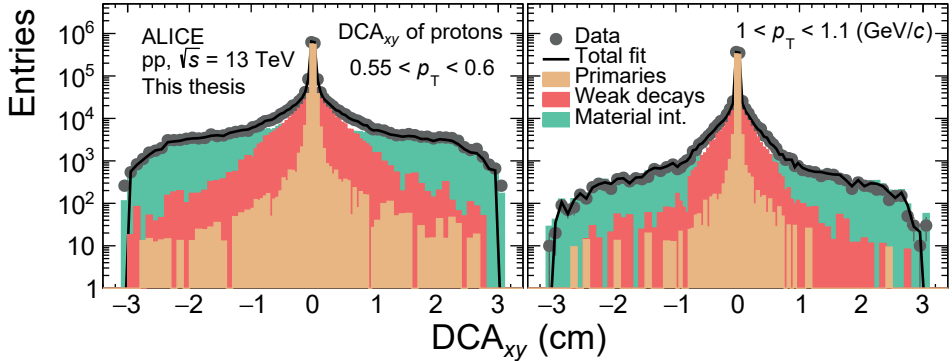


**Figure 8.11:** Examples of  $\text{DCA}_{xy}$  distributions. The  $\text{DCA}_{xy}$  distributions are measured in data for  $p$ . The left (right) panel shows the distributions measured with tracks in the TPC (matched to TOF detector). Three Monte Carlo templates are used to fit the data: primary particles and secondary particles from weak decays and material interactions. The left (right) panel corresponds to tracks with  $0.55 < p_{\text{T}} < 0.6$  ( $1 < p_{\text{T}} < 1.1$ ). Units given in  $\text{GeV}/c$ .

$$|\text{DCA}_{xy}(p_{\text{T}})| < 0.015 + \frac{0.35}{p_{\text{T}}^{1.1}}$$

Then, the ratio between the area within the  $\text{DCA}_{xy}$  cut and the total area of the distribution is weighted by the fraction of primary and secondary particles to estimate the final correction.

Figure 8.12 shows the fraction of primary  $\pi^+$ ,  $\pi^-$ ,  $p$  and  $\bar{p}$ . The left (right) panel shows the correction applied to the  $p_{\text{T}}$  spectra measured in the TPC (TOF) analysis. The correction for  $p$  is larger than for  $\bar{p}$  due to the more significant contamination of secondary protons from material interactions. In the rTPC analysis, an extrapolation of the correction measured in the TOF analysis is applied. For  $\pi$ , this correction is about 1% while for  $p$  is of the order of 5%.

### 8.1.4 Constructing the $p_{\text{T}}$ Spectra

In the previous sections, I described the different methods and techniques to obtain all the necessary elements to build up the corrected  $p_{\text{T}}$  spectra of identified particles. Hence, what remains is to show the equation that puts all the several parts together.

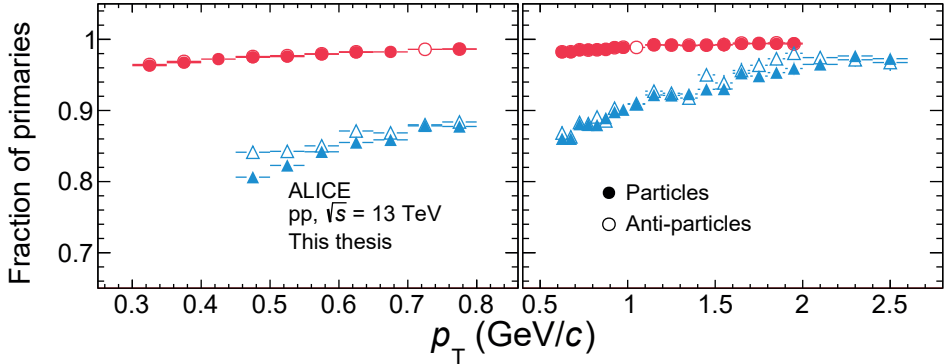


**Figure 8.12:** (Left) Fraction of primary particles in the TPC analysis. (Right) Fraction of primary particles in the TOF analysis. Results for anti-particles (particles) are shown with closed (open) markers. The corrections are obtained from minimum-bias pp collisions.

Equation 8.10 indicates how to get the fully corrected  $p_T$  spectrum (example for p).

$$\frac{dY_p}{dp_T dy} = f_p \cdot J \cdot C \cdot \frac{1}{\varepsilon} \times \left( \frac{dY_{ch}}{dp_T d\eta} \right)_{|\eta| < 0.8}, \quad (8.10)$$

- $f_p$  is the uncorrected particle fractions as a function of  $p_T$ .
- $J$  is the Jacobian transformation ( $\eta \rightarrow y$ )
- $C$  is a correction for secondary particle contamination.
- $\varepsilon$  is the  $p_T$  dependent reconstruction efficiency.
- $\frac{dY_{ch}}{dp_T d\eta}$  is the spectrum of charged particles.

## 8.2 Relative Transverse Activity Classifier

First, I will describe in words what is understood by the Underlying Event (UE). The UE is commonly referred to as the collection of particles produced in hadronic collisions, which do not originate from the primary hard parton-parton scattering nor are related to it in the form of hadronised parton showers. Thus, the UE includes contributions from MPIs, ISR, and FSR and interactions between partons and beam remnants. Figure 8.13

shows the charged-particle number density  $N_{\text{ch}}$  in the “toward”, “away” and “transverse” regions in events with a leading charged-particle as a function of the transverse momentum of the leading particle ( $p_T^{\text{leading}}$ ) in pp collisions at  $\sqrt{s} = 13$  TeV. Here, I want to highlight the measurement in the transverse region (by transverse, I mean perpendicular to the direction of the leading particle). There is a steep rise of the number density from  $p_T^{\text{leading}} \approx 0.5$  GeV/c up to  $p_T^{\text{leading}} \approx 5$  GeV/c. Then one observes that the number density has little dependence on the leading particle for  $p_T^{\text{leading}} \gtrsim 5$  GeV/c. This region is known as the plateau or pedestal region. Similar studies performed in jet events such as the one described in Ref. [118] reported a slow rise of the UE plateau with increasing energy of the jet. This effect was explained by additional contributions from wide-angle radiation associated with the hard scattering.

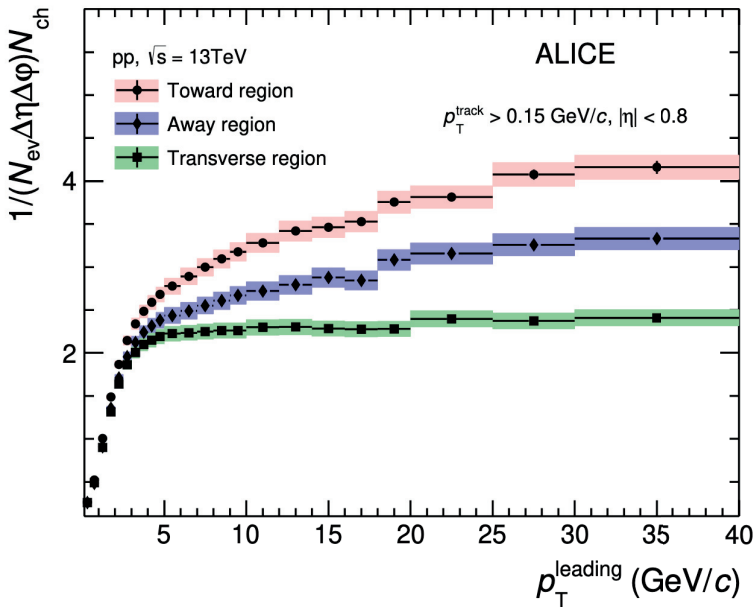


**Figure 8.13:** Charged-particle number density as a function of the  $p_T$  of the leading charged-particle. The results are shown for measurements in the toward, away and transverse region. The figure was taken from Ref. [119]

The first study that I will describe is the production of  $\pi$ , K and p in pp collisions at  $\sqrt{s} = 13$  TeV as a function of the underlying event in events with a leading charged-particle. The leading particle is defined as the one detected in  $|\eta| < 0.8$  and with  $p_T^{\text{leading}}$  in the interval  $5 - 40$  GeV/c. The lower threshold corresponds to the onset of the UE plateau in the transverse region. Although wide-angle radiation becomes significant for jet  $p_T > 50$  GeV/c [118], I use an upper cut of 40 GeV/c to limit its effects. To study the particle production associated with different underlying physics

mechanisms, I adopted the conventional division of the azimuthal angle ( $\varphi$ ) plane into regions relative to the direction of the leading particle of the event [120], see Fig. 8.14. Hence the observables reported in this thesis are measured in three different topological regions, the toward, away and transverse regions. The population of the different topological regions uses the associated particles reconstructed in  $|\eta| < 0.8$  and with transverse momentum ( $p_T^{\text{track}}$ ) in the interval,  $0.3 - 5 \text{ GeV}/c$ . The precise definition of the topological regions is based on the absolute difference in azimuthal angle between the leading and associated particles,  $|\Delta\varphi| = |\varphi^{\text{leading}} - \varphi^{\text{track}}|$ :

- Toward:  $|\Delta\varphi| < 60^\circ$ .
- Transverse:  $60^\circ < |\Delta\varphi| < 120^\circ$ .
- Away:  $|\Delta\varphi| > 120^\circ$ .

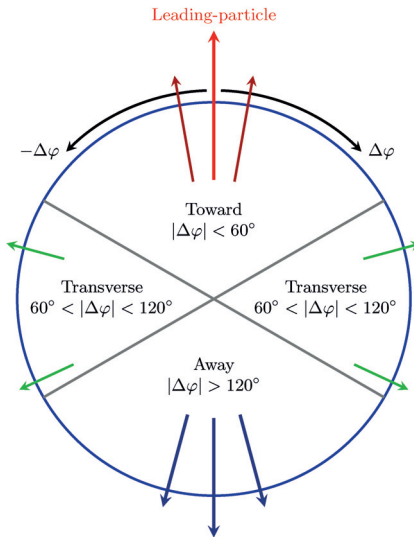


**Figure 8.14:** Definition of the toward, away and transverse regions in the azimuthal angle plane in events with a leading charged-particle. The division of the azimuthal-angle plane into the different topological regions is based on the absolute difference between the azimuthal angle of the leading and associated particles. The figure was taken from Ref. [119]

## Relative Transverse Activity Classifier

This thesis reports the first measurements on the production of  $\pi$ , K and p as a function of the Relative Transverse Activity Classifier [121], referred to as  $R_T$ .

$$R_T = \frac{N_T}{\langle N_T \rangle} , \quad (8.11)$$

where  $N_T$  is the charged-particle multiplicity in the transverse region. By definition,  $R_T$  cleanly divides events with “higher-than-average” UE from “lower-than-average” ones irrespective of the centre-of-mass energy. Of particular interest is whether events with very low UE activity, which are dominated by the jet activity, exhibit particle ratios and spectra consistent with fragmentation models tuned to  $e^+e^-$  data and whether high-UE events exhibit any clear signs of flow or other collective effects [121].

### 8.2.1 One-Dimensional Unfolding

To characterise events as a function of the event activity, we measure the multiplicity distribution of charged particles in the transverse region  $Y(N_{T,m})$ . However, the detector’s finite resolution causes a smearing of the measured quantities. Therefore, this section introduces the one-dimensional unfolding method to correct detector effects and efficiency losses. The followed approach is based on the iterative Bayesian unfolding method by G. D’Agostini [122].

Bayesian unfolding requires the knowledge of the smearing matrix  $S_{mt}$ , which comprises information about the limited acceptance and finite resolution. It represents the conditional probability  $P(N_{T,m}|N_{T,t})$  of an event with multiplicity  $N_{T,t}$  to be measured as one with multiplicity  $N_{T,m}$ . The smearing matrix is typically expressed as a square matrix of size  $N_{T,t} \times N_{T,m}$  as shown on the left panel of Fig. 8.15. While the probability values laying on the diagonal of the smearing matrix represent the measured events with the correct number of true particles, the off-diagonal elements stand for those measured as  $N_{T,m}$  due to detector inefficiencies and background, e.g., secondary particles misidentified as primary particles.

Since the smearing matrix encodes the detector effects, the measured multiplicity distribution  $Y(N_{T,m})$  can be written as the convolution of the smearing matrix with the true distribution  $Y(N_{T,t})$ :

$$Y(N_{T,m}) = \sum_t S_{mt} \cdot Y(N_{T,t}) . \quad (8.12)$$

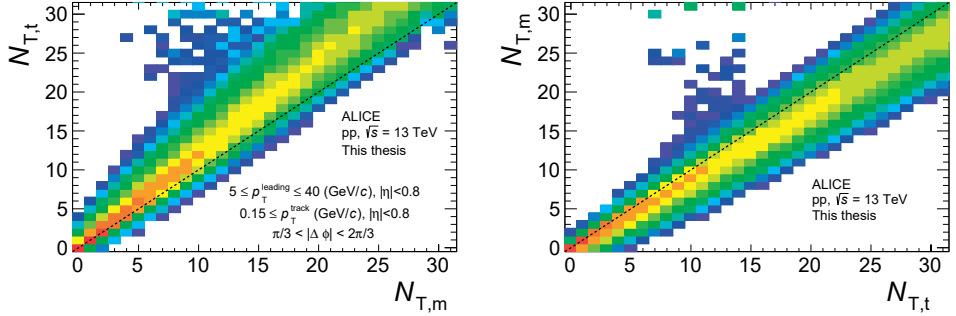


**Figure 8.15:** (Left) Correlation between the true  $N_{T,t}$  and the measured  $N_{T,m}$  multiplicity in the transverse region after row-wise normalisation. (Right) Unfolding matrix  $M_{1tm}$ .

Naively, one can think of solving Eq. 8.12 for  $Y(N_{T,t})$  by inverting the smearing matrix. However, there is no guarantee that the inverse matrix  $S_{mt}^{-1}$  exists or many solutions to Eq. 8.12 might exist.

G. D’Agostini proposed to recover the true distribution using the theorem of Bayes. Suppose that the probabilities of observing a true  $N_{T,t}$  and a measured  $N_{T,m}$  multiplicity are given by  $P(N_{T,t})$  and  $P(N_{T,m})$ , respectively. Thus, the conditional probability of observing  $N_{T,t}$  and  $N_{T,m}$  at the same time is given by the joint probability  $P(N_{T,t} \cap N_{T,m})$ . The conditional probabilities  $P(N_{T,t}|N_{T,m})$  and  $P(N_{T,m}|N_{T,t})$  are connected with  $P(N_{T,t} \cap N_{T,m})$  according to the following equations:

$$P(N_{T,t}|N_{T,m}) = \frac{P(N_{T,t} \cap N_{T,m})}{P(N_{T,m})}. \quad (8.13)$$

$$P(N_{T,m}|N_{T,t}) = \frac{P(N_{T,m} \cap N_{T,t})}{P(N_{T,t})}. \quad (8.14)$$

Using Eq. 8.13 and Eq. 8.14, the theorem of Bayes can be expressed in terms of  $P(N_{T,t})$  and  $P(N_{T,m})$ :

$$P(N_{T,t}|N_{T,m}) = \frac{P(N_{T,m}|N_{T,t})P(N_{T,t})}{P(N_{T,m})}. \quad (8.15)$$

The left-hand side of Eq. 8.15 represents the probability that the actual multiplicity of the event is equal to  $N_{T,t}$ , given that the value of  $N_{T,m}$  was measured.

Using Eq. 8.14, the total probability to measure an event with multiplicity  $N_{T,m}$  can be obtained from summing over the elements of  $P(N_{T,t})$  weighted by the elements of  $P(N_{T,m}|N_{T,t})$ :

$$P(N_{T,m}) = \sum_t P(N_{T,m} \cap N_{T,t}) = \sum_t P(N_{T,m}|N_{T,t})P(N_{T,t}). \quad (8.16)$$

Finally, combining Eq. 8.15 with Eq. 8.16, the theorem of Bayes can be rewritten in the following form:

$$P(N_{T,t}|N_{T,m}) = \frac{P(N_{T,m}|N_{T,t})P(N_{T,t})}{\sum_t P(N_{T,m}|N_{T,t})P(N_{T,t})}. \quad (8.17)$$

The left-hand side of Eq. 8.17 is known as the “un-smearing matrix” or “unfolding matrix”, henceforth called,  $M1_{tm}$ . However, since the true multiplicity distribution  $P(N_{T,t})$  is unknown, one has to replace  $P(N_{T,t})$  by an arbitrary distribution  $P_0(N_{T,t})$  to obtain an estimation of  $P(N_{T,t}|N_{T,m})$ . Different choices of  $P_0(N_{T,t})$  can be used, these include a constant probability distribution or even the measured probability distribution. Now that we have found an explicit form to compute the unfolding matrix, Eq. 8.18 gives an exact expression to obtain the unfolded distribution  $\widehat{Y}(N_{T,t})$ :

$$\widehat{Y}(N_{T,t}) = \sum_m M1_{tm} Y(N_{T,m}). \quad (8.18)$$

Equation 8.18 tell us how to recover the measured multiplicity according to the unfolding matrix. Furthermore, Eq. 8.18 can be used to update the original prior  $P_0(N_{T,t})$ . I call the updated prior:  $\widehat{P}(N_{T,t})$  and Eq. 8.19 gives it. The updated prior  $\widehat{P}(N_{T,t})$  is closer to the one of  $N_{T,t}$ , since the measured distribution  $Y(N_{T,m})$ , which is a direct effect of  $N_{T,t}$  enters in the unfolding procedure (see Eq. 8.18) and thereby constrains  $\widehat{P}(N_{T,t})$ .

$$\widehat{P}(N_{T,t}) = \frac{\widehat{Y}(N_{T,t})}{\sum_{N_{T,t}} \widehat{Y}(N_{T,t})}. \quad (8.19)$$

The substitution of the initial prior  $P_0(N_{T,t})$  by  $\widehat{P}(N_{T,t})$  into Eq. 8.17 yields a new unfolding matrix, which together with Eq. 8.18 give an updated unfolded distribution.

The process described above is an iterative one, which causes the unfolded distribution to converge to the true one. However, it also compounds the effects of statistical

uncertainties in the smearing matrix. Therefore, many iterations do not guarantee a better result: eventually, the true distribution will contain significant imprecisions from stochastical fluctuations in the smearing matrix. Thus, the number of iterations is determined based on the  $\chi^2/N_{\text{df}}$  between the unfolded and true distribution. Figure 8.16 shows the evolution of the  $\chi^2/N_{\text{df}}$  ratio as a function of the number of iterations. The  $\chi^2/N_{\text{df}}$  ratio has a minimum at 3, and after that value, it rises slowly. Hence, I conclude that the optimal number of interactions to unfold the  $N_T$  distribution equals 3.

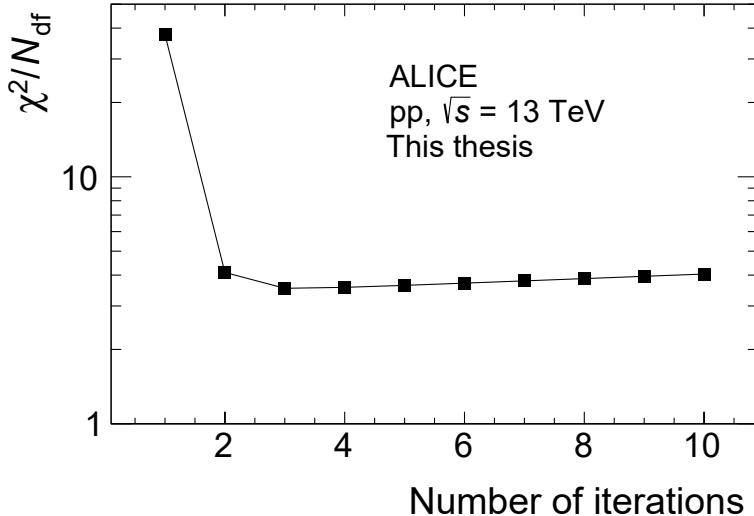


**Figure 8.16:**  $\chi^2/N_{\text{df}}$  ratio as a function of the number of interactions. The minimum at 3 indicates the optimal number of iterations needed to unfold the  $N_T$  distribution.

### 8.2.2 Statistical Uncertainties in the Bayesian Unfolding Method

In Sec. 8.2.1 it was shown that the unfolded distribution  $\widehat{Y}(N_{T,t})$  is given by:

$$\widehat{Y}(N_{T,t}) = \sum_m M1_{tm} Y(N_{T,m}) \quad \text{where} \quad M1_{tm} = \frac{P(N_{T,m}|N_{T,t})P_0(N_{T,t})}{\sum_t P(N_{T,m}|N_{T,t})P_0(N_{T,t})},$$

where  $M1_{tm}$  is the unfolding matrix. At this point, it is important to remember that  $M1_{tm}$  is independent of  $Y(N_{T,m})$  only during the first iteration. For subsequent iterations,  $P_0(N_{T,t})$  is replaced by  $\widehat{P}(N_{T,t})$  from the previous iteration, and  $\widehat{P}(N_{T,t})$  depends on

$Y(N_{T,m})$  (see Eq. 8.18 and Eq. 8.19). Therefore, the covariance matrix on the unfolded distribution  $V(\hat{Y}(N_{T,t}), \hat{Y}(N_{T,k}))$  has to be calculated using error propagation.

First, one computes the error propagation matrix  $\partial\hat{Y}(N_{T,t})/\partial Y(N_{T,k})$ , which is given by:

$$\frac{\partial\hat{Y}(N_{T,t})}{\partial Y(N_{T,k})} = \frac{\partial}{\partial Y(N_{T,k})} \left( \sum_m M1_{tm} Y(N_{T,m}) \right) .$$

$$\frac{\partial\hat{Y}(N_{T,t})}{\partial Y(N_{T,k})} = M1_{tk} + \frac{Y(N_{T,t})}{Y_0(N_{T,t})} \frac{\partial Y_0(N_{T,t})}{\partial Y(N_{T,k})} - \sum_i \sum_j \frac{Y(N_{T,i})}{Y_0(N_{T,j})} M1_{ti} M1_{ji} \frac{\partial Y_0(N_{T,j})}{\partial Y(N_{T,k})} .$$

Using the error propagation matrix together with the covariance matrix on the measured distribution  $V(Y(N_{T,i}), Y(N_{T,j}))$ , the covariance matrix on the unfolded distribution is given by:

$$V(\hat{Y}(N_{T,t}), \hat{Y}(N_{T,k})) = \sum_{i,j} \frac{\partial\hat{Y}(N_{T,t})}{\partial Y(N_{T,i})} V(Y(N_{T,i}), Y(N_{T,j})) \frac{\partial\hat{Y}(N_{T,k})}{\partial Y(N_{T,j})} . \quad (8.20)$$

### 8.2.3 Unfolding the Particle Spectra

Unfolding the  $p_T$  spectra as a function of  $N_T$  has to be treated differently depending on the topological region. However, the toward and away regions turned out to be straightforward cases as there is no overlap between the tracks used for the spectra and the tracks used for the multiplicity – the latter is measured in the transverse region. Therefore, the one-dimensional unfolding matrix  $M1_{tm}$  is directly applied in these two regions. Hence the fully corrected  $p_T$  spectra as a function of  $N_{T,t}$  is obtained in a two-step procedure:

1. Correct the raw  $p_T$  spectra at particle level by tracking inefficiency and secondary particle contamination. The efficiency correction is applied as unfolding preserves the integral but does not correct efficiency losses.
2. Apply the one-dimensional unfolding matrix. The spectra as a function of  $N_{T,t}$  is given by:  $\frac{d\hat{Y}(N_{T,t})}{dp_T} = M1_{tm} \frac{dY(N_{T,m})}{dp_T}$ .

The transverse region requires a more elaborated method as both particle spectra and multiplicity are measured using the same tracks. In other words, we are no longer dealing with the problem of rearranging events but rather how tracks should be unshuffled to match the true  $p_T$  distributions. This poses a four-dimensional problem, two dimensions associated with the true and measured multiplicities plus two dimensions associated with the true and measured  $p_T$  spectra. Instead, an approximate method is employed in which the multiplicity smearing matrix is assumed to be independent of the  $p_T$ . In this approach, a new track response matrix is obtained by multiplying every column of the original multiplicity response matrix with the respective number of measured particles as weights. After row-wise normalization, the desired track response matrix is obtained.

Using this modified response matrix, unfolding is done in a  $p_T$ -bin-by- $p_T$ -bin basis. For a particular  $p_T$  bin, the measured multiplicity distribution is unfolded using the iterative unfolding procedure described in Sec. 8.2.1. This approach yields unfolding matrices that depend on the  $p_T$ . Henceforth these matrices will be called  $M2_{tm}(p_T)$ . It is worth mentioning that this is an approximate method, which works here because the tracking efficiency does not depend strongly on the  $p_T$  for hybrid tracks and because we use the same definition of track selection for the  $p_T$  spectra and to measure  $N_{T,m}$ . This was investigated and concluded in this thesis.

Similar to the toward and away regions, a two-step procedure is followed to obtain the fully corrected  $p_T$  spectra. The only difference is that when unfolding, we use the  $p_T$  dependent  $M2_{tm}(p_T)$  matrices as shown in Eq. 8.21.

$$\frac{d\hat{Y}(N_{T,t}, p_T)}{dp_T} = \sum_m M2_{tm}(p_T) \frac{dY(N_{T,m}, p_T)}{dp_T}. \quad (8.21)$$

The method described above treats the unfolding of the spectra of all charged particles. Such method yielded the unfolding matrices  $M1_{tm}$  and  $M2_{tm}(p_T)$ . When unfolding the spectra of identified particles (for example,  $\pi$  in the transverse region), we apply Eq. 8.21 using the  $M2_{tm}(p_T)$  matrices from charged particles and exchanging  $dY(N_{T,m}, p_T)/dp_T$  for  $dY^\pi(N_{T,m}, p_T)/dp_T$ . Unfolding the spectra of  $\pi$  in the toward and away regions follow the same strategy but using  $M1_{tm}$  instead. Furthermore, the applicability of this method to V0 particles and cascades is valid and such studies will be presented in an upcoming publication.

### 8.2.4 Monte Carlo Closure Test

To validate the correction procedure based on the Bayesian unfolding method described in Sec. 8.2.1, one performs a “Monte Carlo closure test”, defined as the ratio between the unfolded and the true distributions. Thus, if the method were perfect, one would expect a ratio centred at one. However, for these studies, one commonly observes deviations from unity up to 5%. The top panel of Fig. 8.17 shows the uncorrected, unfolded and true  $N_T$  probability distributions. The bottom panel of Fig. 8.17 shows the Monte Carlo closure test. The closure test shows that the unfolding method works fine from  $N_T = 0$  to  $N_T \approx 20$ . Above this value, statistical fluctuations in the distributions and the response matrix become significant. Fig 8.18 shows the closure tests of the  $p_T$  spectra of  $\pi$ , K and p in the toward and transverse regions. The correction procedure works fine within 5% at low  $p_T$  ( $\pi$ , K and p are measured from 0.3, 0.3 and 0.45 GeV/c, respectively) in both regions. Furthermore, the agreement between the unfolded and true distributions improve towards higher  $p_T$  values.

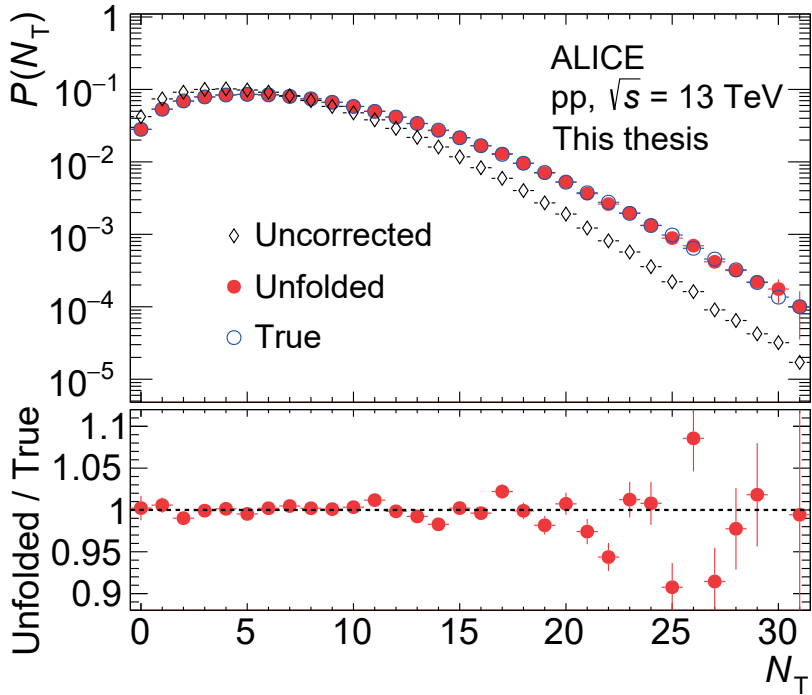


**Figure 8.17:** (Top panel) Uncorrected, unfolded, and true  $N_T$  probability distributions as a function of  $N_T$ . (Bottom panel) Monte Carlo closure test.

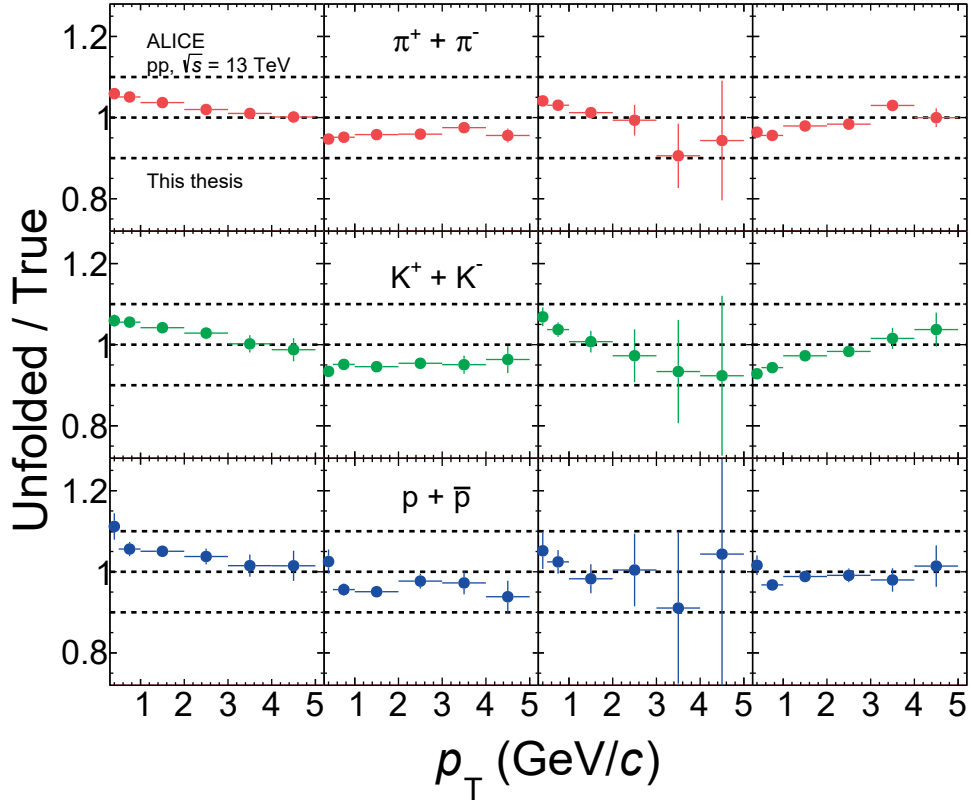


**Figure 8.18:**  $p_T$  spectra Monte Carlo closure test. The results for  $\pi$ ,  $K$  and  $p$  are shown in the top, middle and bottom rows, respectively. Only results in the toward (first two columns) and transverse regions (last two columns) for two  $R_T$  classes are shown:  $0 \leq R_T < 0.5$  (first and third columns) and  $1.5 < R_T < 2.5$  (second and fourth columns). The uncertainty bars in the data points represent only the statistical uncertainty.

## 8.3 Unweighted Transverse Spherocity

The Transverse Spherocity ( $S_0$ ) [123, 124] is used to characterise events based on the geometrical distribution of the azimuthal angle of the particles. In other words,  $S_0$  tells us information about the geometrical shape in the transverse plane of the particles emerging from the collision. To some degree, the event topology reflects the primary mechanism of particle production. For example, events dominated by a single hard scattering will show pronounced back-to-back jet structures like in Fig. 8.19. In contrast, a more isotropic topology will characterise events dominated by several soft scatterings.  $S_0$  is defined in the transverse plane for a unit transverse vector  $\hat{\mathbf{n}}$  which minimises the ratio:

$$S_0 = \frac{\pi^2}{4} \left( \frac{\sum_i \vec{p}_{Ti} \times \hat{\mathbf{n}}}{\sum_i p_{Ti}} \right), \quad (8.22)$$

The range of  $S_0$  lies in the interval  $[0, 1]$ . Thus, in this analysis, I study the following two limits:

$$S_0 = \begin{cases} 0, & \text{"jetty-like" limit} \\ 1, & \text{"isotropic" limit} \end{cases}. \quad (8.23)$$

In this thesis, I use a slightly different definition of  $S_0$ . I use the Unweighted Transverse Spherocity ( $S_0^{p_T=1}$ ), defined as follows:

$$S_0^{p_T=1} = \frac{\pi^2}{4} \left( \frac{\sum_i \widehat{p}_{Ti} \times \hat{\mathbf{n}}}{N_{\text{tracks}}} \right), \quad (8.24)$$

where  $\widehat{p}_{Ti}$  is a unit vector and  $N_{\text{tracks}}$  is the number of charged-particles used to measure  $S_0^{p_T=1}$ . The motivation to use  $S_0^{p_T=1}$  is the following. The top-left and bottom-left panels of Fig. 8.20 represent a jet. The only difference between the two is that the leading particle in the first case is a  $\pi^-$  while in the second case, it is a  $\pi^0$ . However, due to the  $p_T$ -weight in Eq. 8.22 and the fact that  $S_0$  is computed only with charged particles,  $S_0$  will yield two completely different topologies. This effect is known as the neutral jet bias. In contrast,  $S_0^{p_T=1}$  will describe similar topologies whether the leading particle is charged or neutral; see the top-right and bottom-right panels from Fig. 8.20.

Figure 8.21 shows the generated and measured  $S_0^{p_T=1}$  distributions simulated with PYTHIA 8 Monash 2013 tune. The red and blue shaded areas correspond to 20% of the most jetty

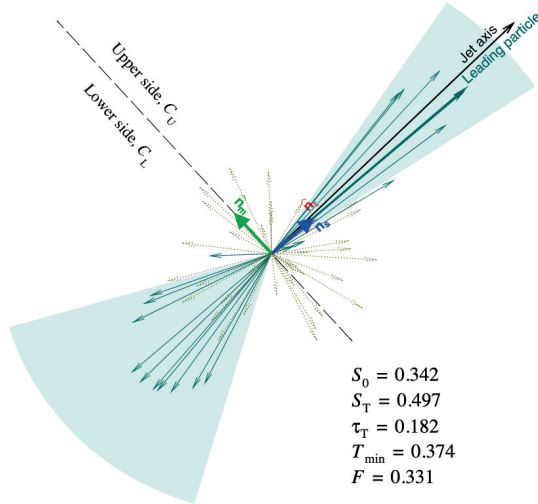


**Figure 8.19:** Sketch of a back-to-back jet. Solid lines represent particles within the jet. Dashed arrows represent particles from the UE. The unitary  $\hat{\mathbf{n}}$  vector is represented with the blue arrow. For this event, the value of  $S_0$  is equal to 0.345. The figure was taken from Ref. [124]

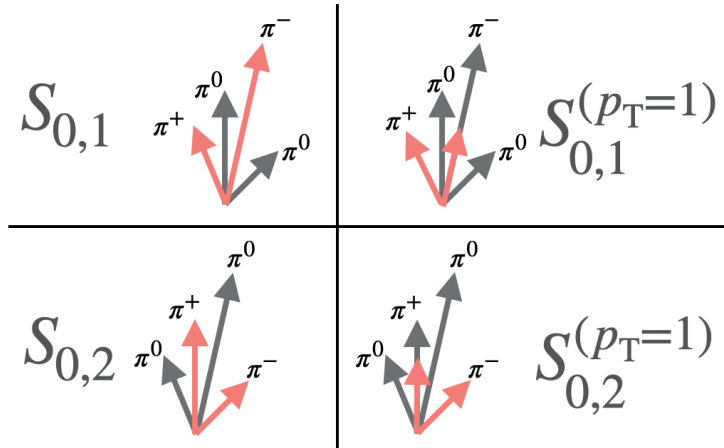


**Figure 8.20:** The top-left and bottom-left panels represent a jetty event reconstructed with the definition of  $S_0$ . The top-right and bottom-right panels represent the same jetty event reconstructed with  $S_0^{p_T=1}$ .

and isotropic events, respectively. The quantiles are estimated using the measured distribution.

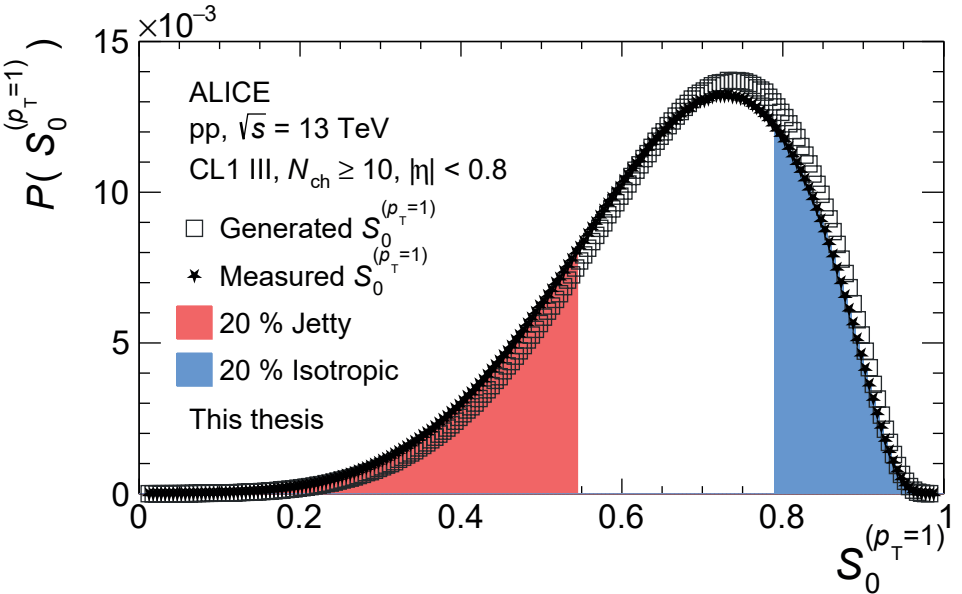


**Figure 8.21:** The generated and measured  $S_0^{p_T=1}$  distributions simulated with PYTHIA 8 Monash 2013 tune. The red and blue areas correspond to 20% of the most jetty and isotropic reconstructed events. The percentiles are estimated using the measured distribution.

### 8.3.1 High-Multiplicity Studies

As described above,  $S_0^{p_T=1}$  can disentangle between jet-like and isotropic topologies and it reduces the effects of the neutral jet bias. Henceforth, I will use the term, Sphericity to unambiguously refer to  $S_0^{p_T=1}$ .

The analysis presented in this thesis describes the measurement of particle production as a function of  $S_0^{p_T=1}$  in high-multiplicity events. High-multiplicity events are selected using two multiplicity estimators covering different pseudorapidity regions. The former is based on the activity recorded in the V0 detector (see Sec. 6.2.1), i.e., a forward multiplicity estimator and its event multiplicity classes are referred to as V0M multiplicity classes. The second multiplicity estimator is based on the number of tracklets reconstructed in  $|\eta| < 0.8$  using the SPD detector. A tracklet is a line segment reconstructed using two hits in the SPD detector where each hit comes from one of the two layers of the SPD. The event multiplicity classes using the SPD detector are be referred to as  $N_{\text{SPD}}$  multiplicity classes.

The high-multiplicity definition corresponds to the 10 % percentile of events containing

the largest number of SPD tracklets or the largest V0 amplitude. This definition is extended to cover also smaller percentages, such as 1 %. The smaller percentages are also colloquially referred to as “high-multiplicity”, however each of the results will explicitly state which quantile cut is used. The convention when referring the top 1 % high-multiplicity events using the V0 and SPD detectors, is to label them as V0M I or  $N_{\text{SPD}} \text{ I}$ , respectively. Similarly, the multiplicity class with the top 10 % high-multiplicity events are labeled as V0M III or  $N_{\text{SPD}} \text{ III}$ .

### 8.3.2 Spherocity Cuts

This analysis has two degrees of freedom: multiplicity and spherocity, which leads to several multiplicity and spherocity classes and combinations among them. For example, some of the combinations are listed below:

- $N_{\text{SPD}} \text{ III}$  and 10 % most jet-like and isotropic events.  
This cut sets the baseline with enough statistics to show smooth  $p_T$  spectra shapes for each particle species.
- $N_{\text{SPD}} \text{ III}$  and 1 % most jet-like and isotropic events.  
This selection is particularly interesting to study particle production in extreme topologies.
- V0M I ( $N_{\text{SPD}} \text{ I}$ ) and 10 % most jet-like and isotropic events.  
This selection can be used to contrast results of the forward and mid-pseudorapidity multiplicity estimators.

In this analysis, I studied four spherocity selections, the top 1 %, 5 %, 10 % and 20 % jet-like and isotropic events, two multiplicity classes, top 1 % and 10 % and two multiplicity estimators, V0M and  $N_{\text{SPD}}$ . This yields twenty combinations between spherocity and multiplicity, however when presenting the results, I will focus on the multiplicity classes V0M I and  $N_{\text{SPD}} \text{ I}$  and the 1 % most jet-like and isotropic events. The remaining results will be shown in the Appendix.

### 8.3.3 Evaluation of the Experimental Bias

Similar to the  $R_T$  analysis, I have performed Monte Carlo closure tests to investigate the existence of experimental biases. Let  $S_{0,\text{rec}}^{p_T=1}$  and  $S_{0,\text{gen}}^{p_T=1}$  be the spherocity distributions obtained from Monte Carlo reconstructed and generated data, respectively. Figure 8.21 shows the reconstructed and generated spherocity probability distributions. Since not

all the generated particles can be reconstructed,  $S_{0,\text{rec}}^{p_{\text{T}}=1}$  and  $S_{0,\text{gen}}^{p_{\text{T}}=1}$  will be different. Furthermore, the jetty and isotropic cuts will depend on which distribution is used. For example, a jetty cut using the  $S_{0,\text{rec}}^{p_{\text{T}}=1}$  distribution will be lower than the one obtained from using the  $S_{0,\text{gen}}^{p_{\text{T}}=1}$  distribution. This is expected due to the bin-migration effect attributed to efficiency losses.

Let  $\text{SP}_{\text{rec}}$  and  $\text{SP}_{\text{gen}}$  be the reconstructed and true spherocity-dependent  $p_{\text{T}}$  spectra obtained from Monte Carlo, for a specific particle specie, respectively. As mention previously, the  $\text{SP}_{\text{rec}}$  and  $\text{SP}_{\text{gen}}$  for jetty and isotropic events can be defined in several ways since there are different spherocity cuts available. For example,  $\text{SP}_{\text{rec-rec}}$  is the reconstructed  $p_{\text{T}}$  spectrum using the spherocity cut from the  $S_{0,\text{rec}}^{p_{\text{T}}=1}$  distribution. In contrast,  $\text{SP}_{\text{rec-gen}}$  is the reconstructed  $p_{\text{T}}$  spectrum using the spherocity cut from the  $S_{0,\text{gen}}^{p_{\text{T}}=1}$  distribution. Table 8.2 shows the different combinations between  $p_{\text{T}}$  spectra and spherocity cuts.

**Table 8.2:** Relation between reconstructed and true spectra and spherocity cuts.

	$S_{0,\text{rec}}^{p_{\text{T}}=1}$	$S_{0,\text{gen}}^{p_{\text{T}}=1}$
$\text{SP}_{\text{rec}}$	$\text{SP}_{\text{rec-rec}}$	$\text{SP}_{\text{rec-gen}}$
$\text{SP}_{\text{gen}}$	$\text{SP}_{\text{gen-rec}}$	$\text{SP}_{\text{gen-gen}}$

Equation 8.25 defines the experimental bias. However, before performing the ratio, the  $p_{\text{T}}$  spectrum in the numerator is corrected for reconstruction inefficiency. Here, the minimum-bias tracking efficiency is used. The assumption is that, since the TPC of ALICE is designed to cope with much larger track densities achieved in Pb–Pb collisions compared to the ones obtained in pp collisions, the reconstruction efficiency of each particle specie should be independent of the multiplicity or spherocity selection.

$$\text{EB} = \frac{\text{SP}_{\text{rec-X}}}{\text{SP}_{\text{gen-X}}} . \quad (8.25)$$

First, the experimental bias ratio is computed using the spherocity cuts obtained from the  $S_{0,\text{rec}}^{p_{\text{T}}=1}$  distribution, for both,  $\text{SP}_{\text{rec}}$  and  $\text{SP}_{\text{gen}}$ . Figure 8.22 shows the EB ratio evaluated for the 1 % most jet-like and isotropic events, where a significant non-closure is seen for jetty events. The non-closure originates from using a fixed value calibrated on the  $S_{0,\text{rec}}^{p_{\text{T}}=1}$  distribution. Using independently calibrated quantiles for the reconstructed and generated event samples, respectively, the two event selections are equivalent and the non-closure is removed as seen in Fig. 8.22. The caveat here is that the  $p_{\text{T}}$  spectra as a function of  $S_0^{p_{\text{T}}=1}$  are presented in quantiles. That means that for model comparisons, the jetty and isotropic quantiles have to be calibrated for each specific Monte Carlo generator.

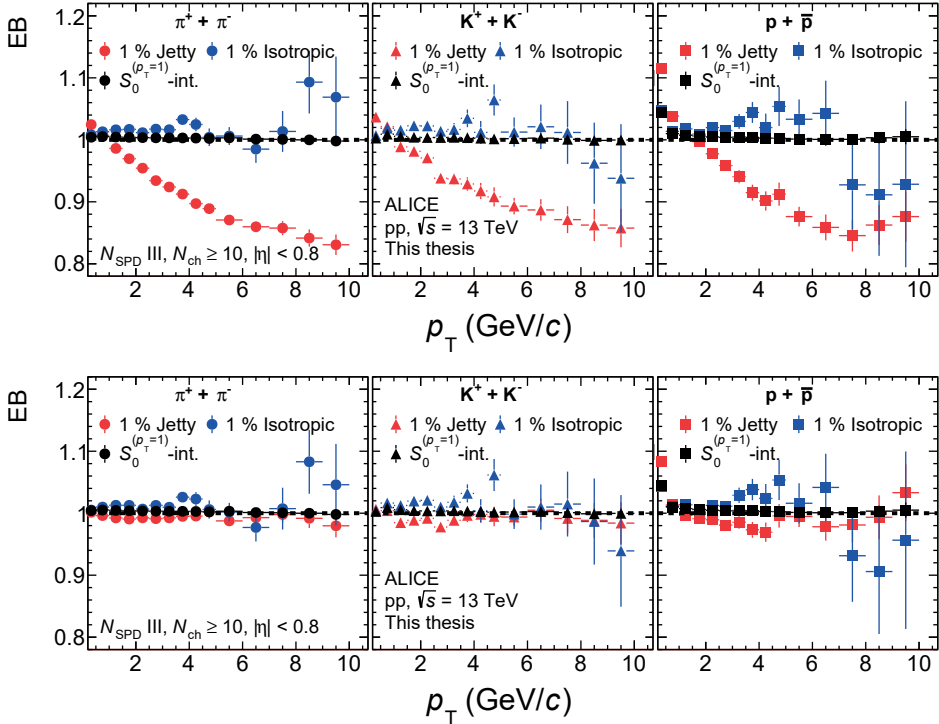


**Figure 8.22:** Experimental Bias ratio. The ratio is between the reconstructed and generated  $p_T$  spectra. The ratios are shown for the most 1 % jet-like and isotropic and  $S_0^{pT=1}$ -integrated selections. The top figure shows the results from using fixed spherocity cuts using the  $S_0^{pT=1}$  distribution. The bottom figure shows the results from using spherocity cuts relative to the reconstructed and true  $S_0^{pT=1}$  distributions. The multiplicity class corresponds to  $N_{SPD}$  III in both cases and the results for  $\pi$ ,  $K$  and  $p$  are shown from left to right.

# Chapter 9

## Systematic Uncertainties

This chapter describes the evaluation of the systematic uncertainties on the  $p_T$  spectra. First, I will describe the evaluation of the uncertainties on the signal extraction in the TPC, TOF and rTPC analyses.

### 9.1 PID Systematic Uncertainties

#### TPC Analysis

I studied the sources of systematic uncertainty associated with signal extraction and the secondary particle contamination correction estimation.

- Signal extraction. The method to extract the yield change from fitting  $n\sigma$  distributions to bin counting in the interval  $\pm 3 n\sigma$  (see Fig. 8.1).
- Secondary particle contamination. The fit range in the multi-template fit to the  $DCA_{xy}$  distributions described in Sec. 8.1.3 changed from  $\pm 3$  cm to  $\pm 1$  cm (see Fig. 8.12).

#### TOF Analysis

The systematic uncertainty related to the signal extraction in the TOF analysis is mainly driven by the imprecise description of the parameterisation of the  $\mu$ ,  $\sigma$  and  $\tau$  curves for

$\pi$ , K and p used during the fitting procedure (see Sec. 8.1.1). Hence, the method adopted to estimate this uncertainty summarises as follows:

1. I measured the relative difference between the parameterisations (see Fig. 8.2) and  $\mu$ ,  $\sigma$  and  $\tau$  values. Figure 9.1 shows the relative differences measured in the four  $|\eta|$ -intervals (represented with black markers). The plots are produced using all the data points from  $\pi$ , K and p. The differences between data points and the  $\mu$  parameterisation are mostly negligible. However, for  $\sigma$  and  $\tau$  parameterisations, there are deviations of up to 3% and 10%, respectively, depending on the  $\beta$  interval.

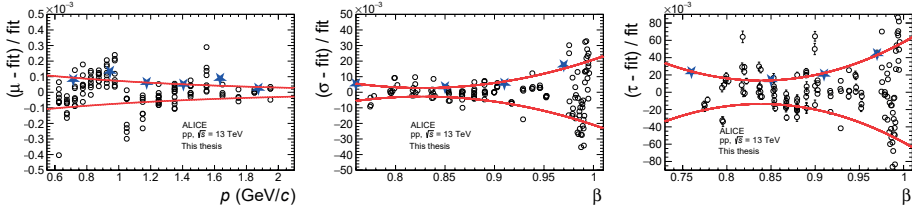


**Figure 9.1:** The relative difference between data points and parameterisations. The relative deviations in the  $\mu$ ,  $\sigma$  and  $\tau$  parameterisations are shown in the left, middle and right figures. The red stars represent the RMS values in different intervals of  $p$  or  $\beta$ . The continuous red line represents a fit to the red stars.

2. To parameterise the variations, I used the correlation between the RMS of the relative variation of  $\mu$ ,  $\sigma$  and  $\tau$  as a function of  $p$  and  $\beta$ , respectively. Figure 9.1 represents the RMS values with red stars. Then, to describe the overall behaviour of the RMS values, the red stars are fitted. The fits are represented with red curves. Finally, the parameterised variations represent the systematic uncertainty of the  $\mu$ ,  $\sigma$  and  $\tau$  parameterisations.
3. The uncorrected particle fractions are measured in each of the  $|\eta|$ -intervals following the standard procedure described in Sec. 8.1.1. However, the fit parameters:  $\mu$ ,  $\sigma$  and  $\tau$  for each species are randomly varied using the curves described in bullet 2. The variation of the parameters is based on the equation (example for  $\mu$ ):

$$\mu = \mu_{\text{NM}} + \alpha \cdot \text{VA} , \quad (9.1)$$

where  $\alpha$  is a random number drawn from a Normal distribution with  $\mu = 0$  and  $\sigma = 1$ , and VA is obtained from evaluating the parameterised variations at the centre of a given  $p$  bin. It is essential to mention that the random number is

different for each fitting parameter. Furthermore, the measurement of the particle fraction was repeated 1000 times.

4. The RMS of the particle fractions distribution represents the systematic uncertainty in a given  $p$ -bin. Then, the  $p$ -dependent RMS is converted to  $p_T$ -dependent using the method described in Sec. 8.1.2.
5. Finally, for each  $p_T$ -interval, the maximum RMS ( $\text{RMS}_{\max}$ ) among the four  $|\eta|$ -intervals is assigned as the systematic uncertainty associated to the signal extraction method.

Furthermore, the systematic uncertainty related to the secondary particle contamination correction estimation was included. This uncertainty was obtained using the method described above for the TPC analysis.

## rTPC Analysis

The imprecise description of both, the Bethe-Bloch and resolution curves account for the most significant source of systematic uncertainty in the rTPC analysis since in the fitting of  $dE/dx$  distributions in  $p$  intervals, the fitting parameters ( $\langle dE/dx \rangle$  and  $\sigma_{dE/dx}$ ) for each of the particle species are fixed. Similar to the TOF analysis, the imprecise description of the Bethe-Bloch and resolution curves is quantified by the relative difference between the  $\langle dE/dx \rangle$  ( $\sigma_{dE/dx}$ ) and the Bethe-Bloch (resolution) parameterisation as a function of  $\beta\gamma$  ( $\langle dE/dx \rangle$ ), see Fig. 8.5. Figure 9.2 shows the relative difference using the four  $|\eta|$ -intervals and all the PID data. To parameterise the variations, I used the correlation between the RMS of the relative variation of  $\langle dE/dx \rangle$  and  $\sigma_{dE/dx}$  in intervals of  $\beta\gamma$  and  $\langle dE/dx \rangle$ , respectively. The RMS values are represented with red stars in Fig. 9.2. The overall behaviour of the RMSs is described with a fit to the RMS values. The fit is represented with the red curves in Fig. 9.2

Once the systematic uncertainty on the Bethe-Bloch and resolution curves is measured, I repeated the procedure described in bullets 3, 4 and 5 from above. Namely, the particle fractions are measured 1000 times, varying the fitting parameters randomly within the red curves of Fig. 9.2 using Eq. 9.1. The RMS of the particle fraction distribution is taken as systematic uncertainty in the  $p$ -bin. Then, the  $p$ -dependent RMS is converted to  $p_T$ -dependent and finally, for each  $p_T$  interval, the  $\text{RMS}_{\max}$  among the four  $|\eta|$ -intervals is assigned as the systematic uncertainty.

Due to the slight separation between the signal of  $\pi$  and K in the relativistic rise, some kaons may be misidentified as pions (and vice-versa). In addition, the particle fractions

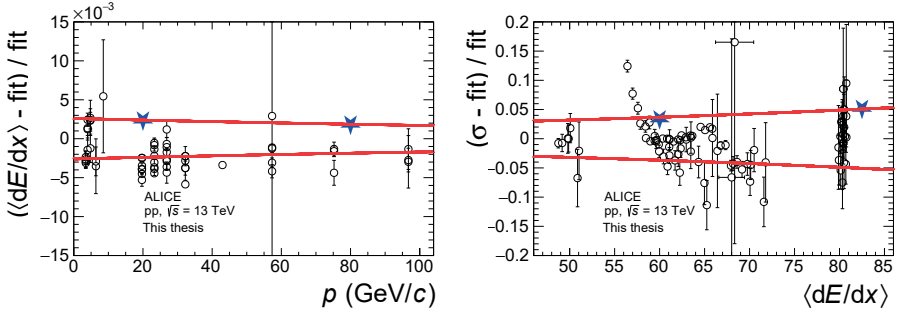


**Figure 9.2:** Relative difference between measured  $\langle dE/dx \rangle$  ( $\sigma_{dE/dx}$ ) and Bethe-Bloch (resolution curves) as a function of  $\beta\gamma$  ( $\langle dE/dx \rangle$ ) represented with black markers. Red star markers represent the RMS of the variations. The solid red lines indicate the fits to the RMS values.

of K and p are fully anti-correlated. This means that measuring a more significant fraction of K will lead to a minor fraction of p. Thus, there is a method for evaluating the  $p_T$ -differential  $K/\pi$  and  $p/\pi$ . The procedure is the following: the particle ratios are directly extracted from the fits. Then the systematic uncertainty on the parameterisations is propagated to the ratios by varying the  $\langle dE/dx \rangle$  and  $\sigma_{dE/dx}$  as described above. Following this procedure, the correct correlations are taken into account. Figure 9.3 shows the systematic uncertainty on the  $K/\pi$  and  $p/\pi$  ratios.

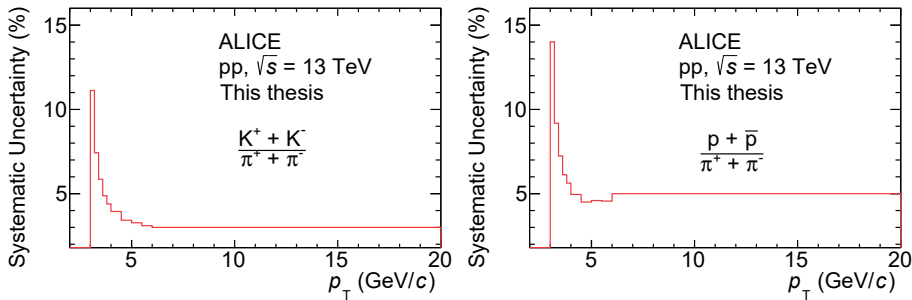


**Figure 9.3:** Systematic uncertainty on the  $K/\pi$  (left) and  $p/\pi$  (right) as a function of  $p_T$ . The results are shown for minimum-bias collisions.

## 9.2 Tracking Uncertainties

I studied the effect of varying the parameters of the track selection criteria. In the Spherocity analysis, the parameters are changed only for the Global tracks (see Sec. 7.3).

Table 9.1 lists the “Lower” and “Higher” variations. Since simulated events are used to calculate the corrections and since the selection criteria are the same for data and Monte Carlo, thus, the same variations are applied to both. For each variation, the fully corrected  $p_T$  spectra are obtained. Then, the nominal  $p_T$  spectrum was compared with the Lower and Higher  $p_T$  spectra for each parameter. Finally, the maximum difference between Lower and Higher was assigned as the systematic uncertainty. The same variations are applied to the Global tracks in the Transverse Activity analysis. In this analysis, I also studied the effect of using different selection parameters to reconstruct the leading charged track. Table 9.1 also lists such variations.

**Table 9.1:** Table of varied parameters to a lower and higher value with respect to the nominal one.

Parameter	Nominal	Lower	Higher
Crossed rows in TPC	70	60	80
Max. $\chi^2/N_{\text{TPC,cl}}$	4	-	5
Max. DCA <sub>z</sub> (cm)	2	1	3
Leading track			
Geo. length (dead TPC area)	2	4	3
Geo. length (track length)	120	140	130

### 9.3 $R_T$ and $S_0^{p_T=1}$ Dependent Systematic Uncertainties

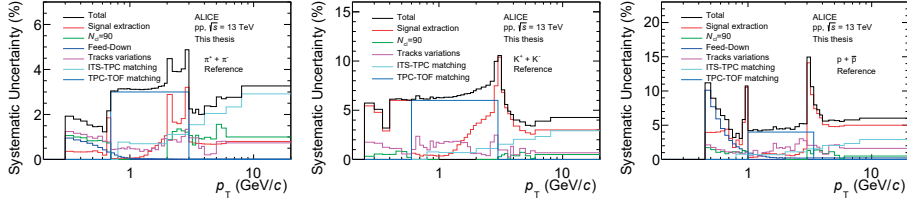
In Sec. 8.2.4, I described how the Monte Carlo closure test could be used to evaluate the performance of the correction method employed, in this case, the Bayesian unfolding one. By comparing the unfolded  $p_T$  spectra as a function of  $R_T$  with the true  $p_T$  spectra, one can assess the method’s reliability. Such Monte Carlo closure tests are shown in Fig. 8.18. Therefore, the systematic uncertainty associated with the correction method is derived from the unfolded-to-true ratio of the  $p_T$  spectra.

Like the  $R_T$  analysis, one can assign a systematic uncertainty associated with the sphericity selection. Thus, I used the Monte Carlo closure tests discussed in Sec. 8.3.3. However, based on the ratios between the true and corrected  $p_T$  spectra of Fig. 8.22, it was concluded that when using  $S_0^{p_T=1}$  quantiles, the systematic uncertainty associated with the  $S_0^{p_T=1}$  selection is negligible.

## Additional Sources of Systematic Uncertainty

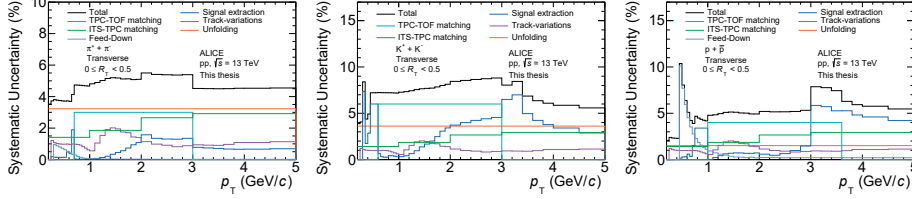
Additional systematic uncertainty sources common to the  $R_T$  and  $S_0^{p_T=1}$  analyses are associated with the ITS-TPC and TPC-TOF matching efficiencies. These values are taken over from [125].

Figure 9.4 shows the systematic uncertainties on the  $S_0^{p_T=1}$ -integrated  $p_T$  spectra of  $\pi$ , K and p. The total systematic uncertainty is given by the sum in quadrature of the different components.



**Figure 9.4:** Total systematic uncertainty on the  $p_T$  spectra of  $\pi$  (left), K (middle) and p (right). The results are shown for the  $S_0^{p_T=1}$ -integrated class.

Figure 9.5 shows the systematic uncertainties on the  $p_T$  spectra of  $\pi$ , K and p in the transverse region for the  $0 \leq R_T < 0.5$  class. The total systematic uncertainty is given by the sum in quadrature of the different components.



**Figure 9.5:** Total systematic uncertainty on the  $p_T$  spectra of  $\pi$  (left), K (middle) and p (right). The results are shown for the transverse region in the  $0 \geq R_T < 0.5$  class.

# Chapter 10

## Results and Discussion

This chapter presents the measurements on the production of  $\pi = (\pi^+ + \pi^-)$ ,  $K = (K^+ + K^-)$  and  $p = (p + \bar{p})$  in pp collisions at  $\sqrt{s} = 13$  TeV as a function of the UE activity using the Relative Transverse Activity Classifier,  $R_T$  and as a function of the Unweighted Transverse Spherocity,  $S_0^{p_T=1}$ . To deliver a comprehensive physics interpretation of the results, in Sec. 10.1, I will focus first on describing the results as a function of  $R_T$ . Then, in Sec. 10.2, I present the measurements as a function of  $S_0^{p_T=1}$ . Furthermore, the data results are compared with calculations from Monte Carlo models commonly used for pp collisions at the LHC: PYTHIA 8 Monash 2013 tune [126], PYTHIA 8 Rope Hadronization [127], Herwig [128, 129] and EPOS LHC [82]. The kinematic domain and the multiplicity selections are the same for Monte Carlo and data, dividing the events sample into classes based on the total charged-particle multiplicity in the forward (V0M) and in the mid-pseudorapidity ( $N_{\text{SPD}}$ ) acceptances.

### 10.1 Production of $\pi$ , $K$ and $p$ as a Function of the UE Activity

It is well established that average standard UE observables such as the charged-particle number density,  $N_{\text{ch}}/\Delta\eta\Delta\varphi$ , measured in the transverse region in triggered-events as a function of the  $p_T^{\text{leading}}$  (see Fig. 8.14 for the definition of the transverse region) saturate for  $p_T^{\text{leading}} \gtrsim 5$  GeV/c. This saturation region is the UE plateau (see Fig. 8.13) and has been measured in pp collisions over a wide range of collision energies [118, 119, 130, 131].

Figure 10.1 shows the unfolded charged-particle multiplicity distribution in the trans-

verse region  $N_T$  measured in events with a leading charged-particle track. This broad distribution implies a large dynamic range between transverse region activities significantly larger or smaller than the  $\langle N_T \rangle$ . This further implies that the rich dynamics are typically hidden in standard average UE observables studies. Thus, I use the Relative Transverse Activity Classifier,  $R_T = N_T / \langle N_T \rangle$  [121] as a variable that allows the study of identified particle production as a function of the UE activity (the  $R_T$  analysis is described in Sec. 8.2). The leading particle is defined on a per-event basis as the most energetic charged-particle track with  $5 \leq p_T < 40 \text{ GeV}/c$ . The associated particles are measured in the  $p_T$  interval  $0.15 - 5 \text{ GeV}/c$ . Both leading and associated particles are reconstructed in  $|\eta| < 0.8$ . Table 10.1 gives the relation between  $N_T$  classes and  $R_T$  intervals. The definition of the  $R_T$  intervals uses the unfolded  $N_T$  distribution with an  $\langle N_T \rangle = 7.366 \pm 0.002 \text{ (stat.)}$ . The third column of the table presents the number of events to which the  $p_T$  spectra of  $\pi$ , K, and p are normalised. These values are obtained by integrating the unfolded  $N_T$  spectrum.

**Table 10.1:** Relation between  $R_T$  intervals and  $N_T$  values. The definition of  $R_T$  uses the unfolded  $N_T$  spectrum. This is true also for calculating the number of events to which the  $p_T$  spectra are normalised.

$R_T = N_T / \langle N_T \rangle$	$N_T$	Number of events	Median $N_T$
[0, 0.5)	[0, 3]	2613151	1.5
(0.5, 1.5)	[4, 11]	4055410	7.5
(1.5, 2.5)	[12, 18]	1302116	15
(2.5, 5.0)	[19, 30]	180652	24.5
[0.0, 5.0)	[0, 30]	8151331	15

Figure 10.1 shows the unfolded  $R_T$  probability distribution in the transverse region integrated over all the events with a leading charged-particle track. The dashed vertical lines in the  $R_T$  distribution define the boundaries for the different  $R_T$  classes. Furthermore, these distributions are compared with model predictions. The  $\langle N_T \rangle$  is obtained from the corresponding distribution for each Monte Carlo model. The  $\langle N_T \rangle$  for PYTHIA 8 Monash, PYTHIA 8 Ropes, EPOS LHC and Herwig are 7.93, 7.88, 8.15 and 6.31, respectively. All the models but Herwig underestimate the low- $N_T$  ( $N_T \lesssim 8$ ) part of the distribution. PYTHIA 8 Monash and PYTHIA 8 Ropes can describe qualitatively better the high-multiplicity ( $N_T \gtrsim 10$ ) data while EPOS LHC (Herwig) overestimate (underestimate) the data at high  $N_T$ . When one computes the  $R_T$  probability distributions with models, it is observed that all of them underestimate the data at high  $R_T$  ( $R_T > 2$ ). The  $\langle N_T \rangle$  is too large due to the low multiplicities being well modelled.

Finally, this  $R_T$  distribution is compared with the one previously published by ALICE [119], where a good agreement is obtained. However, my distribution seems to be shifted to the right with respect to the published result. This can be explained by the fact that in [119], a different data set was used, which yields a slightly different  $\langle N_T \rangle$ .

and hence a somewhat different  $R_T$ .

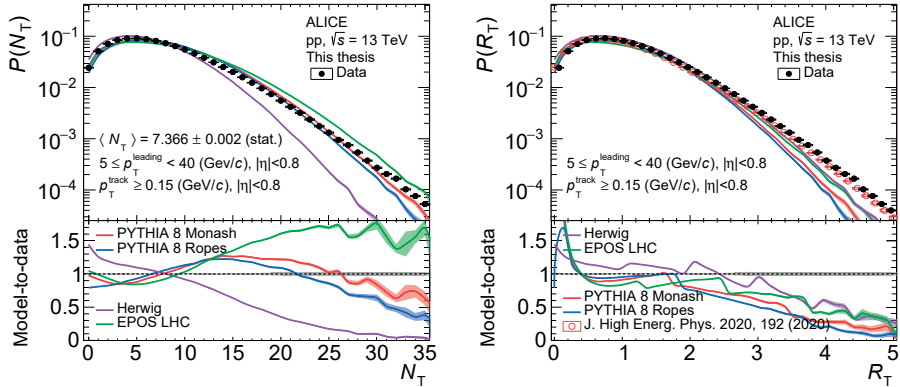


**Figure 10.1:**  $N_T$  (left) and  $R_T$  (right) probability distributions in the transverse region. The data measurements (solid black markers) are compared with different model predictions. The statistical and systematic uncertainties are represented with error bars and boxes around the data points. The statistical uncertainties in the model predictions are described with shaded bands around the model lines. The bottom panels show the model-to-data ratios, and the grey band centred at one corresponds to the sum in quadrature of the statistical and systematic uncertainties.

### 10.1.1 $\langle p_T \rangle$ and $p_T$ -Integrated Particle Ratios

In this section, I describe the average quantities such as the average transverse momentum ( $\langle p_T \rangle$ ) and  $p_T$ -integrated particle ratios as a function of  $R_T$  in the different topological regions. Both quantities are derived from the  $p_T$  spectra. Since the spectra are measured from 300 ( $\pi, K$ ) and 450 ( $p$ ) MeV/c, I extrapolated the measurements down to  $p_T = 0$ . This process is achieved by fitting the spectra with a Lévy-Tsallis parameterisation. The parameterisation is only used in the  $p_T$  intervals where there are no data. Furthermore, since the spectra are integrated up to 5 GeV/c, this procedure is only relevant in the low- $p_T$  region. For example, in the case of  $\pi$ , the fit is used to calculate the yield in the  $p_T$  interval 0 – 300 MeV/c. For the  $0 \leq R_T < 0.5$  interval in the transverse region, the extrapolated yields represent the 38%, 19% and 22% out of the total yield for  $\pi$ ,  $K$  and  $p$ , respectively. Several parameterisations such as the Fermi-Dirac, Bose-Einstein, Blast-Wave and  $m_T$ -exponential are used to estimate the systematic uncertainty associated with the extrapolation procedure. Figure 10.2 shows the fits to the protons spectrum in the transverse region for the  $R_T$ -integrated class. The fit range is restricted to the low- $p_T$  to yield the smallest  $\chi^2/N_{\text{df}}$  values, for this reason, the fit might not be good at high  $p_T$  for some of the parameterisations. Then, the

maximum difference between the nominal and the values obtained from the different parameterisations is assigned as the systematic uncertainty. For example, the systematic uncertainties on the  $dN/dy$  ( $\langle p_T \rangle$ ) amount to 2%(1.7%), 2.7%(2.3%) and 2%(1.5%) for  $\pi$ , K and p, respectively, for the  $0 \leq R_T < 0.5$  bin in the transverse region.

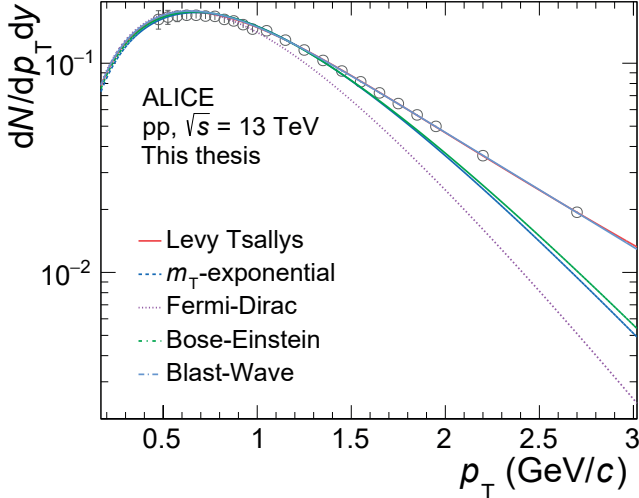


**Figure 10.2:** Examples of fits to the  $p_T$  spectrum of p in the  $R_T$ -integrated class of the transverse region using different parameterisations.

Figure 10.3 shows the  $\langle p_T \rangle$  of  $\pi$ , K and p as a function of  $R_T$  in the different topological regions. In the toward region, the  $\langle p_T \rangle$  of  $\pi$  and K is largest in the  $0 \leq R_T < 0.5$  (low-UE) interval. Also, this is the region where the hard scattering is found with the least UE activity. Hence, the fact that the  $\langle p_T \rangle$  is largest in this  $R_T$  interval compared to higher  $R_T$  results exhibits the presence of the hard scattering that fragments mainly into low-mass hadrons ( $\pi$  and K). Then, the  $\langle p_T \rangle$  is more or less the same for the rest of the  $R_T$  intervals. Furthermore, it can be observed that the values measured in the toward region tend to approach those of the transverse region. At the same time, it can be noticed that the  $\langle p_T \rangle$  of p in low-UE events is lower when compared with the values from high-UE events and that there is a slight increase of its  $\langle p_T \rangle$  with increasing  $R_T$ , possibly due to radial flow. From the model comparisons, it is observed that PYTHIA 8 Monash predicts a large  $\langle p_T \rangle$  in the  $0 \leq R_T < 0.5$  interval for all the particle species and then it tends to flatten out with increasing  $R_T$ . EPOS LHC gives similar predictions to PYTHIA 8 Monash for  $\pi$  and K, and interestingly, this model predicts the evolution of the  $\langle p_T \rangle$  of p with  $R_T$ .

It is essential to mention that the rise of the  $\langle p_T \rangle$  with multiplicity in PYTHIA and

EPOS LHC follows different physics mechanisms. In PYTHIA, the colour reconnection mechanism (see Sec. 4.1) primarily leads to the rise of the  $\langle p_T \rangle$ , while in EPOS LHC, it is associated with radial flow (see Sec. 4.2).

The  $\langle p_T \rangle$  in the transverse area increases with  $R_T$  for all the species; however, the rate of increase exhibits a mass ordering, being largest for heavier particles. While it is true that the  $\langle p_T \rangle$  increases with multiplicity, the rapid rise of the  $\langle p_T \rangle$  of  $\pi$  in this region might be attributed to other effects and not primarily associated with radial flow. It is observed that, in general, all the models qualitatively describe the trends observed in the data. However, none of them can quantitatively describe the data for all the species.

Finally, in the away region, the  $\langle p_T \rangle$  of  $p$  rises over the entire  $R_T$  range while the one of  $\pi$  and  $K$  show a mild dependence on  $R_T$ .

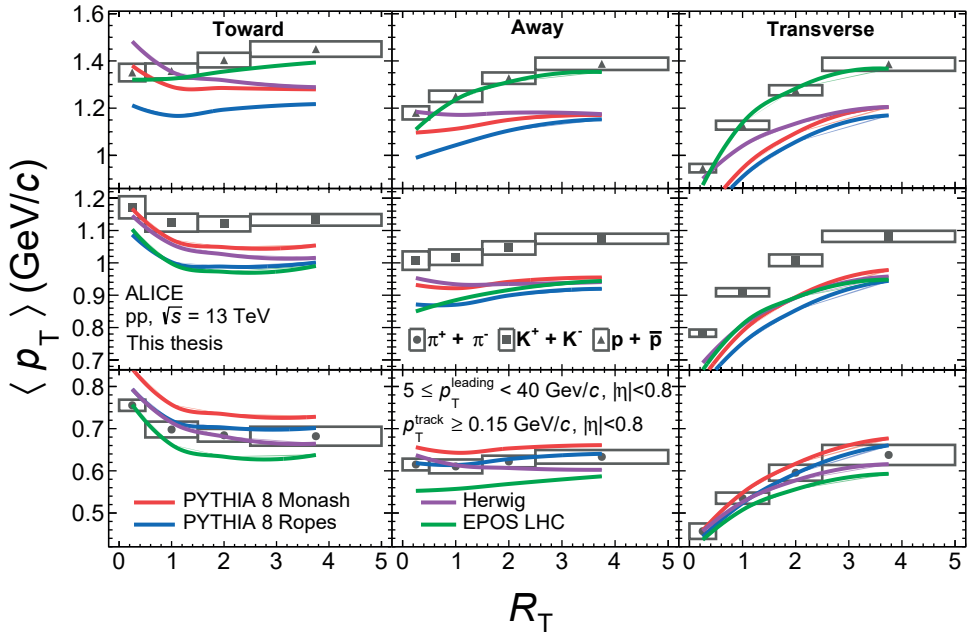


**Figure 10.3:** Average transverse momentum as a function of  $R_T$ . The results from the toward, away, and transverse regions are shown in the left, middle and right columns. The results for  $\pi$ ,  $K$  and  $p$  are shown on the bottom, middle and right row, respectively. Statistical and systematic uncertainties are represented with error bars and boxes around the data points. Model predictions are shown with solid lines and different colours.

Figure 10.4 shows the  $R_T$ -dependence of the  $p_T$ -integrated  $K/\pi$  and  $p/\pi$  ratios and comparisons with model predictions. The  $K/\pi$  and  $p/\pi$  ratios in the transverse region

show a mild increase with increasing UE activity. On the other hand, the  $p/\pi$  ratio in the toward and away regions show a weak decreasing trend with increasing  $R_T$ . The  $K/\pi$  ratios in both the toward and away regions show no significant evolution with  $R_T$ . The comparisons with models in the toward region show that the  $K/\pi$  ratio is qualitatively described by all models, except EPOS LHC, which predicts an increasing  $K/\pi$  ratio with  $R_T$ . At the same time, EPOS LHC and PYTHIA 8 Ropes predict a growing  $p/\pi$  ratio, which is not observed in the data. In the away region, all models predict a mild  $R_T$ -dependence of the  $K/\pi$  ratio; however, it is observed that within systematic uncertainties, the  $K/\pi$  is flat as a function of  $R_T$ . Furthermore, EPOS LHC and PYTHIA 8 Ropes predict a growing  $p/\pi$  ratio in the away region instead of what is observed in the data. Finally, in the transverse region, all the models can reproduce the increasing trend of the  $K/\pi$  and  $p/\pi$  ratios; however, Herwig and PYTHIA 8 Ropes overestimate the  $K/\pi$  and  $p/\pi$  ratios by approximately 10% and 50%, respectively. In contrast, EPOS LHC predicts ratios that are not observed in data.

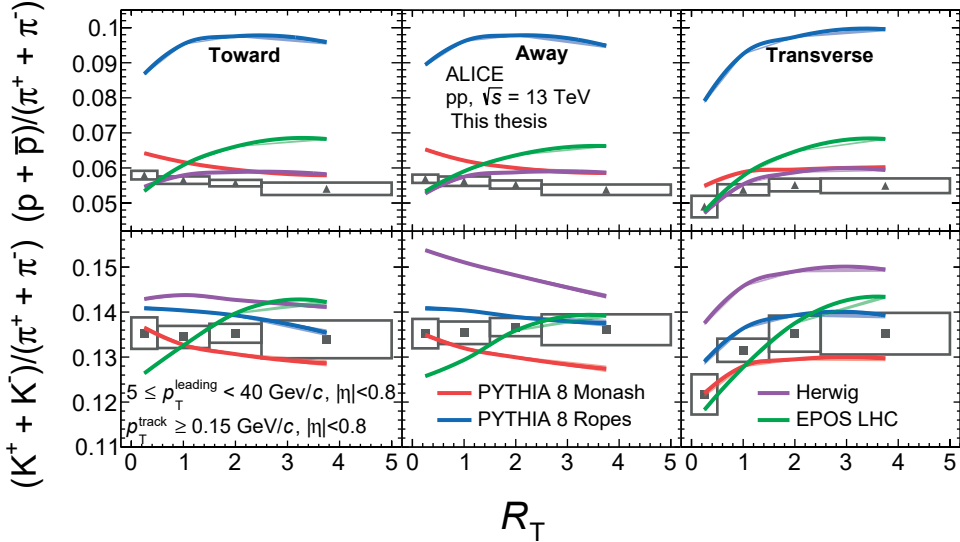


**Figure 10.4:**  $p_T$ -integrated particle ratios as a function of  $R_T$ . The results from the toward, away, and transverse regions are shown in the left, middle and right columns. The top and bottom rows plot the  $p/\pi$  and  $K/\pi$  ratios. The statistical and systematic uncertainties are represented with error bars and boxes around the data points. The model predictions are represented with different line colours.

### 10.1.2 Transverse Momentum Spectra of $\pi$ , K and p

Figures 10.5 to 10.7 show the  $p_T$  spectra of  $\pi$ , K and p as a function of  $R_T$  in the different topological regions. For each particle specie, the results in the toward, away and transverse areas are shown on the left, middle and right panels, respectively. The lower panels display the ratios between the  $R_T$ -dependent  $p_T$  spectra and the  $R_T$ -integrated spectrum. The particle production in the toward and away regions is dominated by the fragmentation of the two outgoing, hard partons and contains many particles with high transverse momentum. The large production of high- $p_T$  particles is observed in the ratios to the  $R_T$ -integrated spectrum in the  $0 \leq R_T < 0.5$  interval (red colour markers) for all the particle species, where one sees an increasing ratio with increasing  $p_T$ . Then, one sees a depletion (enhancement) of low(intermediate)- $p_T$  particles with increasing UE activity. This effect follows a mass ordering, being most significant for protons. This behaviour can be attributed to collective radial flow, boosting low- $p_T$  particles to higher values. At the same time, one observes that the production of particles with  $p_T \gtrsim 2.5 \text{ GeV}/c$  decreases with increasing UE activity for all the particle species. This softening effect of the spectral shapes can be interpreted as the ‘dilution’ of the jet with increasing UE. By dilution, it is meant the following; the jet will always be there, irrespective of  $N_T$ . However, the toward and away regions will be dominated by the UE when  $N_T$  is large. Hence, the jet signal will fade away. On the other hand, the  $p_T$  spectra of all the species in the transverse region share a common feature: they harden with increasing UE activity. This effect might originate from a complex interplay between collective radial flow and contamination by wide-angle radiation off the hard scattering.

Figure 10.8 shows the spectra ratios between models and data for  $\pi$ , K and p in the different topological regions. The comparisons are shown for the two most extreme  $R_T$  bins:  $0 \leq R_T < 0.5$  and  $2.5 < R_T < 5$ . In general, all the models struggle to describe the data measurements; however, it is fair to say that all the models give a good description of the  $\pi$  and K  $p_T$  spectra in the toward region for the  $0 \leq R_T < 0.5$  class. The comparison is within 20 % for all the models. EPOS LHC is the only one that gives a good qualitative description of the p spectra, although it underestimates the data measurements. The fact that models describe the low-UE  $p_T$  spectra in the toward region is expected since the models are tuned to  $e^+e^-$  data. In the transverse region and for the  $0 \leq R_T < 0.5$  interval underpredict the data for  $p_T \gtrsim 1.5 \text{ GeV}/c$ . Finally, the comparisons in the  $2.5 < R_T < 5$  interval show large deviations from unity for all the species and the three topological regions. These model comparisons show what models can describe better (low-UE events) and what they fail at modelling, high-UE. In conclusion, the results presented in this thesis can be useful for Monte Carlo tuning.

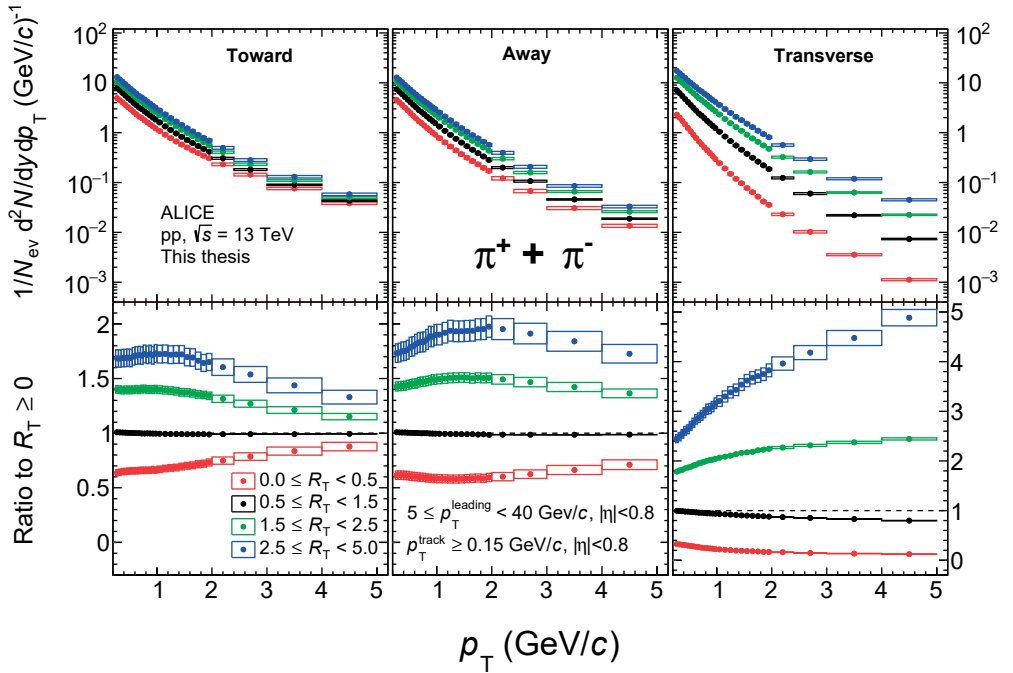


**Figure 10.5:**  $p_T$  spectra (top panels) of  $\pi$  and ratios (bottom panels) to the  $R_T$ -integrated spectrum as a function of  $R_T$  in the different topological regions. The statistical and systematic uncertainties are represented with bars and boxes around the data points. The vertical axes on the left correspond to the results from the toward and away regions, while the right axes correspond to the transverse region's.

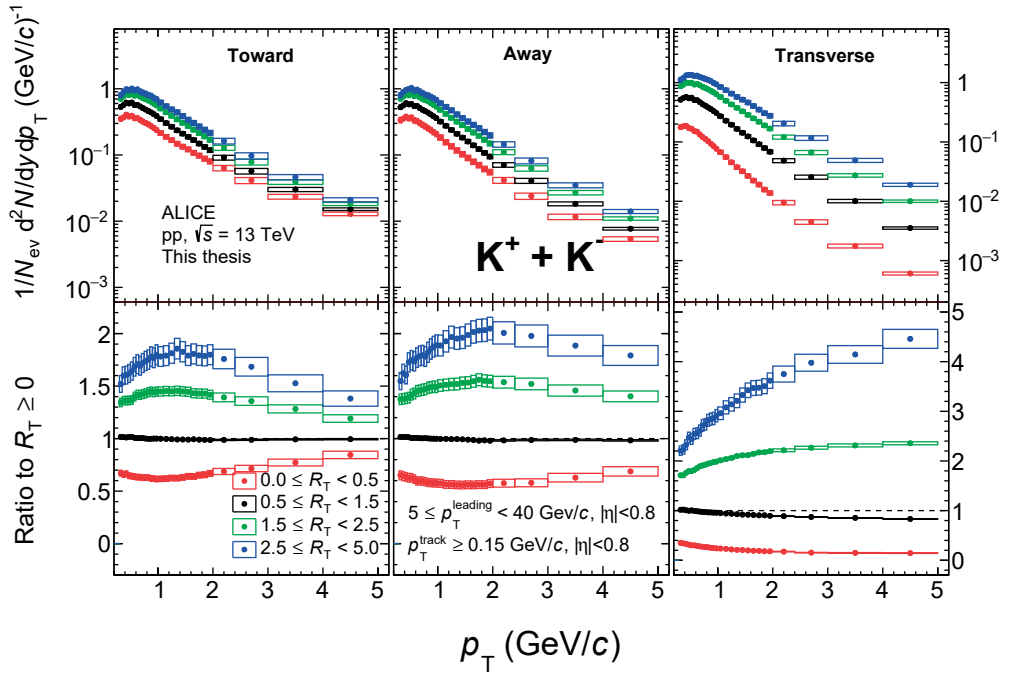


**Figure 10.6:**  $p_T$  spectra (top panels) of  $K$  and ratios (bottom panels) to the  $R_T$ -integrated spectrum as a function of  $R_T$  in the different topological regions. The statistical and systematic uncertainties are represented with bars and boxes around the data points. The vertical axes on the left correspond to the results from the toward and away regions, while the right axes correspond to the transverse region's.

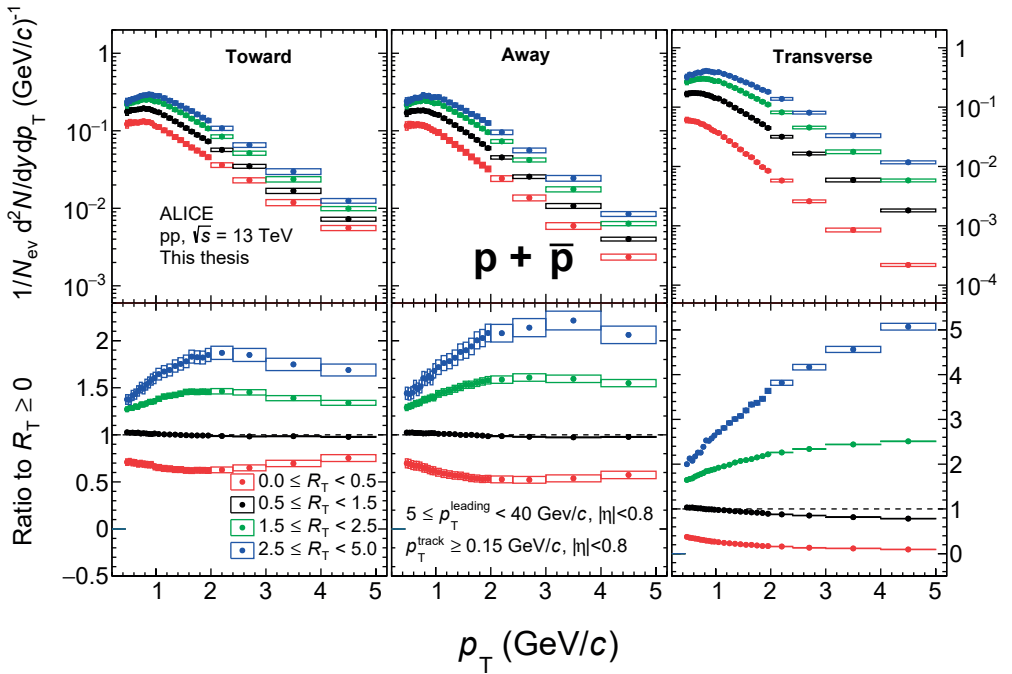


**Figure 10.7:**  $p_T$  spectra (top panels) of  $p$  and ratios (bottom panels) to the  $R_T$ -integrated spectrum as a function of  $R_T$  in the different topological regions. The statistical and systematic uncertainties are represented with bars and boxes around the data points. The vertical axes on the left correspond to the results from the toward and away regions, while the right axes correspond to the transverse region's.

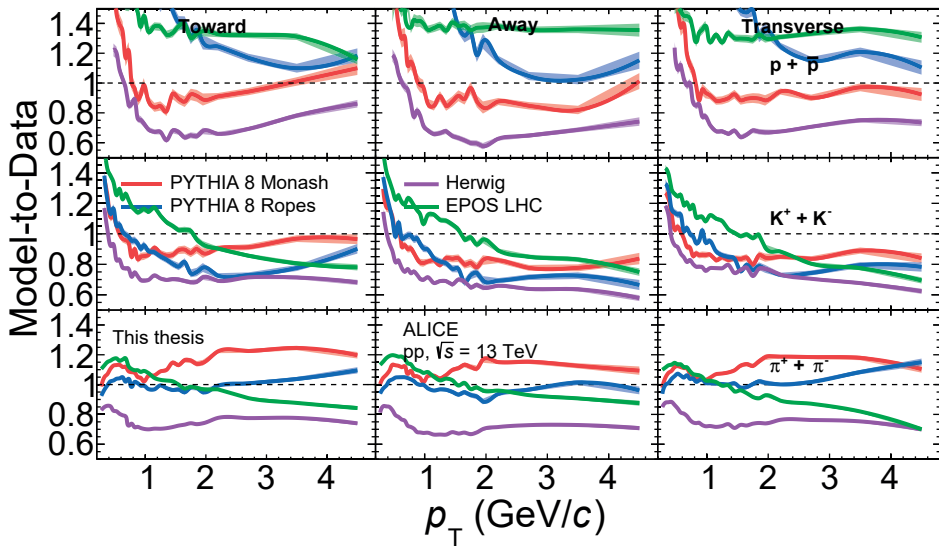
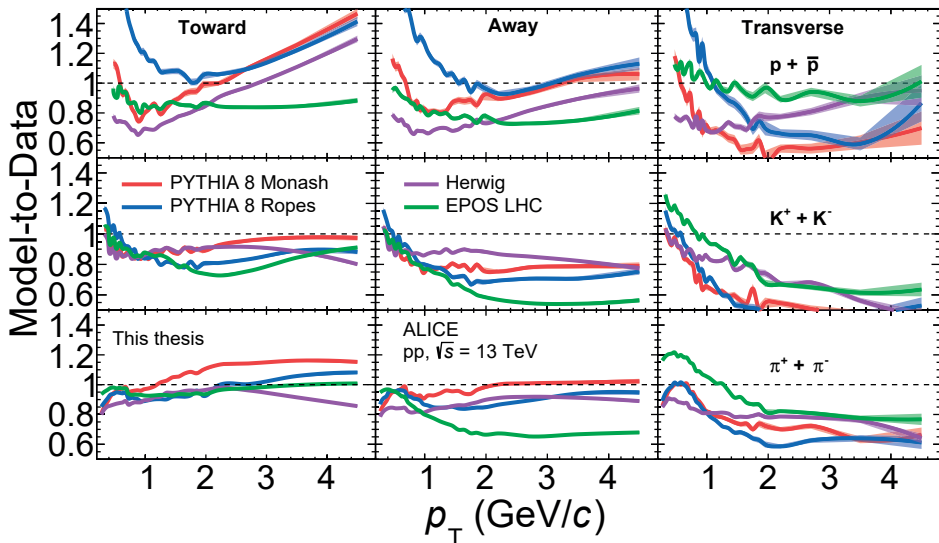


**Figure 10.8:** Comparisons between the spectra in models and data. The results in the toward, away, and transverse regions are shown in the left, middle, and right columns. The results for  $\pi$ ,  $K$  and  $p$  are shown in the bottom, middle and top rows. The comparisons shown in the top (bottom) figure correspond to the  $0 \leq R_T < 0.5$  ( $2.5 < R_T < 5$ ) interval.

### 10.1.3 $p_T$ -Differential Particle Ratios

Figure 10.9 shows the  $p_T$ -differential  $K/\pi$  and  $p/\pi$  ratios as a function of  $R_T$  in the different topological regions. In addition, the ratios from this study are compared with the inclusive measurement in low-multiplicity, high-multiplicity and minimum bias pp collisions at  $\sqrt{s} = 13$  TeV [125]. Both ratios in the toward and away regions show similar features: they increase with increasing UE activity; however, this is true only for  $p_T \gtrsim 1$  GeV/c. The evolution of the ratios with  $R_T$  might be attributed to a gradual increase of the radial flow with increasing UE activity. Furthermore, the ratios in these two regions tend to approach the values of the transverse region in the high-UE limit. Moreover, the  $R_T$ -dependent  $K/\pi$  and  $p/\pi$  ratios are always below the inclusive ratios. This suggests that the bulk particle production mainly drives the behaviour of the particle ratios in minimum bias collisions. The  $K/\pi$  ratios show the opposite behaviour in the transverse region: they decrease with increasing  $R_T$ . It is also observed that the inclusive  $K/\pi$  ratio is very similar to the one measured in  $0 \leq R_T < 0.5$ . The  $p/\pi$  ratio in the transverse region shows a mild dependence on  $R_T$ . However, it is observed that the ratio in the  $2.5 < R_T < 5$  class (high-UE) is below the one in  $0 \leq R_T < 0.5$  (low-UE) for  $p_T \lesssim 2$  GeV/c and then for  $p_T \gtrsim 2$  GeV/c, the high-UE  $p/\pi$  is higher than the low-UE one. This observation is consistent with radial flow. At the same time, the high-UE ratio tends to saturate for  $p_T \gtrsim 2.5$  GeV/c, which is not in the inclusive  $p/\pi$  [97, 132]. A possible explanation for this effect can be attributed to wide-angle gluon radiation from initial and final state radiation. When emitted at wide angles, radiated gluons increase the multiplicity and, in turn, might populate the transverse region.

Figure 10.10 shows the  $p_T$ -differential  $K/\pi$  and  $p/\pi$  in the two extremes of  $R_T$  and are compared with model predictions. In the toward region, the models can describe the low-UE ( $0 \leq R_T < 0.5$ )  $K/\pi$  and  $p/\pi$  ratios over the entire  $p_T$  range, except Herwig predicts an almost monotonic increase of the  $p/\pi$  ratio with  $p_T$ . The fact that the models can describe the low-UE particle ratios is expected since this  $R_T$  interval is mainly dominated by the jet (perturbative processes), where there are few soft QCD processes. When the UE activity increases, PYTHIA 8 Monash predicts almost no evolution with  $R_T$  for both ratios, while PYTHIA 8 Ropes and EPOS LHC overestimate the  $p/\pi$  ratio over the entire  $p_T$  range. The large  $p/\pi$  ratio in EPOS LHC can be attributed to the fact that the relative production of baryons from the core is overestimated at high multiplicities (high-UE); the core contribution dominates over the corona [81, 82]. In the transverse region, PYTHIA 8 Monash and PYTHIA 8 Ropes describe the splitting between low-UE and high-UE  $K/\pi$  ratios qualitatively but underestimate the data. At the same time, Herwig and EPOS LHC predict no dependence on  $R_T$  for the  $K/\pi$  ratio. Finally, the  $p/\pi$  ratio predicted by EPOS LHC in  $0 \leq R_T < 0.5$  agrees with the data, but as previously stated, the transition from corona to core hadronisation is not well

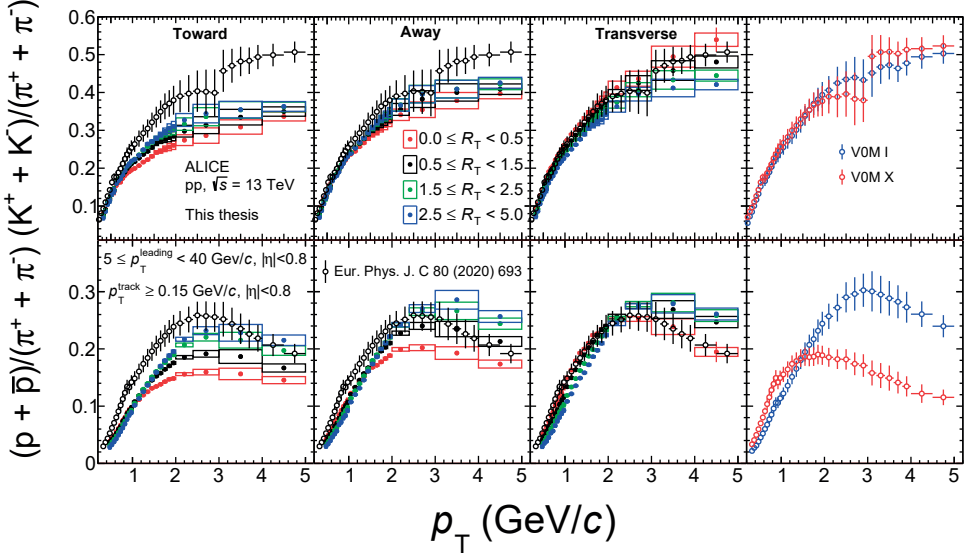


**Figure 10.9:**  $p_T$ -differential  $K/\pi$  (top row) and  $p/\pi$  (bottom row) as a function of  $R_T$ . Statistical and systematic uncertainties are shown as error bars and boxes around the data points. The  $R_T$ -dependent ratios are compared with the inclusive particle ratios measured in low-multiplicity (V0M I), high-multiplicity (V0M X) and minimum-bias events at the same  $\sqrt{s}$ .

modelled.

For all the results presented in this subsection, a strong PID dependence is observed with  $R_T$  that is different for  $\pi$ ,  $K$ , and  $p$ . The models do a good job at describing the jet, low  $R_T$  toward and away regions, but fail to describe the UE evolution, transverse region in general and intermediate/high  $R_T$  toward and away regions. As  $\pi$ ,  $K$ , and  $p$  constitute the bulk particle production, these new results provide unique opportunities for models to nail down the interplay between the jet and the UE in proton-proton collisions.

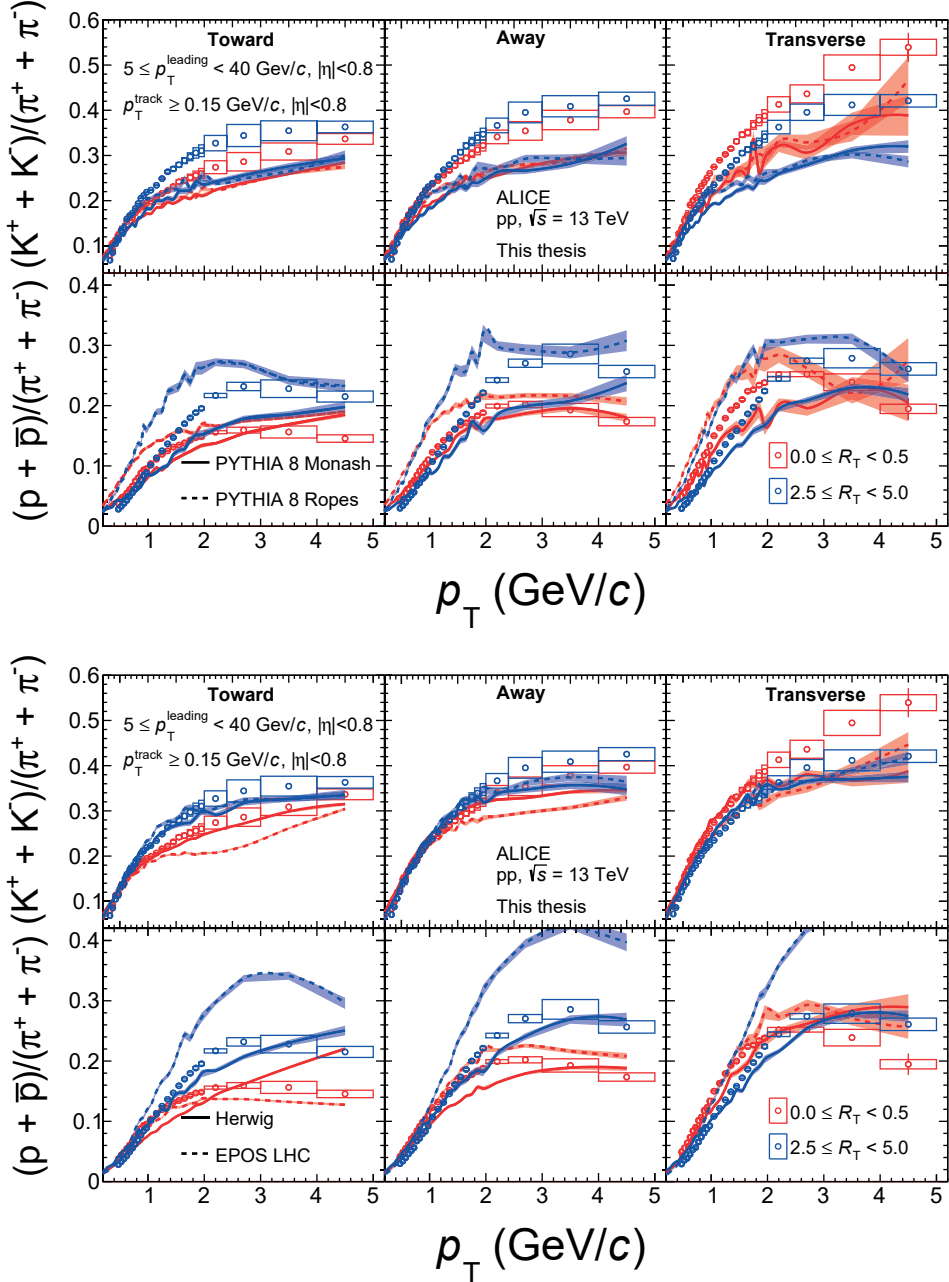


**Figure 10.10:**  $p_T$ -differential  $K/\pi$  and  $p/\pi$  measured in the two extremes of  $R_T$ :  $0 \leq R_T < 0.5$  and  $2.5 \leq R_T < 5$  and in the different topological regions. Model predictions from PYTHIA 8 Monash and PYTHIA 8 Ropes (EPOS LHC and Herwig) are shown in the top (bottom) figure. Statistical and systematic uncertainties are shown as error bars and boxes around the data points.

## 10.2 Production of $\pi$ , K and p as a Function of the Transverse Spherocity

This section presents the measurements of  $\pi$ , K and p production as a function of spherocity. As discussed in Sec. 8.3, the unweighted transverse spherocity,  $S_0^{p_T=1}$ , allows one to select high-multiplicity events with a jet-like topology (where particle production is expected to be dominated by a single hard scattering) or isotropic topology (where one expects particle production to be dominated by soft MPIs). In contrast to the UE activity analysis, I focus on high-multiplicity events selected with the V0 and SPD detectors. The former estimates the multiplicity in the forward region, while the latter uses the mid-pseudorapidity region (see Sec. 6.2.1). The adopted method in ALICE for the multiplicity estimation is to segment the V0 and SPD amplitudes into percentiles and associate them with multiplicity classes. For example, the V0M or  $N_{\text{SPD}}$  I (III) correspond to the top 1% (10%) events with the highest multiplicity values. The mean charged-particle multiplicity density  $\langle dN_{\text{ch}}/d\eta \rangle$  measured at mid-pseudorapidity is a physical observable that relates the multiplicity classes with different collision systems and centre-of-mass energies. Table 10.2 shows the relation between multiplicity classes and  $\langle dN_{\text{ch}}/d\eta \rangle$ , where, on average, the number of charged particles measured in the V0M I ( $N_{\text{SPD}}$  I) multiplicity class is 41.6 (53). Thus, the transverse spherocity analysis aims to study high-multiplicity events with different topologies.

**Table 10.2:** Relation between the V0M and  $N_{\text{SPD}}$  multiplicity classes with the  $\langle dN_{\text{ch}}/d\eta \rangle$  measured in  $|\eta| < 0.5$ . The values are measured internally by the ALICE collaboration.

Class name	I	III
V0M	0-1 %	0-10 %
$\langle dN_{\text{ch}}/d\eta \rangle$	$26.02 \pm 0.35$	$18.7 \pm 0.25$
$N_{\text{SPD}}$	I	III
$\langle dN_{\text{ch}}/d\eta \rangle$	$33.01 \pm 0.55$	$21.57 \pm 0.32$

Figure 10.11 shows the unfolded  $S_0^{p_T=1}$  distributions measured in the  $N_{\text{SPD}}$  I and  $N_{\text{SPD}}$  III multiplicity classes. It is observed that the  $S_0^{p_T=1}$  distribution is multiplicity dependent; there is an evident depletion of the low  $S_0^{p_T=1}$  part in events with the highest multiplicities ( $N_{\text{SPD}}$  I) compared with the lower multiplicity events ( $N_{\text{SPD}}$  III). These results agree with measurements by the ALICE collaboration at lower centre-of-mass energies [133]. In MPI-based models, like PYTHIA, the increase of the multiplicity at mid-rapidity is accompanied by an increasing number of multiple parton interactions. Furthermore, as reported in [123], a more significant average number of MPIs are produced in isotropic than in jetty-like events. This suggests that the bulk properties

mainly drive multiplicity-dependent observables in high-multiplicity events. One can see that PYTHIA 8 Monash and PYTHIA 8 Ropes are in good agreement with the data. EPOS LHC underestimates (overestimates) the production of jet-like (isotropic) events. This observation is consistent with the formation of a core region in high multiplicity events, which leads to the isotropic production of many particles. Conversely, Herwig overestimates (underestimates) the yield of jet-like (isotropic) events. This suggests that Herwig gets high-multiplicity events by favouring the production of back-to-back high- $p_T$  jets (low  $S_0^{p_T=1}$ ). These observations hold for both multiplicity classes ( $N_{\text{SPD}}$  I and  $N_{\text{SPD}}$  III). The  $S_0^{p_T=1}$  distribution measured in events selected with the V0M multiplicity estimator is shown in Appx. B.

Table 10.3 lists the 1 % and 10 % spherocity cuts to select jet-like and isotropic events. It is important to clarify that these cuts are measured using the uncorrected  $S_0^{p_T=1}$  distribution. This is because the  $p_T$  spectra are not unfolded as a function of spherocity. Instead, the results are reported in quantiles.

**Table 10.3:** Spherocity cuts associated with different multiplicity V0M and  $N_{\text{SPD}}$  classes.

Class	Jetty 1 %	Jetty 10 %	Isotropic 1 %	Isotropic 10 %
V0M I	0 – 0.433	0 – 0.589	0.936 – 1	0.882 – 1
V0M III	0 – 0.357	0 – 0.529	0.927 – 1	0.864 – 1
$N_{\text{SPD}}$ I	0 – 0.408	0 – 0.561	0.93 – 1	0.871 – 1
$N_{\text{SPD}}$ III	0 – 0.487	0 – 0.624	0.942 – 1	0.892 – 1

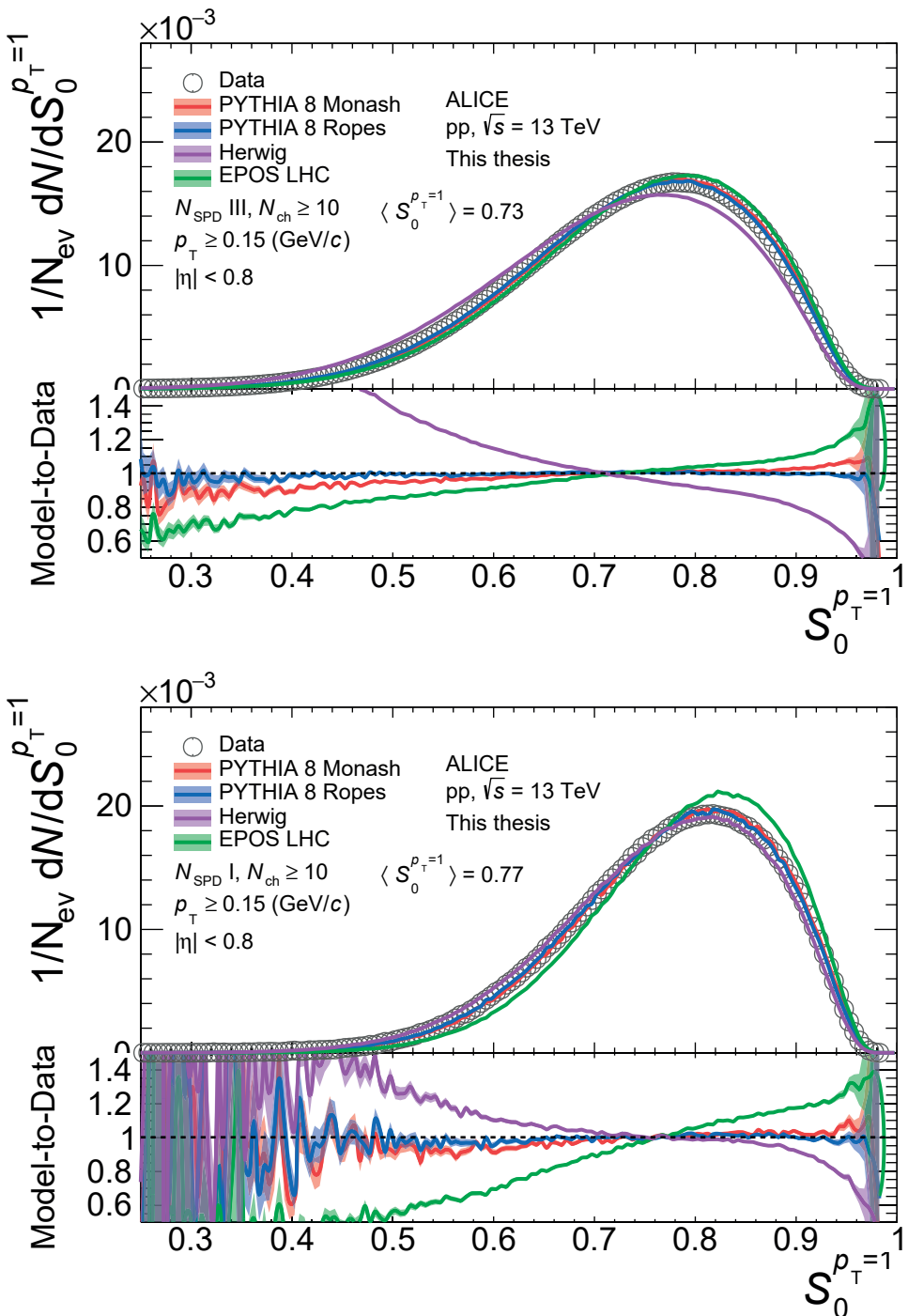


**Figure 10.11:** Unfolded  $S_0^{p_T=1}$  distributions for 1 % (top) and 10 % (bottom)  $N_{\text{SPD}}$  multiplicity classes.

Before getting to the  $p_T$ -differential observables, I want to show the different types of events that one gets by using spherocity. Specifically, one can look at the correlation between  $\langle p_T \rangle$  and  $\langle dN/dy \rangle$  as a function of  $S_0^{p_T=1}$  and, at the same time, contrast the results from the forward and mid-pseudorapidity multiplicity estimators. Such average quantities are derived from the corrected  $p_T$  spectra and following the procedure described in Sec. 10.1.1.

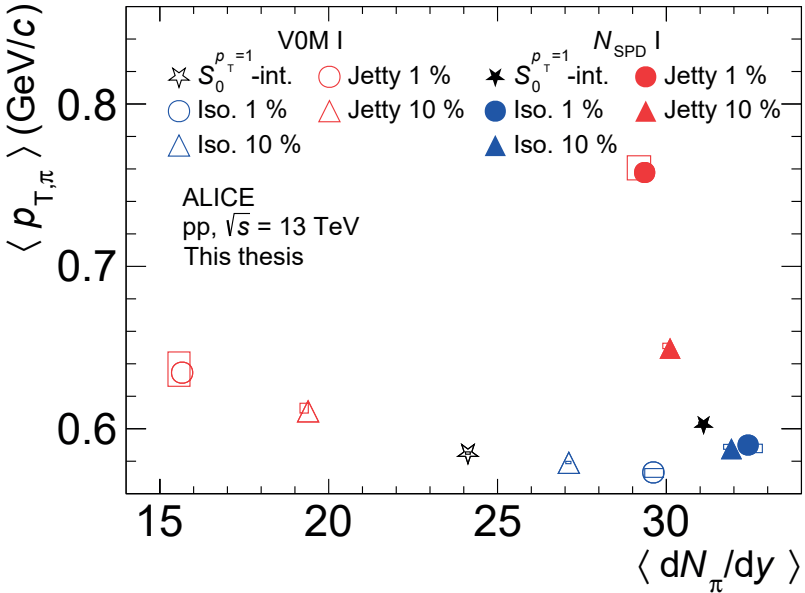


**Figure 10.12:** Correlation between the  $\langle p_T \rangle$  and  $\langle dN/dy \rangle$  of pions as a function of  $S_0^{p_T=1}$ , measured in the V0M I and  $N_{\text{SPD}}$  I multiplicity classes. The statistical and systematic uncertainties are represented with bars and empty boxes.

Figure 10.12 shows the correlation between the  $\langle p_T \rangle$  and  $\langle dN/dy \rangle$  of pions measured in the multiplicity classes, V0M I and  $N_{\text{SPD}}$  I and for the 1 % and 10 % most jet-like and isotopic events. Here, I use the  $\langle p_T \rangle$  of pions as the proxy for all the charged particles since pions compose most of the particle composition in a hadronic collision. One observes a clear distinction between how the different multiplicity estimators relate to the hardness of the events. Namely, for events in the V0M I multiplicity class, the change in  $\langle p_{T,\pi} \rangle$  is of about 10 % when going from the most isotropic (Iso. 1 %) to the most jet-like (Jetty 1 %) events. In contrast, the change in  $\langle dN_\pi/dy \rangle$  is almost a factor of two. For events whose multiplicity classification is based on the mid-pseudorapidity multiplicity estimator and for the same spherocity percentiles, the change in  $\langle p_{T,\pi} \rangle$  is of about 30 %, while  $\langle dN_\pi/dy \rangle$  changes approximately by 10 %. Similar statements hold for the correlation between  $\langle p_T \rangle$  and  $\langle dN/dy \rangle$  of K and p. These results can be

found in the Appx B.

The correlation between  $\langle p_T \rangle$  and  $\langle dN/dy \rangle$  shown above suggests that the V0M multiplicity estimator selects events with similar  $\langle p_T \rangle$  over a wide  $\langle dN/dy \rangle$  interval. In contrast, the  $N_{\text{SPD}}$  multiplicity estimator selects events whose properties are mainly driven by the hardness of the event, and at the same time, the implicit multiplicity dependence of  $S_0^{p_T=1}$  is minimised. These results agree with the study in [123], where a jet-finder algorithm is applied to events with a pre-selection based on spherocity. In such a study, it was observed that the average number of jets in jet-like events is about four, and at the same time, the  $\langle p_T \rangle$  of these events is much larger than the one measured in isotropic events with an average number of jets below one.

In the coming subsections, I will focus mainly on the extremes of multiplicity and spherocity. Namely, I will describe the measurements in the multiplicity classes; V0M I and  $N_{\text{SPD}}$  I. I will concentrate on the top 1 % jet-like and isotropic topologies for these events. Some similarity between  $R_T$  and  $S_0^{p_T=1}$  is expected. Particle production in jet-like events should resemble that of low- $R_T$  events in the toward region, and therefore the same colour is used (red). It is expected that isotropic-like particle production will be similar to high- $R_T$  and use the colour blue. However, one should stress that here one is looking at extremes of full events, i.e., for the jet-like, we search for high-multiplicity events dominated by a single hard scattering, which is very different from the low- $R_T$  in the toward region and which allows answering the question of how homogeneous high-multiplicity events are.

### 10.2.1 Studying the Extremes of Multiplicity and Spherocity

Figure 10.13 and Fig. 10.14 show the  $p_T$  spectra of  $\pi$ , K and p for the top 1 % jet-like and isotropic and the  $S_0^{p_T=1}$ -integrated events in the multiplicity classes  $N_{\text{SPD}}$  I and V0M I, respectively. The two lower panels show the ratios to the  $S_0^{p_T=1}$ -integrated spectrum in linear and logarithmic scales. The first feature is that the spectral shapes and  $p_T$ -dependent ratios for jet-like and isotropic events are similar among the different particle species and for both multiplicity estimators. Second, the  $p_T$  spectra for jet-like events are less steep with increasing  $p_T$  than the spectra measured in the  $S_0^{p_T=1}$ -integrated sample for  $p_T > 3 \text{ GeV}/c$ . This is true for both multiplicity estimators, however, the spherocity dependence is more robust when using the  $N_{\text{SPD}}$  multiplicity estimator. Furthermore, this is in line with the larger average transverse momentum values measured in the  $N_{\text{SPD}}$  I sample than in the V0M I one. The ratios to the  $S_0^{p_T=1}$ -integrated  $p_T$  spectrum exhibit two distinct features. When using the  $N_{\text{SPD}}$  multiplicity estimator and at low  $p_T$  ( $< 1 \text{ GeV}/c$ ,  $< 2 \text{ GeV}/c$  and  $< 3 \text{ GeV}/c$  for  $\pi$ , K and p) the ratios exhibit a mild  $p_T$  dependence while for higher  $p_T$  the jet-like ratio shows a

stronger  $p_T$  dependence than isotropic ratios. In the case of the V0M I sample, the  $p_T$  dependence of the ratios is less remarkable. These results support the fact that the  $N_{\text{SPD}}$  multiplicity estimator combined with spherocity can yield an enhanced sensitivity to very hard processes (jets). Similar results are observed in the  $p_T$  spectra of all charged particles as a function of the multiplicity [134]. In isotropic events measured in the  $N_{\text{SPD}}$  I sample, one sees a slightly larger production of low- $p_T$  particles than in the  $S_0^{p_T=1}$ -integrated sample. From  $p_T$  of about 2 (3) GeV/ $c$ , the  $p_T$  distributions show a rapid decrease with  $p_T$  for  $\pi$  (K and p). Furthermore, the larger production of low- $p_T$  particles is also observed in events selected with the V0M multiplicity estimator. One sees an almost flat ratio between isotropic and  $S_0^{p_T=1}$ -integrated events for  $p_T \lesssim 3$  GeV/ $c$ . This suggests that the spectra in inclusive (without any selection on the event topology) events from [97, 125, 132] are dominated by the UE (isotropic topologies) in these  $p_T$  regions.

Figure 10.15 shows the ratios between the  $p_T$  spectra from model predictions to those in data for the 1 % jet-like, isotropic and  $S_0^{p_T=1}$ -integrated samples in the  $N_{\text{SPD}}$  I and V0M I multiplicity classes. Given the statistical limitations in the models, the ratios are only shown up to 10 GeV/ $c$ .

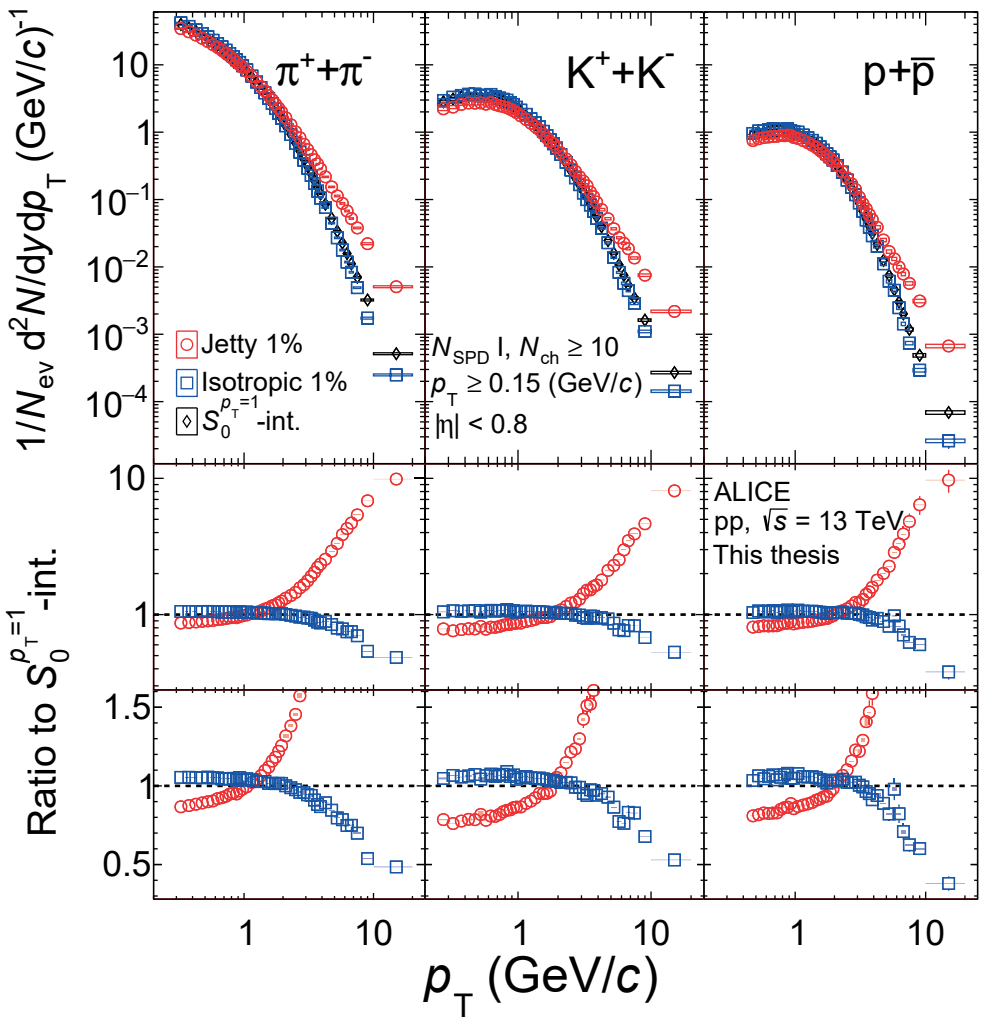


**Figure 10.13:** Transverse momentum spectra of  $\pi$  (left),  $K$  (middle) and  $p$  (right). The ratios to the  $S_0^{p_T=1}$ -integrated spectrum are shown in the bottom and middle rows in linear and logarithmic scales, respectively. The results are shown for the top 1 % jetty-like and isotropic events selected in the  $N_{\text{SPD I}}$  multiplicity class. The statistical and systematic uncertainties are represented with bars and boxes around the data points.

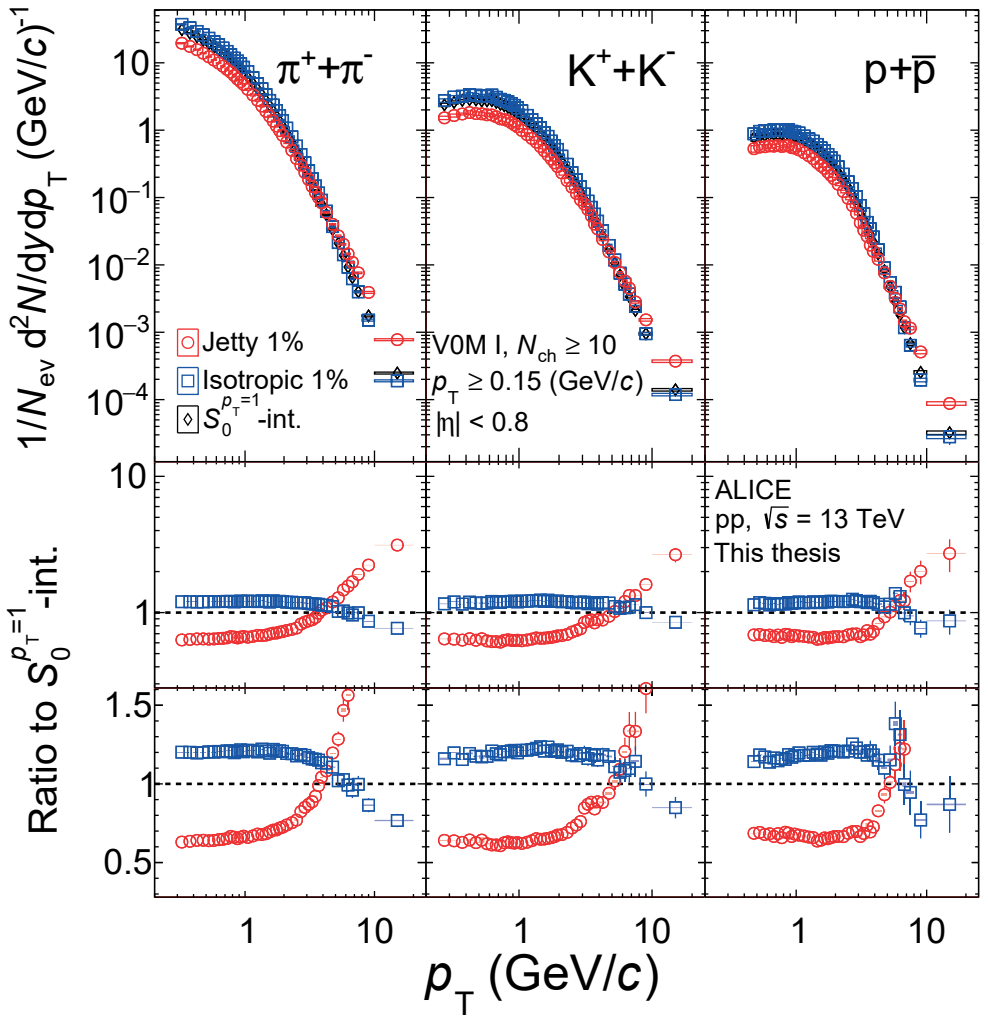


**Figure 10.14:** Transverse momentum spectra of  $\pi$  (left),  $K$  (middle) and  $p$  (right) and ratios to the  $S_0^{p_T=1}$ -integrated spectrum (bottom and middle rows). The statistical and systematic uncertainties are represented with bars and boxes around the data points. Results are shown for the top 1 % jetty-like and isotropic events selected in the V0M I multiplicity class.

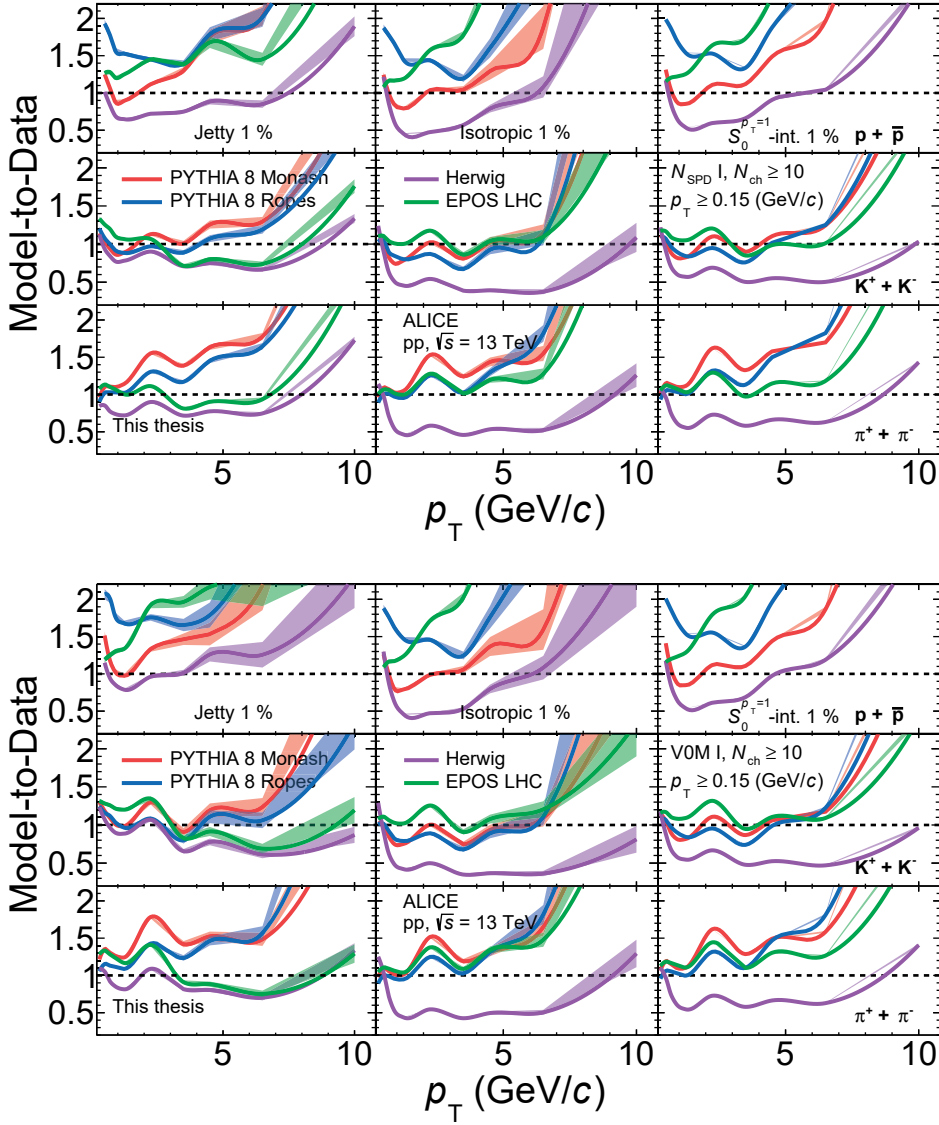


**Figure 10.15:** Ratios between the  $p_T$  spectra from model prediction and data. The results for the 1% jet-like and isotropic and  $S_0^{p_{\text{r}}=1}$ -integrated cases are shown in the left, middle and right columns, respectively. The spectra ratios for  $\pi$ ,  $K$  and  $p$  are shown in the bottom, middle and top rows. The results from the  $N_{\text{SPD}} \text{ I}$  ( $V0M \text{ I}$ ) sample are shown in the top (bottom) figure. The shaded bands represent the statistical uncertainty of the ratios.

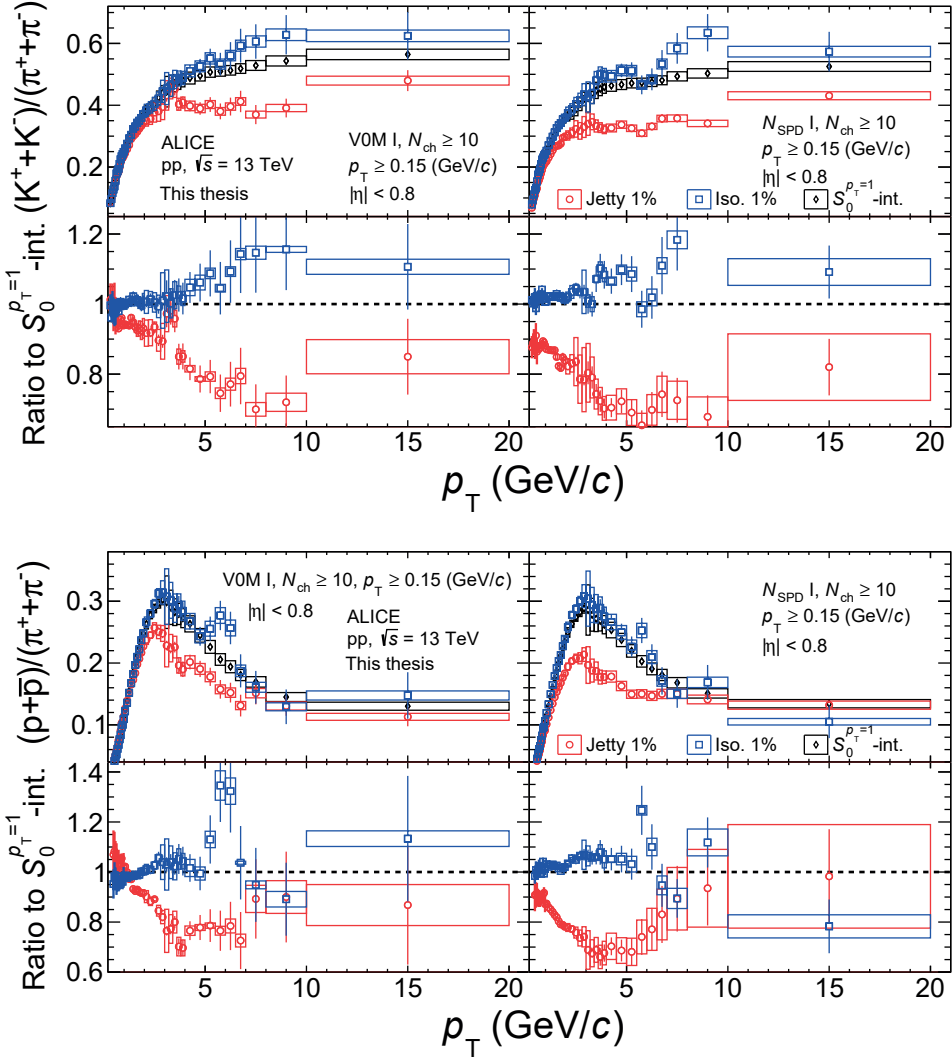
## Particle Ratios and Double-Ratios

Figure 10.16 shows the  $p_T$ -differential  $K/\pi$  and  $p/\pi$  ratios for the 1% jet-like and isotropic events measured in the  $N_{\text{SPD}}$  I and V0M I multiplicity classes. In addition, the double-ratios as defined in Eq. 10.1 are shown. The common systematic uncertainties between the  $S_0^{p_T=1}$ -dependent and  $S_0^{p_T=1}$ -integrated ratios will cancel out by performing the double-ratio. It also allows studying the effects of the spherocity selection with respect to the  $S_0^{p_T=1}$ -integrated particle ratios.

$$\left( \frac{dN/dydp_T}{dN_\pi/dydp_T} \right)_{S_0^{p_T=1}} / \left( \frac{dN/dydp_T}{dN_\pi/dydp_T} \right)_{S_0^{p_T=1}-\text{int.}} . \quad (10.1)$$

The evolution of the  $S_0^{p_T=1}$ -dependent  $K/\pi$  ratio between the two multiplicity estimators is similar. Also, one can see that the  $K/\pi$  ratios in isotropic events are closer in magnitude to the one measured in the  $S_0^{p_T=1}$ -integrated sample for both multiplicity estimators. This suggests that the multiplicity dependent  $K/\pi$  ratios can be explained by the  $K/\pi$  ratio measured in isotropic events. For  $p_T \gtrsim 1$  (3)  $\text{GeV}/c$ , the  $K/\pi$  ratio in isotropic and jet-like topologies deviate from each other for the  $N_{\text{SPD}}$  I (V0M I) sample. While the  $K/\pi$  ratios in isotropic events continue increasing, the ones measured in jet-like events saturate. Furthermore, at high- $p_T$  ( $> 5 \text{ GeV}/c$ ), the isotropic ratios are higher than the  $S_0^{p_T=1}$ -integrated ones. These observations suggest that strange particle production is favoured in isotropic topologies. In contrast, the  $K/\pi$  ratio measured in jet-like topologies is suppressed, with an even larger suppression when using the  $N_{\text{SPD}}$  multiplicity estimator. This behaviour can be attributed to the fact that events in the  $N_{\text{SPD}}$  I sample are more sensitive to pQCD processes (jets), and as discussed in [124], the particle ratios are lower (higher) when the event contains a hard scattering with large (small)  $\hat{p}_T$ .

The  $S_0^{p_T=1}$ -dependent  $p/\pi$  ratio is similar between the two multiplicity estimators. However, one sees that the baryon-to-meson ratio measured using the V0M multiplicity estimator shows a suppression (enhancement) with respect to the  $S_0^{p_T=1}$ -integrated ratio in isotropic (jet-like) events for  $p_T \lesssim 1.5 \text{ GeV}/c$ . This effect is not observed when the events are selected with the  $N_{\text{SPD}}$  multiplicity estimator. For events selected with the  $N_{\text{SPD}}$  multiplicity estimator, the jet-like ratio is always below the  $S_0^{p_T=1}$ -integrated result, and one sees a small “bump” centred at  $p_T \approx 2.5 \text{ GeV}/c$ . A recent ALICE publication [135] shows no enhancement in the  $p_T$ -differential  $(\Lambda + \bar{\Lambda})/2K_S^0$  measured in jets (after subtracting the UE contribution). This might suggest that the bump in the  $p/\pi$  ratio is mainly driven by collective radial flow since, in these studies, the UE contribution is not being subtracted. Conversely, the  $p/\pi$  ratio measured in isotropic and  $S_0^{p_T=1}$ -integrated events shows a big bump centred at  $p_T \approx 3 \text{ GeV}/c$  for both multiplic-



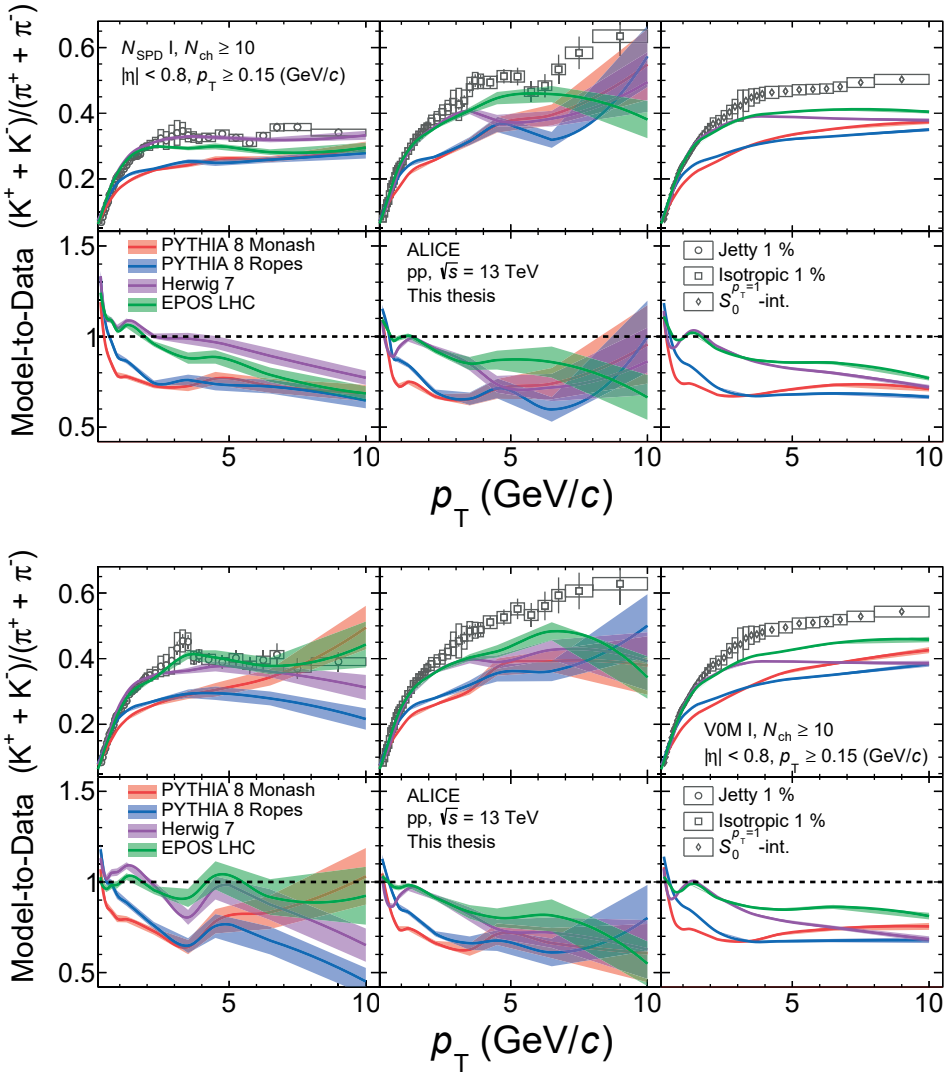
**Figure 10.16:**  $p_T$ -differential  $K/\pi$  (top),  $p/\pi$  (bottom) and ratios to the  $S_0^{p_T=1}$ -integrated result. The results are shown for the top 1% jetty-like and isotropic events selected in the V0 I (left panels) and  $N_{SPD}$  I (right panels) multiplicity classes. The statistical and systematic uncertainties are represented with bars and boxes around the data points.

ity estimators, attributed to collective radial flow. Furthermore, the baryon-to-meson ratio in isotropic events reaches higher values than the  $S_0^{p_T=1}$ -integrated ratio in the  $p_T$

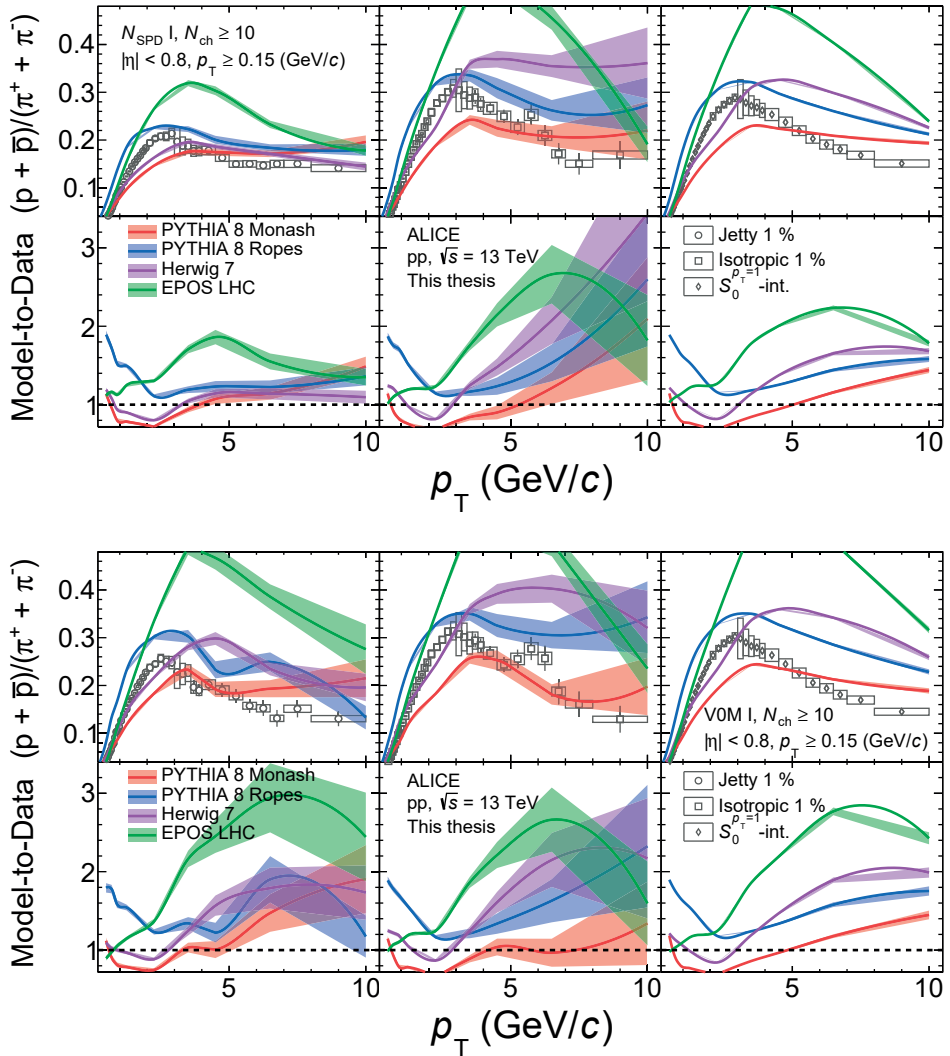
interval  $2 - 7 \text{ GeV}/c$ . This is expected since collective radial flow effects are more relevant for particle production in bulk (outside the jet region). Also, one sees that the  $p/\pi$  ratio in isotropic events converges to the one in jet-like events for  $p_T \gtrsim 7 \text{ GeV}/c$ . This is also expected, since in the high- $p_T$ , we are mainly looking at jet fragmentation.

Figure 10.17 shows the measured  $K/\pi$  ratios along with model predictions. The comparisons are only shown up to  $10 \text{ GeV}/c$  due to statistics limitations in the models. The comparisons in the  $N_{\text{SPD}}$  I sample show that all the models overpredict the  $K/\pi$  ratio for  $p_T < 1 \text{ GeV}/c$  in jet-like, isotropic and the  $S_0^{p_T=1}$ -integrated ratios. For  $p_T \gtrsim 2 \text{ GeV}/c$  PYTHIA 8 Monash and PYTHIA 8 Ropes give a good qualitative description and predict the saturation of the  $K/\pi$  ratio in jet-like events; however, both models underpredict the ratio in this  $p_T$  region. Herwig and EPOS LHC also give a good qualitative description of the ratio, however, for jet-like events, the magnitude of the ratios decreases with increasing  $p_T$  with respect to the  $K/\pi$  ratio measured in data. In the case of the  $K/\pi$  ratio in isotropic events, all the models predict an increasing  $K/\pi$  ratio with increasing  $p_T$ , however, they underpredict the data measurement. Finally, all the models give a good qualitative description of the  $K/\pi$  ratio in the  $S_0^{p_T=1}$ -integrated sample however, Herwig and EPOS LHC (PYTHIA 8 Monash and PYTHIA 8 Ropes) underpredict the data result by about 20 % (30 %) for  $p_T \gtrsim 4$  (2)  $\text{GeV}/c$ .

Figure 10.18 compares the measured  $p/\pi$  ratios as a function of spherocity with model predictions. Similar to the  $K/\pi$  ratio, due to statistical limitations in the models, the comparisons are only shown up to  $10 \text{ GeV}/c$ . At low- $p_T$  ( $\lesssim 4 \text{ GeV}/c$ ) and for jetty-like events, all the models struggle to predict the small bump. However, PYTHIA 8 Ropes predicts a bump centred at  $p_T \approx 3 \text{ GeV}/c$ , close to the  $p_T$  value where the maximum in data is observed. At higher  $p_T$  ( $\gtrsim 4 \text{ GeV}/c$ ), PYTHIA 8 Monash, PYTHIA 8 Ropes and Herwig give a good qualitative description of the data. PYTHIA 8 Ropes predicts the same magnitude of the baryon-to-meson ratio in isotropic events, while PYTHIA 8 Monash underpredicts the measurement below  $p_T \approx 4 \text{ GeV}/c$ . Also, above  $p_T \approx 4 \text{ GeV}/c$ , Herwig and EPOS LHC predict a  $p/\pi$  ratio that is not observed in the data.



**Figure 10.17:**  $p_T$ -differential  $K/\pi$  ratio and comparisons with model predictions. The results are shown for events in the  $V0M \text{ I}$  (top figure) and  $N_{\text{SPD}} \text{ I}$  (bottom figure) multiplicity classes. The  $K/\pi$  ratio in jet-like, isotropic and  $S_0^{p_T=1}$ -integrated events are displayed from left to right.



**Figure 10.18:**  $p_T$ -differential  $p/\pi$  ratio and comparisons with model predictions. The results are shown for events in the V0M I (top figure) and  $N_{\text{SPD}}$  I (bottom figure) multiplicity classes. The  $p/\pi$  ratio in jet-like, isotropic and  $S_0^{p_T=1}$ -integrated events are displayed from left to right. The bottom panels show the model-to-data ratios.

## Particle Yield Ratios as a Function of $S_0^{p_T=1}$

Figure 10.19 shows the p,  $\Lambda$  and  $\Xi$  yield ratios to  $\pi$  normalised to the values measured in the  $S_0^{p_T=1}$ -integrated sample as a function of  $S_0^{p_T=1}$  in the  $N_{\text{SPD}}$  I and V0M I multiplicity classes and model predictions. These results are part of a publication that is currently being written and includes the production of  $\pi$ , K, p,  $K_S^0$ ,  $\Lambda$ ,  $\Xi$ ,  $\varphi$  and  $K^{*0}$  as a function of  $S_0^{p_T=1}$ . The integrated particle ratios in the multiplicity class  $N_{\text{SPD}}$  I show a strange-hadron suppression in jet-like events and decreases with increasing  $S_0^{p_T=1}$ . This suggests that jet-like events driven by significant variations in  $\langle p_T \rangle$  disfavour the strangeness production. On the other hand, isotropic topologies, mainly dominated by soft processes, yield a more substantial production of strange particles. The more significant production of strange particles was also observed in the  $p_T$ -differential  $K/\pi$  ratio from Fig. 10.16.

Since the suppression is more significant for the  $\Xi$  than for the  $\Lambda$  baryon, this might suggest that the observed (suppression) enhancement depends on the strangeness content. It is observed that the PYTHIA 8 Monash tune overpredicts the  $p/\pi$  in the most jet-like events and predicts no evolution of the strange-hadron ratios as a function of  $S_0^{p_T=1}$ . Conversely, the PYTHIA 8 Ropes tune, which allows the interaction strings close in space to fuse and form colour ropes, predicts an increased production of  $\Lambda$  and  $\Xi$  baryons with increasing spherocity. However, it predicts a more significant suppression for  $\Lambda$  than for  $\Xi$ , not observed in the data. In EPOS LHC, high-multiplicity events are primarily dominated by the hadronisation of the core. The core hadronises statistically, where strangeness production is not suppressed. It is observed that EPOS LHC also predicts the increase of the strangeness production with spherocity. On the other hand, Herwig predicts particle ratios with very different behaviour when compared with data.

Remarkably, when the integrated particle ratios are measured using the forward multiplicity estimator, the  $S_0^{p_T=1}$ -dependent suppression (enhancement) of strange hadrons for jet-like (isotropic) events vanishes. This result seems to go against the ALICE results on the production of strange hadrons as a function of V0M multiplicity in pp collisions [10]. There it was shown that large variations in multiplicity mainly drove the enhancement of strange hadrons. This result is very puzzling since, as seen in Fig. 10.12, the gap in multiplicity between jet-like and isotropic events is rather broad when using the V0M multiplicity estimator. Moreover, PYTHIA 8 Ropes and EPOS LHC predict no significant evolution of the double-ratios with spherocity.

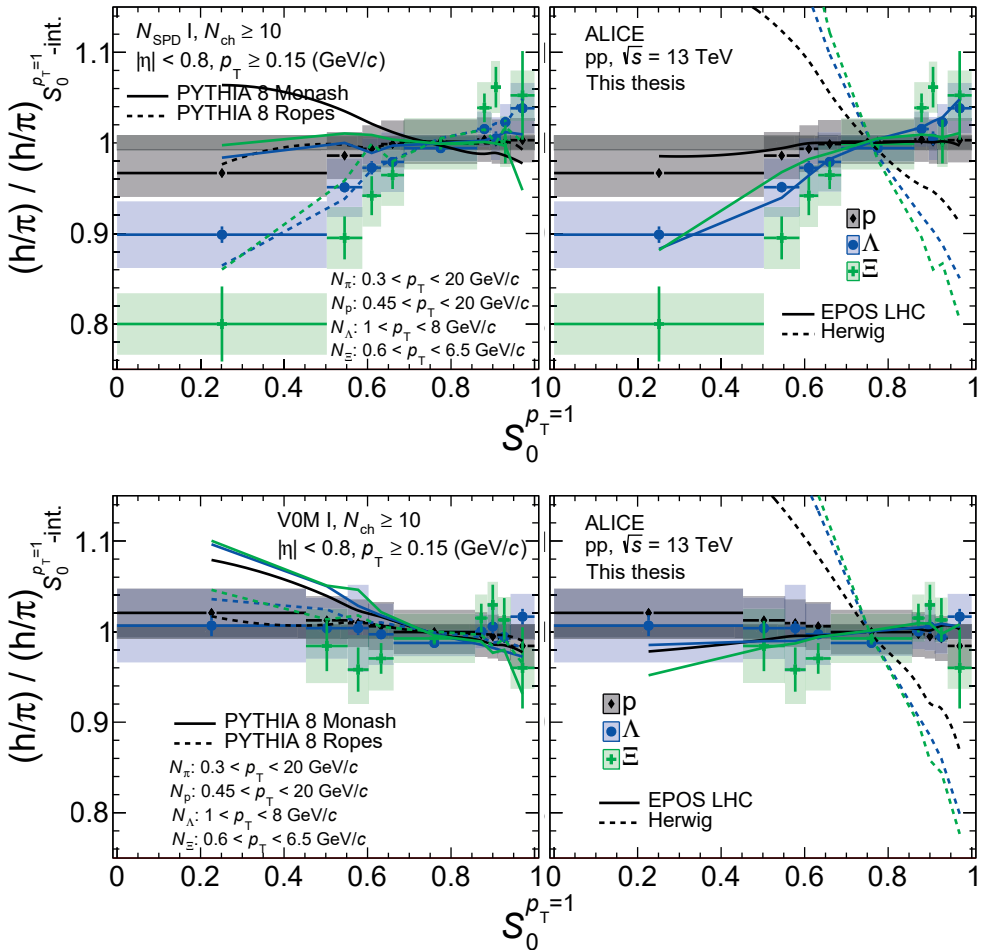


**Figure 10.19:** Particle yield ratios to pions normalised to the values measured in the  $S_0^{p_T=1}$ -integrated sample as a function of  $S_0^{p_T=1}$ . The statistical and systematic uncertainties are represented with bars and shaded areas around the data points. The results are shown for the  $N_{\text{SPD I}}$  (top row) and  $V0M I$  (bottom row) multiplicity classes. The left (right) panel shows the model predictions from PYTHIA 8 Monash and PYTHIA 8 Ropes (EPOS LHC and Herwig). The uncertainty bar in dark grey colour centred at one corresponds to the pions yields' systematic uncertainty. The different lines correspond to model predictions.

# Chapter 11

## Conclusions

The goal of the work presented in this thesis has been to carry out a suite of differential measurements to provide new insights into the observed collective effects and strangeness enhancement in pp collisions. The Relative Transverse Activity,  $R_T$  and the Unweighted Transverse Spherocity,  $S_0^{p_T=1}$  have been utilised to differentially “zoom in” on kinematic regions where the particle production is expected to be driven by well understood hard pQCD-like processes and regions where soft non-perturbative QCD dominates. By measuring  $\pi$ , K and p, which constitute the bulk of the particles produced in pp collisions, the aim has been to constrain the big picture. The results presented for the production of primary  $\pi$ , K and p as a function of  $R_T$  and  $S_0^{p_T=1}$  in pp collisions at  $\sqrt{s} = 13$  TeV using the ALICE detector are the first-ever measurements of this type.

A significant amount of the work has been done to ensure that  $R_T$  and  $S_0^{p_T=1}$  could be directly compared between data and model predictions. I was part of the team that developed the unweighted  $S_0^{p_T=1}$  estimator, which was used for the first time in these studies, and I developed the whole unfolding procedure for the identified  $R_T$  results. Moreover, the latter studies set the ground to potentially become a standard procedure in ALICE for the measurements of strange hadrons and heavy-flavour as a function of  $R_T$ .

The transverse activity analysis allows for studying particle production in distinct topological regions. Using  $R_T$ , it was possible to control the underlying event in all the topological areas. It was observed that the  $p_T$ -differential particle ratios (K/ $\pi$  and p/ $\pi$ ) show a clear evolution with  $R_T$  in the toward and away regions. This evolution with increasing event activity is attributed to a combination of the increase of the UE contribution to particle production and the collective radial flow-like effects of the UE. In

the transverse region, the change in the particle ratios is mild. Moreover, a saturation effect is observed in the  $p/\pi$  ratio in events with significant event activity. Comparisons with QCD inspired Monte Carlo models, which are known to describe traditional UE measurements well, have been presented. For low  $R_T$ , it was possible to isolate the jet in the toward region, and the models do a good job there. This is expected because they were tuned to reproduce  $e^+e^-$  measurements, which are jet-like. However, when the underlying event increases, all the models fail to describe the data. This highlights that by measuring  $\pi$ , K, and p and  $R_T$ , one can go beyond traditional UE measurements and indicates that substantial progress must be made on the model side to ensure that the UE is correctly described.

For the transverse spherocity, studies have been presented for multiplicity selection using both forward and mid-rapidity estimators. For the forward estimator, the  $\langle p_T \rangle$  is more or less the same between isotropic and jet-like events. Conversely, when the multiplicity estimation is based on the mid-rapidity estimator, it was possible to narrow the multiplicity gap between isotropic and jet-like events while at the same time selecting events with significant  $\langle p_T \rangle$  variations. In this way, it was demonstrated that  $S_0^{p_T=1}$  could be used to distinguish jet-like from isotropic topologies in high-multiplicity events. Furthermore, the results for the  $p_T$ -differential  $K/\pi$  and  $p/\pi$  ratios demonstrate that particle production in high-multiplicity events is very similar to isotropic events. On the contrary, it was possible to reduce the radial flow significantly by selecting jet-like topologies. Similarly, a remarkable result from this study was that the integrated yield of strange baryons is significantly suppressed in jet-like events while it is slightly for isotropic topologies.

When put together, the results of the  $R_T$  and  $S_0^{p_T=1}$  studies seem to indicate that jet-like pQCD-based production plays a minor role in bulk production in high-multiplicity pp collisions. Instead, soft QGP-like collective processes in the UE dominate these collisions.

## **Part IV**

# **Appendices**



## Appendix A

# Geometrical Cut In The rTPC Analysis

In general clusters close to the edges of a TPC pad are not included in the  $dE/dx$  calculation. Hence, the rTPC analysis includes an additional cut to select only good quality high- $p_T$  tracks for PID. To have only one cut, i.e., use the same cut for different magnetic polarities and positive and negative charge settings, the cut is done in terms of an azimuthal angle variable  $\varphi'$ :

- $\varphi' = \varphi$ .
- if  $B < 0$  then  $\varphi' = 2\pi - \varphi$ .
- if  $q < 0$  then  $\varphi' = 2\pi - \varphi$ .
- $\varphi' = \varphi' + \pi/18$

Then, one compares the remainder of the division between  $\varphi'$  and  $\pi/9$ . If the remainder  $< 0.12/p_T + \pi/18.0 + 0.035$  and  $> 0.1/p_T^2 + \pi/18.0 - 0.025$ , then the track is excluded. It was realised in Ref. [52] that for tracks with  $p_T > 3 \text{ GeV}/c$ , the number of assigned TPC clusters used for the  $dE/dx$  calculation is much larger than for tracks with lower  $p_T$ . Furthermore, after the  $\varphi'$  cut, the average number of clusters is nearly independent of  $p_T$ .

## Appendix B

## Complementary Figures

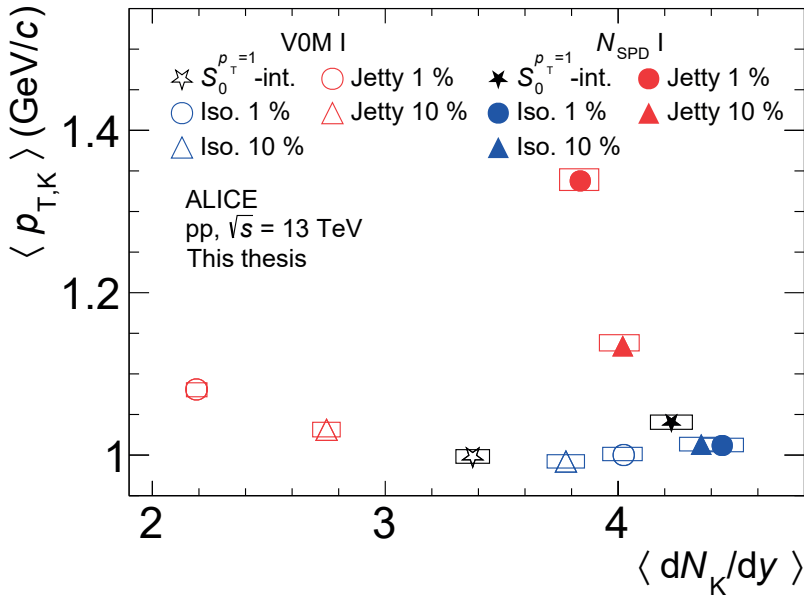


**Figure B.1:** Correlation between the  $\langle p_T \rangle$  and  $\langle dN/dy \rangle$  of kaons as a function of  $S_0^{p_T=1}$ , measured in the V0M I and  $N_{\text{SPD}}$  I multiplicity classes. The statistical and systematic uncertainties are represented with bars and empty boxes, respectively.

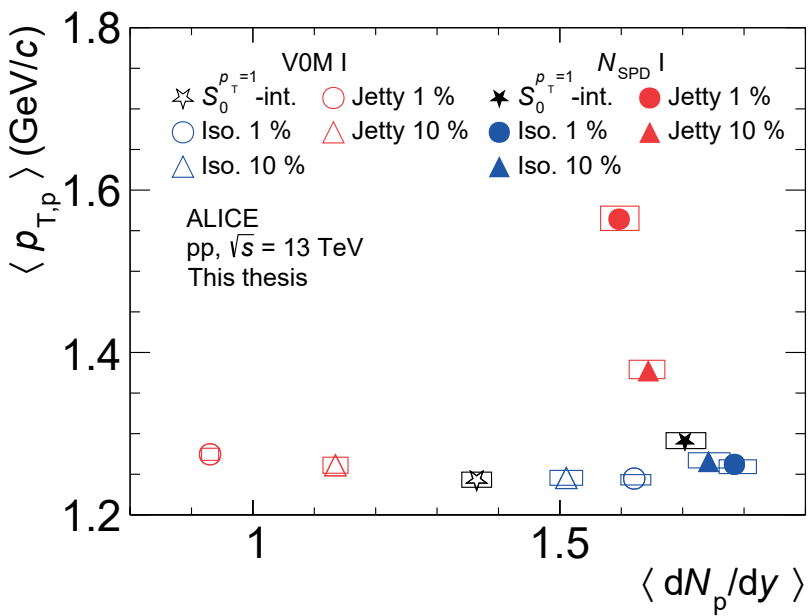


**Figure B.2:** Correlation between the  $\langle p_T \rangle$  and  $\langle dN/dy \rangle$  of protons as a function of  $S_0^{p_T=1}$ , measured in the VOM I and  $N_{\text{SPD}}$  I multiplicity classes. The statistical and systematic uncertainties are represented with bars and empty boxes, respectively.

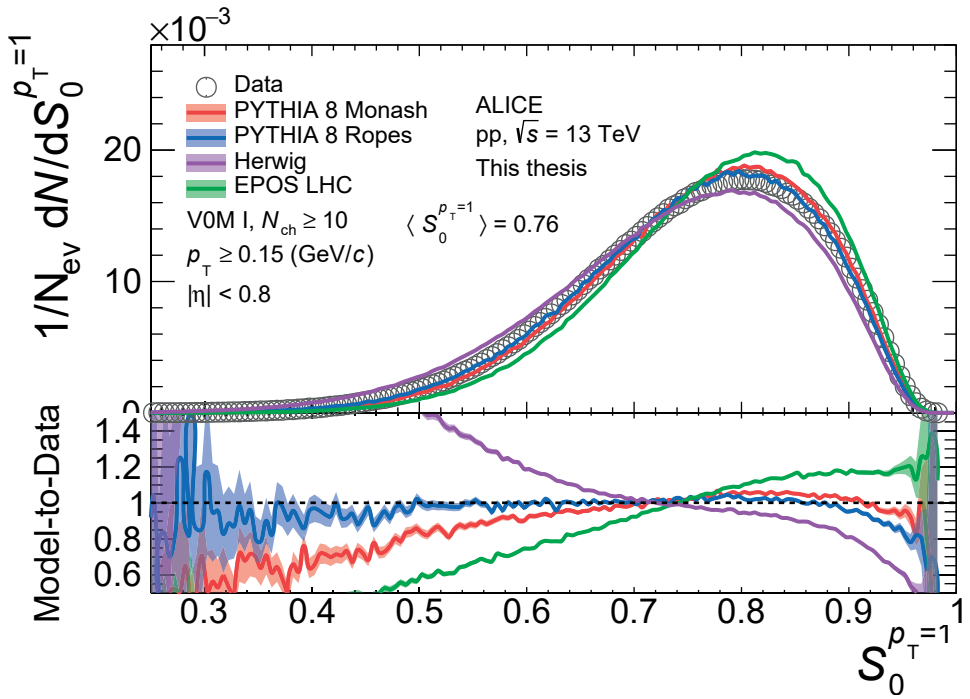


**Figure B.3:** Unfolded  $S_0^{p_T=1}$  distributions for 1 % V0M multiplicity class.

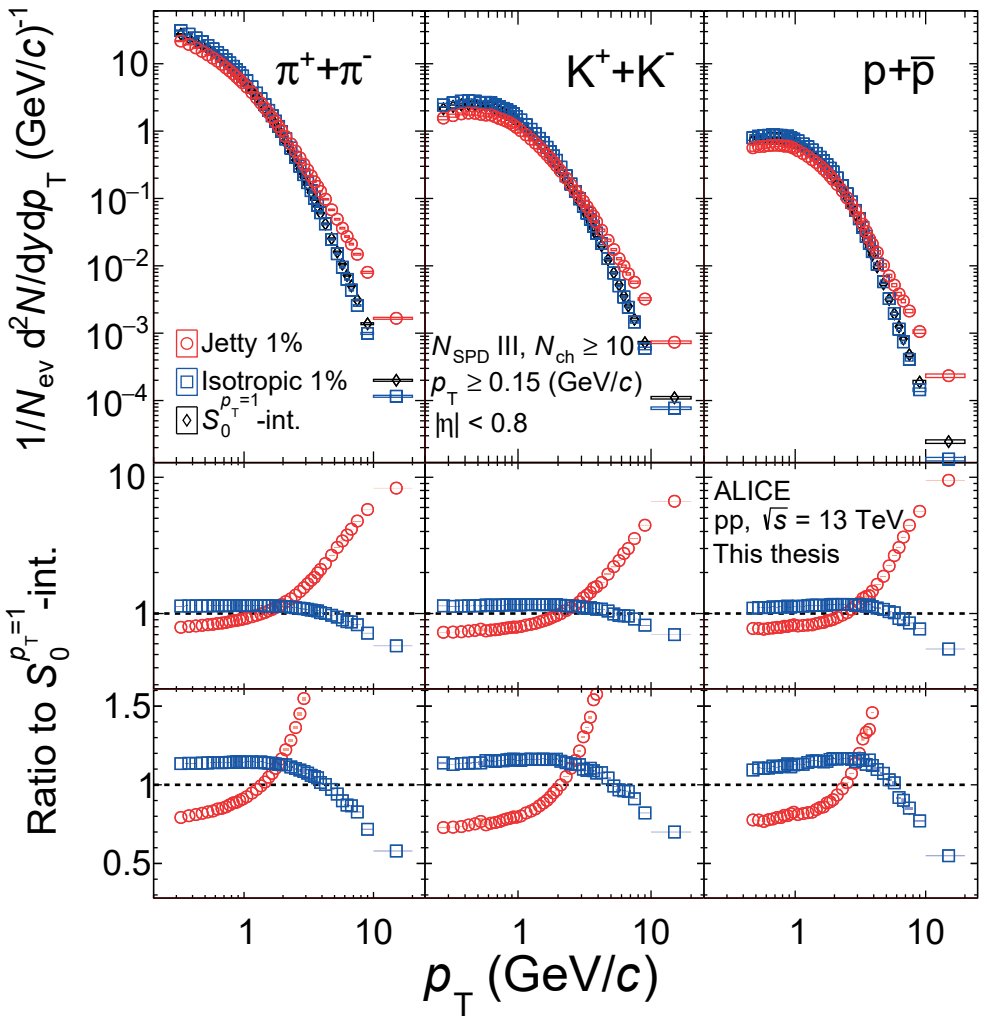


**Figure B.4:** Transverse momentum spectra of  $\pi$  (left),  $K$  (middle) and  $p$  (right). The ratios to the  $S_0^{p_T=1}$ -integrated spectrum are shown in the bottom and middle rows in linear and logarithmic scale, respectively. The results are shown for the top 1 % jetty-like and isotropic events selected in the  $N_{\text{SPD III}}$  multiplicity class. The statistical and systematic uncertainties are represented with bars and boxes around the data points, respectively.

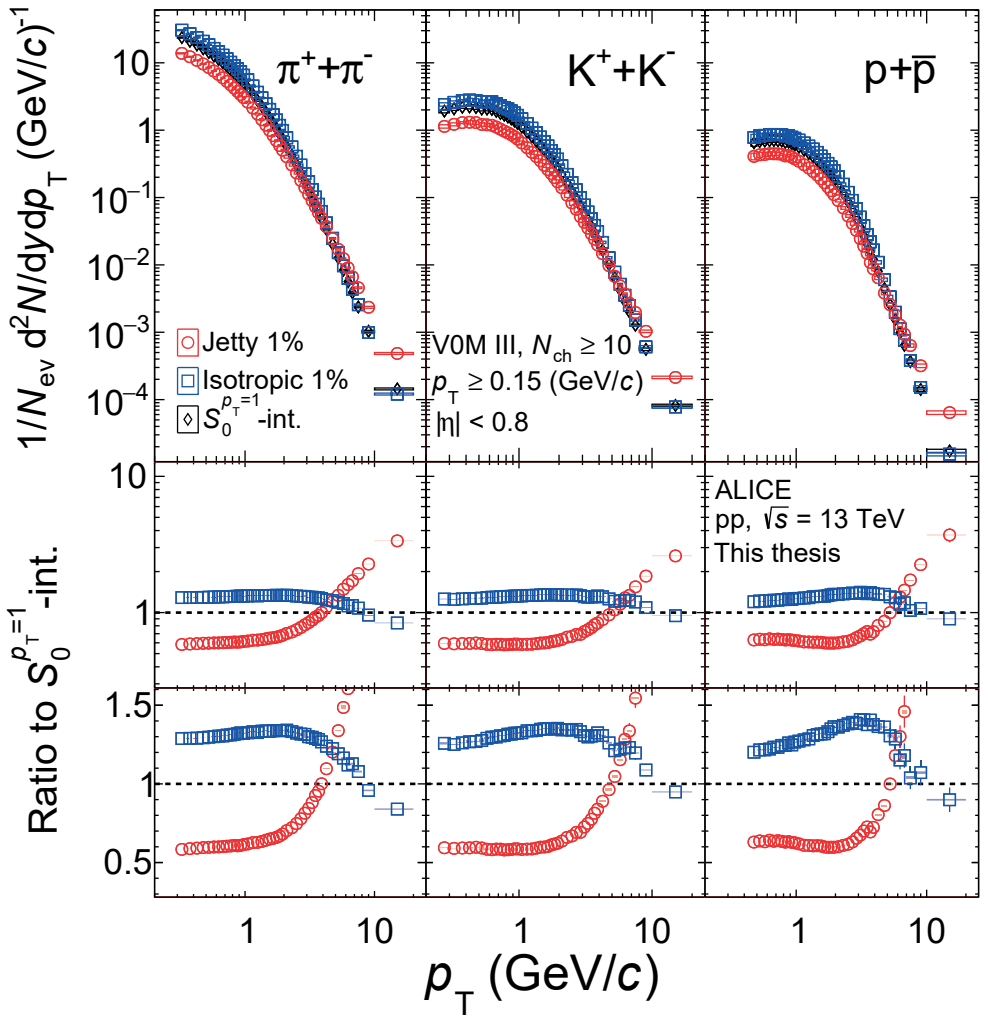


**Figure B.5:** Transverse momentum spectra of  $\pi$  (left),  $K$  (middle) and  $p$  (right) and ratios to the  $S_0^{p_T=1}$ -integrated spectrum (bottom and middle rows). The statistical and systematic uncertainties are represented with bars and boxes around the data points, respectively. Results shown for the top 1 % jetty-like and isotropic events selected in the V0M III multiplicity class.

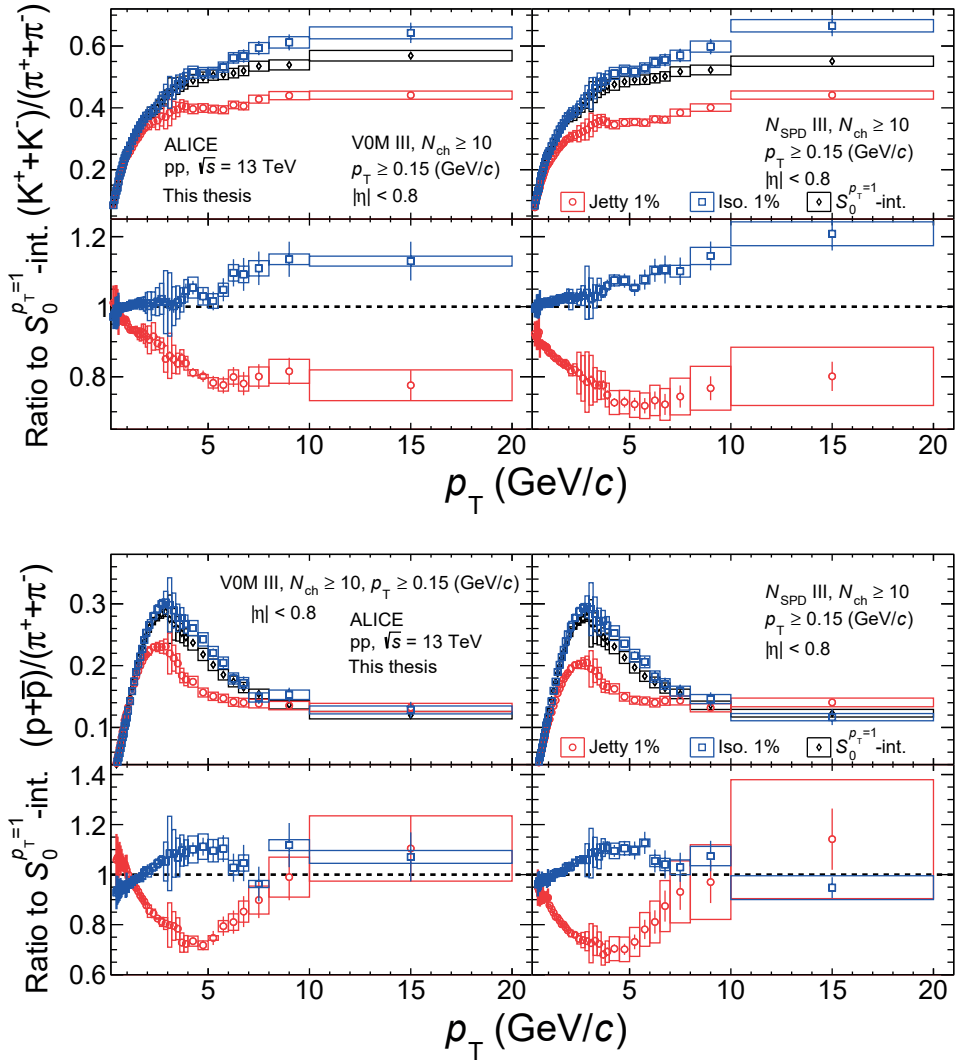


**Figure B.6:**  $p_T$ -differential  $K/\pi$  (top),  $p/\pi$  (bottom) and ratios to the  $S_0^{p_T=1}$ -integrated result. The results are shown for the top 1% jetty-like and isotropic events selected in the VOM III (left panels) and  $N_{SPD}$  III (right panels) multiplicity classes. The statistical and systematic uncertainties are represented with bars and boxes around the data points, respectively.

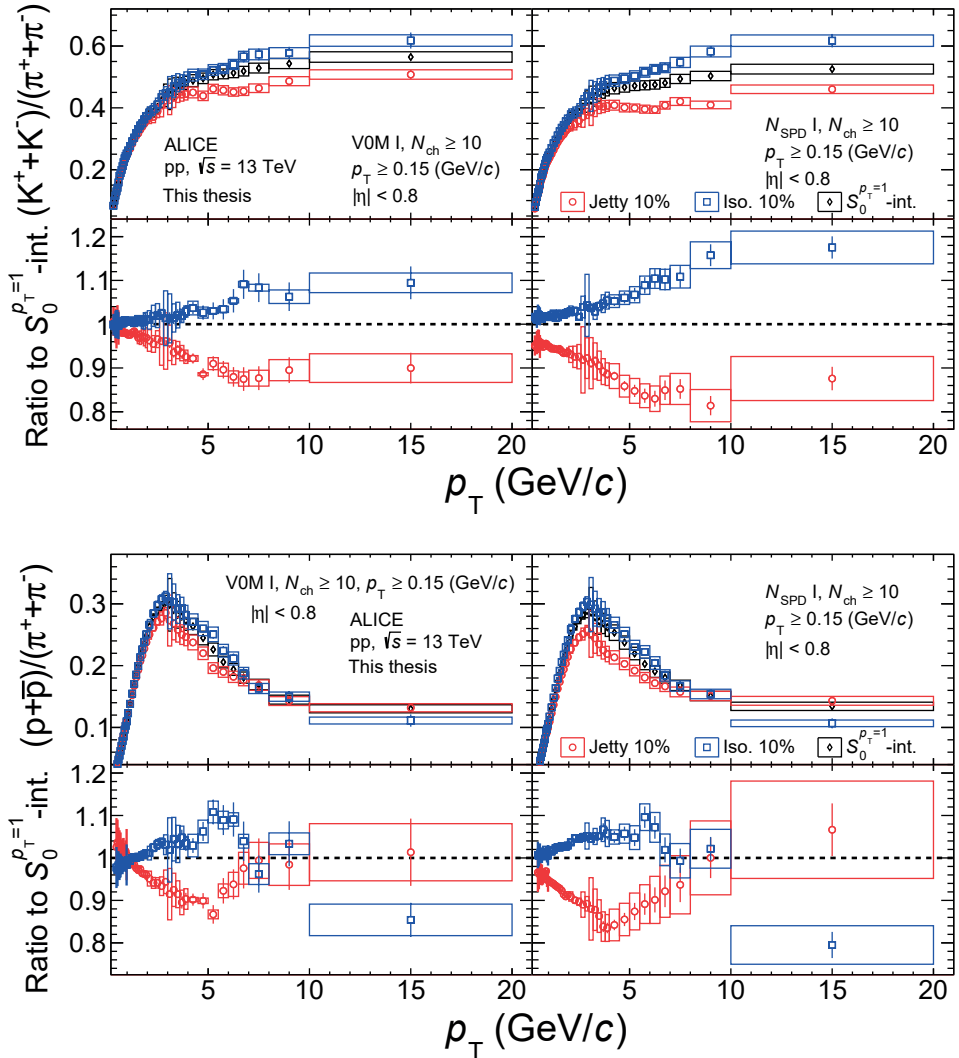


**Figure B.7:**  $p_T$ -differential  $K/\pi$  (top) and  $p/\pi$  (bottom) and ratios to the  $S_0^{p_T=1}$ -integrated result. The results are shown for the top 10 % jetty-like and isotropic events selected in the V0M I (left panels) and  $N_{SPD}$  I (right panels) multiplicity classes. The statistical and systematic uncertainties are represented with bars and boxes around the data points, respectively.

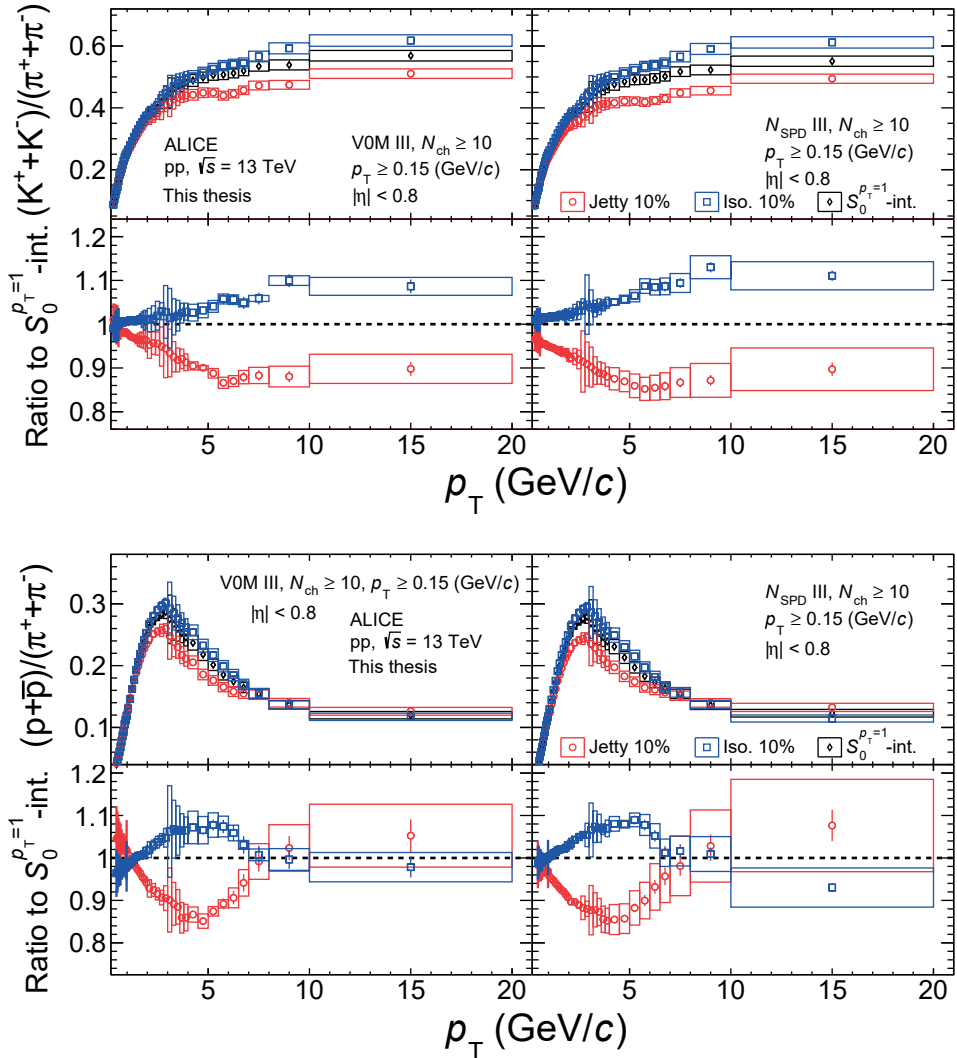


**Figure B.8:**  $p_T$ -differential  $K/\pi$  (top),  $p/\pi$  (bottom) and ratios to the  $S_0^{p_T=1}$ -integrated result. The results are shown for the top 10 % jetty-like and isotropic events selected in the VOM III (left panels) and  $N_{SPD}$  III (right panels) multiplicity classes. The statistical and systematic uncertainties are represented with bars and boxes around the data points, respectively.

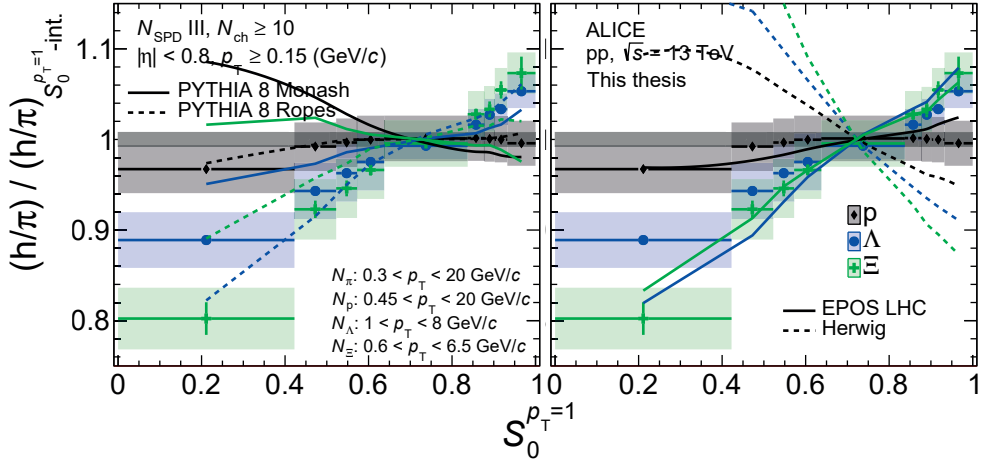


**Figure B.9:** Particle yield ratios to pions normalised to the values measured in the  $S_0^{p_T=1}$ -integrated sample as a function of  $S_0^{p_T=1}$ . The results are shown for the  $N_{\text{SPD III}}$  multiplicity class. The statistical and systematic uncertainties are represented with bars and shaded areas around the data points. The uncertainty bar in dark grey colour centred at one corresponds to the pions yields' systematic uncertainty. The different lines correspond to model predictions.

# References

- [1] J. C. Collins and M. J. Perry, “Superdense matter: Neutrons or asymptotically free quarks?”, *Phys. Rev. Lett.* **34** (May, 1975) .
- [2] N. Cabibbo and G. Parisi, “Exponential hadronic spectrum and quark liberation”, *Physics Letters B* **59** no. 1, (1975) .
- [3] D. Boyanovsky, H. J. de Vega, and D. J. Schwarz, “Phase transitions in the early and the present universe”, *Ann. Rev. Nucl. Part. Sci.* **56** (2006) , [arXiv:hep-ph/0602002](https://arxiv.org/abs/hep-ph/0602002).
- [4] **PHOBOS** Collaboration, B. B. Back *et al.*, “The PHOBOS perspective on discoveries at RHIC”, *Nucl. Phys. A* **757** (2005) , [arXiv:nucl-ex/0410022](https://arxiv.org/abs/nucl-ex/0410022).
- [5] **PHENIX** Collaboration, K. Adcox *et al.*, “Formation of dense partonic matter in relativistic nucleus-nucleus collisions at RHIC: Experimental evaluation by the PHENIX collaboration”, *Nucl. Phys. A* **757** (2005) , [arXiv:nucl-ex/0410003](https://arxiv.org/abs/nucl-ex/0410003).
- [6] **STAR** Collaboration, J. Adams *et al.*, “Experimental and theoretical challenges in the search for the quark gluon plasma: The STAR Collaboration’s critical assessment of the evidence from RHIC collisions”, *Nucl. Phys. A* **757** (2005) , [arXiv:nucl-ex/0501009](https://arxiv.org/abs/nucl-ex/0501009).
- [7] **ALICE** Collaboration, J. Adam *et al.*, “Direct photon production in Pb-Pb collisions at  $\sqrt{s_{NN}} = 2.76$  TeV”, *Phys. Lett. B* **754** (2016) , [arXiv:1509.07324 \[nucl-ex\]](https://arxiv.org/abs/1509.07324).
- [8] **HotQCD** Collaboration, P. Steinbrecher, “The QCD crossover at zero and non-zero baryon densities from Lattice QCD”, *Nucl. Phys. A* **982** (2019) , [arXiv:1807.05607 \[hep-lat\]](https://arxiv.org/abs/1807.05607).
- [9] **CMS** Collaboration, V. Khachatryan *et al.*, “Evidence for collectivity in pp collisions at the LHC”, *Phys. Lett. B* **765** (2017) , [arXiv:1606.06198 \[nucl-ex\]](https://arxiv.org/abs/1606.06198).

- [10] ALICE Collaboration, J. Adam *et al.*, “Enhanced production of multi-strange hadrons in high-multiplicity proton-proton collisions”, *Nature Phys.* **13** (2017) , arXiv:1606.07424 [nucl-ex].
- [11] C. Wong, *Introduction To High-energy Heavy-ion Collisions*. World Scientific Publishing Company, 1994.
- [12] D. H. Perkins, *Introduction to High Energy Physics*. Cambridge University Press, 4 ed., 2000.
- [13] B. Martin and G. Shaw, *Particle Physics*. Manchester Physics Series. Wiley, 2013.
- [14] **Particle Data Group** Collaboration, P. Zyla *et al.*, “Review of Particle Physics”, *PTEP* **2020** no. 8, (2020) .
- [15] K. G. Wilson, “Confinement of quarks”, *Phys. Rev. D* **10** (Oct, 1974) .
- [16] **HotQCD** Collaboration, A. Bazavov *et al.*, “Equation of state in ( 2+1 )-flavor QCD”, *Phys. Rev. D* **90** (2014) , arXiv:1407.6387 [hep-lat].
- [17] A. Bazavov, “The qcd equation of state”, *Nuclear Physics A* **931** (2014) . QUARK MATTER 2014.
- [18] A. Andronic, “An overview of the experimental study of quark-gluon matter in high-energy nucleus-nucleus collisions”, *Int. J. Mod. Phys. A* **29** (2014) , arXiv:1407.5003 [nucl-ex].
- [19] B. Muller, J. Schukraft, and B. Wyslouch, “First Results from Pb+Pb collisions at the LHC”, *Ann. Rev. Nucl. Part. Sci.* **62** (2012) , arXiv:1202.3233 [hep-ex].
- [20] J. N. Guenther, “Overview of the QCD phase diagram: Recent progress from the lattice”, *Eur. Phys. J. A* **57** no. 4, (2021) , arXiv:2010.15503 [hep-lat].
- [21] T. K. Nayak, “Probing the QCD phase structure using event-by-event fluctuations”, *J. Phys. Conf. Ser.* **1602** no. 1, (2020) , arXiv:2008.04643 [nucl-ex].
- [22] R. Snellings, “Collective Expansion at the LHC: selected ALICE anisotropic flow measurements”, *J. Phys. G* **41** no. 12, (2014) , arXiv:1408.2532 [nucl-ex].
- [23] R. Snellings, “How much does the hadronic phase contribute to the observed anisotropic flow at the lhc?”, *EPJ Web of Conferences* **97** (11, 2014) .

- [24] L. McLerran, “Relativistic heavy-ion physics: Three lectures”, in 2006 European School of High-Energy Physics, pp. 75–114. 2007.
- [25] E. Iancu and R. Venugopalan, The Color glass condensate and high-energy scattering in QCD, pp. 249–3363. 3, 2003. arXiv:hep-ph/0303204.
- [26] **ZEUS** Collaboration, J. Breitweg *et al.*, “ZEUS results on the measurement and phenomenology of  $F(2)$  at low  $x$  and low  $Q^{**2}$ ”, Eur. Phys. J. C **7** (1999) , arXiv:hep-ex/9809005.
- [27] L. McLerran and R. Venugopalan, “Computing quark and gluon distribution functions for very large nuclei”, Phys. Rev. D **49** (Mar, 1994) .
- [28] L. McLerran and R. Venugopalan, “Gluon distribution functions for very large nuclei at small transverse momentum”, Phys. Rev. D **49** (Apr, 1994) .
- [29] F. Gelis, E. Iancu, J. Jalilian-Marian, and R. Venugopalan, “The Color Glass Condensate”, Ann. Rev. Nucl. Part. Sci. **60** (2010) , arXiv:1002.0333 [hep-ph].
- [30] T. LAPPI, “Small  $x$  physics and RHIC data”, Int. J. Mod. Phys. E **20** no. 1, (2011) , arXiv:1003.1852 [hep-ph].
- [31] L. McLerran, “A Brief Introduction to the Color Glass Condensate and the Glasma”, in 38th International Symposium on Multiparticle Dynamics, pp. 3–18. 2009. arXiv:0812.4989 [hep-ph].
- [32] **BRAHMS** Collaboration, I. Arsene *et al.*, “Quark gluon plasma and color glass condensate at RHIC? The Perspective from the BRAHMS experiment”, Nucl. Phys. A **757** (2005) , arXiv:nucl-ex/0410020.
- [33] E. V. Shuryak, “What RHIC experiments and theory tell us about properties of quark-gluon plasma?”, Nucl. Phys. A **750** (2005) , arXiv:hep-ph/0405066.
- [34] U. W. Heinz, “Concepts of heavy ion physics”, in 2nd CERN-CLAF School of High Energy Physics, pp. 165–238. 7, 2004. arXiv:hep-ph/0407360.
- [35] K. Kajantie and H. I. Miettinen, “Temperature measurement of quark-gluon plasma formed in high energy nucleus-nucleus collisions”, Zeitschrift für Physik C Particles and Fields **9** no. 4, (1981) .
- [36] E. L. Feinberg, “Direct production of photons and dileptons in thermodynamical models of multiple hadron production”, Il Nuovo Cimento A (1965-1970) **34** no. 3, (1976) .

- [37] P. Braun-Munzinger, K. Redlich, and J. Stachel, “Particle production in heavy ion collisions”, [arXiv:nucl-th/0304013](https://arxiv.org/abs/nucl-th/0304013).
- [38] A. Andronic, P. Braun-Munzinger, and J. Stachel, “Hadron production in central nucleus-nucleus collisions at chemical freeze-out”, [Nucl. Phys. A 772](https://doi.org/10.1016/j.nuclphysa.2006.06.003) (2006) , [arXiv:nucl-th/0511071](https://arxiv.org/abs/nucl-th/0511071).
- [39] J. Stachel, A. Andronic, P. Braun-Munzinger, and K. Redlich, “Confronting LHC data with the statistical hadronization model”, [J. Phys. Conf. Ser. 509](https://doi.org/10.1088/1742-6596/509/1/012001) (2014) , [arXiv:1311.4662 \[nucl-th\]](https://arxiv.org/abs/1311.4662).
- [40] A. Andronic, P. Braun-Munzinger, and J. Stachel, “Thermal hadron production in relativistic nuclear collisions: The Hadron mass spectrum, the horn, and the QCD phase transition”, [Phys. Lett. B 673](https://doi.org/10.1016/j.physlettb.2009.07.040) (2009) , [arXiv:0812.1186 \[nucl-th\]](https://arxiv.org/abs/0812.1186). [Erratum: [Phys.Lett.B 678, 516 \(2009\)](https://doi.org/10.1016/j.physlettb.2009.09.040)].
- [41] A. Andronic *et al.*, “Hadron Production in Ultra-relativistic Nuclear Collisions: Quarkyonic Matter and a Triple Point in the Phase Diagram of QCD”, [Nucl. Phys. A 837](https://doi.org/10.1016/j.nuclphysa.2010.02.002) (2010) , [arXiv:0911.4806 \[hep-ph\]](https://arxiv.org/abs/0911.4806).
- [42] E. Schnedermann, J. Sollfrank, and U. W. Heinz, “Thermal phenomenology of hadrons from 200-A/GeV S+S collisions”, [Phys. Rev. C 48](https://doi.org/10.1103/PhysRevC.48.014902) (1993) , [arXiv:nucl-th/9307020](https://arxiv.org/abs/nucl-th/9307020).
- [43] **ALICE** Collaboration, S. Acharya *et al.*, “Production of charged pions, kaons, and (anti-)protons in Pb-Pb and inelastic  $p\bar{p}$  collisions at  $\sqrt{s_{NN}} = 5.02$  TeV”, [Phys. Rev. C 101](https://doi.org/10.1103/PhysRevC.101.044902) no. 4, (2020) , [arXiv:1910.07678 \[nucl-ex\]](https://arxiv.org/abs/1910.07678).
- [44] N. Herrmann, J. P. Wessels, and T. Wienold, “Collective flow in heavy-ion collisions”, [Annual Review of Nuclear and Particle Science 49](https://doi.org/10.1146/annurev-nucl-101998-021440) no. 1, (1999) .
- [45] **ALICE** Collaboration, K. Aamodt *et al.*, “Harmonic decomposition of two-particle angular correlations in Pb-Pb collisions at  $\sqrt{s_{NN}} = 2.76$  TeV”, [Phys. Lett. B 708](https://doi.org/10.1016/j.physlettb.2012.02.020) (2012) , [arXiv:1109.2501 \[nucl-ex\]](https://arxiv.org/abs/1109.2501).
- [46] **ALICE** Collaboration, K. Aamodt *et al.*, “Higher harmonic anisotropic flow measurements of charged particles in Pb-Pb collisions at  $\sqrt{s_{NN}}=2.76$  TeV”, [Phys. Rev. Lett. 107](https://doi.org/10.1103/PhysRevLett.107.192301) (2011) , [arXiv:1105.3865 \[nucl-ex\]](https://arxiv.org/abs/1105.3865).
- [47] B. Alver and G. Roland, “Collision-geometry fluctuations and triangular flow in heavy-ion collisions”, [Phys. Rev. C 81](https://doi.org/10.1103/PhysRevC.81.054902) (May, 2010) .
- [48] **ALICE** Collaboration, B. B. Abelev *et al.*, “Elliptic flow of identified hadrons in Pb-Pb collisions at  $\sqrt{s_{NN}} = 2.76$  TeV”, [JHEP 06](https://doi.org/10.1007/JHEP06(2015)045) (2015) , [arXiv:1405.4632 \[nucl-ex\]](https://arxiv.org/abs/1405.4632).

- [49] J. D. Bjorken, “Energy loss of energetic partons in quark-gluon plasma: possible extinction of high  $p_T$  jets in hadron-hadron collisions”, tech. rep., FERMILAB, Batavia, IL, Aug, 1982.
- [50] **STAR** Collaboration, J. Adams *et al.*, “Evidence from d + Au measurements for final state suppression of high p(T) hadrons in Au+Au collisions at RHIC”, *Phys. Rev. Lett.* **91** (2003) , arXiv:nucl-ex/0306024.
- [51] **STAR** Collaboration, C. Adler *et al.*, “Disappearance of back-to-back high  $p_T$  hadron correlations in central Au+Au collisions at  $\sqrt{s_{NN}} = 200\text{-GeV}$ ”, *Phys. Rev. Lett.* **90** (2003) , arXiv:nucl-ex/0210033.
- [52] **ALICE** Collaboration, J. Adam *et al.*, “Centrality dependence of the nuclear modification factor of charged pions, kaons, and protons in Pb-Pb collisions at  $\sqrt{s_{NN}} = 2.76\text{ TeV}$ ”, *Phys. Rev. C* **93** no. 3, (2016) , arXiv:1506.07287 [nucl-ex].
- [53] H. Yukawa, “On the Interaction of Elementary Particles I”, *Proc. Phys. Math. Soc. Jap.* **17** (1935) .
- [54] E. Hückel, “Zur theorie der elektrolyte”, *Phys. Z.* **24** (07, 2015) .
- [55] A. Bazavov and J. H. Weber, “Color Screening in Quantum Chromodynamics”, *Prog. Part. Nucl. Phys.* **116** (2021) , arXiv:2010.01873 [hep-lat].
- [56] S. Digal, P. Petreczky, and H. Satz, “Quarkonium feed down and sequential suppression”, *Phys. Rev. D* **64** (2001) , arXiv:hep-ph/0106017.
- [57] T. Matsui and H. Satz, “ $J/\psi$  suppression by quark-gluon plasma formation”, *Physics Letters B* **178** no. 4, (1986) .
- [58] A. Mocsy and P. Petreczky, “Color screening melts quarkonium”, *Phys. Rev. Lett.* **99** (2007) , arXiv:0706.2183 [hep-ph].
- [59] **CMS** Collaboration, A. M. Sirunyan *et al.*, “Measurement of nuclear modification factors of  $\Upsilon(1S)$ ,  $\Upsilon(2S)$ , and  $\Upsilon(3S)$  mesons in PbPb collisions at  $\sqrt{s_{NN}} = 5.02\text{ TeV}$ ”, *Phys. Lett. B* **790** (2019) , arXiv:1805.09215 [hep-ex].
- [60] **PHOBOS** Collaboration, B. Alver *et al.*, “System size dependence of cluster properties from two-particle angular correlations in Cu+Cu and Au+Au collisions at  $s(NN)^{(1/2)} = 200\text{-GeV}$ ”, *Phys. Rev. C* **81** (2010) , arXiv:0812.1172 [nucl-ex].

- [61] **PHOBOS** Collaboration, B. Alver *et al.*, “High transverse momentum triggered correlations over a large pseudorapidity acceptance in Au+Au collisions at  $s_{\text{NN}}^{**1/2} = 200 \text{ GeV}$ ”, *Phys. Rev. Lett.* **104** (2010) , arXiv:0903.2811 [nucl-ex].
- [62] **STAR** Collaboration, B. I. Abelev *et al.*, “Long range rapidity correlations and jet production in high energy nuclear collisions”, *Phys. Rev. C* **80** (2009) , arXiv:0909.0191 [nucl-ex].
- [63] C. Gale, S. Jeon, and B. Schenke, “Hydrodynamic Modeling of Heavy-Ion Collisions”, *Int. J. Mod. Phys. A* **28** (2013) , arXiv:1301.5893 [nucl-th].
- [64] J.-Y. Ollitrault, “Anisotropy as a signature of transverse collective flow”, *Phys. Rev. D* **46** (Jul, 1992) .
- [65] U. Heinz and R. Snellings, “Collective flow and viscosity in relativistic heavy-ion collisions”, *Ann. Rev. Nucl. Part. Sci.* **63** (2013) , arXiv:1301.2826 [nucl-th].
- [66] **ALICE** Collaboration, O. Vázquez Rueda, “Baryon production from small to large collision systems at ALICE”, *PoS EPS-HEP2019* (2020) , arXiv:2001.03156 [hep-ex].
- [67] A. Ortiz Velasquez, P. Christiansen, E. Cuautle Flores, I. Maldonado Cervantes, and G. Paic, “Color Reconnection and Flowlike Patterns in  $pp$  Collisions”, *Phys. Rev. Lett.* **111** no. 4, (2013) , arXiv:1303.6326 [hep-ph].
- [68] **ALICE** Collaboration, J. Adam *et al.*, “Multi-strange baryon production in p-Pb collisions at  $\sqrt{s_{\text{NN}}} = 5.02 \text{ TeV}$ ”, *Phys. Lett. B* **758** (2016) , arXiv:1512.07227 [nucl-ex].
- [69] **ALICE** Collaboration, B. Abelev *et al.*, “Multi-strange baryon production in  $pp$  collisions at  $\sqrt{s} = 7 \text{ TeV}$  with ALICE”, *Phys. Lett. B* **712** (2012) , arXiv:1204.0282 [nucl-ex].
- [70] **ALICE** Collaboration, S. Acharya *et al.*, “Multiplicity dependence of (multi-)strange hadron production in proton-proton collisions at  $\sqrt{s} = 13 \text{ TeV}$ ”, *Eur. Phys. J. C* **80** no. 2, (2020) , arXiv:1908.01861 [nucl-ex].
- [71] M. L. Mangano, “Introduction to QCD”,  
<https://cds.cern.ch/record/454171>.
- [72] S. Ferreres-Solé and T. Sjöstrand, “The space–time structure of hadronization in the Lund model”, *Eur. Phys. J. C* **78** no. 11, (2018) , arXiv:1808.04619 [hep-ph].

- [73] G. S. Bali and K. Schilling, “Static quark-antiquark potential: Scaling behavior and finite-size effects in su (3) lattice gauge theory”, *Physical Review D* **46** no. 6, (1992) .
- [74] B. Andersson, G. Gustafson, G. Ingelman, and T. Sjöstrand, “Parton fragmentation and string dynamics”, *Physics Reports* **97** no. 2-3, (1983) .
- [75] **ALICE** Collaboration, B. B. Abelev *et al.*, “Multiplicity dependence of the average transverse momentum in pp, p-Pb, and Pb-Pb collisions at the LHC”, *Phys. Lett. B* **727** (2013) , arXiv:1307.1094 [nucl-ex].
- [76] **ATLAS** Collaboration, G. Aad *et al.*, “Charged-particle multiplicities in pp interactions measured with the ATLAS detector at the LHC”, *New J. Phys.* **13** (2011) , arXiv:1012.5104 [hep-ex].
- [77] **CMS** Collaboration, V. Khachatryan *et al.*, “Charged Particle Multiplicities in pp Interactions at  $\sqrt{s} = 0.9, 2.36$ , and  $7$  TeV”, *JHEP* **01** (2011) , arXiv:1011.5531 [hep-ex].
- [78] T. Sjöstrand, “Colour reconnection and its effects on precise measurements at the LHC”, 10, 2013. arXiv:1310.8073 [hep-ph].
- [79] G. Gustafson, “Multiple interactions, saturation, and final states in pp collisions and dis”, *Acta Physica Polonica B* **40** (05, 2009) .
- [80] K. Werner, I. Karpenko, T. Pierog, M. Bleicher, and K. Mikhailov, “Event-by-Event Simulation of the Three-Dimensional Hydrodynamic Evolution from Flux Tube Initial Conditions in Ultrarelativistic Heavy Ion Collisions”, *Phys. Rev. C* **82** (2010) , arXiv:1004.0805 [nucl-th].
- [81] K. Werner, “Core-corona separation in ultra-relativistic heavy ion collisions”, *Phys. Rev. Lett.* **98** (2007) , arXiv:0704.1270 [nucl-th].
- [82] T. Pierog, I. Karpenko, J. M. Katzy, E. Yatsenko, and K. Werner, “EPOS LHC: Test of collective hadronization with data measured at the CERN Large Hadron Collider”, *Phys. Rev. C* **92** no. 3, (2015) , arXiv:1306.0121 [hep-ph].
- [83] J. D. Jackson, “Classical electrodynamics, 3rd ed.”, *American Journal of Physics* **67** no. 9, (1999) .
- [84] H. Kolanoski and N. Wermes, *Particle Detectors: Fundamentals and Applications*. Oxford University Press, 2020.
- [85] H. Bethe, “Zur Theorie des Durchgangs schneller Korpuskularstrahlen durch Materie”, *Annalen der Physik* **397** no. 3, (Jan., 1930) .

- [86] F. Bloch, “Bremsvermögen von Atomen mit mehreren Elektronen”, *Zeitschrift für Physik* **81** no. 5-6, (May, 1933) .
- [87] F. Bloch, “Zur bremsung rasch bewegter teilchen beim durchgang durch materie”, *Annalen der Physik* **408** no. 3, (1933) .
- [88] R. Fernow and R. Fernow, *Introduction to Experimental Particle Physics*. Cambridge University Press, 1989.
- [89] C. Lippmann, “Performance of the ALICE Time Projection Chamber”, *Phys. Procedia* **37** (2012) .
- [90] P. V. Vavilov, “Ionization losses of high-energy heavy particles”, *Sov. Phys. JETP* **5** (1957) .
- [91] L. Landau, “On the energy loss of fast particles by ionization”, *J. Phys. (USSR)* **8** (1944) .
- [92] **ALICE** Collaboration, B. B. Abelev *et al.*, “Performance of the ALICE Experiment at the CERN LHC”, *Int. J. Mod. Phys. A* **29** (2014) , arXiv:1402.4476 [nucl-ex].
- [93] **ALICE** Collaboration, K. Aamodt *et al.*, “The ALICE experiment at the CERN LHC”, *Journal of Instrumentation* **3** no. 08, (Aug, 2008) .
- [94] **ALICE** Collaboration, K. Aamodt *et al.*, “Centrality dependence of the charged-particle multiplicity density at mid-rapidity in Pb-Pb collisions at  $\sqrt{s_{NN}} = 2.76$  TeV”, *Phys. Rev. Lett.* **106** (2011) , arXiv:1012.1657 [nucl-ex].
- [95] **ALICE** Collaboration, E. Abbas *et al.*, “Performance of the ALICE VZERO system”, *JINST* **8** (2013) , arXiv:1306.3130 [nucl-ex].
- [96] **ALICE** Collaboration, B. Abelev *et al.*, “Centrality determination of Pb-Pb collisions at  $\sqrt{s_{NN}} = 2.76$  TeV with ALICE”, *Phys. Rev. C* **88** no. 4, (2013) , arXiv:1301.4361 [nucl-ex].
- [97] **ALICE** Collaboration, S. Acharya *et al.*, “Multiplicity dependence of light-flavor hadron production in pp collisions at  $\sqrt{s} = 7$  TeV”, *Phys. Rev. C* **99** no. 2, (2019) , arXiv:1807.11321 [nucl-ex].
- [98] M. L. Miller, K. Reygers, S. J. Sanders, and P. Steinberg, “Glauber modeling in high energy nuclear collisions”, *Ann. Rev. Nucl. Part. Sci.* **57** (2007) , arXiv:nucl-ex/0701025.

- [99] **ALICE** Collaboration, K. Aamodt et al., “First proton-proton collisions at the LHC as observed with the ALICE detector: Measurement of the charged particle pseudorapidity density at  $s^{**}(1/2) = 900\text{-GeV}$ ”, *Eur. Phys. J. C* **65** (2010) , arXiv:0911.5430 [hep-ex].
- [100] **ALICE** Collaboration, K. Aamodt et al., “Charged-particle multiplicity measurement in proton-proton collisions at  $\sqrt{s} = 0.9$  and  $2.36$  TeV with ALICE at LHC”, *Eur. Phys. J. C* **68** (2010) , arXiv:1004.3034 [hep-ex].
- [101] D. Kharzeev, E. Levin, and M. Nardi, “Color glass condensate at the LHC: Hadron multiplicities in pp, pA and AA collisions”, *Nucl. Phys. A* **747** (2005) , arXiv:hep-ph/0408050.
- [102] W.-T. Deng, X.-N. Wang, and R. Xu, “Hadron production in p+p, p+Pb, and Pb+Pb collisions with the HIJING 2.0 model at energies available at the CERN Large Hadron Collider”, *Phys. Rev. C* **83** (2011) , arXiv:1008.1841 [hep-ph].
- [103] **ALICE** Collaboration, K. Aamodt et al., “Alignment of the ALICE Inner Tracking System with cosmic-ray tracks”, *JINST* **5** (2010) , arXiv:1001.0502 [physics.ins-det].
- [104] J. Alme et al., “The ALICE TPC, a large 3-dimensional tracking device with fast readout for ultra-high multiplicity events”, *Nucl. Instrum. Meth. A* **622** (2010) , arXiv:1001.1950 [physics.ins-det].
- [105] **ALICE** Collaboration, G. Dellacasa et al., *ALICE time projection chamber: Technical Design Report*. Technical design report. ALICE. CERN, Geneva, 2000.
- [106] A. Kalweit, *Production of light flavor hadrons and anti-nuclei at the LHC*. PhD thesis, Darmstadt, Tech. Hochsch., 2012.
- [107] **ALICE** Collaboration, *ALICE Time-Of-Flight system (TOF): Technical Design Report*. Technical design report. ALICE. CERN, Geneva, 2000.  
<http://cds.cern.ch/record/430132>.
- [108] **ALICE** Collaboration, J. Adam et al., “Determination of the event collision time with the ALICE detector at the LHC”, *Eur. Phys. J. Plus* **132** no. 2, (2017) , arXiv:1610.03055 [physics.ins-det].
- [109] M. Ivanov, K. Safarik, Y. Belikov, and J. Bracinik, “TPC tracking and particle identification in high-density environment”, *arXiv e-prints* (June, 2003) , arXiv:physics/0306108 [physics.data-an].

- [110] M. Ivanov, I. Belikov, P. Hristov, and K. Šafařík, “Track reconstruction in high density environment”, *Nuclear Instruments and Methods in Physics Research Section A: Accelerators, Spectrometers, Detectors and Associated Equipment* **566** no. 1, (2006) .
- [111] R. Fruhwirth, “Application of Kalman filtering to track and vertex fitting”, *Nucl. Instrum. Meth. A* **262** (1987) .
- [112] J. M. Gronefeld, *Transverse Momentum Distributions and Nuclear Modification Factors in Heavy-Ion Collisions with ALICE at the Large Hadron Collider*. PhD thesis, Technische Universität, Darmstadt, 2018.
- [113] **ALICE** Collaboration, B. B. Abelev *et al.*, “Production of charged pions, kaons and protons at large transverse momenta in pp and Pb–Pb collisions at  $\sqrt{s_{\text{NN}}} = 2.76 \text{ TeV}$ ”, *Phys. Lett. B* **736** (2014) , arXiv:1401.1250 [nucl-ex].
- [114] R. Brun, F. Bruyant, M. Maire, A. C. McPherson, and P. Zanarini, *GEANT 3: user’s guide Geant 3.10, Geant 3.11; rev. version*. CERN, Geneva, 1987. <https://cds.cern.ch/record/1119728>.
- [115] **ALICE** Collaboration, “The ALICE definition of primary particles”., <https://cds.cern.ch/record/2270008>.
- [116] **ALICE** Collaboration, K. Aamodt *et al.*, “Midrapidity antiproton-to-proton ratio in pp collisions at  $\sqrt{s} = 0.9$  and  $7\text{--}70 \text{ TeV}$  measured by the ALICE experiment”, *Phys. Rev. Lett.* **105** (2010) , arXiv:1006.5432 [hep-ex].
- [117] V. Vislavicius, “Identified Hadron Production as a Function of Event Multiplicity and Transverse Spherocity in pp Collisions at  $\sqrt{s} = 7$  and  $13 \text{ TeV}$  with the ALICE Detector”, 2018. Presented 23 Mar 2018.
- [118] **ATLAS** Collaboration, G. Aad *et al.*, “Measurement of the underlying event in jet events from  $7 \text{ TeV}$  proton-proton collisions with the ATLAS detector”, *Eur. Phys. J. C* **74** no. 8, (2014) , arXiv:1406.0392 [hep-ex].
- [119] **ALICE** Collaboration, S. Acharya *et al.*, “Underlying Event properties in pp collisions at  $\sqrt{s} = 13 \text{ TeV}$ ”, *JHEP* **04** (2020) , arXiv:1910.14400 [nucl-ex].
- [120] **CDF** Collaboration, T. Affolder *et al.*, “Charged jet evolution and the underlying event in proton-antiproton collisions at  $1.8 \text{ TeV}$ ”, *Phys. Rev. D* **65** (Apr, 2002) .
- [121] T. Martin, P. Skands, and S. Farrington, “Probing Collective Effects in Hadronisation with the Extremes of the Underlying Event”, *Eur. Phys. J. C* **76** no. 5, (2016) , arXiv:1603.05298 [hep-ph].

- [122] G. D'Agostini, “A Multidimensional unfolding method based on Bayes' theorem”, *Nucl. Instrum. Meth. A* **362** (1995) .
- [123] A. Ortiz, G. Paić, and E. Cuautle, “Mid-rapidity charged hadron transverse spherocity in pp collisions simulated with Pythia”, *Nucl. Phys. A* **941** (2015) , arXiv:1503.03129 [hep-ph].
- [124] A. Ortiz, “Experimental results on event shapes at hadron colliders”, *Adv. Ser. Direct. High Energy Phys.* **29** (2018) , arXiv:1705.02056 [hep-ex].
- [125] **ALICE** Collaboration, S. Acharya et al., “Multiplicity dependence of  $\pi$ , K, and p production in pp collisions at  $\sqrt{s} = 13$  TeV”, *Eur. Phys. J. C* **80** no. 8, (2020) , arXiv:2003.02394 [nucl-ex].
- [126] P. Skands, S. Carrazza, and J. Rojo, “Tuning PYTHIA 8.1: the Monash 2013 Tune”, *Eur. Phys. J. C* **74** no. 8, (2014) , arXiv:1404.5630 [hep-ph].
- [127] C. Bierlich, G. Gustafson, L. Lönnblad, and A. Tarasov, “Effects of Overlapping Strings in pp Collisions”, *JHEP* **03** (2015) , arXiv:1412.6259 [hep-ph].
- [128] M. Bahr et al., “Herwig++ Physics and Manual”, *Eur. Phys. J. C* **58** (2008) , arXiv:0803.0883 [hep-ph].
- [129] J. Bellm et al., “Herwig 7.0/Herwig++ 3.0 release note”, *Eur. Phys. J. C* **76** no. 4, (2016) , arXiv:1512.01178 [hep-ph].
- [130] **ALICE** Collaboration, B. Abelev et al., “Underlying Event measurements in pp collisions at  $\sqrt{s} = 0.9$  and 7 TeV with the ALICE experiment at the LHC”, *JHEP* **07** (2012) , arXiv:1112.2082 [hep-ex].
- [131] **CMS** Collaboration, S. Chatrchyan et al., “Jet and Underlying Event Properties as a Function of Charged-Particle Multiplicity in Proton–Proton Collisions at  $\sqrt{s} = 7$  TeV”, *Eur. Phys. J. C* **73** no. 12, (2013) , arXiv:1310.4554 [hep-ex].
- [132] **ALICE** Collaboration, B. B. Abelev et al., “Multiplicity Dependence of Pion, Kaon, Proton and Lambda Production in p-Pb Collisions at  $\sqrt{s_{NN}} = 5.02$  TeV”, *Phys. Lett. B* **728** (2014) , arXiv:1307.6796 [nucl-ex].
- [133] **ALICE** Collaboration, B. Abelev et al., “Transverse sphericity of primary charged particles in minimum bias proton-proton collisions at  $\sqrt{s} = 0.9$ , 2.76 and 7 TeV”, *Eur. Phys. J. C* **72** (2012) , arXiv:1205.3963 [hep-ex].

- [134] **ALICE** Collaboration, S. Acharya *et al.*, “Charged-particle production as a function of multiplicity and transverse spherocity in pp collisions at  $\sqrt{s} = 5.02$  and 13 TeV”, *Eur. Phys. J. C* **79** no. 10, (2019) , arXiv:1905.07208 [nucl-ex].
- [135] **ALICE** Collaboration, S. Acharya *et al.*, “Production of  $\Lambda$  and  $K_s^0$  in jets in p–Pb collisions at  $\sqrt{s_{NN}}=5.02$  TeV and pp collisions at  $\sqrt{s}=7$  TeV”, *Phys. Lett. B* **827** (2022) , arXiv:2105.04890 [nucl-ex].



Department of Physics  
Particle Physics

ISBN 978-91-8039-281-5

